TECHNISCHE UNIVERSITÄT DRESDEN

Fakultät für Mathematik und Naturwissenschaften Fachrichtung Physik, Institut für Theoretische Physik

Professur für Theoretische Atom- und Molekülphysik

SEMICLASSICAL INITIAL VALUE REPRESENTATION FOR COMPLEX DYNAMICS

Max Buchholz

Born on: 11th May 1984 in Schwerin

DISSERTATION

to achieve the academic degree

DOKTOR DER NATURWISSENSCHAFTEN (DR. RER. NAT.)

First referee

Prof. Dr. Rüdiger Schmidt

Second referee

Prof. Dr. Jiří Vaníček

Submitted on: 10th March 2017

ABSTRACT

Semiclassical initial value representations (SC-IVRs) are popular methods for an approximate description of the quantum dynamics of atomic and molecular systems. A very efficient special case is the propagator by Herman and Kluk, which will be the basis for the investigations in this work. It consists of a phase space integration over initial conditions of classical trajectories which are guiding Gaussian wavepackets. A complex phase factor in the integrand allows for interference between different trajectories, which leads to soft quantum effects being naturally included in the description. The underlying classical trajectories allow for an approximate description of the dynamics of large quantum systems that are inaccessible for a full quantum propagation. Moreover, they also provide an intuitive understanding of quantum phenomena in terms of classical dynamics. The main focus of this work is on further approximations to Herman-Kluk propagation whose applicability to complex dynamics is limited by the number of trajectories that are needed for numerical convergence of the phase space integration. The central idea for these approximations is the semiclassical hybrid formalism which utilizes the costly Herman-Kluk propagator only for a small number of system degrees of freedom (DOFs). The remaining environmental DOFs are treated on the level of Heller's thawed Gaussian wavepacket dynamics, a single trajectory method which is exact only for at most harmonic potentials. If the environmental DOFs are weakly coupled and therefore close to their potential minimum, this level of accuracy is sufficient to account for their effect on the system. Thus, the hybrid approximation efficiently combines accuracy and low numerical cost. As a central theoretical result, we apply this hybrid idea to a time-averaging scheme to arrive at a method for the calculation of vibrational spectra of molecules that is both accurate and efficient.

This time-averaged hybrid propagation is then used to study the vibrational dynamics of an iodine-like Morse oscillator bilinearly coupled to a Caldeira-Leggett bath of harmonic oscillators. We first validate the method by comparing it to full quantum and Herman-Kluk propagation for appropriately sized environments. After having established its accuracy, we include more bath DOFs to investigate the influence of the Caldeira-Leggett counter term on the shift of the vibrational levels of the Morse oscillator. As a result, we find out that a redshift, which is observed experimentally for, e.g., iodine in a rare gas matrix, occurs only if the counter term is not included in the Hamiltonian. We then move away from the model bath and on to a realistic, experimentally relevant environment consisting of krypton atoms. We put the iodine molecule into a cluster of 17 krypton atoms and investigate the loss of coherence of the iodine vibration upon coupling to just a few normal coordinates of the bath. These modes with the same symmetry as the iodine vibration turn out to be sufficient to reproduce the expected qualitative dependence on bath temperature and initial state of the iodine molecule. With these few normal modes, a full quantum calculation yields values for coherence loss rates that are close to experimental results. Furthermore, a comparison to semiclassical calculations with more bath modes included confirms the importance of the few highly symmetric normal coordinates. Then, we apply the time-averaged hybrid formalism once more to calculate the vibrational spectrum of the iodine molecule in this now anharmonic krypton environment. Using a krypton matrix instead of a cluster geometry, we find the correct qualitative and also quite good quantitative agreement for the shift of the iodine potential.

Finally, we will investigate a more fundamental question, namely, if SC-IVRs contain the spin effects due to the Pauli exclusion principle. To this end, we apply a number of SC-IVRs to the scattering of two electrons with initial states corresponding to either parallel or antiparallel spin. We compare the outcome to full quantum results and find that the difference is resolved by those methods that comprise multiple interfering trajectories.

CONTENTS

1. INTRODUCTION

The description of the dynamics of quantum systems is an important task in many fields of theoretical physics. At first sight, the solution is obvious – just take the almost century-old Schrödinger equation, plug in the potential and solve for psi, which usually denotes the wave function. Alas, as is known from any introduction to quantum mechanics, analytic solutions exist only for few textbook examples. As soon as there is nontrivial coupling between the degrees of freedom (DOFs) of the quantum system, one has to resort to numerical solutions. In a (numerically) exact fashion, this again works only within tight limits, namely, for a low number of DOFs, because the number of basis states or grid points required for representing the wave function grows exponentially with the system's dimensions. Without the possibility of finding an analytically or numerically exact, full quantum solution to a general system, alternative descriptions and approximations of some kind have to be introduced in order to make its dynamics accessible. To date, there is no single method that is ideally suited to describe every conceivable quantum system; instead, the approach has to be chosen according to the properties of the particular atomic or molecular system and according to the specific problem under investigation.

Therefore, over the last decades, a host of different numerical treatments of time-dependent quantum systems has been developed. It would be far beyond the scope of this introduction to compile an exhaustive list, but we want to name at least two widely popular methods before we describe our approach as another alternative. In time-dependent density functional theory (TDDFT), one does not calculate the wavefunction but rather the single-particle density, from which, in principle, all time-evolved observables can be found. The correspondence of this approach with results obtained from the Schrödinger equation is ensured through the Runge-Gross theorem that establishes a one-to-one mapping between the density and the external potential [1]. It gives rise to numerous quantum-classical methods, where the electronic density is calculated quantum mechanically, while the nuclei are treated classically; an example for one such method is non-adiabatic quantum molecular dynamics [2]. TDDFT has seen many successful applications in all areas of quantum dynamics, as exemplified by a recent review and extensive references therein [3]. Another approach, again with a wide range of applications, is known under the name of multi-configurational time-dependent Hartree (MCTDH) [4, 5]. It relies on a representation of the wavefunction in terms of (a combination of) single-particle wave functions. Using the Dirac-Frenkel variational principle, equations of motion can be derived for the coefficients as well as for the expansion functions. In order for the method to work efficiently and avoid exponential scaling, the Hamiltonian has to be represented in an

appropriate product form, which is one of the main challenges of this methodology. In the 25 years since its introduction, MCTDH has seen several extensions such as multilayer MCTDH, which allows for the inclusion of hundreds of DOFs [6].

In this work, we will focus on a methodology that takes a different route towards describing the time evolution of a quantum system, namely, semiclassical dynamics, and in particular semiclassical initial value representations (SC-IVRs). While TDDFT and MCTDH take a top-down approach – starting from the full quantum problem and finding approximations to the potential such that analytical or numerical calculations become feasible –, SC-IVRs go the other way, using classical trajectories as the backbone and adding a complex, action-dependent phase factor in order to allow for interference and thus incorporate quantum effects. This uniform description of all DOFs with interfering trajectories is different from quantum-classical schemes like the ones mentioned above, which are sometimes also referred to as semiclassical in the literature. Apart from possible numerical savings, relying on classical trajectories brings about the conceptual advantage of explaining and understanding quantum results intuitively in terms of classical mechanics. On the other hand, unlike in classical molecular dynamics, soft quantum effects such as zero-point energy and interference are an inherent part of semiclassical theories without having to resort to any ad-hoc additions to the equations of motion.

The semiclassical expression for the time evolution of a quantum system can be derived from the (exact) path integral formulation of the position space matrix element of the time evolution operator, or propagator, that has been introduced by R. Feynman [7]. The so-called semiclassical approximation makes a stationary phase approximation to the propagator, assuming that the typical action of the system is much larger than the reduced Planck constant $\hbar$ [8]. The resulting van Vleck-Gutzwiller propagator consists of a sum of all classical trajectories connecting initial and final position, weighted with a complex phase factor. Finding the propagator thus entails a root search for solving the boundary value problem, which may be numerically unfavorable. In addition, the van Vleck-Gutzwiller propagator contains a determinantial prefactor that becomes singular at caustics. These issues are addressed elegantly in the dephasing representation for quantum fidelity and more general correlation functions. By making use of the shadowing theorem, the prefactor is removed and the resulting expression needs very few trajectories for convergence [9, 10]. Alternatively, one can express the exact propagator in terms of coherent states and replace the resulting coherent state matrix element of the time evolution operator by its semiclassical approximation, which is found in the same way as before. Evaluating the integration over final positions in another stationary phase approximation [11] then yields an expression where only an integration over the initial phase space positions is left. This is referred to as initial value representation (IVR). While it is possible to express the IVR time evolution operator in terms of Cartesian position and momentum eigenstates [12], the most widely used form is the one suggested by M. Herman and E. Kluk in 1984 [13]. This Herman-Kluk (HK) propagator makes use of coherent states $|g(\mathbf{p}_0, \mathbf{q}_0)\rangle$ represented by Gaussian wave packets, which are in between position and momentum eigenstates in the sense that they become one or the other in the limit of their width going to zero and infinity, respectively. Like any other SC-IVR, the HK propagator contains a phase space integration over initial conditions, and, as before, each trajectory is weighted with a complex phase allowing for interference as well as a prefactor that depends on the stability of a given trajectory. Ten years after its first appearance, the HK propagator was shown to be an efficient special case of a more general IVR in a rederivation by K. Kay [14, 15].

Converging the phase space integral is the main numerical challenge of SC-IVR calculations. In spite of efficient sampling algorithms such as Monte Carlo, a growing number of DOFs necessitates larger and larger numbers of trajectories. Early SC-IVR applications have thus

been focusing on relatively small systems. For example, eigenvalue spectra turned out to be in good agreement with quantum results for the two-dimensional stadium billiard [16] and the HCI dimer [17]. Furthermore, the HK propagator is not restricted to molecular systems, but can also be applied to electronic dynamics. The high-harmonic generation spectrum of an electron in a laser field has been studied semiclassically by G. van de Sand and J.-M. Rost with the instructive result that a relatively small partition of trapped and stranded trajectories are responsible for reproducing the characteristic features of this spectrum [18]. If one is interested in more complex systems with many DOFs, for example the chemical reaction of a molecule embedded in a solid, cluster or liquid, approximations to the HK propagator are in order. One way to proceed is writing the quantity of interest in the form of a generalized time correlation function [12]. The resulting double phase-space integration is over trajectories going forward or backward in time, respectively. It can be simplified either by assuming infinitely close forward and backward trajectories, leading to a linearized SC-IVR (LSC-IVR) that yield essentially classical results [19], or, in a more refined way, by propagating trajectories forward in time, then adding a momentum jump at the final time and propagating back to the initial time [20]. The latter approach gives a more well-behaved integrand than the original HK expression while retaining its accuracy and one can treat a few tens of DOFs, as has been done in the calculation of the flux side correlation of a double well potential coupled to a harmonic bath with 40 oscillators [21] or the resonance Raman spectrum of molecular iodine surrounded by ten xenon atoms [22].

Our main interest in this work will also be system-bath situations as described before, namely, iodine embedded either in a Caldeira-Leggett bath [23,24] of harmonic oscillators or in a cluster of krypton atoms. We will employ a hybrid method that is based on the HK propagator, but utilizes the full phase space integration only for the system of interest, i.e., a small number of DOFs. The remaining many bath DOFs are propagated with the thawed Gaussian wave packet dynamics (TGWD), a method that has first been introduced by E. Heller [25]. TGWD can be thought of as an approximation to HK propagation that replaces the phase space integration over many fixed-width ("frozen") Gaussian wave packets (GWPs) with a single trajectory whose width varies in time. This substantial simplification comes at the price of being exact only for potentials of at most quadratic order. While being unsuitable for arbitrarily anharmonic potentials, TGWD is thus a good choice for somewhat weakly coupled bath DOFs that can be expected to stay close to the region of harmonic dynamics. By restricting the costly HK propagation to few degrees of freedom that really need the enhanced accuracy, while describing the majority of environmental DOFs with the much cheaper TGWD, the semiclassical hybrid dynamics (SC-HD) combines a sizable speedup of the numerics with still high accuracy. It has been developed by F. Grossmann for wave functions [26] and by C. Goletz for reduced density matrices [27] and was used mainly for studying the quenching of quantum behavior of an anharmonic system coupled to Caldeira-Leggett baths with different parameters [27,28]. We will continue this work by looking at the vibrational decoherence of iodine in a krypton bath at different temperatures, where experimental results allow for a direct comparison of coherence loss rates. Secondly, we present a new method for the calculation of vibrational spectra of molecules, which can be found from the quantum dynamics by Fourier transforming the autocorrelation function. To this end, we combine the hybrid idea with a time-averaging formalism that has been suggested by A. Kaledin and W. Miller [29]. This time-averaged SC-IVR (TA SC-IVR) smooths the phase space integrand by introducing an additional time integration; its accuracy and numerical feasibility has been proven for systems such as CO attached to a copper surface [30,31] and ammonium [32,33]. Starting at the TA SC-IVR, we will use the divide-and-conquer approach of SC-HD in order to devise a method that allows for

very efficient calculations of the full spectrum of systems with a few tens of DOFs. Applications will comprise both model and experimentally relevant systems, proving that this method might be a valuable tool for future first-principle calculations of complex molecular systems.

Finally, we will turn away from molecular systems and address a question of more fundamental nature, namely, a minimum requirement for the semiclassical IVR description of multi-electron systems where in particular spin effects due to the Pauli exclusion principle have to be taken into account. Existing schemes for the classical and semiclassical treatment of such systems in nuclear and molecular physics have to resort to artificial potentials and very complicated equations of motion in order to account for the additional mutual repulsion of electrons with identical spin [34–36]. We will consider the simplest case of two electrons scattering and use the above SC-IVRs together with appropriately (anti)symmetrized initial states to find out how well such a minimalistic approach fares when it comes to reproducing the different dynamics correctly.

The thesis is organized as follows. In Ch. 2, we will give an overview of semiclassical propagation schemes that are of interest for this work. A particular focus will be on initial value representation methods such as Herman-Kluk and its approximations, namely, thawed Gaussian wavepacket dynamics and the semiclassical hybrid dynamics. Ch. 3 is dedicated to developing SC-HD expressions for essential quantities of interest. We will review the SC-HD reduced density formalism for the description of a system in a temperature dependent bath that was developed by C. Goletz [37]. In the second part of that chapter, we will shortly repeat the arguments leading to the time-averaged SC-IVR expression for the calculation of molecular spectra. Then, we will present a hybrid approximation to the existing formalism that treats few DOFs of interest on the level of HK and the remaining DOFs with TGWD. In particular, we will introduce a separable approximation that turns the resulting two-time integral into a single time integration in order to get a computationally cheap algorithm. The application of the hybrid TA SC-IVR to the Caldeira-Leggett model system is discussed in Ch. 4. First, we show for a Morse oscillator coupled to one and two bath DOFs that results are in agreement with full quantum spectra over a wide range of bath frequencies and coupling strengths. Then, we test the accuracy compared to full HK calculations for spectral calculations of a bath comprising ten harmonic oscillators. Having established the reliability of the hybrid method with these reduced calculations, we then take bath sizes of up to 60 harmonic oscillators and study the role of the Caldeira-Leggett counter term on the spectrum of the anharmonic system for different bath parameters. In Ch. 5, we will go a step further and investigate an experimentally relevant system, namely, iodine in solid krypton. Other than in the case of the Caldeira-Leggett Hamilton, interactions between system and bath are nonlinear, and bath potentials are no longer harmonic. First, we will calculate the loss of iodine vibrational coherence for different bath temperatures using a hierarchical normal mode description of the bath. Then, we will take a look at the change of the iodine vibrational spectrum in the presence of the krypton bath. Chapter 6 is about an altogether different sort of problem. We turn away from molecular systems and look at the semiclassical outcome for two electron scattering, providing an answer for the minimum requirement to a semiclassical propagation of a fermionic system such that the effect of different spin configurations is accounted for. In Ch. 7, we will summarize our findings and provide an outlook especially to possible future applications of the spectral calculations with the hybrid TA SC-IVR.

A few remarks on unit conventions: in the theory chapters, we will use SI units. For the applications, we will switch to atomic units (a.u.) unless stated otherwise. This means in particular that most energies will be given in multiples of the Hartree energy, $E_\mathrm{h} = 4.359744 \times 10^{-18}$ J, distances in multiples of the Bohr radius, $a_0 = 0.529177 \times 10^{-10}$ m, and masses in

multiples of the electron mass, $m_e = 9.109384 \times 10^{-31}$ kg. In some cases where we are not interested in the absolute value of a given quantity, we will simply employ arbitrary units (arb.u.).

2. SEMICLASSICAL INITIAL VALUE REPRESENTATION METHODS

In this work, we will describe the time evolution of different quantum systems. For the typical non-relativistic energy scales of atomic and molecular systems, this is achieved by the time dependent Schrödinger equation (TDSE),

$$\mathrm{i}\hbar\frac{\partial}{\partial t}\left|\Psi(t)\right\rangle = \hat{H}(t)\left|\Psi(t)\right\rangle, \tag{2.1}$$

where the Hamiltonian $\hat{H}(t) = \hat{T} + \hat{V}(t)$ is a Hermitian operator comprising kinetic energy $\hat{T}$ and explicitly or implicitly time-dependent potential energy $\hat{V}(t)$, and $|\Psi(t)\rangle$ is the wavefunction of the system. Equation (2.1) can be solved analytically only for very simple model systems [8]. A straightforward numerical solution can be obtained with high accuracy using, for example, a split operator fast Fourier transform (FFT) algorithm. Since the number of coefficients (e.g., grid points) that are needed to describe the wavefunction $|\Psi(t)\rangle$ grows exponentially with the number of degrees of freedom of the problem, a full numerical solution of the TDSE is limited to systems with up to five or six degrees of freedom, i.e., no bigger than the hydrogen molecule [38].

In order to describe the time evolution of larger many-body systems, a huge variety of approximate methods exists. As mentioned in the Introduction, TDDFT and MCTDH are examples for very popular approaches to the numerical treatment of large quantum systems, tackling the exponential scaling by resorting to the single-particle density (TDDFT) or single-particle wavefunctions and a product form approximation to the Hamiltonian (MCTDH). In both cases, quantum-classical descriptions can be employed [2, 39], treating nuclei classically and electrons on the quantum level. We will focus here on methods that are based on the semiclassical approximation to the full quantum propagator. The exponential scaling of the full quantum wavefunction is circumvented by running independent classical trajectories which are then integrated including a complex phase that allows for interference between trajectories. Apart from this numerical advantage, basing a quantum propagation on classical trajectories also provides a more illustrative and intuitive picture of the dynamics. In this chapter, we will first describe the basic idea of semiclassical propagators, mainly following the book of F. Grossmann [8]. We briefly touch the differences between boundary value problem based propagators such as van Vleck-Gutzwiller [40, 41] and initial value representations, where we will focus on the Herman-Kluk propagator [13]. It is then shown which further approximations can be made in order to include more degrees of freedom into numerical calculations.

2.1. SEMICLASSICAL PROPAGATORS

The time evolved wavefunction $|\Psi(t)\rangle$ of an N-dimensional system subject to Hamilton $\hat{H}(t)$ can formally be expressed in position representation as

$$\Psi(\mathbf{x},t) = \int \mathrm{d}\mathbf{x}' K(\mathbf{x},t;\mathbf{x}',0)\Psi(\mathbf{x}',0), \tag{2.2}$$

where the propagator $K(\mathbf{x},t;\mathbf{x}',0) = \langle\mathbf{x}|\mathrm{e}^{-\mathrm{i}\hat{H}(t)t/\hbar}|\mathbf{x}'\rangle$ is the matrix element of the time evolution operator in position representation. In order for $\Psi(\mathbf{x},t)$ to be the exact solution of the TDSE (2.1), the propagator has to take the form of a functional integral over all paths leading from initial position $\mathbf{x}(0) = (x_1(0),\ldots,x_N(0))^{\mathrm{T}}$ to final position $\mathbf{x}(t) = (x_1(t),\ldots,x_N(t))^{\mathrm{T}}$

$$K(\mathbf{x},t;\mathbf{x}',0) = \int\limits_{\mathbf{x}(0)=\mathbf{x}'}^{\mathbf{x}(t)=\mathbf{x}} \mathrm{d}[\mathbf{x}] \exp\left\{\mathrm{i}\frac{S[\mathbf{x}]}{\hbar}\right\}, \tag{2.3}$$

as shown by Feynman [7]. Since this expression is fully equivalent to the TDSE, it is not surprising that an exact solution is not feasible for arbitrary systems. It can, however, be used as a starting point for a semiclassical description. Assuming that the action $S[\mathbf{x}]$ of the classical path is much larger than $\hbar$, the rapidly oscillating integrand in Eq. (2.3) can be evaluated in stationary phase approximation around this classical path. Van Vleck [40] has first, in a different way, derived a semiclassical expression that has later been generalized by Gutzwiller [41] for multiple points of stationary phase to the form

$$K^{\mathrm{VVG}}(\mathbf{x},t;\mathbf{x}',0) = \left(\frac{1}{2\pi\mathrm{i}\hbar}\right)^{N/2} \sum_k \sqrt{\left|\det\left(\frac{\partial^2 S[\mathbf{x}_k]}{\partial\mathbf{x}\partial\mathbf{x}'}\right)\right|} \exp\left\{\frac{\mathrm{i}}{\hbar}S[\mathbf{x}_k] - \frac{\mathrm{i}\nu\pi}{2}\right\}, \tag{2.4}$$

where the index k runs over all classical paths connecting $\mathbf{x}(0)$ and $\mathbf{x}(t)$ and the Maslov index ν counts how many times the path has gone through a caustic. While the quantities entering into Eq. (2.4) are purely classical, it still contains interference due to the sum of trajectories that are weighted with a complex phase factor. There are, however, two things that make it difficult to evaluate this expression: First, finding the classical paths constitutes a boundary value problem that is increasingly hard to solve as the number of DOFs gets bigger. Second, since the action derivative fulfills

$$\frac{\partial^2 S[\mathbf{x}_k]}{\partial\mathbf{x}\partial\mathbf{x}'} = -\frac{\partial\mathbf{p}'}{\partial\mathbf{x}}, \tag{2.5}$$

this expression becomes singular at points where $\partial\mathbf{x}/\partial\mathbf{p}' = 0$. Fortunately, both problems can be solved elegantly by expressing the original propagator from Eq. (2.2) in terms of coherent states by inserting unity twice. Then one can use the semiclassical expression for the coherent state propagator and finally evaluate the integration over final positions in another stationary phase approximation [11] to arrive at the Herman-Kluk (HK) propagator [13]

$$K^{\mathrm{HK}}(\mathbf{x},t;\mathbf{x}',0) = \frac{1}{(2\pi\hbar)^N} \int \mathrm{d}^N p\, \mathrm{d}^N q\, \langle\mathbf{x}|g_{\boldsymbol{\gamma}}(\mathbf{p}_t,\mathbf{q}_t)\rangle\, C_t(\mathbf{p},\mathbf{q}) \mathrm{e}^{\mathrm{i}S_t(\mathbf{p},\mathbf{q})/\hbar} \left\langle g_{\boldsymbol{\gamma}}(\mathbf{p},\mathbf{q})\middle|\mathbf{x}'\right\rangle. \tag{2.6}$$

This expression now only depends on initial phase space points, making it an initial value representation of the propagator instead of the boundary value problem before. The phase

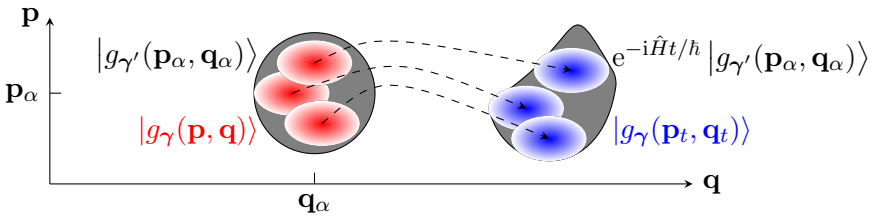

Figure 2.1.: Herman-Kluk propagation of an initial GWP centered at $(\mathbf{p}_\alpha, \mathbf{q}_\alpha)$. Red ellipses: GWPs centered at sampled initial phase space points, blue: GWPs centered at final points of time evolved trajectories (dashed lines). The exact wavefunction is represented by the gray shaded area.

space integration is performed over initial conditions, which serve as starting points for trajectories that are propagated in time. These classical trajectories are represented by Gaussian wavepackets (GWPs)

$$\langle \mathbf{x}|g_{\boldsymbol{\gamma}}(\mathbf{p}_t, \mathbf{q}_t)\rangle = \left(\frac{\det \boldsymbol{\gamma}}{\pi^N}\right)^{1/4} \exp\left\{-\frac{1}{2}\left(\mathbf{x}-\mathbf{q}_t\right)^{\mathrm{T}} \boldsymbol{\gamma}\left(\mathbf{x}-\mathbf{q}_t\right) + \frac{\mathrm{i}}{\hbar}\mathbf{p}_t^{\mathrm{T}}\left(\mathbf{x}-\mathbf{q}_t\right)\right\}, \tag{2.7}$$

where $\boldsymbol{\gamma}$ is a diagonal $N \times N$ matrix containing the width parameters of the respective DOFs. As the width of the GWPs in Eq. (2.6) stays constant throughout the propagation, it is also referred to as "frozen" Gaussian approximation. The classical action no longer depends on the path from initial to final position, but only on the initial conditions and therefore becomes

$$S_t(\mathbf{p}, \mathbf{q}) = \int_0^t \mathrm{d}t' L, \tag{2.8}$$

with L the classical Lagrangian of the system. The HK prefactor which ensures approximate normalization of the resulting expression has the (generalized) form [26, 42]

$$C_t(\mathbf{p}, \mathbf{q}) = \sqrt{\det\left[\frac{1}{2}\left(\mathbf{m}_{11,t} + \boldsymbol{\gamma}\mathbf{m}_{22,t}\boldsymbol{\gamma}^{-1} - \mathrm{i}\hbar\boldsymbol{\gamma}\mathbf{m}_{21,t} + \frac{\mathrm{i}}{\hbar}\mathbf{m}_{12,t}\boldsymbol{\gamma}^{-1}\right)\right]} \equiv \sqrt{\det\left(\mathbf{h}_t\right)}, \tag{2.9}$$

with matrices $\mathbf{m}_{ij,t}$ as its main ingredients. These $\mathbf{m}_{ij,t}$, which are sometimes defined with indices p and q instead of 1 and 2, are time-dependent submatrices of the stability matrix

$$\mathbf{M}(t) = \begin{pmatrix} \mathbf{m}_{11,t} & \mathbf{m}_{12,t} \\ \mathbf{m}_{21,t} & \mathbf{m}_{22,t} \end{pmatrix} \equiv \begin{pmatrix} \frac{\partial \mathbf{p}_t}{\partial \mathbf{p}} & \frac{\partial \mathbf{p}_t}{\partial \mathbf{q}} \\ \frac{\partial \mathbf{q}_t}{\partial \mathbf{p}} & \frac{\partial \mathbf{q}_t}{\partial \mathbf{q}} \end{pmatrix} \tag{2.10}$$

that describes the time evolution of (small) deviations from the initial conditions and thereby the stability of the system under investigation [8]. Some of its properties are collected in App. A, in particular its time evolution.

The full potential of HK propagation is revealed when it is applied to a GWP according to Eq. (2.2). With an initial state $\Psi_\alpha(\mathbf{x}', 0) = \langle \mathbf{x}'|g_{\boldsymbol{\gamma}}(\mathbf{p}_\alpha, \mathbf{q}_\alpha)\rangle$ that is centered at $(\mathbf{p}_\alpha, \mathbf{q}_\alpha)$ and has the same width parameters as the propagator wavepackets, the $\mathbf{x}'$ integration can be done analytically and the propagated wavefunction becomes

$$\Psi(\mathbf{x}, t) = \frac{1}{(2\pi\hbar)^N} \int \mathrm{d}^N p\, \mathrm{d}^N q\, \langle \mathbf{x}|g_{\boldsymbol{\gamma}}(\mathbf{p}_t, \mathbf{q}_t)\rangle\, C_t(\mathbf{p}, \mathbf{q}) \mathrm{e}^{\mathrm{i}S_t(\mathbf{p},\mathbf{q})/\hbar}\, \langle g_{\boldsymbol{\gamma}}(\mathbf{p}, \mathbf{q})|g_{\boldsymbol{\gamma}}(\mathbf{p}_\alpha, \mathbf{q}_\alpha)\rangle\,. \tag{2.11}$$

The necessary numerical phase space integration can be made very efficiently using the Box-Muller algorithm [43] in order to sample initial phase space points weighted with the overlap $\langle g_{\boldsymbol{\gamma}}(\mathbf{p},\mathbf{q})|g_{\boldsymbol{\gamma}}(\mathbf{p}_\alpha,\mathbf{q}_\alpha)\rangle$ which emerges after a Gaussian integration as

$$\begin{aligned}\langle g_{\boldsymbol{\gamma}}(\mathbf{p},\mathbf{q})|g_{\boldsymbol{\gamma}}(\mathbf{p}_\alpha,\mathbf{q}_\alpha)\rangle = \exp\Bigg\{ &-\frac{1}{4}\left(\mathbf{q}-\mathbf{q}_\alpha\right)^{\mathrm{T}}\boldsymbol{\gamma}\left(\mathbf{q}-\mathbf{q}_\alpha\right) - \frac{1}{4\hbar^2}\left(\mathbf{p}-\mathbf{p}_\alpha\right)^{\mathrm{T}}\boldsymbol{\gamma}^{-1}\left(\mathbf{p}-\mathbf{p}_\alpha\right) \\ &+\frac{\mathrm{i}}{2\hbar}\left(\mathbf{q}-\mathbf{q}_\alpha\right)^{\mathrm{T}}\left(\mathbf{p}+\mathbf{p}_\alpha\right)\Bigg\}.\end{aligned} \tag{2.12}$$

It should be noted here that the identity of the width parameters of initial state and propagated wave packets is not necessary for an analytic calculation of the overlap, only the notation becomes a bit simpler. Figure 2.1 is a pictorial representation of HK propagation. The initial wavepacket is expanded in a basis of GWPs (which have a different width parameter here for better visibility). These GWPs do not change their shape during propagation; the time evolved wavefunction, however, is a summation over GWPs weighted with a complex phase factor and will therefore reproduce non-Gaussian distortions and interference correctly. Since it has classical trajectories for a backbone, tunneling effects are not contained in this description. The HK propagator (2.6) conserves unitarity in the semiclassical limit [44]. Its derivation as sketched here is only one of many alternative ways that have been described in the literature. A precursor had been found by E. Heller in 1981 under the name 'Frozen Gaussian approximation' [45]. In the 1990s, Kay rediscovered the HK propagator as a special case of more general SC-IVRs [14] and showed its outstanding efficiency in a number of numerical applications [15, 46]. Honoring these contributions, the HK propagator is also referred to as HHKK, or Heller-Herman-Kluk-Kay, propagator. Grossmann and Xavier showed that the HK propagator can be found directly from the semiclassical coherent state path integral [11]. More recently, Shalashilin and Child [47] as well as Miller [48] have pointed out that the HK propagator can also be understood as an approximation to the exact quantum method of coupled coherent states. Yet another approach has been found by Miller [49] who derived the HK propagator by Filinov transformation of the VVG expression, thus emphasizing the favorable numerical behavior.

In a numerical calculation, both the trajectories and the stability matrix from Eq. (2.11) can be propagated using a symplectic integration scheme. This method is explained generally in [8, 50] and specifically for the $\mathbf{m}_{ij}$ in App. B of [37]. An important property of $\mathbf{M}(t)$ is that its determinant remains unity for all times, thus providing a means to check the quality of the numerical propagation scheme. The prefactor C_t is the main computational challenge in the evaluation of the phase space integrand in Eq. (2.6), as its propagation necessitates $4N^2$ calculations of second derivatives at each time step. This is especially expensive for on-the-fly calculations where no analytic potential surfaces are provided. Alternatives for an efficient approximate propagation of $\mathbf{M}(t)$ have been suggested, either using additional trajectories to calculate the time evolved stability matrix numerically [51], or propagating the Hessian with a finite difference scheme [52, 53]. Numerical difficulties get especially severe for chaotic trajectories, for which the prefactor C_t grows exponentially due to its stability matrix dependence. This problem can be alleviated by smoothing the integrand with a Filinov transformation [54], which does, however, introduce some additional complexity because one has to device a systematic way to find appropriate smoothing parameters. In this work, chaotic trajectories will be so scarce that we simply discard their contributions, as suggested by Kay [46].

2.2. HYBRID APPROXIMATION TO THE HERMAN-KLUK PROPAGATOR

While application of the HK propagator alleviates the memory problem in numerical calculations, the number of trajectories that are needed to converge the phase space integral scales very unfavorably with each additional DOF. Several methods of different complexity, such as forward-backward IVR that will be discussed in the next section, have been suggested to tackle this problem.

Our approach to achieve an accelerated convergence is a mixed treatment where HK propagation is used for a few DOFs of interest and single trajectory TGWD for the remaining larger number of environmental DOFs. Unlike other methods aimed at improving the efficiency of HK propagation, it is not based on smoothing the phase space integrand, but instead on a drastic reduction of the dimensionality of the initial conditions phase space that has to be sampled. Assuming a sufficiently weak coupling of bath modes to the system, the very crude description of the almost harmonic bath DOFs with TGWD is a well-justified approximation at very low computational cost. The interesting DOFs, on the other hand, are described as accurately as possible on the superior HK level. Following the original derivation by Grossmann [26], we will first describe the TGWD approach and then apply this idea to the HK propagated wavefunction (2.11).

2.2.1. THAWED GAUSSIAN WAVEPACKET DYNAMICS

Thawed Gaussian Wavepacket Dynamics (TGWD) is a wavepacket propagation method that relies on a single classical trajectory represented by a GWP with time-dependent width. It has first been derived by E. Heller for one and two dimensions [25]. We will present the multidimensional version [55, 56] by using an ansatz for the wavefunction that reads

$$\begin{aligned}\Psi_\alpha(\mathbf{x},t) = &\left(\frac{2^N \det\boldsymbol{\gamma}_0}{\pi^N}\right)^{1/4} \\ &\times \exp\left\{-\left(\mathbf{x}-\mathbf{q}_{\alpha,t}\right)^{\mathrm{T}}\boldsymbol{\gamma}_t\left(\mathbf{x}-\mathbf{q}_{\alpha,t}\right)+\frac{\mathrm{i}}{\hbar}\mathbf{p}_{\alpha,t}^{\mathrm{T}}\left(\mathbf{x}-\mathbf{q}_{\alpha,t}\right)+\frac{\mathrm{i}}{\hbar}\delta_t\right\},\end{aligned} \tag{2.13}$$

where $\mathbf{p}_{\alpha,t}$ and $\mathbf{q}_{\alpha,t}$ are real-valued vectors of length N describing a trajectory evolving from $(\mathbf{p}_\alpha, \mathbf{q}_\alpha)$, while $\boldsymbol{\gamma}_t$ is a complex-valued $N \times N$ matrix and δ_t is a complex scalar. The generalized width parameter $\boldsymbol{\gamma}_t$ is clearly distinct from the real-valued, diagonal matrix $\boldsymbol{\gamma}$ that enters the HK wavefunction (2.11) via Eq. (2.7). The ansatz is plugged into the TDSE (2.1) and the potential $V(\mathbf{x},t)$ is expanded to second order around the central trajectory. Comparing coefficients of the resulting equation yields classical equations of motion for $\mathbf{p}_{\alpha,t}$ and $\mathbf{q}_{\alpha,t}$, and the phase δ_t evolves according to

$$\dot{\delta}_t = L - \hbar^2 \operatorname{Tr}(\mathbf{m}^{-1}\boldsymbol{\gamma}_t), \tag{2.14}$$

where $\mathbf{m}$ is a diagonal matrix containing the mass of each DOF, L is the Lagrangian from Eq. (2.8), and the abbreviation Tr denotes the trace operation. The width parameter matrix follows a Riccati equation

$$\dot{\boldsymbol{\gamma}}_t = -2\mathrm{i}\hbar\boldsymbol{\gamma}_t\mathbf{m}^{-1}\boldsymbol{\gamma}_t + \frac{\mathrm{i}}{2\hbar}\frac{\partial^2 V}{\partial\mathbf{q}\partial\mathbf{q}^{\mathrm{T}}}(\mathbf{q}_{\alpha,t},t). \tag{2.15}$$

Unlike in the previous section, the width parameters now depend on time, hence the name "thawed" Gaussian wavepacket dynamics. Furthermore, the TGWD wavefunction (2.13) does

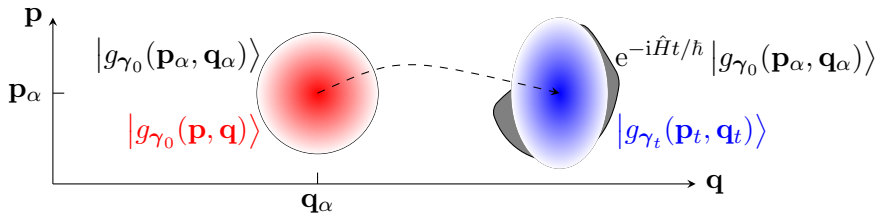

Figure 2.2.: TGWD propagation of an initial GWP centered at $(\mathbf{p}_\alpha, \mathbf{q}_\alpha)$. Red ellipse: Initial GWP, blue: final GWP, dashed line: time evolved central trajectory. The exact wavefunction is represented by the gray shaded area.

not require a phase space integration like the HK propagated one from Eq. (2.11), making this scheme computationally much cheaper. Due to the second order approximation of the potential in the derivation, however, TGWD is exact only for at most harmonic potential. In Fig. 2.2, TGWD propagation is illustrated in the same fashion as HK propagation in the previous section. While an initial Gaussian state is reproduced exactly, anharmonic distortions of the time-evolved wavepacket cannot be reproduced by a single GWP.

The connection between HK and TGWD propagation has been established in [26] for wavefunctions and in more detail in [37] for reduced densities. The derivation starts with the HK expression (2.11). Expanding the exponent to second order around the central initial phase space point $(\mathbf{p}_\alpha, \mathbf{q}_\alpha)$ leaves a Gaussian integral that can be performed analytically. After some tedious algebra, one can recover an alternative formulation of TGWD [56], namely,

$$\begin{aligned}\Psi_\alpha(\mathbf{x}, t) = &\left(\frac{\det \boldsymbol{\gamma}}{\pi^N}\right)^{1/4} \left[\det\left(\mathbf{m}_{22,t} + \mathrm{i}\hbar \mathbf{m}_{21,t}\boldsymbol{\gamma}\right)\right]^{-1/2} \\ &\times \exp\left\{-\frac{1}{2}\left(\mathbf{x} - \mathbf{q}_{\alpha,t}\right)^{\mathrm{T}} \left(\mathbf{m}_{11,t}\boldsymbol{\gamma} - \frac{\mathrm{i}}{\hbar}\mathbf{m}_{12,t}\right)\left(\mathbf{m}_{22,t} + \mathrm{i}\hbar \mathbf{m}_{21,t}\boldsymbol{\gamma}\right)^{-1}\left(\mathbf{x} - \mathbf{q}_{\alpha,t}\right)\right. \\ &\left. + \frac{\mathrm{i}}{\hbar}\mathbf{p}_{\alpha,t}^{\mathrm{T}}\left(\mathbf{x} - \mathbf{q}_{\alpha,t}\right) + \frac{\mathrm{i}}{\hbar} S_t(\mathbf{p}_\alpha, \mathbf{q}_\alpha)\right\},\end{aligned} \tag{2.16}$$

The equivalence of Eq. (2.16) with Eqs. (2.13) to (2.15) has been shown for the 1D case in [8]. For multiple dimensions, it is established in [55, 56], where the width parameter and the phase are defined differently. In order to be self-contained, we lay out an adapted version in App. A.

We will use the connection between HK and TGWD in the next section to show the derivation of a mixed approach according to [26], where TGWD is applied to describe weakly coupled bath modes close to their vibrational groundstate, where almost harmonic behavior can be assumed.

2.2.2. SEMICLASSICAL HYBRID DYNAMICS

In order to derive the mixed phase space approach of semiclassical hybrid dynamics (SC-HD), we start by explicitly writing out the Gaussians in Eq. (2.11) with a slightly adapted notation,

$$\begin{aligned}\Psi(\mathbf{x},t) =& \frac{1}{(2\pi\hbar)^N}\left(\frac{\det\boldsymbol{\gamma}}{\pi^N}\right)^{1/4}\int \mathrm{d}^N p\ \mathrm{d}^N q\ C_t(\mathbf{p},\mathbf{q})\mathrm{e}^{\mathrm{i}S_t(\mathbf{p},\mathbf{q})/\hbar}\\ &\times\exp\left\{-\frac{1}{2}\left(\mathbf{x}-\mathbf{q}_t\right)^{\mathrm{T}}\boldsymbol{\gamma}\left(\mathbf{x}-\mathbf{q}_t\right)+\frac{\mathrm{i}}{2\hbar}\mathbf{p}_t^{\mathrm{T}}\left(\mathbf{x}-\mathbf{q}_t\right)\right\}\\ &\times\exp\left\{-\frac{1}{4}\left(\mathbf{q}-\mathbf{q}_\alpha\right)^{\mathrm{T}}\boldsymbol{\gamma}\left(\mathbf{q}-\mathbf{q}_\alpha\right)-\frac{1}{4\hbar^2}\left(\mathbf{p}-\mathbf{p}_\alpha\right)^{\mathrm{T}}\boldsymbol{\gamma}^{-1}\left(\mathbf{p}-\mathbf{p}_\alpha\right)\right.\\ &\left.-\frac{\mathrm{i}}{2\hbar}\left(\mathbf{q}-\mathbf{q}_\alpha\right)^{\mathrm{T}}\left(\mathbf{p}+\mathbf{p}_\alpha\right)\right\}.\end{aligned} \tag{2.17}$$

Now, the phase space is divided into a HK and a TGWD part, $N = N_{\mathrm{hk}} + N_{\mathrm{tg}}$. The combined initial phase space points are defined as

$$\mathbf{p}_{\alpha,0} \equiv \begin{pmatrix}\mathbf{p}_{\mathrm{hk}}\\ \mathbf{p}_{\alpha,\mathrm{tg}}\end{pmatrix} \qquad\qquad \mathbf{q}_{\alpha,0} \equiv \begin{pmatrix}\mathbf{q}_{\mathrm{hk}}\\ \mathbf{q}_{\alpha,\mathrm{tg}}\end{pmatrix} \tag{2.18}$$

where $\mathbf{p}_{\mathrm{hk}}$ and $\mathbf{q}_{\mathrm{hk}}$ are N_{hk} dimensional vectors sampled around $(\mathbf{p}_{\alpha,\mathrm{hk}}, \mathbf{q}_{\alpha,\mathrm{hk}})$, and $\mathbf{p}_{\alpha,\mathrm{tg}}$ and $\mathbf{q}_{\alpha,\mathrm{tg}}$ are N_{tg} dimensional vectors fixed at the center of the central GWP. Trajectories propagated from these initial conditions are denoted by $(\mathbf{p}_{\alpha,t}, \mathbf{q}_{\alpha,t})$, thus redefining the naming convention from the TGWD section. It should be noted that there is no decoupling of the classical dynamics of HK and TG DOFs, i.e., $\mathbf{p}_{\alpha,t} = \mathbf{p}\left(\mathbf{p}_{\alpha,0}, \mathbf{q}_{\alpha,0}, t\right)$ and $\mathbf{q}_{\alpha,t} = \mathbf{q}\left(\mathbf{p}_{\alpha,0}, \mathbf{q}_{\alpha,0}, t\right)$.

As mentioned before, the TG part of the exponent is expanded to second order in the displacements $\delta\mathbf{p}_{\mathrm{tg}},\ \delta\mathbf{q}_{\mathrm{tg}}$ from the wave packet center. This makes the action

$$\begin{aligned}S_t\left(\mathbf{p},\mathbf{q}\right) =& S_t\left(\mathbf{p}_{\alpha,0},\mathbf{q}_{\alpha,0}\right) + \mathbf{p}_{\alpha,t}^{\mathrm{T}}\tilde{\mathbf{m}}_{21,t}\delta\mathbf{p}_{\mathrm{tg}} + \left(\mathbf{p}_{\alpha,t}^{\mathrm{T}}\tilde{\mathbf{m}}_{22,t} - \mathbf{p}_{\alpha,\mathrm{tg}}^{\mathrm{T}}\right)\delta\mathbf{q}_{\mathrm{tg}}\\ &+\frac{1}{2}\delta\mathbf{p}_{\mathrm{tg}}^{\mathrm{T}}\tilde{\mathbf{m}}_{11,t}^{\mathrm{T}}\tilde{\mathbf{m}}_{21,t}\delta\mathbf{p}_{\mathrm{tg}} + \frac{1}{2}\delta\mathbf{q}_{\mathrm{tg}}^{\mathrm{T}}\tilde{\mathbf{m}}_{12,t}^{\mathrm{T}}\tilde{\mathbf{m}}_{22,t}\delta\mathbf{q}_{\mathrm{tg}} + \delta\mathbf{q}_{\mathrm{tg}}^{\mathrm{T}}\tilde{\mathbf{m}}_{12,t}^{\mathrm{T}}\tilde{\mathbf{m}}_{21,t}\delta\mathbf{p}_{\mathrm{tg}},\end{aligned} \tag{2.19}$$

with N_{tg} dimensional displacement vectors, defined as the difference between the originally sampled TG initial conditions and the wave packet center,

$$\delta\mathbf{p}_{\mathrm{tg}} = \mathbf{p}_{\mathrm{tg}} - \mathbf{p}_{\alpha,\mathrm{tg}} \tag{2.20}$$

$$\delta\mathbf{q}_{\mathrm{tg}} = \mathbf{q}_{\mathrm{tg}} - \mathbf{q}_{\alpha,\mathrm{tg}}, \tag{2.21}$$

and non-square $N \times N_{\mathrm{tg}}$ dimensional stability matrices

$$\begin{aligned}\tilde{\mathbf{m}}_{11,t} &= \frac{\partial\mathbf{p}_{\alpha,t}}{\partial\mathbf{p}_{\alpha,\mathrm{tg}}} & \tilde{\mathbf{m}}_{21,t} &= \frac{\partial\mathbf{q}_{\alpha,t}}{\partial\mathbf{p}_{\alpha,\mathrm{tg}}}\\ \tilde{\mathbf{m}}_{12,t} &= \frac{\partial\mathbf{p}_{\alpha,t}}{\partial\mathbf{q}_{\alpha,\mathrm{tg}}} & \tilde{\mathbf{m}}_{22,t} &= \frac{\partial\mathbf{q}_{\alpha,t}}{\partial\mathbf{q}_{\alpha,\mathrm{tg}}}.\end{aligned} \tag{2.22}$$

These newly defined submatrices will be used in the TG part of the hybrid expression only. The HK prefactor C_t still contains the full stability matrices as defined in Eq. (2.9).

We also need to expand the original trajectory $(\mathbf{p}_t, \mathbf{q}_t)$, where each DOF has sampled initial conditions, to linear order in the displacements

$$\mathbf{p}_t = \mathbf{p}_{\alpha,t} + \tilde{\mathbf{m}}_{12,t}\delta\mathbf{q}_{\mathrm{tg}} + \tilde{\mathbf{m}}_{11,t}\delta\mathbf{p}_{\mathrm{tg}} \tag{2.23}$$

$$\mathbf{q}_t = \mathbf{q}_{\alpha,t} + \tilde{\mathbf{m}}_{22,t}\delta\mathbf{q}_{\mathrm{tg}} + \tilde{\mathbf{m}}_{21,t}\delta\mathbf{p}_{\mathrm{tg}}. \tag{2.24}$$

After inserting expressions (2.19), (2.23) and (2.24) into the HK wavefunction (2.17), one proceeds by grouping terms in powers of the difference coordinates to get to the form of a Gaussian integral

$$\begin{aligned}\Psi(\mathbf{x},t) =&\frac{1}{(2\pi\hbar)^N}\left(\frac{\det\boldsymbol{\gamma}}{\pi^N}\right)^{1/4}\\ &\times\int \mathrm{d}^{N_{\mathrm{hk}}}p_{\mathrm{hk}}\mathrm{d}^{N_{\mathrm{hk}}}q_{\mathrm{hk}}\; C_t(\mathbf{p}_{\alpha,0},\mathbf{q}_{\alpha,0})\left\langle g_{\boldsymbol{\gamma}_{\mathrm{hk}}}(\mathbf{p}_{\mathrm{hk}},\mathbf{q}_{\mathrm{hk}})\middle| g_{\boldsymbol{\gamma}_{\mathrm{hk}}}(\mathbf{p}_{\alpha,\mathrm{hk}},\mathbf{q}_{\alpha,\mathrm{hk}})\right\rangle\\ &\times\int \mathrm{d}^{N_{\mathrm{tg}}}\delta p_{\mathrm{tg}}\mathrm{d}^{N_{\mathrm{tg}}}\delta q_{\mathrm{tg}}\exp\left\{-\begin{pmatrix}\delta\mathbf{p}_{\mathrm{tg}}\\ \delta\mathbf{p}_{\mathrm{tg}}\end{pmatrix}^{\mathrm{T}}\mathbf{A}_t^{\mathrm{wf}}\begin{pmatrix}\delta\mathbf{p}_{\mathrm{tg}}\\ \delta\mathbf{p}_{\mathrm{tg}}\end{pmatrix}+\left(\mathbf{b}_t^{\mathrm{wf}}\right)^{\mathrm{T}}\begin{pmatrix}\delta\mathbf{p}_{\mathrm{tg}}\\ \delta\mathbf{p}_{\mathrm{tg}}\end{pmatrix}+c_t^{\mathrm{wf}}\right\},\end{aligned}\tag{2.25}$$

where we have changed the integration variables of the TG part and made the assumption $C_t(\mathbf{p},\mathbf{q})\approx C_t(\mathbf{p}_{\alpha,0},\mathbf{q}_{\alpha,0})$ to remove the $(\mathbf{p}_{\mathrm{tg}},\mathbf{q}_{\mathrm{tg}})$ dependence of the prefactor. Carrying out the integration over the TG part reveals the final hybrid form of the wavefunction

$$\begin{aligned}\Psi(\mathbf{x},t) =&\frac{1}{(2\hbar)^N}\frac{1}{\pi^{N-N_{\mathrm{tg}}}}\left(\frac{\det\boldsymbol{\gamma}}{\pi^N}\right)^{1/4}\\ &\times\int \mathrm{d}^{N_{\mathrm{hk}}}p_{\mathrm{hk}}\;\mathrm{d}^{N_{\mathrm{hk}}}q_{\mathrm{hk}}\; C_t(\mathbf{p}_{\alpha,0},\mathbf{q}_{\alpha,0})\left\langle g_{\boldsymbol{\gamma}_{\mathrm{hk}}}(\mathbf{p}_{\mathrm{hk}},\mathbf{q}_{\mathrm{hk}})\middle| g_{\boldsymbol{\gamma}_{\mathrm{hk}}}(\mathbf{p}_{\alpha,\mathrm{hk}},\mathbf{q}_{\alpha,\mathrm{hk}})\right\rangle\\ &\times\sqrt{\frac{1}{\det\mathbf{A}_t^{\mathrm{wf}}}}\exp\left\{\frac{1}{4}\left(\mathbf{b}_t^{\mathrm{wf}}\right)^{\mathrm{T}}\left(\mathbf{A}_t^{\mathrm{wf}}\right)^{-1}\mathbf{b}_t^{\mathrm{wf}}+c_t^{\mathrm{wf}}\right\}.\end{aligned}\tag{2.26}$$

As can be seen in Eq. (2.25), the new quantities $\mathbf{A}_t$, $\mathbf{b}_t$ and c_t are the collection of second, first and zeroth order terms, respectively, in the displacement coordinates. All of these quantities depend on the initial conditions of the full problem, i.e., for example, $\mathbf{A}_t^{\mathrm{wf}}=\mathbf{A}_t^{\mathrm{wf}}(\mathbf{p}_{\alpha,0},\mathbf{q}_{\alpha,0})$. Terms of this nature will also appear in the reduced density formalism and in the context of spectral calculations, which is why we introduce an additional upper index. The second order terms take the form of a symmetric block matrix

$$\mathbf{A}_t^{\mathrm{wf}}=\begin{pmatrix}\mathbf{A}_{11,t}^{\mathrm{wf}} & \mathbf{A}_{12,t}^{\mathrm{wf}}\\ \mathbf{A}_{21,t}^{\mathrm{wf}} & \mathbf{A}_{22,t}^{\mathrm{wf}}\end{pmatrix}\tag{2.27}$$

with $N_{\mathrm{tg}}\times N_{\mathrm{tg}}$ entries

$$\mathbf{A}_{11,t}^{\mathrm{wf}}=\frac{1}{4\hbar^2}\boldsymbol{\gamma}_{\mathrm{tg}}^{-1}+\frac{1}{2}\left[\tilde{\mathbf{m}}_{21,t}^{\mathrm{T}}\boldsymbol{\gamma}+\frac{\mathrm{i}}{\hbar}\tilde{\mathbf{m}}_{11,t}^{\mathrm{T}}\right]\tilde{\mathbf{m}}_{21,t}\tag{2.28}$$

$$\mathbf{A}_{12,t}^{\mathrm{wf}}=\frac{\mathrm{i}}{4\hbar}+\frac{1}{2}\tilde{\mathbf{m}}_{21,t}^{\mathrm{T}}\left[\boldsymbol{\gamma}\tilde{\mathbf{m}}_{22,t}+\frac{\mathrm{i}}{\hbar}\tilde{\mathbf{m}}_{12,t}\right]\tag{2.29}$$

$$\mathbf{A}_{21,t}^{\mathrm{wf}}=\frac{\mathrm{i}}{4\hbar}+\frac{1}{2}\left[\tilde{\mathbf{m}}_{22,t}^{\mathrm{T}}\boldsymbol{\gamma}+\frac{\mathrm{i}}{\hbar}\tilde{\mathbf{m}}_{12,t}^{\mathrm{T}}\right]\tilde{\mathbf{m}}_{21,t}=\left(\mathbf{A}_{12,t}^{\mathrm{wf}}\right)^{\mathrm{T}}\tag{2.30}$$

$$\mathbf{A}_{22,t}^{\mathrm{wf}}=\frac{1}{4}\boldsymbol{\gamma}_{\mathrm{tg}}+\frac{1}{2}\left[\tilde{\mathbf{m}}_{22,t}^{\mathrm{T}}\boldsymbol{\gamma}+\frac{\mathrm{i}}{\hbar}\tilde{\mathbf{m}}_{12,t}^{\mathrm{T}}\right]\tilde{\mathbf{m}}_{22,t}.\tag{2.31}$$

The first order terms are collected in a vector of length $2N_{\mathrm{tg}}$

$$\mathbf{b}_t^{\mathrm{wf}}=\begin{pmatrix}\mathbf{b}_{1,t}^{\mathrm{wf}}\\ \mathbf{b}_{2,t}^{\mathrm{wf}}\end{pmatrix}\tag{2.32}$$

with components

$$\left(\mathbf{b}_{1,t}^{\mathrm{wf}}\right)^{\mathrm{T}} = \left(\mathbf{x} - \mathbf{q}_{\alpha,t}\right)^{\mathrm{T}} \left[\boldsymbol{\gamma}\tilde{\mathbf{m}}_{21,t} + \frac{\mathrm{i}}{\hbar}\tilde{\mathbf{m}}_{11,t}\right] \tag{2.33}$$

$$\left(\mathbf{b}_{2,t}^{\mathrm{wf}}\right)^{\mathrm{T}} = \left(\mathbf{x} - \mathbf{q}_{\alpha,t}\right)^{\mathrm{T}} \left[\boldsymbol{\gamma}\tilde{\mathbf{m}}_{22,t} + \frac{\mathrm{i}}{\hbar}\tilde{\mathbf{m}}_{12,t}\right], \tag{2.34}$$

and the scalar term is

$$c_t^{\mathrm{wf}} = \frac{\mathrm{i}}{\hbar} S_t\left(\mathbf{p}_{\alpha,0}, \mathbf{q}_{\alpha,0}\right) - \frac{1}{2}\left(\mathbf{x} - \mathbf{q}_{\alpha,t}\right)^{\mathrm{T}} \boldsymbol{\gamma}\left(\mathbf{x} - \mathbf{q}_{\alpha,t}\right) + \frac{\mathrm{i}}{\hbar}\mathbf{p}_{\alpha,t}^{\mathrm{T}}\left(\mathbf{x} - \mathbf{q}_{\alpha,t}\right). \tag{2.35}$$

The hybrid dynamics approximation provides a versatile tool that can be employed very naturally to the description of system-bath situations, as we will discuss in the next chapter. As long as a distinction between few strongly coupled and many weakly coupled DOFs can be made, SC-HD will significantly reduce the number of trajectories that are needed to converge the phase space integral. For model systems such as the Caldeira-Leggett model in Ch. 4, this separation can be very easy. For realistic systems, the choice of HK and TG DOFs requires certain assumptions about the problem at hand; in molecular physics, a normal mode description is usually a good starting point.

2.3. LINEARIZED SEMICLASSICAL INITIAL VALUE REPRESENTATION

In the final section of this chapter, we will present one last HK-based method that will later serve as a classical comparison to semiclassical results, the so-called Linearized Semiclassical Initial Value Representation (LSC-IVR) introduced by Sun, Wang and Miller [19, 20, 57–59] (it is also known as classical Wigner dynamics [60, 61]). It is a special case of a more general semiclassical formalism, where an observable is written in the form of a generalized time-correlation function as it is often the case for system-bath dynamics

$$C_{AB}(t) = \mathrm{Tr}\left(\hat{A}\mathrm{e}^{\mathrm{i}\hat{H}t/\hbar}\hat{B}\mathrm{e}^{-\mathrm{i}\hat{H}t/\hbar}\right). \tag{2.36}$$

The operators $\hat{A}$ and $\hat{B}$ have to be chosen such that $C_{AB}(t)$ describes the quantity of interest. Usually, $\hat{A}$ describes the environmental degrees of freedom, while $\hat{B}$ contains the system properties. For a semiclassical evaluation of expression (2.36), the HK propagator has to be inserted twice, resulting in a double phase space integral. In order to facilitate the numerical treatment of this class of problems, a forward-backward (FB) formalism has been devised. It is based on trajectories that first go forward in time, then undergo a jump in the momentum coordinate of the system (or in momentum and position) at the final time, and are propagated back to time zero. In this way, only a single phase space integration and an integration over the jump coordinate(s) is required. The resulting integrand is numerically well-behaved because oscillatory contributions of a given forward trajectory are canceled by its backward counterpart. The underlying idea has been suggested by Makri and Thompson for the influence functional in path integral calculations [62]. It has subsequently been applied to smoothing HK propagation of time-correlation functions by Sun and Miller [20], by Shao and Makri [63], and more recently in a generalized way by Martin-Fierro and Pollak [64].

We are interested in a simplification to FB SC-IVR, namely, LSC-IVR, where the forward trajectory does not "jump" at the final time, leading to infinitely close forward and backward trajectories and thus to a classical model that does not include quantum interference. As

shown in [19], it can be derived from Eq. (2.36) by transforming the integration variables to sum and difference variables. After expansion of the action and the trajectories to second order and first order in the difference variables, respectively, the integration over the these variables can be performed analytically. The result is a single phase space integration over the Wigner transformed operators

$$C_{AB}(t) = \frac{1}{(2\pi\hbar)^N} \int \mathrm{d}^N p \; \mathrm{d}^N q \; A_\mathrm{w}(\mathbf{p},\mathbf{q}) B_\mathrm{w}(\mathbf{p}_t,\mathbf{q}_t), \tag{2.37}$$

where the Wigner transform [65] is defined as

$$A_\mathrm{w}(\mathbf{p},\mathbf{q}) = \int \mathrm{d}^N \Delta q \; \mathrm{e}^{-\mathrm{i}\mathbf{p}^\mathrm{T}\Delta\mathbf{q}/\hbar} \left\langle \mathbf{q} + \frac{\Delta\mathbf{q}}{2} \middle| \hat{A} \middle| \mathbf{q} - \frac{\Delta\mathbf{q}}{2} \right\rangle. \tag{2.38}$$

With the two quasi-probability distributions in the integrand, Eq. (2.37) is reminiscent of a classical correlation function [12]. Due to this correlation function form of LSC-IVR in Eq. (2.36), in general we now get a density operator $\rho(\mathbf{x},\mathbf{x}',t)$ rather than a wave function $\Psi(\mathbf{x},t)$. Using the notation of the following chapter and restricting ourselves to the reduced density $\rho(\mathbf{s},t)$, i.e., the diagonal elements of the density operator defined in Eq. (3.3), we choose operators $\hat{A}$ and $\hat{B}$ according to

$$\hat{A} = |\Psi_\alpha\rangle \langle\Psi_{\alpha'}| \tag{2.39}$$

$$\hat{B} = |\mathbf{s}\rangle \langle\mathbf{s}|, \tag{2.40}$$

where $|\Psi_\alpha\rangle$ is a product state of Gaussians and the indices α and α' denote different system states. $|\mathbf{s}\rangle\langle\mathbf{s}|$ is the projection operator of the system coordinates. Then, we can calculate the corresponding Wigner transforms. The system coordinate operator becomes a product of delta functions,

$$\begin{aligned}
B_\mathrm{w}(\mathbf{p}_t,\mathbf{q}_t) &= \int \mathrm{d}^N \xi \; \mathrm{e}^{-\mathrm{i}\mathbf{p}_t^\mathrm{T}\boldsymbol{\xi}/\hbar} \left\langle \mathbf{q}_t + \frac{\boldsymbol{\xi}}{2} \middle| \mathbf{s} \right\rangle \left\langle \mathbf{s} \middle| \mathbf{q}_t - \frac{\boldsymbol{\xi}}{2} \right\rangle \\
&= \int \mathrm{d}^{N_\mathrm{s}} \xi_\mathrm{s} \; \mathrm{e}^{-\mathrm{i}\mathbf{p}_t^\mathrm{T}\boldsymbol{\xi}/\hbar} \left\langle \mathbf{q}_{\mathrm{s},t} + \frac{\boldsymbol{\xi}_\mathrm{s}}{2} \middle| \mathbf{s} \right\rangle \left\langle \mathbf{s} \middle| \mathbf{q}_{\mathrm{s},t} - \frac{\boldsymbol{\xi}_\mathrm{s}}{2} \right\rangle \\
&\quad \times \prod_{i=1}^{N_\mathrm{b}} \int \mathrm{d}\xi_i \; \left\langle q_{\mathrm{b},t,i} + \frac{\xi_{\mathrm{b},i}}{2} \middle| q_{\mathrm{b},t,i} - \frac{\xi_{\mathrm{b},i}}{2} \right\rangle \\
&= \prod_{i=1}^{N_\mathrm{s}} \int \mathrm{d}\xi_i \; \mathrm{e}^{-\mathrm{i}p_{i,t}\xi_i/\hbar} \delta\left(q_{i,t} + \frac{\xi_i}{2} - s_i \right) \delta\left(q_{i,t} - \frac{\xi_i}{2} - s_i \right) \\
&= \prod_{i=1}^{N_\mathrm{s}} \lim_{\epsilon_i \to 0} \frac{1}{2\pi\epsilon_i} \int \mathrm{d}\xi_i \; \exp\left\{ -\frac{1}{4\epsilon_i}\xi_i^2 - \frac{\mathrm{i}}{\hbar} p_{i,t}\xi_i - \frac{1}{\epsilon_i}\left(q_{i,t} - s_i\right)^2 \right\} \\
&= \prod_{i=1}^{N_\mathrm{s}} \lim_{\epsilon_i \to 0} \frac{1}{\sqrt{\pi\epsilon_i}} \exp\left\{ -\frac{1}{\epsilon_i}\left(q_{i,t} - s_i\right)^2 - \epsilon_i \frac{p_{i,t}^2}{\hbar^2} \right\} \\
&= \prod_{i=1}^{N_\mathrm{s}} \delta\left(q_{i,t} - s_i\right).
\end{aligned} \tag{2.41}$$

For the initial state, the Wigner transform amounts to some algebraic rearrangement and a Gaussian integration

$$
\begin{aligned}
A_{\mathrm{w}}(\mathbf{p},\mathbf{q}) &= \int \mathrm{d}^N\xi\ \mathrm{e}^{-\mathrm{i}\mathbf{p}^{\mathrm{T}}\boldsymbol{\xi}/\hbar} \left\langle \mathbf{q}+\frac{\boldsymbol{\xi}}{2}\middle|\Psi_\alpha\right\rangle \left\langle \Psi_{\alpha'}\middle|\mathbf{q}-\frac{\boldsymbol{\xi}}{2}\right\rangle \\
&= \prod_{i=1}^{N} \langle q_i|\Psi_{\alpha,i}\rangle \left\langle \Psi_{\alpha',i}|q_i\right\rangle \int \mathrm{d}\xi_i \\
&\quad \times \exp\left\{-\frac{\gamma_i}{4}\xi_i^2 + \left[\frac{\gamma_i}{2}\left(q_{\alpha,i}-q_{\alpha',i}\right)+\frac{\mathrm{i}}{2\hbar}\left(p_{\alpha,i}+p_{\alpha',i}-2p_i\right)\right]\xi_i\right\} \qquad (2.42)\\
&= \prod_{i=1}^{N} \langle q_i|\Psi_{\alpha,i}\rangle \left\langle \Psi_{\alpha',i}|q_i\right\rangle \exp\left\{\frac{\gamma_i}{4}\left(q_{\alpha,i}-q_{\alpha',i}\right)^2 - \frac{1}{4\hbar^2\gamma_i}\left(p_{\alpha,i}+p_{\alpha',i}-2p_i\right)^2\right\} \\
&\quad \times \exp\left\{\frac{\mathrm{i}}{2\hbar}\left(q_{\alpha,i}-q_{\alpha',i}\right)\left(p_{\alpha,i}+p_{\alpha',i}-2p_i\right)\right\}.
\end{aligned}
$$

In Ch. 6, where we want to calculate the time evolution of two scattering electrons, we will use Eqs. (2.37), (2.41), and (2.42) to show the classical counterpart of quantum and semiclassical results.

With this, we end the introductory chapter on semiclassical methods. We have introduced several different techniques, starting with the most accurate, but also most numerically demanding method by Herman and Kluk. Then, we have derived several simplifications, among which the hybrid method will be the most important one in this work. We will proceed by giving a detailed description of the calculation of two important quantities within the hybrid framework, namely, reduced density matrices of systems embedded in a temperature dependent bath and vibrational spectra of molecular systems.

3. HYBRID PROPAGATION SCHEME FOR DENSITY MATRICES AND SPECTRA OF MOLECULES

After introducing the basic idea of several trajectory based propagation schemes in the previous chapter, we will proceed with two applications of semiclassical hybrid dynamics to the calculation of reduced density matrices and vibrational spectra. Again, we divide the DOFs of the problem at hand into a small system and a larger bath part which are then described by HK propagator and thawed Gaussian (TG) dynamics, respectively.

The two quantities for which we will derive hybrid expressions are naturally suited to this approach. Reduced density matrices are a ubiquitous tool for the description of systems embedded in (finite or infinite) environments. They contain the full information about the system, and will be used later for the calculation of the purity. In the calculation of vibrational spectra, a separation of DOFs is both computationally necessary and well justified, because typically just a small part of the normal modes of a chemical system is significantly excited. These vibrations of interest can then be picked out for a more accurate HK description, while the others are assumed to be close to the ground state and therefore nearly harmonic.

3.1. HYBRID REDUCED DENSITY MATRIX FORMALISM FOR FINITE TEMPERATURE BATHS

The reduced density matrix formulation of semiclassical hybrid dynamics has been introduced in the doctoral work of C. Goletz both for zero [27] and finite bath temperature [28, 37]. We will shortly repeat the main steps leading to those equations that we will use later to describe the decoherence of iodine molecular vibrations in a krypton environment [66]. Since we will propagate initial superposition states $|\Phi(0)\rangle = (|\Phi_1\rangle + |\Phi_2\rangle)/\sqrt{2}$, the generalized total density matrix will be a double sum

$$\hat{\rho}(t) = \frac{1}{2}\sum_{\alpha=1}^{2}\sum_{\alpha'=1}^{2}\hat{\rho}_{\alpha,\alpha'}(t), \tag{3.1}$$

where $\hat{\rho}_{\alpha,\alpha'}(t)$ is the contribution to the time evolved density operator with initial state

$$\hat{\rho}_{\alpha,\alpha'}(0) = |\Phi_\alpha\rangle\langle\Phi_{\alpha'}|. \tag{3.2}$$

In order to make the system-bath separation, the DOFs of the total system are divided into system and bath parts, $\mathbf{x}^{\mathrm{T}} \equiv \left(\mathbf{s}^{\mathrm{T}}, \mathbf{y}^{\mathrm{T}}\right)$. The reduced density matrix is then defined as the trace over all bath DOFs of the total density matrix and can be written in position representation as

$$\rho_{\mathrm{s},\alpha,\alpha'}(\mathbf{s},\mathbf{s}',t) = \int \mathrm{d}^{N_\mathrm{b}}y \; \mathrm{d}^{N_\mathrm{b}}y' \; \delta(\mathbf{y}-\mathbf{y}')\Phi^*_{\alpha'}(\mathbf{x}',t)\Phi_\alpha(\mathbf{x},t). \tag{3.3}$$

We plug in Eq. (2.11) twice to express the time evolved wave functions, $\Phi^*_{\alpha'}(\mathbf{x}',t)$ and $\Phi_\alpha(\mathbf{x},t)$, with the HK propagator,

$$\begin{aligned}\rho_{\mathrm{s},\alpha,\alpha'}(\mathbf{x},\mathbf{x}',t) = \frac{1}{(2\pi\hbar)^{2N}} \int \mathrm{d}^{N_\mathrm{b}}y \; \mathrm{d}^{N_\mathrm{b}}y' \; \delta(\mathbf{y}-\mathbf{y}') \int \mathrm{d}^N p \; \mathrm{d}^N p' \; \mathrm{d}^N q \; \mathrm{d}^N q' \; C_t (C'_t)^* \\ \times \, \mathrm{e}^{\mathrm{i}(S_t - S'_t)/\hbar} \left\langle \mathbf{x} | g_{\boldsymbol{\gamma}}(\mathbf{p}_t,\mathbf{q}_t) \right\rangle \left\langle g_{\boldsymbol{\gamma}}(\mathbf{p}'_t,\mathbf{q}'_t) | \mathbf{x}' \right\rangle \left\langle g_{\boldsymbol{\gamma}}(\mathbf{p},\mathbf{q}) \middle| \hat{\rho}_{\alpha,\alpha'}(0) \middle| g_{\boldsymbol{\gamma}}\left(\mathbf{p}',\mathbf{q}'\right) \right\rangle ,\end{aligned} \tag{3.4}$$

where we use primes for quantities that depend on primed initial conditions $(\mathbf{p}',\mathbf{q}')$. The integration over the bath coordinates can be performed analytically to yield

$$\begin{aligned}\rho_{\mathrm{s},\alpha,\alpha'}(\mathbf{s},\mathbf{s}',t) = \frac{1}{(2\pi\hbar)^{2N}} \int \mathrm{d}^N p \; \mathrm{d}^N p' \; \mathrm{d}^N q \; \mathrm{d}^N q' \; \sqrt{\det\left[\mathbf{h}_t(\mathbf{p},\mathbf{q})\mathbf{h}^*_t(\mathbf{p}',\mathbf{q}')\right]} \mathrm{e}^{\mathrm{i}(S_t(\mathbf{p},\mathbf{q}) - S_t(\mathbf{p}',\mathbf{q}'))/\hbar} \\ \times \left\langle g_{\boldsymbol{\gamma}_\mathrm{b}}(\mathbf{p}_t,\mathbf{q}_t) \middle| g_{\boldsymbol{\gamma}_\mathrm{b}}(\mathbf{p}'_t,\mathbf{q}'_t) \right\rangle \left\langle \mathbf{s} \middle| g_{\boldsymbol{\gamma}_\mathrm{s}}(\mathbf{p}_t,\mathbf{q}_t) \right\rangle \left\langle g_{\boldsymbol{\gamma}_\mathrm{s}}(\mathbf{p}'_t,\mathbf{q}'_t) \middle| \mathbf{s}' \right\rangle \\ \times \left\langle g_{\boldsymbol{\gamma}_\mathrm{s}}\left(\mathbf{p}_\mathrm{s},\mathbf{q}_\mathrm{s}\right) \middle| \Psi_\alpha \right\rangle \left\langle \Psi_{\alpha'} \middle| g_{\boldsymbol{\gamma}_\mathrm{s}}\left(\mathbf{p}'_\mathrm{s},\mathbf{q}'_\mathrm{s}\right) \right\rangle \left\langle g_{\boldsymbol{\gamma}_\mathrm{b}}\left(\mathbf{p}_\mathrm{b},\mathbf{q}_\mathrm{b}\right) \middle| \frac{\mathrm{e}^{-\beta\hat{H}_\mathrm{b}}}{Z_\mathrm{b}} \middle| g_{\boldsymbol{\gamma}_\mathrm{b}}\left(\mathbf{p}'_\mathrm{b},\mathbf{q}'_\mathrm{b}\right) \right\rangle .\end{aligned} \tag{3.5}$$

In Eq. (3.5) and throughout this work, system and bath are chosen to be in a product state initially and therefore the contributions to the density factorize as well. We will use different initial states for the system DOFs only and thus get an initial density

$$|\Phi_\alpha\rangle\langle\Phi_{\alpha'}| = |\Psi_\alpha\rangle\langle\Psi_{\alpha'}| \frac{\mathrm{e}^{-\beta\hat{H}_\mathrm{b}}}{Z_\mathrm{b}} \tag{3.6}$$

with the newly introduced inverse temperature $\beta = 1/(k_\mathrm{B}T)$ containing the Boltzmann constant k_B and the temperature T as well as the partition function Z_b. In a temperature dependent formulation, the initial bath density is described by a thermal density operator, which takes the coherent state representation form [37]

$$\begin{aligned}\left\langle g_{\boldsymbol{\gamma}_\mathrm{b}}\left(\mathbf{p}_\mathrm{b},\mathbf{q}_\mathrm{b}\right) \middle| \frac{\mathrm{e}^{-\beta\hat{H}_\mathrm{b}}}{Z_\mathrm{b}} \middle| g_{\boldsymbol{\gamma}_\mathrm{b}}\left(\mathbf{p}'_\mathrm{b},\mathbf{q}'_\mathrm{b}\right) \right\rangle = \underbrace{\prod_{i=1}^{N_\mathrm{b}} \left(1 - \mathrm{e}^{-\beta\omega_i\hbar}\right)}_{\tilde{Z}_\mathrm{b}} \exp\left\{ -\frac{1}{4}\left(\mathbf{q}_\mathrm{b}^{\mathrm{T}}\boldsymbol{\gamma}_\mathrm{b}\mathbf{q}_\mathrm{b} + \mathbf{q}_\mathrm{b}'^{\mathrm{T}}\boldsymbol{\gamma}_\mathrm{b}\mathbf{q}'_\mathrm{b}\right)\right\} \\ \times \exp\left\{ -\frac{1}{4\hbar^2}\left(\mathbf{p}_\mathrm{b}^{\mathrm{T}}\boldsymbol{\gamma}_\mathrm{b}^{-1}\mathbf{p}_\mathrm{b} + \mathbf{p}_\mathrm{b}'^{\mathrm{T}}\boldsymbol{\gamma}_\mathrm{b}^{-1}\mathbf{p}'_\mathrm{b}\right) + \frac{\mathrm{i}}{2\hbar}\left(\mathbf{p}_\mathrm{b}^{\mathrm{T}}\mathbf{q}_\mathrm{b} - \mathbf{p}_\mathrm{b}'^{\mathrm{T}}\mathbf{q}'_\mathrm{b}\right)\right\} \\ \times \exp\left\{ +\frac{1}{2}\left(\boldsymbol{\gamma}_\mathrm{b}\mathbf{q}_\mathrm{b} - \frac{\mathrm{i}}{\hbar}\mathbf{p}_\mathrm{b}\right)^{\mathrm{T}} \mathrm{e}^{-\beta\boldsymbol{\gamma}_\mathrm{b}\hbar^2}\left(\mathbf{q}'_\mathrm{b} + \frac{\mathrm{i}}{\hbar}\boldsymbol{\gamma}_\mathrm{b}^{-1}\mathbf{p}'_\mathrm{b}\right)\right\}\end{aligned} \tag{3.7}$$

Since we assume the bath degrees of freedom to be harmonic and have unit mass with Eq. (3.7), the bath width parameter matrix $\boldsymbol{\gamma}_\mathrm{b}$ has diagonal entries $\omega_{\mathrm{b},i}/\hbar$, where $\omega_{\mathrm{b},i}$ is the frequency of the i-th bath oscillator.

In spite of the reduction in Cartesian coordinate space, the computational effort for the convergence of the $4N$ dimensional phase space integral in Eq. (3.5) renders simulations impossible as soon as the number of DOFs exceeds a handful. Further approximations are needed; one such way is to bring the hybrid idea into play. We should stress right at the start of the derivation that we will restrict ourselves such that the system DOFs will always be treated with HK and the bath DOFs will always be treated with TG. In general, this is not necessary and sometimes not even desirable, but it is sufficient for the reduced density calculations in this work and we will therefore use "system" and "HK" synonymously, as well as "bath" and "TG", in this section. The more general approach is laid out in [37].

As in Eqs. (2.19), (2.23) and (2.24) of Sec. 2.2.2, the action and the trajectories are expanded to second order in the difference coordinates around a central trajectory for a subset of DOFs only. We insert the approximated quantities into the full density from Eq. (3.4) and regroup the exponent in powers of the displacement variables

$$\begin{aligned}\rho_{\alpha,\alpha'}(\mathbf{x},\mathbf{x}',t) = \frac{1}{(2\pi\hbar)^{2N}} \int \mathrm{d}^N p\ \mathrm{d}^N p'\ \mathrm{d}^N q\ \mathrm{d}^N q'\ \tilde{Z}_\mathrm{b} \sqrt{\det\left[\mathbf{h}_t(\mathbf{h}'_t)^*\right]} \\ \times \left\langle g_{\boldsymbol{\gamma}_\mathrm{s}}\left(\mathbf{p}_\mathrm{s},\mathbf{q}_\mathrm{s}\right)\middle|\Psi_\alpha\right\rangle \left\langle\Psi_{\alpha'}\middle|g_{\boldsymbol{\gamma}_\mathrm{s}}\left(\mathbf{p}'_\mathrm{s},\mathbf{q}'_\mathrm{s}\right)\right\rangle \\ \times \left\langle\mathbf{x}\middle|g_{\boldsymbol{\gamma}}(\mathbf{p}_{\alpha,t},\mathbf{q}_{\alpha,t})\right\rangle \left\langle g_{\boldsymbol{\gamma}}(\mathbf{p}'_{\alpha',t},\mathbf{q}'_{\alpha',t})\middle|\mathbf{x}'\right\rangle \\ \times \exp\left\{ -\begin{pmatrix}\delta\mathbf{p}_\mathrm{tg}\\ \delta\mathbf{q}_\mathrm{tg}\\ \delta\mathbf{p}'_\mathrm{tg}\\ \delta\mathbf{q}'_\mathrm{tg}\end{pmatrix}^\mathrm{T} \mathbf{A}_t^\mathrm{rd} \begin{pmatrix}\delta\mathbf{p}_\mathrm{tg}\\ \delta\mathbf{q}_\mathrm{tg}\\ \delta\mathbf{p}'_\mathrm{tg}\\ \delta\mathbf{q}'_\mathrm{tg}\end{pmatrix} + \left(\mathbf{b}_t^\mathrm{rd}\right)^\mathrm{T} \begin{pmatrix}\delta\mathbf{p}_\mathrm{tg}\\ \delta\mathbf{q}_\mathrm{tg}\\ \delta\mathbf{p}'_\mathrm{tg}\\ \delta\mathbf{q}'_\mathrm{tg}\end{pmatrix} + \frac{\mathrm{i}}{\hbar}\left(S_{\alpha,t} - S'_{\alpha',t}\right) \right\}\end{aligned} \tag{3.8}$$

where we introduce the index α for quantities that depend on initial conditions $(\mathbf{p}_{\alpha,0},\mathbf{q}_{\alpha,0})$, for example $\mathbf{p}_{\alpha,t} \equiv \mathbf{p}\left(\mathbf{p}_{\alpha,0},\mathbf{q}_{\alpha,0},t\right)$, and likewise the index α' for initial conditions $\left(\mathbf{p}'_{\alpha',0},\mathbf{q}'_{\alpha',0}\right)$. Assuming $\mathbf{h}(\mathbf{p},\mathbf{q},t) \approx \mathbf{h}(\mathbf{p}_{\alpha,0},\mathbf{q}_{\alpha,0},t)$ like we did in Sec. 2.2.2, we can again perform a Gaussian integration over the bath DOFs to get

$$\begin{aligned}\rho_{\alpha,\alpha'}(\mathbf{x},\mathbf{x}',t) = \frac{1}{(2\hbar)^{2N}\pi^{2N_\mathrm{hk}}} \int \mathrm{d}^{N_\mathrm{hk}} p\ \mathrm{d}^{N_\mathrm{hk}} p'\ \mathrm{d}^{N_\mathrm{hk}} q\ \mathrm{d}^{N_\mathrm{hk}} q'\ \tilde{Z}_\mathrm{b} \sqrt{\frac{\det\left[\mathbf{h}_{\alpha,t}(\mathbf{h}'_{\alpha',t})^*\right]}{\det\left(\mathbf{A}_t^\mathrm{rd}\right)}} \\ \times \left\langle g_{\boldsymbol{\gamma}_\mathrm{s}}\left(\mathbf{p}_\mathrm{s},\mathbf{q}_\mathrm{s}\right)\middle|\Psi_\alpha\right\rangle \left\langle\Psi_{\alpha'}\middle|g_{\boldsymbol{\gamma}_\mathrm{s}}\left(\mathbf{p}'_\mathrm{s},\mathbf{q}'_\mathrm{s}\right)\right\rangle \\ \times \left\langle\mathbf{x}\middle|g_{\boldsymbol{\gamma}}(\mathbf{p}_{\alpha,t},\mathbf{q}_{\alpha,t})\right\rangle \left\langle g_{\boldsymbol{\gamma}}(\mathbf{p}'_{\alpha',t},\mathbf{q}'_{\alpha',t})\middle|\mathbf{x}'\right\rangle \\ \times \exp\left\{ \frac{1}{4}\left(\mathbf{b}_t^\mathrm{rd}\right)^\mathrm{T}\left(\mathbf{A}_t^\mathrm{rd}\right)^{-1}\mathbf{b}_t^\mathrm{rd} + \frac{\mathrm{i}}{\hbar}\left(S_{\alpha,t} - S'_{\alpha',t}\right)\right\}\end{aligned} \tag{3.9}$$

Except for the prefactor, the bath initial state from Eq. (3.7) is fully contained in the newly defined variables $\mathbf{A}^\mathrm{rd}$ and $\mathbf{b}^\mathrm{rd}$. In order to shorten these expressions, we introduce two further abbreviations, namely, $N_\mathrm{tg} \times N$ matrices defined as

$$\tilde{\mathbf{u}}_t = \tilde{\mathbf{m}}_{21,t}^\mathrm{T}\boldsymbol{\gamma} + \frac{\mathrm{i}}{\hbar}\tilde{\mathbf{m}}_{11,t}^\mathrm{T} \tag{3.10}$$

$$\tilde{\mathbf{v}}_t = \tilde{\mathbf{m}}_{22,t}^\mathrm{T}\boldsymbol{\gamma} + \frac{\mathrm{i}}{\hbar}\tilde{\mathbf{m}}_{12,t}^\mathrm{T}, \tag{3.11}$$

with the non-square stability submatrices $\tilde{\mathbf{m}}_{ij}$ introduced in Eq. (2.22). Parameters of quadratic terms in the bath initial conditions are collected in the $4N_\mathrm{b} \times 4N_\mathrm{b}$ matrix

$$\mathbf{A}_t^\mathrm{rd} = \begin{pmatrix}\mathbf{A}_{1,t} & \mathbf{A}_{2,t}\\ \mathbf{A}_{2,t}^\mathrm{T} & \left(\mathbf{A}'_{1,t}\right)^*\end{pmatrix} \tag{3.12}$$

whose $2N_\mathrm{b} \times 2N_\mathrm{b}$ submatrices are defined as follows:

$$\mathbf{A}_{1,t} = \begin{pmatrix} \frac{\gamma_\mathrm{tg}^{-1}}{4\hbar^2} + \frac{\tilde{\mathbf{u}}_t \tilde{\mathbf{m}}_{21,t}}{2} & \frac{\mathrm{i}}{4\hbar} + \frac{\tilde{\mathbf{m}}_{21,t}^\mathrm{T} \tilde{\mathbf{v}}_t^\mathrm{T}}{2} \\ \frac{\mathrm{i}}{4\hbar} + \frac{\tilde{\mathbf{v}} \tilde{\mathbf{m}}_{21,t}}{2} & \frac{\gamma_\mathrm{tg}}{4} + \frac{\tilde{\mathbf{v}}_t \tilde{\mathbf{m}}_{22,t}}{2} \end{pmatrix} = \mathbf{A}_t^\mathrm{wf} \qquad \mathbf{A}_{2,t} = \mathrm{e}^{-\beta\boldsymbol{\gamma}_\mathrm{tg}\hbar} \begin{pmatrix} -\frac{\gamma_\mathrm{tg}^{-1}}{4\hbar^2} & \frac{\mathrm{i}}{4\hbar} \\ -\frac{\mathrm{i}}{4\hbar} & -\frac{\gamma_\mathrm{tg}}{4} \end{pmatrix}. \tag{3.13}$$

The parameters of terms linear in the bath initial conditions are again written in the form of a $4N_\mathrm{tg}$ dimensional vector

$$\left(\mathbf{b}_t^\mathrm{rd}\right)^\mathrm{T} = \begin{pmatrix} \mathbf{x} - \mathbf{q}_{\alpha,t} \\ \mathbf{x}' - \mathbf{q}'_{\alpha',t} \end{pmatrix}^\mathrm{T} \begin{pmatrix} \begin{bmatrix} \tilde{\mathbf{u}}_t^\mathrm{T} & \tilde{\mathbf{v}}_t^\mathrm{T} \end{bmatrix} & \mathbf{0} \\ \mathbf{0} & \begin{bmatrix} (\tilde{\mathbf{u}}_t'^*)^\mathrm{T} & (\tilde{\mathbf{v}}_t'^*)^\mathrm{T} \end{bmatrix} \end{pmatrix} = \begin{pmatrix} \mathbf{b}_t^\mathrm{wf} \\ \left[\mathbf{b}_t^\mathrm{wf}\right]' \end{pmatrix}^\mathrm{T}. \tag{3.14}$$

Comparing the above quantities with their wave function counterparts in Sec. 2.2.2, one finds that the reduced density formalism is just a generalization of this previous section. We also note that the elements of $\mathbf{A}_{2,t}$ become zero for vanishing temperature.

The remaining integration over the Cartesian bath DOFs in Eq. (3.9) poses no fundamental difficulty, but we need an explicit expression for the inverse of the previously defined matrix $\mathbf{A}^\mathrm{rd}$ because the term $\left(\mathbf{b}_t^\mathrm{rd}\right)^\mathrm{T} \left(\mathbf{A}_t^\mathrm{rd}\right)^{-1} \mathbf{b}_t^\mathrm{rd}$ depends on the Cartesian DOFs via $\mathbf{b}_t^\mathrm{rd}$. We use the definition from [37] and define

$$\frac{1}{4} \left(\mathbf{b}_t^\mathrm{rd}\right)^\mathrm{T} \left(\mathbf{A}_t^\mathrm{rd}\right)^{-1} \mathbf{b}_t^\mathrm{rd} \equiv \frac{1}{4} \left(\mathbf{b}_t^\mathrm{rd}\right)^\mathrm{T} \begin{pmatrix} \mathbf{D}_{1,t} & \mathbf{D}_{2,t} \\ \mathbf{D}_{2,t}^\mathrm{T} & \mathbf{D}_{3,t} \end{pmatrix} \mathbf{b}_t^\mathrm{rd} \tag{3.15}$$

$$\equiv \begin{pmatrix} \mathbf{x} - \mathbf{q}_{\alpha,t} \\ \mathbf{x}' - \mathbf{q}'_{\alpha',t} \end{pmatrix}^\mathrm{T} \begin{pmatrix} \mathbf{K}_t & \mathbf{L}_t \\ \mathbf{L}_t^\mathrm{T} & \mathbf{K}'_t \end{pmatrix} \begin{pmatrix} \mathbf{x} - \mathbf{q}_{\alpha,t} \\ \mathbf{x}' - \mathbf{q}'_{\alpha',t} \end{pmatrix} \tag{3.16}$$

System and bath Cartesian coordinates are now separable by expressing both $\mathbf{K}$ and $\mathbf{L}$ in the form

$$\mathbf{K}_t \equiv \begin{pmatrix} \mathbf{K}_{\mathrm{ss},t} & \mathbf{K}_{\mathrm{sb},t} \\ \mathbf{K}_{\mathrm{bs},t} & \mathbf{K}_{\mathrm{bb},t} \end{pmatrix} \qquad \mathbf{L}_t \equiv \begin{pmatrix} \mathbf{L}_{\mathrm{ss},t} & \mathbf{L}_{\mathrm{sb},t} \\ \mathbf{L}_{\mathrm{bs},t} & \mathbf{L}_{\mathrm{bb},t} \end{pmatrix}. \tag{3.17}$$

With this notational clarification in place, we can once more reshuffle terms. First, we carry out the $\mathrm{d}^{N_\mathrm{b}} y' \delta(\mathbf{y} - \mathbf{y}')$ integration according to Eq. (3.3). Then, we regroup the modified exponent from Eq. (3.9) in orders of bath Cartesian coordinates $\mathbf{y}$ to obtain the desired quadratic form $\mathbf{y}^\mathrm{T}\mathbf{H}\mathbf{y} + \mathbf{e}^\mathrm{T}\mathbf{y} + f$. After another Gaussian integration over the remaining bath coordinates, we arrive at the final result for the hybrid formulation of a reduced density matrix of a system in a temperature dependent bath

$$\begin{aligned} \rho_{\mathrm{s},\alpha,\alpha'}(\mathbf{s}, \mathbf{s}', t) = {} & \frac{1}{(2\hbar)^{2N} \pi^{5N_\mathrm{hk}/2}} \int \mathrm{d}^{N_\mathrm{hk}} p_\mathrm{hk}\ \mathrm{d}^{N_\mathrm{hk}} p'_\mathrm{hk}\ \mathrm{d}^{N_\mathrm{hk}} q_\mathrm{hk}\ \mathrm{d}^{N_\mathrm{hk}} q'_\mathrm{hk}\ \left[\prod_{i=1}^{N_\mathrm{b}} \left(1 - \mathrm{e}^{-\beta\omega_i\hbar}\right)\right] \\ & \times \sqrt{\frac{\det(\boldsymbol{\gamma}) \det\left[\mathbf{h}_{\alpha,t}(\mathbf{h}'_{\alpha,t})^*\right]}{\det\left(\mathbf{A}_t^\mathrm{rd}\right) \det(\mathbf{H}_t)}} \left\langle g_{\boldsymbol{\gamma}_\mathrm{s}}(\mathbf{p}_\mathrm{s}, \mathbf{q}_\mathrm{s}) \middle| \Psi_\alpha \right\rangle \left\langle \Psi_{\alpha'} \middle| g_{\boldsymbol{\gamma}_\mathrm{s}}(\mathbf{p}'_\mathrm{s}, \mathbf{q}'_\mathrm{s}) \right\rangle \\ & \times \exp\left\{ \begin{pmatrix} \mathbf{s} - \mathbf{q}_{\alpha,\mathrm{s},t} \\ \mathbf{s}' - \mathbf{q}'_{\alpha',\mathrm{s},t} \end{pmatrix}^\mathrm{T} \boldsymbol{\Lambda}_t \begin{pmatrix} \mathbf{s} - \mathbf{q}_{\alpha,\mathrm{s},t} \\ \mathbf{s}' - \mathbf{q}'_{\alpha',\mathrm{s},t} \end{pmatrix} + \boldsymbol{\sigma}_t^\mathrm{T} \begin{pmatrix} \mathbf{s} - \mathbf{q}_{\alpha,\mathrm{s},t} \\ \mathbf{s}' - \mathbf{q}'_{\alpha',\mathrm{s},t} \end{pmatrix} + h_t + \frac{\mathrm{i}}{\hbar}(S_{\alpha,t} - S'_{\alpha',t}) \right\}. \end{aligned} \tag{3.18}$$

This expression contains a number of new abbreviations that we will list shortly in the following. The quadratic terms in $\mathbf{y}$ are assembled in the symmetric $N_\mathrm{b} \times N_\mathrm{b}$ matrix

$$\mathbf{H}_t = -\left(\mathbf{K}_{\mathrm{bb},t} + \mathbf{K}'_{\mathrm{bb},t} + \mathbf{L}_{\mathrm{bb},t} + \mathbf{L}'_{\mathrm{bb},t} - \boldsymbol{\gamma}_\mathrm{b}\right). \tag{3.19}$$

Contributions in the different orders of $(\mathbf{s}-\mathbf{q}_{\alpha,\mathrm{s},t})$ arise either from the last Gaussian integration, from the position representation Gaussians in Eq. (3.9) or from the system part of expression (3.16). Terms that are quadratic in the system coordinates are summarized as

$$\mathbf{\Lambda}_t = \begin{pmatrix} \mathbf{F}_{\mathrm{sb},t}\mathbf{H}_t^{-1}\mathbf{F}_{\mathrm{sb},t}^{\mathrm{T}} - \frac{\gamma_\mathrm{s}}{2} + \mathbf{K}_{\mathrm{ss},t} & \mathbf{F}_{\mathrm{sb},t}\mathbf{H}_t^{-1}\mathbf{F}_{\mathrm{sb},t}'^{\mathrm{T}} + \mathbf{L}_{\mathrm{ss},t} \\ \mathbf{F}_{\mathrm{sb},t}'^{\mathrm{T}}\mathbf{H}_t^{-1}\mathbf{F}_{\mathrm{sb},t} + \mathbf{L}_{\mathrm{ss},t}^{\mathrm{T}} & \mathbf{F}_{\mathrm{sb},t}'\mathbf{H}_t^{-1}\mathbf{F}_{\mathrm{sb},t}'^{\mathrm{T}} - \frac{\gamma_\mathrm{s}}{2} + \mathbf{K}_{\mathrm{ss},t}' \end{pmatrix} \tag{3.20}$$

with auxiliary matrices

$$\mathbf{F}_{\mathrm{sb},t} \equiv \mathbf{K}_{\mathrm{sb},t} + \mathbf{L}_{\mathrm{sb},t} \qquad \mathbf{F}_{\mathrm{sb},t}' \equiv \mathbf{K}_{\mathrm{sb},t}' + \mathbf{L}_{\mathrm{bs},t}^{\mathrm{T}}. \tag{3.21}$$

Linear contributions in $(\mathbf{s}-\mathbf{q}_{\alpha,\mathrm{s},t})$ are collected as

$$\boldsymbol{\sigma}_t = \begin{pmatrix} \mathbf{F}_{\mathrm{sb},t}\mathbf{H}_t^{-1}\mathbf{d}_t - 2\mathbf{K}_{\mathrm{bs},t}^{\mathrm{T}}\mathbf{q}_{\alpha,\mathrm{b},t} - 2\mathbf{L}_{\mathrm{sb},t}\mathbf{q}_{\alpha',\mathrm{b},t}' + \frac{\mathrm{i}}{\hbar}\mathbf{p}_{\alpha,\mathrm{s},t} \\ \mathbf{F}_{\mathrm{sb},t}'\mathbf{H}_t^{-1}\mathbf{d}_t - 2\mathbf{K}_{\mathrm{bs},t}'^{\mathrm{T}}\mathbf{q}_{\alpha',\mathrm{b},t}' - 2\mathbf{L}_{\mathrm{bs},t}^{\mathrm{T}}\mathbf{q}_{\alpha,\mathrm{b},t} - \frac{\mathrm{i}}{\hbar}\mathbf{p}_{\alpha',\mathrm{s},t}' \end{pmatrix}, \tag{3.22}$$

where we have defined another auxiliary vector

$$\begin{aligned} \mathbf{d}_t = {} & \left(\boldsymbol{\gamma}_\mathrm{b} - 2\mathbf{K}_{\mathrm{bb},t} - 2\mathbf{L}_{\mathrm{bb},t}\right)^{\mathrm{T}}\mathbf{q}_{\alpha,\mathrm{b},t} + \left(\boldsymbol{\gamma}_\mathrm{b} - 2\mathbf{K}_{\mathrm{bb},t}' - 2\mathbf{L}_{\mathrm{bb},t}\right)^{\mathrm{T}}\mathbf{q}_{\alpha',\mathrm{b},t}' \\ & + \frac{\mathrm{i}}{\hbar}\left(\mathbf{p}_{\alpha,\mathrm{b},t} - \mathbf{p}_{\alpha',\mathrm{b},t}'\right) \end{aligned} \tag{3.23}$$

All remaining contributions except for the action form a scalar

$$\begin{aligned} h_t = {} & -\left[\frac{1}{2}\mathbf{q}_{\alpha,\mathrm{b},t}^{\mathrm{T}}\left(\boldsymbol{\gamma}_\mathrm{b} - 2\mathbf{K}_{\mathrm{bb}}\right) + \frac{\mathrm{i}}{\hbar}\mathbf{p}_{\alpha,\mathrm{b},t}\right]^{\mathrm{T}}\mathbf{q}_{\alpha,\mathrm{b},t} \\ & -\left[\frac{1}{2}(\mathbf{q}_{\alpha',\mathrm{b},t}')^{\mathrm{T}}\left(\boldsymbol{\gamma}_\mathrm{b} - 2\mathbf{K}_{\mathrm{bb}}'\right) - \frac{\mathrm{i}}{\hbar}\mathbf{p}_{\alpha',\mathrm{b},t}'\right]^{\mathrm{T}}\mathbf{q}_{\alpha',\mathrm{b},t}' - 2\mathbf{q}_{\alpha,\mathrm{b},t}^{\mathrm{T}}\mathbf{L}_{\mathrm{bb}}\mathbf{q}_{\alpha',\mathrm{b},t}' + \frac{1}{4}\mathbf{d}_t^{\mathrm{T}}\mathbf{H}_t^{-1}\mathbf{d}_t. \end{aligned} \tag{3.24}$$

With Eq. (3.18), we have a tool at our disposal that allows for the calculation of the system dynamics in a temperature dependent bath. It should be pointed out that we achieve a twofold reduction in computational effort. Most importantly, the hybrid formalism reduces the $4N$ dimensional phase space integral from Eq. (3.5) into an integral of $4N_{\mathrm{hk}}$ dimensions. Second, the memory required for the storage of the reduced density depends only on the number of system DOFs. With these measures, we obtain a mechanism that scales very favorably with the bath size in terms of computational time and memory. In Ch. 5 it will be applied to the dynamics of iodine in a krypton environment. We also will perform full quantum calculations for small bath sizes as a means of comparison; the theoretical considerations for the description of the bath temperature in this case are sketched in App. B.

3.1.1. MEASURING THE QUANTUMNESS OF A SYSTEM: PURITY AND COHERENCE

We will conclude the section on the hybrid reduced density formalism by introducing the quantities that we will be interested in later. In Ch. 5, we will investigate the decay of quantum properties of an iodine molecule embedded in a krypton bath. A common measure for the quantum character of a physical system is the purity [67] of the kth DOF,

$$P_k(t) = \mathrm{Tr}_k\left(\hat{\rho}_k(t)^2\right), \tag{3.25}$$

where $\hat{\rho}_k(t)$ is the density matrix reduced to coordinate k. For a pure state, the projection property of the density matrix obviously results in a value of 1. For a fully mixed state, where K different basis states contribute with equal probability, the purity takes on its minimum value of $1/K$.

Another, experimentally more relevant, quantity is the coherence between two states. We will specifically investigate the coherence between two vibrational states. The coherence in this sense is defined as one specific off-diagonal element of the reduced density matrix,

$$\Pi_{kj}(t) = |\langle k|\hat{\rho}_{\mathrm{s}}(t)|j\rangle| \,. \tag{3.26}$$

If we take an initial state comprising a superposition of two vibrational eigenstates of the system, $(|k\rangle + |j\rangle)/\sqrt{2}$, the maximum value for this quantity is 1/2. The minimum value of zero is reached once the coherence between these specific states has been completely damped out by the interaction with environmental DOFs.

3.2. VIBRATIONAL SPECTRA OF MOLECULES

Spectra of molecular vibrations are a fundamental and ubiquitous observable in quantum physics that provides valuable insight in the composition and dynamics of complex molecular systems. A lot of experiments in molecular physics result in spectral information of some sort. Predicting and explaining experimental outcomes theoretically is therefore a task with a lot of applications and very closely related to experimental findings.

From the theoretical point of view, there are several ways to calculate the spectrum of a given system. The first idea might be to diagonalize the Hamiltonian either analytically, which can be done only for very simple systems, or numerically [68, 69]. One such approach is the class of vibrational self-consistent field methods where the basic idea is to approximate the total wavefunction as a product of 1D wave functions. These wave functions are subject to effective 1D potentials obtained by averaging over all remaining degrees of freedom. The arising equations are solved self-consistently; correlations due to the coupling of different DOFs can be included by second order perturbation theory [69]. Another way is to calculate the spectrum dynamically by computing the time evolution arising from the Hamiltonian to get the autocorrelation function and then find the spectrum as its Fourier transform. This approach requires a computationally feasible method for calculation of the system dynamics. We will focus on semiclassical methods based on the propagator by Herman and Kluk for the calculation of the autocorrelation function. The simplest implementation without any further approximations has, for example, been used successfully to calculate the spectrum of the 3D hydrogen atom [18]. Problems that contain more than a few degrees of freedom, however, require further approximations to the HK propagator to keep the number of trajectories that are needed for convergence of the phase space integral as low as possible.

As one way to achieve this reduction, a time-averaging formalism for the calculation of wave functions with the HK propagator has been proposed by Y. Elran and K. Kay in 1999 [70, 71] that introduces an additional time average (TA) of the phase space integrand. The additional integration pre-averages the phase space integrand in such a way that considerably fewer trajectories are needed to achieve the same level of accuracy for the resulting wave function, as is shown for two one-dimensional model systems. This idea has been used specifically for the calculation of vibrational energy levels by A. L. Kaledin and W. H. Miller [29] who introduced an additional, so-called separable approximation to reduce computational effort. The resulting expression requires only one instead of two time integrations, but is exact only for the harmonic

oscillator (HO) and still very accurate for low energy states in Morse-like potentials. Within this approximation, systems with about ten DOFs have been investigated [29–33, 53, 72–76]. However, for the more complex calculations, additional measures such as specific initial states had to be employed to keep computational effort on a feasible level.

Another way to lower numerical cost has been introduced in the previous chapter. With the semiclassical hybrid dynamics, we have a tool at hand that allows for a divide-and-conquer approach by keeping the costly HK calculations restricted to few DOFs of interest and describing the majority of DOFs with the single trajectory thawed Gaussian method. In the context of spectral calculations, such a separation makes sense because usually only (excited) vibrational states of a few bonds or normal coordinates are of interest, while the exact energies of environmental DOFs are not important. As the main theoretical achievement of this work, we will apply the hybrid idea to the TA SC-IVR formalism to make calculations for systems with a few tens of DOFs possible.

In this section, we first repeat the argument by Kaledin and Miller that leads to the TA SC-IVR. Then, we will derive a hybrid expression and propose another approximation to get a compact and computationally cheap method to find the full vibrational spectrum of small systems of interest embedded into a large environment. The effect of the different approximations will be demonstrated for two simple numerical examples to give an idea about their respective quality.

3.2.1. TIME AVERAGED SEMICLASSICAL CALCULATION OF VIBRATIONAL SPECTRA

We start by laying out the basic idea of the time averaging formalism for the semiclassical calculation of spectra, as it has been proposed in [29]. A given state $|\chi\rangle$ of a system described by Hamiltonian $\hat{H}$ has a spectrum

$$I(E) = \sum_i |\langle\chi|\psi_i\rangle|^2 \, \delta(E - E_i), \tag{3.27}$$

where E_i are the eigenenergies and $|\psi_i\rangle$ are the associated eigenstates of the Hamiltonian. This spectrum can be calculated from the dynamical evolution of an initial state $|\chi\rangle$ subject to Hamilton $\hat{H}$ by taking the Fourier transform of the resulting autocorrelation function,

$$I(E) = \frac{1}{2\pi\hbar} \int_{-\infty}^{\infty} \mathrm{d}t \; \mathrm{e}^{\mathrm{i}Et/\hbar} \left\langle \chi \left| \mathrm{e}^{-\mathrm{i}\hat{H}t/\hbar} \right| \chi \right\rangle \tag{3.28}$$

$$= \mathrm{Re} \left(\frac{1}{\pi\hbar} \int_{0}^{\infty} \mathrm{d}t \; \mathrm{e}^{\mathrm{i}Et/\hbar} \left\langle \chi \left| \mathrm{e}^{-\mathrm{i}\hat{H}t/\hbar} \right| \chi \right\rangle \right), \tag{3.29}$$

where the symbol Re signifies taking the real part of the expression that follows in brackets. The semiclassical approximation is introduced into this expression by using the HK propagator for the evaluation of the autocorrelation function. One then gets

$$\begin{aligned} I(E) = & \frac{1}{(2\pi\hbar)^N} \frac{1}{\pi\hbar} \int \mathrm{d}^N p \int \mathrm{d}^N q \\ & \times \mathrm{Re} \left(\int_0^{\infty} \mathrm{d}t \; \mathrm{e}^{\mathrm{i}Et/\hbar} C_t(\mathbf{p},\mathbf{q}) \mathrm{e}^{\mathrm{i}S_t(\mathbf{p},\mathbf{q})/\hbar} \langle\chi|g(\mathbf{p}_t,\mathbf{q}_t)\rangle \langle g(\mathbf{p},\mathbf{q})|\chi\rangle \right), \end{aligned} \tag{3.30}$$

where $(\mathbf{p}_t, \mathbf{q}_t) = [\mathbf{p}(\mathbf{p}, \mathbf{q}, t), \mathbf{q}(\mathbf{p}, \mathbf{q}, t)]$ are classical trajectories, C_t is the HK prefactor, S_t is the classical action, and $|g(\mathbf{p}_t, \mathbf{q}_t)\rangle$ is a GWP centered at $(\mathbf{p}_t, \mathbf{q}_t)$. In principle, Eq. (3.30) can be used for system with any number of DOFs, however, the need to converge the phase space integral numerically narrows down its application range to very small systems. In order to describe larger systems, one has to find a way to reduce the number of trajectories that are necessary for convergence. Kaledin and Miller [29] therefore suggested to replace the phase space integral I_{PS} is by its time averaged version $I_{\mathrm{PS,TA}}$

$$I_{\mathrm{PS}} = \int \mathrm{d}^N p \int \mathrm{d}^N q \; A(\mathbf{q}, \mathbf{p}) \quad \rightarrow \quad I_{\mathrm{PS,TA}} = \int \mathrm{d}^N p \int \mathrm{d}^N q \; \frac{1}{T} \int \mathrm{d}t \; A(\mathbf{q}_t, \mathbf{p}_t). \tag{3.31}$$

This leaves the phase space average unchanged as can be shown by first exchanging the order of integration in $I_{\mathrm{PS,TA}}$ and then using Liouville's theorem to change integration variables from $(\mathbf{p}, \mathbf{q})$ to $(\mathbf{p}_t, \mathbf{q}_t)$. The expected result of this pre-averaging of the phase space integrand along each trajectory is a smoother integrand. After some algebra, application of the time averaging (3.31) to the semiclassical expression for the spectrum, Eq. (3.30), leads to

$$\begin{aligned} I(E) = & \frac{1}{(2\pi\hbar)^N} \int \mathrm{d}^N p \int \mathrm{d}^N q \; \mathrm{Re} \left(\frac{1}{\pi\hbar T} \int_0^T \mathrm{d}t_1 \int_{t_1}^{\infty} \mathrm{d}t_2 \; C_{t_2}(\mathbf{p}_{t_1}, \mathbf{q}_{t_1}) \right. \\ & \left. \times \langle \chi | \mathbf{p}_{t_2}, \mathbf{q}_{t_2} \rangle \, \mathrm{e}^{\mathrm{i}/\hbar \left(S_{t_2}(\mathbf{p},\mathbf{q}) + E t_2 \right)} \left[\langle \chi | \mathbf{p}_{t_1}, \mathbf{q}_{t_1} \rangle \, \mathrm{e}^{\mathrm{i}/\hbar \left(S_{t_1}(\mathbf{p},\mathbf{q}) + E t_1 \right)} \right]^* \right). \end{aligned} \tag{3.32}$$

In order to avoid evaluating the cumbersome double time integration, one would like to collapse it into the absolute value squared of just one time integration. The only term that prevents this step is the prefactor $C_{t_2}(\mathbf{p}_{t_1}, \mathbf{q}_{t_1})$. Consequently, Kaledin and Miller propose an approximation to enforce factorization, namely,

$$C_{t_2}(\mathbf{p}_{t_1}, \mathbf{q}_{t_1}) \approx \mathrm{e}^{\mathrm{i}\phi_{t_2}/\hbar} \mathrm{e}^{-\mathrm{i}\phi_{t_1}/\hbar} \tag{3.33}$$

where $\phi_t/\hbar$ is the phase of the HK prefactor C_t. This separable approximation is exact for the harmonic oscillator and gives very accurate results also for more complicated bound systems, as has been shown in a lot of publications [29–33, 53, 72–76]. Inserting Eq. (3.33) and setting the upper boundary of the t_2 integration to T makes Eq. (3.32)

$$\begin{aligned} I(E) = & \frac{1}{(2\pi\hbar)^N} \frac{1}{2\pi\hbar T} \int \mathrm{d}^N p \int \mathrm{d}^N q \\ & \times \left| \int_0^T \mathrm{d}t \, \langle \chi | g(\mathbf{p}_t, \mathbf{q}_t) \rangle \exp\left\{ \mathrm{i} \left[S_t(\mathbf{p}, \mathbf{q}) + E t + \phi_t(\mathbf{p}, \mathbf{q}) \right] / \hbar \right\} \right|^2 . \end{aligned} \tag{3.34}$$

From a comparison to the original HK spectral density (3.30), it is obvious that this new expression is more well-behaved since the phase space integration is now over a strictly positive quantity and therefore very likely to converge with a smaller number of trajectories. Kaledin and Miller applied this approximated form to small molecules such as water [29], methane and ammonia [32]. M. Ceotto and different coworkers employed the separable TA SC-IVR method for a variety of molecular systems with up to eight coupled and 21 uncoupled DOFs [30, 31, 33, 53, 72–76]. They showed that an initial state that is specifically tailored to the system under investigation greatly reduces the number of trajectories required to get accurate

energy levels. Capitalizing on the intuitive nature of semiclassical IVRs, they take a coherent superposition of GWPs centered at phase space points with energies close to the actual spectral positions and just have to run a single trajectory for each initial GWP [30, 31]. It has also been pointed out that such an initial state can be used to filter out specific lines from an otherwise unreadable spectrum [74], as we will see in Sec. 4.3.2. Additionally, there are other ways to speed up TA SC-IVR computations by using a Hessian update scheme for faster calculation of the HK prefactor [53] or by performing the phase space integration in parallel on a graphic processing unit (GPU) [75]. Combined, this methodology even allows for expensive first principles calculations of realistic systems.

However, in spite of the measures that have been taken to speed up computations, the principal bottleneck of the phase space integration remains: with each additional DOF of the overall system, the phase space dimension grows by two, thus requiring more trajectories for convergence. In the next section, we will therefore once more employ the hybrid method as a way to pick out just the DOFs of interest and describe the remaining part of the overall system with single trajectories that do not require additional phase space sampling.

3.2.2. HYBRID APPROACH TO TIME AVERAGED SEMICLASSICAL INITIAL VALUE REPRESENTATIONS

We have already laid out in Eq. (2.18) of Sec. 2.2.2 how the phase space is divided into a smaller part that is described by the HK propagator and a bigger part whose time evolution takes place on the TG level. For the phase space integration in Eqs. (3.32) and (3.34), this means, again, that we no longer sample over each DOF of the full problem, but only over N_{hk} DOFs. We assume the reference state $|\chi\rangle$ to be a GWP centered at $(\mathbf{p}_\alpha^{\mathrm{T}}, \mathbf{q}_\alpha^{\mathrm{T}}) = \left[\left(\mathbf{p}_{\alpha,\mathrm{hk}}^{\mathrm{T}}, \mathbf{p}_{\alpha,\mathrm{tg}}^{\mathrm{T}}\right), \left(\mathbf{q}_{\alpha,\mathrm{hk}}^{\mathrm{T}}, \mathbf{q}_{\alpha,\mathrm{tg}}^{\mathrm{T}}\right)\right]$ and expand the remaining $N_{\mathrm{tg}} = N - N_{\mathrm{hk}}$ DOFs around this point, thus getting new initial phase space coordinates $(\mathbf{p}_{\alpha,0}^{\mathrm{T}}, \mathbf{q}_{\alpha,0}^{\mathrm{T}})$ as defined in Eq. (2.18). In order to derive the hybrid expression, we start with Eq. (3.34) and write the overlap of Gaussian reference state and time evolved trajectory explicitly

$$
\begin{aligned}
I(E) =& \frac{1}{2\pi\hbar T} \frac{1}{(2\pi\hbar)^N} \int \mathrm{d}^N p \int \mathrm{d}^N q \left| \int_0^T \mathrm{d}t \exp\left\{ \frac{\mathrm{i}}{\hbar} E t + \frac{\mathrm{i}}{\hbar} \phi_t\left(\mathbf{p}, \mathbf{q}\right) + \frac{\mathrm{i}}{\hbar} S_t\left(\mathbf{p}, \mathbf{q}\right) \right\} \right. \\
& \times \exp\left\{ -\frac{1}{4} \left(\mathbf{q}_t - \mathbf{q}_\alpha\right)^{\mathrm{T}} \boldsymbol{\gamma} \left(\mathbf{q}_t - \mathbf{q}_\alpha\right) - \frac{1}{4\hbar^2} \left(\mathbf{p}_t - \mathbf{p}_\alpha\right)^{\mathrm{T}} \boldsymbol{\gamma}^{-1} \left(\mathbf{p}_t - \mathbf{p}_\alpha\right) \right\} \\
& \left. \times \exp\left\{ +\frac{\mathrm{i}}{2\hbar} \left(\mathbf{q}_\alpha - \mathbf{q}_t\right)^{\mathrm{T}} \left(\mathbf{p}_t + \mathbf{p}_\alpha\right) \right\} \right|^2 .
\end{aligned}
\tag{3.35}
$$

As before, the action is expanded to second order in the displacement coordinates, yielding Eq. (2.19). The overlap is approximated by expanding the original trajectory to linear order in the displacements, Eqs. (2.23) and (2.24). Inserting Eqs. (2.19), (2.23) and (2.24) into Eq. (3.35)

and collecting terms of the same order in the displacement coordinates results in

$$\begin{aligned} I(E) = \frac{1}{2\pi\hbar T}\frac{1}{(2\pi\hbar)^N}\int \mathrm{d}^N p \int \mathrm{d}^N q \\ \times \left| \int_0^T \mathrm{d}t \exp\left\{ \frac{\mathrm{i}}{\hbar} Et + \frac{\mathrm{i}}{\hbar}\phi_t\left(\mathbf{p},\mathbf{q}\right)\right\} \langle g_{\alpha,\mathrm{hk}} | g_{\alpha,\mathrm{hk},t}(\mathbf{p}_{\alpha,0},\mathbf{q}_{\alpha,0})\rangle \right. \\ \left. \times \exp\left\{ -\begin{pmatrix}\delta\mathbf{p}_{\mathrm{tg}}\\ \delta\mathbf{q}_{\mathrm{tg}}\end{pmatrix}^{\mathrm{T}} \mathbf{A}_t^{\mathrm{sd}} \begin{pmatrix}\delta\mathbf{p}_{\mathrm{tg}}\\ \delta\mathbf{q}_{\mathrm{tg}}\end{pmatrix} + \left[\mathbf{b}_t^{\mathrm{sd}}\right]^{\mathrm{T}} \begin{pmatrix}\delta\mathbf{p}_{\mathrm{tg}}\\ \delta\mathbf{q}_{\mathrm{tg}}\end{pmatrix} + c_t^{\mathrm{sd}} \right\} \right|^2, \end{aligned} \tag{3.36}$$

where $\langle g_{\alpha,\mathrm{hk}} | g_{\alpha,\mathrm{hk},t}(\mathbf{p}_{\alpha,0},\mathbf{q}_{\alpha,0})\rangle$ is the overlap of the initial reference state with the HK part of the time evolved trajectories. The zeroth order contribution in $(\delta\mathbf{p}_{\mathrm{tg}},\delta\mathbf{q}_{\mathrm{tg}})$ arising from the approximation contains the action and the overlap of the TG part of the trajectories with the reference state,

$$\begin{aligned} c_t^{\mathrm{sd}} = \frac{\mathrm{i}}{\hbar} S_t\left(\mathbf{p}_{\alpha,0},\mathbf{q}_{\alpha,0}\right) - \frac{1}{4}\left(\mathbf{q}_{\alpha,\mathrm{tg},t}-\mathbf{q}_{\alpha,\mathrm{tg}}\right)^{\mathrm{T}} \boldsymbol{\gamma}_{\mathrm{tg}} \left(\mathbf{q}_{\alpha,\mathrm{tg},t}-\mathbf{q}_{\alpha,\mathrm{tg}}\right) \\ - \frac{1}{4\hbar^2}\left(\mathbf{p}_{\alpha,\mathrm{tg},t}-\mathbf{p}_{\alpha,\mathrm{tg}}\right)^{\mathrm{T}} \boldsymbol{\gamma}_{\mathrm{tg}}^{-1} \left(\mathbf{p}_{\alpha,\mathrm{tg},t}-\mathbf{p}_{\alpha,\mathrm{tg}}\right) \\ + \frac{\mathrm{i}}{2\hbar}\left(\mathbf{q}_{\alpha,\mathrm{tg}}-\mathbf{q}_{\alpha,\mathrm{tg},t}\right)^{\mathrm{T}} \left(\mathbf{p}_{\alpha,\mathrm{tg},t}+\mathbf{p}_{\alpha,\mathrm{tg}}\right). \end{aligned} \tag{3.37}$$

The first order terms are collected in a $2N_{\mathrm{tg}}$ dimensional vector

$$\mathbf{b}_t^{\mathrm{sd}} = \begin{pmatrix}\mathbf{b}_{1,t}^{\mathrm{sd}}\\ \mathbf{b}_{2,t}^{\mathrm{sd}}\end{pmatrix}, \tag{3.38}$$

where $\mathbf{b}_{1,t}^{\mathrm{sd}}$ and $\mathbf{b}_{2,t}^{\mathrm{sd}}$ are multiplied with $\delta\mathbf{p}_{\mathrm{tg}}$ and $\delta\mathbf{q}_{\mathrm{tg}}$, respectively, and the two parts have a slightly asymmetric form

$$\begin{aligned} \mathbf{b}_{1,t}^{\mathrm{sd}} = & -\frac{1}{2}\left[\boldsymbol{\gamma}\tilde{\mathbf{m}}_{21,t} + \frac{\mathrm{i}}{\hbar}\tilde{\mathbf{m}}_{11,t}\right]^{\mathrm{T}} \left(\mathbf{q}_{\alpha,t}-\mathbf{q}_{\alpha,0}\right) \\ & -\frac{1}{2\hbar^2}\left[\boldsymbol{\gamma}^{-1}\tilde{\mathbf{m}}_{11,t} - \mathrm{i}\hbar\tilde{\mathbf{m}}_{21,t}\right]^{\mathrm{T}} \left(\mathbf{p}_{\alpha,t}-\mathbf{p}_{\alpha,0}\right) \end{aligned} \tag{3.39}$$

$$\begin{aligned} \mathbf{b}_{2,t}^{\mathrm{sd}} = & -\frac{1}{2}\left[\boldsymbol{\gamma}\tilde{\mathbf{m}}_{22,t} + \frac{\mathrm{i}}{\hbar}\tilde{\mathbf{m}}_{12,t}\right]^{\mathrm{T}} \left(\mathbf{q}_{\alpha,t}-\mathbf{q}_{\alpha,0}\right) \\ & -\frac{1}{2\hbar^2}\left[\boldsymbol{\gamma}^{-1}\tilde{\mathbf{m}}_{12,t} - \mathrm{i}\hbar\tilde{\mathbf{m}}_{22,t}\right]^{\mathrm{T}} \left(\mathbf{p}_{\alpha,t}-\mathbf{p}_{\alpha,0}\right) - \frac{\mathrm{i}}{\hbar}\mathbf{p}_{\alpha,\mathrm{tg}}. \end{aligned} \tag{3.40}$$

We note in passing that the additional contribution to $\mathbf{b}_{2,t}^{\mathrm{sd}}$ is a constant in time and can therefore be taken out of the time integration, where it becomes just an overall phase that vanishes in the modulus. The matrix that is multiplied with the second order contributions is the $2N_{\mathrm{tg}} \times 2N_{\mathrm{tg}}$ matrix $\mathbf{A}_t^{\mathrm{sd}}$ with quadratic submatrices

$$\mathbf{A}_{11,t}^{\mathrm{sd}} = \frac{1}{4}\tilde{\mathbf{m}}_{21,t}^{\mathrm{T}}\boldsymbol{\gamma}\tilde{\mathbf{m}}_{21,t} + \frac{1}{4\hbar^2}\tilde{\mathbf{m}}_{11,t}^{\mathrm{T}}\boldsymbol{\gamma}^{-1}\tilde{\mathbf{m}}_{11,t} \tag{3.41}$$

$$\mathbf{A}_{12,t}^{\mathrm{sd}} = \frac{1}{4}\tilde{\mathbf{m}}_{21,t}^{\mathrm{T}}\boldsymbol{\gamma}\tilde{\mathbf{m}}_{22,t} + \frac{1}{4\hbar^2}\tilde{\mathbf{m}}_{11,t}^{\mathrm{T}}\boldsymbol{\gamma}^{-1}\tilde{\mathbf{m}}_{12,t} \tag{3.42}$$

$$\mathbf{A}_{21,t}^{\mathrm{sd}} = \frac{1}{4}\tilde{\mathbf{m}}_{22,t}^{\mathrm{T}}\boldsymbol{\gamma}\tilde{\mathbf{m}}_{21,t} + \frac{1}{4\hbar^2}\tilde{\mathbf{m}}_{12,t}^{\mathrm{T}}\boldsymbol{\gamma}^{-1}\tilde{\mathbf{m}}_{11,t} + \frac{\mathrm{i}}{2\hbar} \tag{3.43}$$

$$\mathbf{A}_{22,t}^{\mathrm{sd}} = \frac{1}{4}\tilde{\mathbf{m}}_{22,t}^{\mathrm{T}}\boldsymbol{\gamma}\tilde{\mathbf{m}}_{22,t} + \frac{1}{4\hbar^2}\tilde{\mathbf{m}}_{12,t}^{\mathrm{T}}\boldsymbol{\gamma}^{-1}\tilde{\mathbf{m}}_{12,t}. \tag{3.44}$$

The only imaginary contribution $-\mathrm{i}/(2\hbar)$ is a constant in time and can therefore be regarded as another global phase that can be discarded, making $\mathbf{A}_t^{\mathrm{sd}}$ real and symmetric. The modulus in Eq. (3.36) is now unraveled, the prefactor phase is approximated as $\phi_t(\mathbf{p},\mathbf{q}) \approx \phi_t(\mathbf{p}_{\alpha,0},\mathbf{q}_{\alpha,0})$ as before in order to take it out of the integration over the TG subspace and we transform the TG integration variables linearly from $(\mathbf{p}_{\mathrm{tg}},\mathbf{q}_{\mathrm{tg}})$ to displacements $(\delta\mathbf{p}_{\mathrm{tg}},\delta\mathbf{q}_{\mathrm{tg}})$ to get

$$\begin{aligned} I(E) =& \frac{1}{2\pi\hbar T}\frac{1}{(2\pi\hbar)^N}\int_0^T \mathrm{d}t_1 \int_0^T \mathrm{d}t_2 \int \mathrm{d}^{N_{\mathrm{hk}}}p_{\mathrm{hk}} \int \mathrm{d}^{N_{\mathrm{hk}}}q_{\mathrm{hk}} \\ & \times \exp\left\{\frac{\mathrm{i}}{\hbar}E(t_1-t_2) + \frac{\mathrm{i}}{\hbar}\left[\phi_{t_1}(\mathbf{p}_{\alpha,0},\mathbf{q}_{\alpha,0}) - \phi_{t_2}(\mathbf{p}_{\alpha,0},\mathbf{q}_{\alpha,0})\right] + c_{t_1}^{\mathrm{sd}} + \left(c_{t_2}^{\mathrm{sd}}\right)^*\right\} \\ & \times \langle g_{\alpha,\mathrm{hk}}|g_{\alpha,t_1,\mathrm{hk}}(\mathbf{p}_{\alpha,0},\mathbf{q}_{\alpha,0})\rangle \langle g_{\alpha,\mathrm{hk}}|g_{\alpha,t_2,\mathrm{hk}}(\mathbf{p}_{\alpha,0},\mathbf{q}_{\alpha,0})\rangle^* \\ & \times \int \mathrm{d}^{N_{\mathrm{tg}}}\delta p_{\mathrm{tg}} \int \mathrm{d}^{N_{\mathrm{tg}}}\delta q_{\mathrm{tg}} \exp\left\{-\begin{pmatrix}\delta\mathbf{p}_{\mathrm{tg}}\\ \delta\mathbf{q}_{\mathrm{tg}}\end{pmatrix}^{\mathrm{T}}\left(\mathbf{A}_{t_1}^{\mathrm{sd}} + \left[\mathbf{A}_{t_2}^{\mathrm{sd}}\right]^*\right)\begin{pmatrix}\delta\mathbf{p}_{\mathrm{tg}}\\ \delta\mathbf{q}_{\mathrm{tg}}\end{pmatrix}\right\} \\ & \quad \times \exp\left\{\left(\mathbf{b}_{t_1}^{\mathrm{sd}} + \left[\mathbf{b}_{t_2}^{\mathrm{sd}}\right]^*\right)^{\mathrm{T}}\begin{pmatrix}\delta\mathbf{p}_{\mathrm{tg}}\\ \delta\mathbf{q}_{\mathrm{tg}}\end{pmatrix}\right\}. \end{aligned} \tag{3.45}$$

The integration over the TG DOFs is another Gaussian integration that can be done analytically, and we arrive at the hybrid approximation of Eq. (3.34)

$$\begin{aligned} I(E) =& \frac{1}{2\pi\hbar T}\frac{1}{(2\hbar)^N\pi^{N-N_{\mathrm{tg}}}}\int \mathrm{d}^{N_{\mathrm{hk}}}p_{\mathrm{hk}} \int \mathrm{d}^{N_{\mathrm{hk}}}q_{\mathrm{hk}} \int_0^T \mathrm{d}t_1 \int_0^T \mathrm{d}t_2 \\ & \times \exp\left\{\frac{\mathrm{i}}{\hbar}E(t_1-t_2) + \frac{\mathrm{i}}{\hbar}\left[\phi_{t_1}(\mathbf{p}_{\alpha,0},\mathbf{q}_{\alpha,0}) - \phi_{t_2}(\mathbf{p}_{\alpha,0},\mathbf{q}_{\alpha,0})\right]\right\} \\ & \times \langle g_{\alpha,\mathrm{hk}}|g_{\alpha,t_1,\mathrm{hk}}(\mathbf{p}_{\alpha,0},\mathbf{q}_{\alpha,0})\rangle \langle g_{\alpha,\mathrm{hk}}|g_{\alpha,t_2,\mathrm{hk}}(\mathbf{p}_{\alpha,0},\mathbf{q}_{\alpha,0})\rangle^* \sqrt{\frac{1}{\det\left(\mathbf{A}_{t_1}^{\mathrm{sd}} + \left[\mathbf{A}_{t_2}^{\mathrm{sd}}\right]^*\right)}} \\ & \times \exp\left\{\frac{1}{4}\left(\mathbf{b}_{t_1}^{\mathrm{sd}} + \left[\mathbf{b}_{t_2}^{\mathrm{sd}}\right]^*\right)^{\mathrm{T}}\left(\mathbf{A}_{t_1}^{\mathrm{sd}} + \left[\mathbf{A}_{t_2}^{\mathrm{sd}}\right]^*\right)^{-1}\left(\mathbf{b}_{t_1}^{\mathrm{sd}} + \left[\mathbf{b}_{t_2}^{\mathrm{sd}}\right]^*\right) + c_{t_1}^{\mathrm{sd}} + \left(c_{t_2}^{\mathrm{sd}}\right)^*\right\}, \end{aligned} \tag{3.46}$$

where it should be stressed that the TG quantities emerging from the second order approximation of the exponent also depend on the HK initial conditions, $\mathbf{A}_t^{\mathrm{sd}} = \mathbf{A}^{\mathrm{sd}}(\mathbf{p}_{\alpha,0},\mathbf{q}_{\alpha,0},t)$, $\mathbf{b}_t^{\mathrm{sd}} = \mathbf{b}^{\mathrm{sd}}(\mathbf{p}_{\alpha,0},\mathbf{q}_{\alpha,0},t)$ and $c_t^{\mathrm{sd}} = c^{\mathrm{sd}}(\mathbf{p}_{\alpha,0},\mathbf{q}_{\alpha,0},t)$. The above expression can be naturally expanded to treat the total system on the TG level by setting $N = N_{\mathrm{tg}}$. In that case, the remaining phase space integration vanishes as well as the third line in Eq. (3.46). We show in Appendix C that the emerging expression indeed reproduces the harmonic oscillator spectrum exactly both in terms of peak positions and weights. This is an important finding because in an equilibrated bound system with relatively small system-bath coupling, the ground state of the bath contributes heavily to the spectrum.

With the hybrid approximation, we have again reduced the phase space region, that has to be sampled over, to few HK DOFs. This is clearly an advantage over Eqs. (3.32) and (3.34). However, compared to the separable TA HK expression from (3.34), the computational improvement from the greatly reduced number of trajectories will be canceled out by the two dimensional time integration. While the result of a time integration over an expression of the form $\exp\{\mathrm{i}E(t_1-t_2)/\hbar\} \times f(t_1,t_2)$ is the off-diagonal of a two dimensional Fourier transform and can be done numerically cheap with an FFTW algorithm, the computation of the integrand

itself is very costly. It involves N_{steps}^2 inversions of the matrix $\mathbf{A}_{t_1}^{\text{sd}} + \left(\mathbf{A}_{t_2}^{\text{sd}}\right)^*$, which scale with N_{tg}^3. For a large number of environmental DOFs N_{tg}, the computation of a single phase space integrand will therefore take orders of magnitude longer compared to the evaluation of the integrand of the separable TA HK expression in Eq. (3.34).

In order to get a hybrid approximation that will always be superior in terms of computational time, it is necessary to recover a single time integration in Eq. (3.46). Clearly, this invokes the need for an approximation of the two terms depending on $\mathbf{A}_{t_1}^{\text{sd}} + \left(\mathbf{A}_{t_2}^{\text{sd}}\right)^*$, which are the only contributions that cannot be factorized in t_1 and t_2 parts. Since there is no rigorous analytical way to find such a simplification, we proceed in the spirit of the separable approximation that lead to Eq. (3.34) and look for an expression that reproduces the harmonic oscillator result. This approach is well justified if we recall that it concerns the TG part of the integrand only, i. e. the part of the overall system that has already been approximated to be close to harmonic. There are several ways to achieve the identity with the harmonic oscillator spectrum. We will simply state our result here and show the underlying analytic considerations in more detail in App. C.

The part of the exponential in Eq. (3.46), that has to be separable, is approximated as

$$\begin{aligned}\left(\mathbf{b}_{t_1}^{\text{sd}} + \left[\mathbf{b}_{t_2}^{\text{sd}}\right]^*\right)^{\mathrm{T}} \left(\mathbf{A}_{t_1}^{\text{sd}} + \left[\mathbf{A}_{t_2}^{\text{sd}}\right]^*\right)^{-1} \left(\mathbf{b}_{t_1}^{\text{sd}} + \left[\mathbf{b}_{t_2}^{\text{sd}}\right]^*\right) \approx\ & \left(\mathbf{b}_{\text{m},t_1}^{\text{sd}}\right)^{\mathrm{T}} \left(\mathbf{A}_{\text{re},t_1}^{\text{sd}}\right)^{-1} \mathbf{b}_{\text{m},t_1}^{\text{sd}} \\ & + \left(\mathbf{b}_{\text{m},t_2}^{\text{sd}}\right)^{\mathrm{T}} \left(\mathbf{A}_{\text{re},t_2}^{\text{sd}}\right)^{-1} \mathbf{b}_{\text{m},t_2}^{\text{sd}},\end{aligned} \tag{3.47}$$

where we have introduced the real-valued quantity $\mathbf{A}_{\text{re},t}^{\text{sd}}$ to replace $\mathbf{A}_t^{\text{sd}}$ from Eqs. (3.41) to (3.44) notationally convenient

$$\mathbf{A}_{\text{re},t}^{\text{sd}} \equiv \mathbf{A}_t^{\text{sd}} + \left(\mathbf{A}_t^{\text{sd}}\right)^* = 2\mathrm{Re}\big(\mathbf{A}_t^{\text{sd}}\big) \tag{3.48}$$

and canceled the constant imaginary part from the second component of $\mathbf{b}_t^{\text{sd}}$ from Eq. (3.40)

$$\mathbf{b}_{\text{m},t}^{\text{sd}} = \begin{pmatrix} \mathbf{b}_{1,t}^{\text{sd}} \\ \mathbf{b}_{2,t}^{\text{sd}} + \mathrm{i}\mathbf{p}_{\alpha,\text{tg}}/\hbar \end{pmatrix}. \tag{3.49}$$

The TG prefactor is simplified in the fashion of a geometric average,

$$\sqrt{\frac{1}{\det\left(\mathbf{A}_{t_1}^{\text{sd}} + \left[\mathbf{A}_{t_2}^{\text{sd}}\right]^*\right)}} \approx \left(\frac{1}{\det\left(\mathbf{A}_{\text{re},t_1}^{\text{sd}}\right)}\right)^{1/4} \left(\frac{1}{\det\left(\mathbf{A}_{\text{re},t_2}^{\text{sd}}\right)}\right)^{1/4}. \tag{3.50}$$

Inserting these new separable approximations (3.47) and (3.50) into the hybrid result from Eq. (3.46) we can recover a squared absolute value of a single time integration like in Eq. (3.34),

$$\begin{aligned} I(E) = \frac{1}{2\pi\hbar T} \frac{1}{(2\hbar)^N \pi^{N-N_{\text{tg}}}} \int \mathrm{d}^{N_{\text{hk}}} p_{\text{hk}} \int \mathrm{d}^{N_{\text{hk}}} q_{\text{hk}} \Bigg| \int_0^T \mathrm{d}t\ \mathrm{e}^{\mathrm{i}Et/\hbar + \mathrm{i}\phi_t(\mathbf{p}_{\alpha,0},\mathbf{q}_{\alpha,0})/\hbar} \\ \times \langle g_{\alpha,\text{hk}} | g_{\alpha,\text{hk},t}(\mathbf{p}_{\alpha,0},\mathbf{q}_{\alpha,0}) \rangle \\ \times \frac{1}{\left[\det\left(\mathbf{A}_{\text{re},t}^{\text{sd}}\right)\right]^{1/4}} \exp\left\{\frac{1}{4}\left(\mathbf{b}_{\text{m},t}^{\text{sd}}\right)^{\mathrm{T}} \left(\mathbf{A}_{\text{re},t}^{\text{sd}}\right)^{-1} \mathbf{b}_{\text{m},t}^{\text{sd}} + c_t^{\text{sd}}\right\} \Bigg|^2. \end{aligned} \tag{3.51}$$

Within this expression, we have achieved a reduction of the dimension of the phase space to be sampled while retaining the single time integration and the strictly positive integrand of the

separable HK result. As will be seen below, the main difference of the resulting spectra from the full hybrid result in Eq. (3.46) lies only in a suppression of peaks that correspond to excited states of TG DOFs. While their relative peak weight is much smaller, peaks positions of TG DOFs are still on the same level of accuracy as in Eq. (3.46). This is shown analytically for the harmonic oscillator in App. C. We want to point out that the suppression of excited state peaks of the environment is not necessarily a bad thing given that these peaks are typically not the main interest for a given problem. Prominent frequencies can thus be more easily attributed to vibrations of HK propagated DOFs.

3.2.3. NUMERICAL EXAMPLES

In the previous sections, we have described a number of trajectory based propagation schemes for the computation of vibrational spectra. In order to make these methods computationally efficient, separable approximations have been necessary which are exact only for harmonic potentials. We will now show for two simple numerical examples, how the different levels of approximation influence the resulting spectra. One example is a Morse potential, where the harmonicity assumption is justified close to the potential minimum. The other example is an extreme case of a potential that is nowhere harmonic, namely, the three-dimensional Coulomb problem. We will check the spectra against analytic results, and we will also show results from HK calculations without time averaging according to Eq. (3.30).

ONE DIMENSIONAL MORSE OSCILLATOR

We start with a very basic anharmonic potential, namely, the Morse oscillator (MO) [77]. It describes the vibration of a diatomic molecule on a given single electronic surface and reads

$$V(s) = D_\mathrm{e}\left(1 - \mathrm{e}^{-\alpha(s-s_\mathrm{e})}\right)^2 - D_\mathrm{e}, \tag{3.52}$$

where s_e is the equilibrium distance between the two constituent nulcei, D_e is the dissociation energy, and α is the range parameter. As shown by the plot in Fig. 4.5, the Morse potential has a repulsive side at distances smaller than s_e, and an attractive side at distances larger than s_e. At energies larger than the dissociation energy, the attraction is overcome and the atoms no longer return towards each other. Eigenfunctions and eigenenergies can be found analytically; in atomic units, the latter ones are

$$E_n = \omega_\mathrm{e}\left(n + \frac{1}{2}\right) - x_\mathrm{e}\omega_\mathrm{e}\left(n + \frac{1}{2}\right)^2, \tag{3.53}$$

where $\omega_\mathrm{e} = \alpha\sqrt{2D_\mathrm{e}/m_\mathrm{r}}$ is the frequency of the harmonic approximation of $V(s)$ and $x_\mathrm{e} = \omega_\mathrm{e}/(4D_\mathrm{e})$ is the anharmonicity constant. This result for the eigenenergies is approximate, but the deviations are negligible for diatomic molecules [78]. The two parameters ω_e and $x_\mathrm{e}\omega_\mathrm{e}$ showing up in Eq. 3.53 can be determined experimentally, and the Morse potential turns out to provide an appropriate description not only for the vibrations of real diatomic molecules such as iodine [79, 80], but also for more complex systems such as the O-H stretch in water [81] and even the interaction of DNA bases [82]. Semiclassical studies have, for example, investigated the quenching of quantum coherence of a MO coupled to a bath [27, 28, 59], and reproduced the correct long-time behavior of a single MO [83].

Here, we will use parameters corresponding to an iodine-like molecule [27, 59], namely, $D_\mathrm{e} = 0.057$ a.u., $s_\mathrm{e} = 5.038$ a.u., and $\alpha = 0.983$ a.u., from which we find $\omega_\mathrm{e} \approx 9.723 \times 10^{-4}$ a.u.

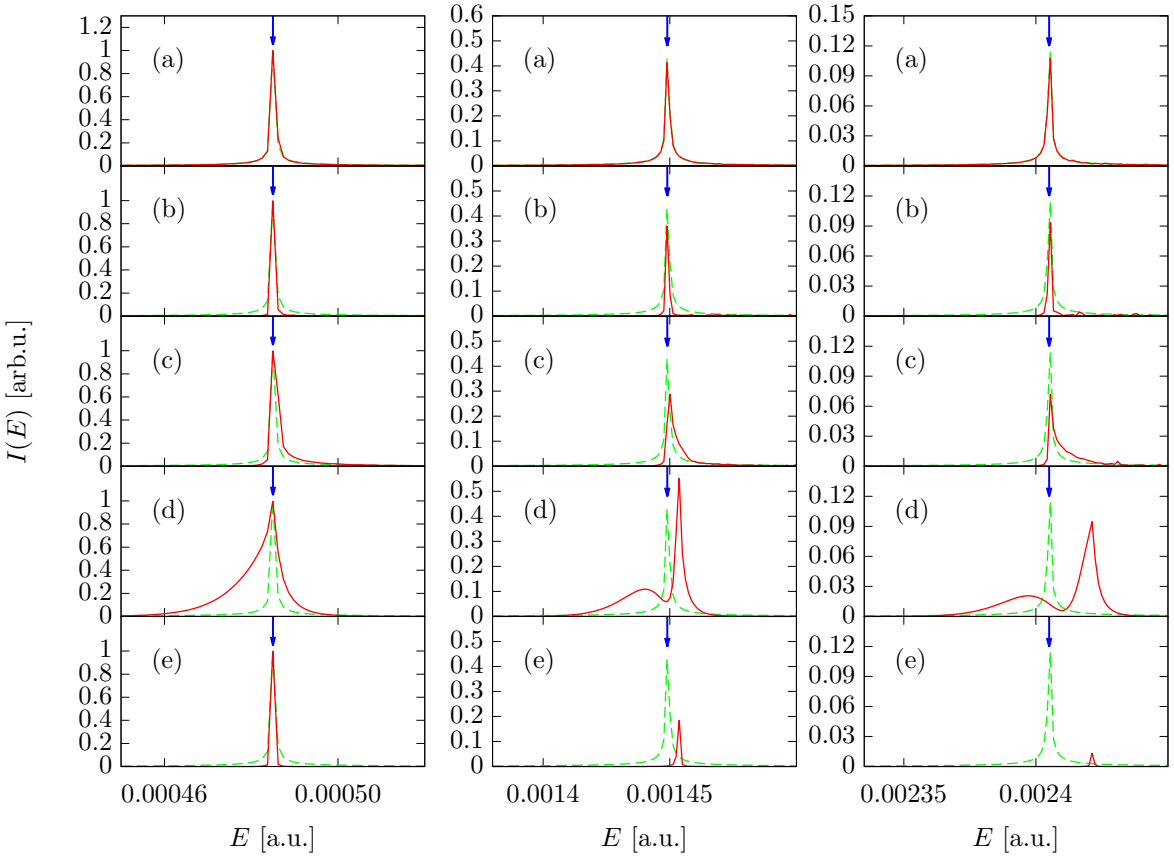

Figure 3.1.: Ground and first two excited states of a one-dimensional Morse oscillator (from left to right). The peak weights have been rescaled for better visibility. The dashed green lines are full quantum, solid red lines are semiclassical results (from top to bottom): (a) standard HK, (b) TA HK without separable approximation, (c) separable TA HK, (d) TA hybrid, and (e) separable TA hybrid. Blue arrows indicate the analytic eigenenergies.

and $x_\mathrm{e} \approx 4.264 \times 10^{-3}$ a.u. The reduced mass is $m_\mathrm{r} = 1.165 \times 10^5$ a.u. Initial position and momentum are chosen as $(q_0, p_0) = (s_\mathrm{e}, \sqrt{m_\mathrm{r}\omega_\mathrm{e}})$, placing the molecule at its potential minimum with a momentum corresponding to the harmonic approximation ground state energy. Figure 3.1 shows results for the spectrum from calculations with 10^5 trajectories for simple HK and separable TA HK, 10^4 trajectories for the two-time TA HK, and 1 trajectory for the hybrid calculations. The latter two are pure TG for this 1D calculation, with the spectrum calculated according to Eqs. (C.6) and (C.24). Most importantly, the ground state peak is reproduced exactly by each of the semiclassical methods. This is not surprising, since the harmonic approximation is best close to the minimum energy. If we look at the excited peaks, we see the differences emerging. All HK methods find the exact peak position, while the two TG results (d) and (e) are equally shifted to a more harmonic, higher energy. The peak weights also reveal some interesting features. The standard HK calculation reproduces the quantum peak weight exactly, as expected. The full TA HK calculation, which emerges from standard HK without the separable approximation, should in principle reproduce the peak weights but is not quite converged due to the double time integral. Interestingly, we see a somewhat narrower peak due to the pre-averaging of the phase space integrand. The exact peak weight

is lost once the separable approximation is made. For the TG results, we see that the excited peaks resulting from the separable calculation (Fig. 3.1(e)) are far smaller than the ones from the full calculation, as suggested by the harmonic considerations in App. C.

Finally, peak shapes also deserve some mention. The quantum result shows symmetric peaks. This is reproduced by the standard HK result and also by the full TA HK result – the time averaging alone does not alter the peak shape. After the separation of the prefactor, however, peaks are no longer symmetric. The tail to the right of the excited peaks is made up from contributions of trajectories that have either higher or lower energy than these peaks, as explained in some detail in App. D. Peak shapes of the full TG result are very different from the ones before. Because of the width of the GWP varies with time, the "sampling" of the phase space by the time evolving trajectory is now different, thus including a broader frequency range in the final result. The separable TG result, on the other hand, is very similar to a calculation with a single frozen Gaussian here, so the peak shape is again close to symmetric.

This example of an anharmonic oscillator close to the classical potential minimum is naturally suited for a description with the separable TA HK method. One might now wonder what happens for highly excited states of the Morse oscillator whose dynamics takes place in the very anharmonic phase space region. In App. D, we discuss one such example and find that the separable TA HK is capable of reproducing the whole range of highly excited states of this model potential.

THREE DIMENSIONAL COULOMB PROBLEM

Our second example is the three-dimensional hydrogen potential (again in atomic units),

$$V(\mathbf{r}) = -\frac{1}{|\mathbf{r}|}. \tag{3.54}$$

The analytic calculation of its spectrum is part of any introductory quantum mechanics course and results in eigenenergies

$$E_n = -\frac{1}{2n^2}. \tag{3.55}$$

As the Coulomb potential is nowhere harmonic, any thawed Gaussian description is bound to fail. We will, however, see that different approximations to the HK propagator reproduce the expected spectrum. In 2001, G. van de Sand and J.-M. Rost have shown that a HK propagation yields a perfect hydrogen spectrum both in terms of position and weights of the peaks. To keep propagation times as low as possible, they used the harmonic inversion technique [84,85] rather than FFT for the calculation of the Fourier transform of the autocorrelation function; we will stick to FFT here to keep the comparison simple. We calculate the spectrum for initial position $\mathbf{q}_\alpha = (0, 20 \text{ a.u.})$, zero initial momentum and width parameters $\gamma_i = 0.1$ a.u. Propagation time is restricted to 4096 steps of length 5 a.u. to reduce computational cost especially for the TA HK with two time integrations, and any high energy trajectories that do not contribute to the spectral window of interest are discarded.

Results are displayed in Fig. 3.2. As shown before, the standard HK calculation from Eq. (3.30) reproduces the exact peak positions, where about 3.5×10^6 trajectories have been needed to reach convergence. The exact TA HK approach as described in Eq. (3.32) is not fully converged yet, but still reproduces peak positions very accurately in spite of just 1.7×10^5 trajectories contributing to the result, so the time averaging has the desired effect here. With the assumption of at least a certain degree of harmonicity in the separable approximation, on

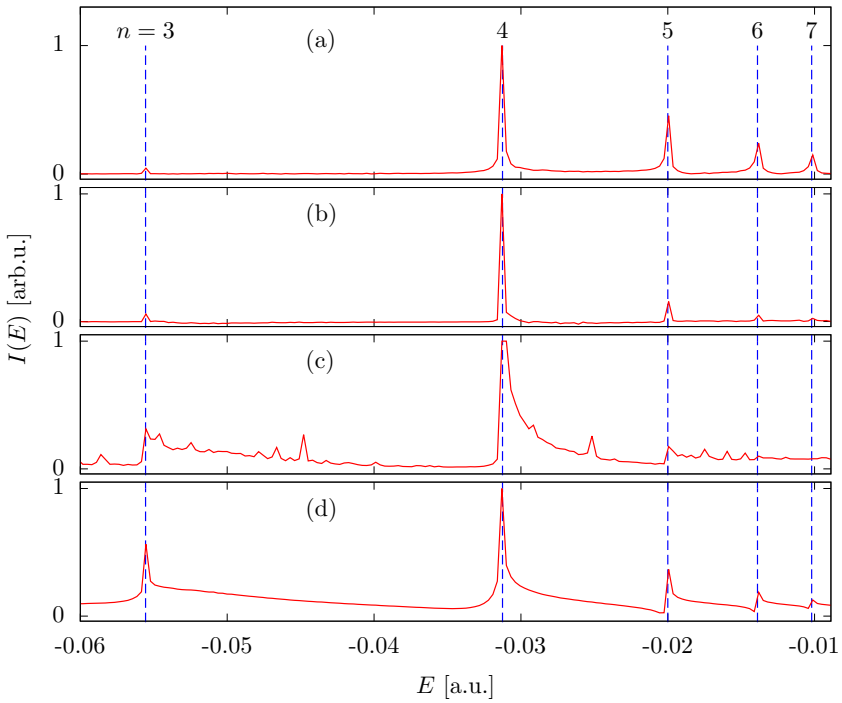

Figure 3.2.: Hydrogen spectrum calculated with different semiclassical IVR methods (red lines, from top to bottom): (a) standard HK, (b) TA HK without separable approximation, (c) separable TA HK, and (d) standard HK with prefactor set to unity. Blue dashed lines are the exact peak positions.

the other hand, results become far worse. Due to the modulus in the integrand of Eq. (3.34), noisy contributions no longer cancel out each other, but appear as a shoulder to the right of each peak. While these contributions did not play a big role for the Morse potential in the last section, they now render the spectrum almost useless, with only the main energy level close to the mean energy of the trajectory clearly recognizable as a peak.

How much this scattering problem differs from the system in the previous section can also be seen from the bottom picture in Fig. 3.2. It displays the outcome of a standard HK calculation as in Eq. (3.30) with the HK prefactor set to unity. For a system that is harmonic around its potential minimum, this would result in a shift of the spectrum by the zero point energy, as can be seen in the analytic harmonic oscillator considerations in App. C. Here, peak positions are in perfect agreement with the original HK result. Comparing Fig. 3.2(a) and Fig. 3.2(d), we see that setting the prefactor to unity results in peaks that are less sharp and more asymmetric than in the original propagation. The overall shape of the spectrum is similar to the separable TA result in Fig. 3.2(c), where the modulus of the prefactor is unity as well.

With the two numerical examples above, we conclude this section. We have derived a novel approach to spectral calculations, combining a time averaging scheme with the hierarchical semiclassical hybrid dynamics to arrive at an expression that requires sampling over only few DOFs and benefits from a positive definite integrand. Using a 1D Morse oscillator, we have demonstrated the consequences of the thawed Gaussian approximation for a non-Gaussian system and motivated its applications to near harmonic bath DOFs. In a second numerical

example, we have utilized the 3D Coulomb problem to illustrate how the time averaging reduces the number of trajectories that are needed to converge the phase space integral, and to show the failure of the separable approximation for systems that are nowhere harmonic.

In the following two chapters, we will explore the capabilities of the hybrid TA method for the treatment of system-bath problems. In Ch. 4, we will look at a Morse oscillator coupled to a Caldeira-Leggett bath with different parameters. Chapter 5 is dedicated to an investigation of an experimentally studied system, namely, iodine embedded in krypton.

4. MORSE OSCILLATOR IN A CALDEIRA-LEGGETT BATH

This chapter will be dedicated to the exploration of the applicability of the newly developed hybrid method for spectral calculations [86]. In order to find out how it performs compared to exact results on the one hand and the existing time averaged HK method on the other, we will use a well-investigated test system, namely, the Caldeira-Leggett model [23, 24]. This model Hamiltonian has been widely employed in the study of open systems [87, 88]. Due to its very nature, an arbitrary system DOF embedded into a bath of harmonic oscillators, it has in particular been shown to be suitably described by the semiclassical hybrid dynamics [27, 28].

4.1. CALDEIRA-LEGGETT MODEL

In this chapter, we will use the Caldeira-Leggett (CL) model system [23,24] in order to show the capacities of the newly developed hybrid method for spectral calculations. The bath comprises N_b harmonic oscillators (HOs) of unit mass that are coupled bilinearly to a system as depicted in Fig. 4.1. In the notation of [59], the Hamiltonian reads

$$H = \frac{p_\mathrm{s}^2}{2m_\mathrm{s}} + V_\mathrm{s}(s) + \sum_{i=1}^{N_\mathrm{b}} \left\{ \frac{p_i^2}{2} + \frac{1}{2}\omega_i^2 y_i^2 + c_i y_i (s - s_\mathrm{eq}) + \frac{c_i^2}{2\omega_i^2}(s - s_\mathrm{eq})^2 \right\}, \tag{4.1}$$

where ω_i are the frequencies of the bath and y_i and p_i are the corresponding positions and momenta, respectively. The system is one-dimensional for this model, and its mass, position and momentum are denoted by m_s, s and p_s. Each bath mode is coupled to the system via a coupling strength c_i that will be specified further below. The last term in the above equation is known as the counter term. In general, it is necessary to prevent unphysical renormalization of the potential due to the system-bath coupling, as explained in [89]. We will shed some light on its role for the system spectrum later in this chapter. The system DOF will be represented by an anharmonic Morse potential with iodine-like parameters as in Sec. 3.2.3.

In order to find a meaningful distribution of bath couplings and frequencies, we follow the approach of [27]. The coupling coefficients c_i determine the discretized spectral density $J(\omega)$,

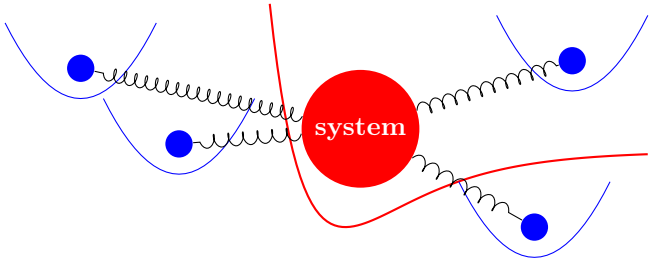

Figure 4.1.: Graphical representation of Caldeira-Leggett model: an anharmonic system mode (red) is coupled to a number of harmonic oscillators (blue) by springs of different coupling strength.

which completely characterizes the environment [87] and takes the form

$$J(\omega) = \frac{\pi}{2} \sum_{j=1}^{N_\mathrm{b}} \frac{c_j^2}{\omega_j} \delta(\omega - \omega_j). \tag{4.2}$$

This discretized density can be used to approximate any given continuous spectral density J_c by a finite number of harmonic oscillators with coupling coefficients

$$c_j^2 = \frac{2}{\pi} \omega_j \frac{J_\mathrm{c}(\omega_j)}{\rho_\mathrm{f}(\omega_j)}, \tag{4.3}$$

where $\rho_\mathrm{f}(\omega)$ is the frequency distribution from which the individual frequencies ω_j are chosen. It is normalized such that it reproduces the number of bath DOFs,

$$N_\mathrm{b} = \int_0^{\omega_\mathrm{max}} \mathrm{d}\omega \rho_\mathrm{f}(\omega), \tag{4.4}$$

with ω_max the maximum frequency contained in the bath. Furthermore, one can determine each individual frequency with the integration

$$j = \int_0^{\omega_j} \mathrm{d}\omega \rho_\mathrm{f}(\omega), \tag{4.5}$$

where the index j is an integer number. In App. A of [37], specific forms of the frequency distribution are discussed. In this work, we will restrict the discussion to an Ohmic bath with exponential cutoff as in [59],

$$J(\omega) = \eta \omega \mathrm{e}^{-\omega/\omega_\mathrm{c}}, \tag{4.6}$$

where ω_c is called the cutoff frequency and η is a macroscopic parameter that describes the coupling strength. For simplicity, we also define a dimensionless effective coupling strength $\eta_\mathrm{eff} \equiv \eta/(\omega_\mathrm{s} m_\mathrm{s})$. The corresponding frequency density is chosen as

$$\rho_\mathrm{f}(\omega) = a \frac{J(\omega)}{\omega}, \tag{4.7}$$

with a normalization parameter a that follows from Eq. (4.4) to become

$$a = \frac{N_\mathrm{b}}{\eta\omega_\mathrm{c}}\left(1 - \mathrm{e}^{-\omega_\mathrm{max}/\omega_\mathrm{c}}\right)^{-1} \overset{(4.3)}{=} \frac{\pi}{2}\frac{\omega_j^2}{c_j^2}. \tag{4.8}$$

The second equality illustrates that the relation between coupling coefficient and frequency is a constant and therefore independent of the bath mode index. Using Eq. (4.5), the frequencies turn out to be logarithmically distributed according to

$$\omega_j = -\omega_\mathrm{c} \ln\left[1 - \frac{j}{N_\mathrm{b}}\left(1 - \mathrm{e}^{-\omega_\mathrm{max}/\omega_\mathrm{c}}\right)\right]. \tag{4.9}$$

This frequency spectrum has been employed, for example, in a semiclassical investigation on the quenching of interference effects in the wavefunction of an anharmonic oscillator coupled to a low-frequency bath, and the hybrid approximation was shown to yield good results [27]. We will use it here as a prototypical example for a bath where most bath modes are much slower than the system frequency, as it will be the case in Ch. 5, but there are also a few that are close to or even resonant with the system frequency.

4.2. MORSE OSCILLATOR COUPLED TO ONE AND TWO HARMONIC OSCILLATORS

We will first present results from 2 and 3 DOF calculations for a variety of effective coupling parameters and cutoff frequencies in order to get an idea how the hybrid method performs in these situations. Then, we will investigate more realistic bath sizes between 10 and 60 bath oscillators. The first test systems for the investigation of the TA SC-IVR hybrid formalism will be very simple. We use a Morse potential with the parameters from Sec. 3.2.3 as the system and couple it to one or two harmonic oscillators according to the prescriptions of the previous section. The maximum bath frequency ω_max is set equal to the cutoff frequency ω_c. For the case with just one bath oscillator, this oscillator's frequency is thus ω_c, and for the case with two bath oscillators, there is one additional HO with lower frequency. We investigate three different values for ω_c, namely, a low-frequency bath with $\omega_\mathrm{c} = 0.1\ \omega_\mathrm{s}$, one resonant case with $\omega_\mathrm{c} = 1.0\ \omega_\mathrm{s}$, and one frequency in between, $\omega_\mathrm{c} = 0.5\ \omega_\mathrm{s}$. The system frequency is the harmonic approximation of the iodine Morse potential as defined in Sec. 3.2.3. For the effective coupling strength, two different values will be used, namely, $\eta_\mathrm{eff} = 0.2$ and $\eta_\mathrm{eff} = 1.0$. Initially, all modes are placed at equilibrium with momentum corresponding to the HO groundstate energy, $(0, \sqrt{m_i\omega_i})$, to get a spectrum with a maximum peak at the groundstate and others with decreasing weight at excited states. The initial width parameter is chosen as $\gamma_i = m_i\omega_i$. We use a time step of $\Delta t = T_\mathrm{s}/20$, where $T_\mathrm{s} = 2\pi/\omega_\mathrm{s}$ is the system's harmonic approximation oscillation period. The number of time steps is $N_\mathrm{steps} = 2^{14}$, except for the full hybrid case, which requires two time integrations and therefore scales quadratically with the number of steps. In that case, we choose $N_\mathrm{steps} = 2^{13}$ to keep computational time low.

In all cases, we perform full quantum calculations with the WavePacket software [90, 91] for comparison. We can then systematically do semiclassical calculations with presumably decreasing accuracy, namely, TA HK in separable approximation (labeled "HK") according to Eq. (3.34), the hybrid approximation from Eq. (3.46) without the time separation approximation ("full hybrid") and finally the separable hybrid approximation from Eq. (3.51) ("separable hybrid"). From the nature of the hybrid approximation, one might expect very good agreement for low bath frequency and weak coupling, and disagreement for the opposite case.

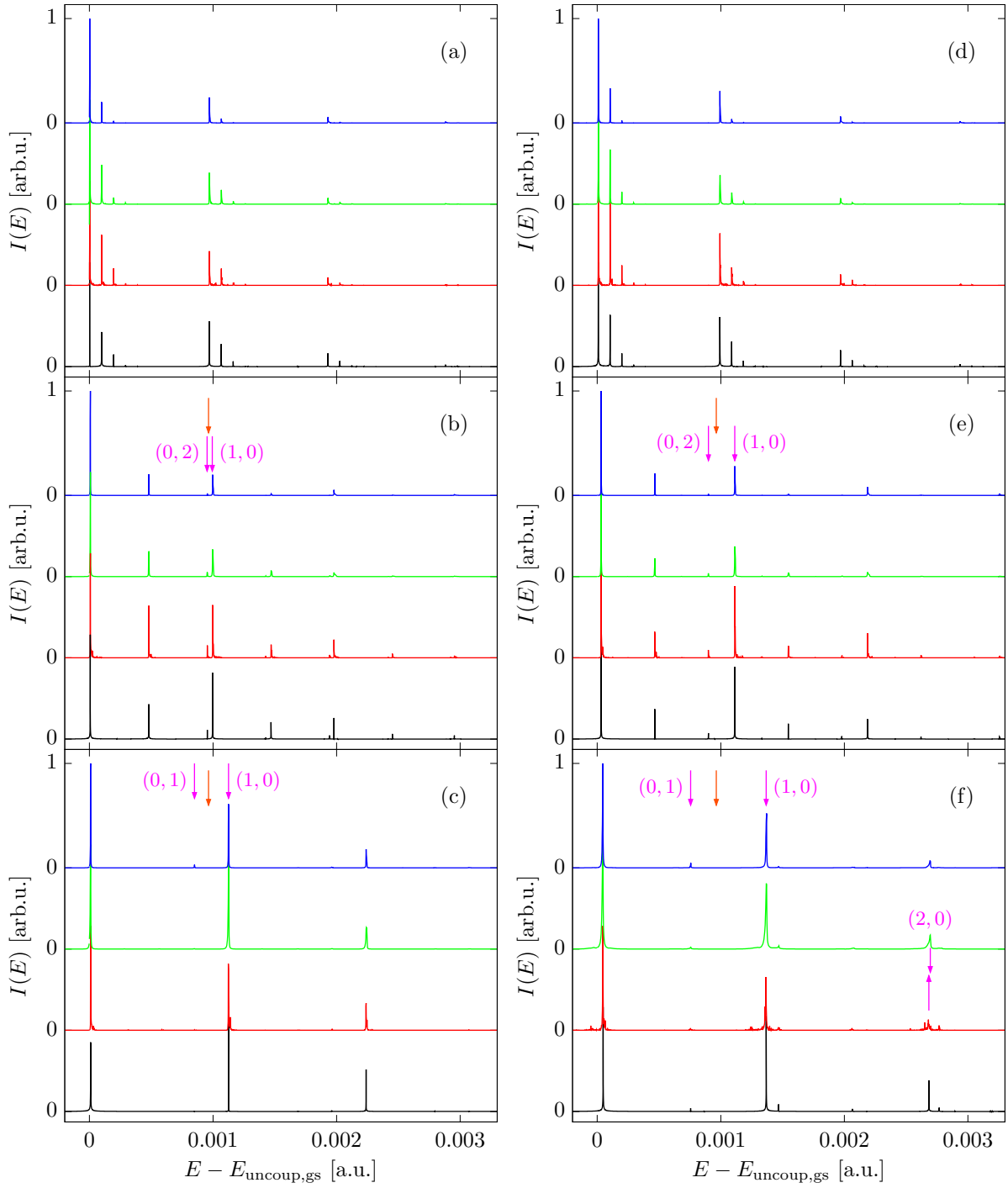

Figure 4.2.: Spectrum of an iodine-like Morse oscillator coupled to a single harmonic oscillator with different frequencies and effective coupling strengths. All spectra are renormalized such that the respective largest peak has a value of 1 arb.u., and the spectra are slightly overlapped to improve visibility of the excited peaks. The effective system-bath coupling strength is $\eta_{\text{eff}} = 0.2$ in panels (a) to (c) on the left, and $\eta_{\text{eff}} = 1.0$ in (d) to (f) on the right side. From top to bottom, the bath cutoff frequency increases: $\omega_c = \omega_s/10$ in panels (a) and (d), $\omega_c = \omega_s/2$ in panels (b) and (e), and $\omega_c = \omega_s$ in panels (c) and (f). Within each panel, the accuracy of the methods increases from top to bottom: Separable TA hybrid (blue), full TA hybrid (green), separable TA HK (red), and full quantum results (black). Orange arrows indicate the first excited Morse peak from the analytic one-dimensional result in order to highlight the blueshift.

	separable TA HK (Eq. (3.34))	full TA hybrid (Eq. (3.46))	separable TA hybrid (Eq. (3.51))
trajectories	2×10^5	1×10^4	1×10^4
time steps	2^{14}	2^{13}	2^{14}
computational time	10 hours	33 hours	40 min

Table 4.1.: Number of trajectories and computational times needed for tight convergence of the spectrum of a Morse oscillator coupled to one bath oscillator with $\eta_{\text{eff}} = 0.2$ and $\omega_{\text{b}} = \omega_{\text{s}}/10$. All propagation times are from single CPU calculations on a standard desktop computer.

Results for the 2 DOF and 3 DOF calculations are plotted in Fig. 4.2 and 4.3, respectively, for all six parameter combinations. Here and in the remainder of this work, all results are normalized such that the biggest peak value equals one, and the spectra are overlapped a little bit in order to make higher excitations more visible. The order from bottom to top is always quantum (black), HK (red), full hybrid (green), and separable hybrid (blue). In each panel, we have subtracted the groundstate energy of the uncoupled system from the energy on the abscissa, i.e.,

$$E_{\text{plot}} = E - \left(\frac{\omega_{\text{e}}}{2} - \frac{x_{\text{e}}\omega_{\text{e}}}{4}\right) - \sum_{i=1}^{N_{\text{b}}} \frac{\omega_i}{2}, \tag{4.10}$$

where the terms inside the bracket are the analytic result for the Morse oscillator according to Eq. (3.53), and $\omega_{\text{s}} = \omega_{\text{e}}$ here. In order to point out the shift of the Morse oscillator levels, we have indicated the analytic result from Eq. (3.53), again with the groundstate subtracted, with orange arrows. Selected other peaks have been marked with magenta arrows, where we use the notation (l, m, n) to indicate the lth Morse oscillator excited state, the mth excited state of the higher frequency bath mode and n for the remaining mode (if applicable).

First, we discuss the 2 DOF results from Fig. 4.2. Here, 10^4 trajectories were used for the semiclassical calculations. This number is sufficiently high to ensure that the first excited peaks are clearly visible, but not always high enough for tight convergence, as can be seen from Tab. 4.1. The overall agreement of the different methods in terms of peak positions is excellent. The only exception are the $(2, 0)$ peaks in the strongly coupled resonant case on the lower right panel, where small deviations of the hybrid results from the exact spectra can be seen. Peak intensities, on the other hand, are less well reproduced by the separable hybrid method. The two upper panels in Fig. 4.2 illustrate this difference: compared to the other three methods, excited bath peaks are systematically suppressed. For example, the $(0, 2)$ peak can be seen very clearly in the quantum, HK, and full hybrid spectra, but it is barely visible in the separable hybrid result. This behavior is explained by the analytical results for the harmonic oscillator from App. C, where we have shown that the weight of the excited state peaks decreases quadratically compared to the exact result. Peak shapes of the separable hybrid reproduce those of the full hybrid method nicely, for example in the $(2, 0)$ peak in Fig. 4.2(f), and we stress that no unphysical "ghost peaks" are introduced by the separable hybrid approximation.

Especially for the higher bath frequencies (Figs. 4.2(b),(c),(e),(f)), it is apparent that the Morse oscillator is shifted towards higher energies (blueshift) and the harmonic oscillator to-

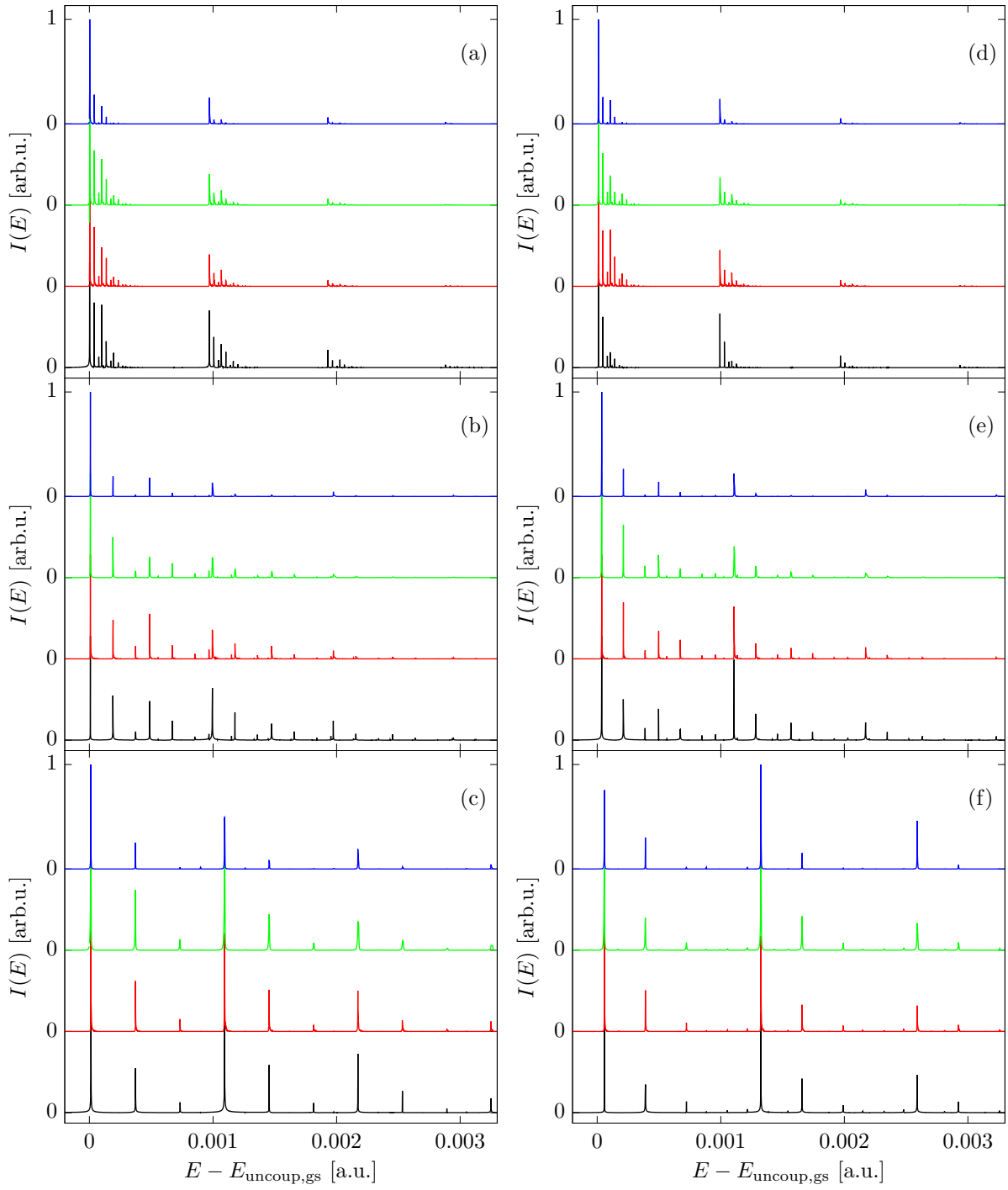

Figure 4.3.: Spectrum of an iodine-like Morse oscillator coupled to two CL bath harmonic oscillators with different cutoff frequencies and different coupling strengths. All plot specifications are identical to those of Fig. 4.2.

wards lower energies (redshift). We have highlighted the $(1,0)$ peak in each of these panels together with the $(0,2)$ and the $(0,1)$ peak for the intermediate and the resonant case, respectively. In an uncoupled calculation, the excited Morse peak would be almost on top of the excited HO peaks, with a slight shift to the left due to the correction term in Eq. (3.53). Because of the coupling, however, the Morse oscillator is blueshifted, while the bath HO has lower frequency. This tendency increases for more resonant bath frequencies and for higher values of η_{eff}, both of which amount to a stronger coupling of the two DOFs. In the case of two bath oscillators instead of one, numerical calculations and spectroscopic features already become more complex. Due to the higher phase space dimension, we now use 5×10^4 trajectories for the semiclassical calculations. Results in Fig. 4.3 show once again the very good reliability of full and separable hybrid approximations. Peak positions are still reproduced faithfully in each case, again with the exception of the most strongly coupled case in Fig. 4.3(f) where a slight difference can be made out. As before, the separable hybrid result is inaccurate with respect to peak intensity and a few highly excited overtones are missing for the same systematic reasons as in the two-dimensional case.

From a numerical point of view, the advantage of the hybrid methods is obvious, especially for the two-dimensional calculations. For the same number of trajectories, the hybrid results are already converged, while the HK results still contain quite a lot of noise, even to a point where no clear (2,0) peak can be picked out in the strongly coupled resonant case (Fig. 4.2(f)). One example of computational times for fully converged results is listed in Tab. 4.1. Due to the much lower number of trajectories, the separable hybrid result is obtained faster than the converged HK result. The full hybrid calculation, on the other hand, takes much longer due to the double time integration which dramatically increases the numerical cost per trajectory. In spite of using an efficient 2D FFT algorithm for the integration itself, the integrand from Eq. (3.51) still has to be calculated $N_{\text{steps}}^2/2$ times, thus canceling out the effect of the reduced number of trajectories. This unfavorable result is, however, partly due to the simplicity of the analytic potential. For realistic systems, where the potential is not given analytically, calculating the classical trajectories on-the-fly takes much longer and therefore requires a higher percentage of the overall computational time [76], so even the full hybrid approximation might be faster in that case.

More generally speaking, the drastic simplification of the hybrid approximation, where the phase space sampling of the bath modes is replaced by single trajectories, still allows for exact results in terms of peak positions. This is true even for strongly coupled bath DOFs where the harmonicity assumption is violated due to the anharmonic driving by the Morse system. In particular the separable hybrid method promises an impressive speedup at still very good accuracy, with the only drawback being some missing highly excited bath peaks. From a more optimistic point of view, this disadvantage might even be helpful for the interpretation of the spectrum in question, when one is not interested in bath excitations.

4.3. MORSE OSCILLATOR COUPLED TO A CALDEIRA-LEGGETT BATH OF HARMONIC OSCILLATORS

After demonstrating the accuracy of the hybrid approximations, we now turn our attention to actual CL systems with a number of environmental DOFs that is suitable to describe even continuous baths. For the Ohmic spectral density from above, it has been shown that about 40 bath HOs are sufficient to describe such a continuous bath in the case of a very low bath cutoff frequency [59]. We first discuss results for a ten-dimensional bath where individual bath

excitations still can be attributed relatively easily. After that, we will increase the number of bath DOFs and take a look at the role of the counter term in Eq. (4.1).

This time there are only two different frequency combinations, a resonant one similar to the previous examples, $\omega_c = \omega_s/2$ and $\omega_{max} = \omega_s$, and a low-frequency bath with $\omega_c = \omega_s/10$ and $\omega_{max} = \omega_s/5$. Again, we choose different effective coupling parameters, namely, $\eta_{eff} = 0.5$ and $\eta_{eff} = 2.0$ for the bath with small cutoff frequency and $\eta_{eff} = 0.1$ and $\eta_{eff} = 0.5$ for the big cutoff. In order to keep the spectra reasonably "clean", the initial conditions are chosen a bit differently than before. The system DOF still starts at equilibrium with nonzero momentum, $(0, \sqrt{m_s\omega_s})$, but the bath oscillators are all at $(0, 0)$ at the beginning of the propagation because otherwise the spectrum becomes impossible to read due to the huge number of excited bath peaks (for an example with 19 DOFs, see Fig. 3 of [73]). In general, these simplified initial conditions might not be adequate to describe the system frequency shift because possible anharmonic contributions of the bath DOFs are neglected by a dynamics that explores only the harmonic neighborhood of the potential minimum. For the harmonic CL bath, however, the difference arising from initially excited bath DOFs is very small, as we will discuss shortly at the end of this chapter. The number as well as the length of the time steps stays the same as in the two and three DOF examples, resulting in a frequency resolution of 1.2×10^{-6} a.u. (0.26 cm^{-1}).

We first discuss an interesting but relatively simple example, a resonant and strongly coupled bath with ten bath oscillators (Fig. 4.4). On Fig. 4.4(a), we give an overview of results obtained with the different methods. Quantum calculations are no longer possible now, so only TA-HK, full hybrid and separable hybrid are employed with the same color code as before. We also show one full hybrid result where not only the system mode, but also the resonant bath HO has been treated with HK (magenta lines). Only 10^4 trajectories have been used in each case, both to achieve reasonable computational costs and to work out the efficiency of the new methods. Like in the lowest dimensional cases, agreement is very good between all methods. Bath peaks are generally less prominent now because there is no initial excitation in the bath; the only dynamics is induced by the system. This is reflected especially in the TA-HK and full hybrid spectra by the fact that the biggest bath peaks are those that correspond to the modes whose frequency is closest to the system. By contrast, just one bath peak is featured significantly in the separable hybrid spectrum, namely, the resonant bath HO.

The right-hand side of Fig. 4.4 highlights some details of the spectra. A zoom into the region of the third and fourth excited system peak is shown on panels (b) and (c). The respective left peak in these pictures is a bath excitation, and the right peak is the system excitation. We should first stress that peaks in these pictures are three to four orders of magnitude smaller than the groundstate and therefore quite noisy, but they can nevertheless be clearly identified as peaks. The full hybrid result with one HK DOF clearly disagrees with the TA-HK spectrum. However, this deviation can be alleviated by treating also the most strongly coupled bath DOF with HK, so one might conclude that the resonant bath mode shows non-Gaussian distortions due to the anharmonic driving by the system. Another way to reproduce these distortions with just one HK DOF might have been to use significantly more trajectories, thus sampling the resonant bath mode indirectly by its coupling to the system mode via the classical dynamics, as discussed in [66]. The separable hybrid result, in spite of developing a prominent shoulder to the right of the system excitation, displays these peaks more clearly than the other methods. Especially the fourth excited system peak (Fig. 4.4(c)) can be identified at first sight, while it shows up only as a minor bump compared to the bath peak next to it with the more advanced methods. Agreement of the separable hybrid with the other approaches in terms of peak position is again excellent.

In Fig. 4.4(d), we put the bath excitations under the spotlight. The rightmost peak is the sec-

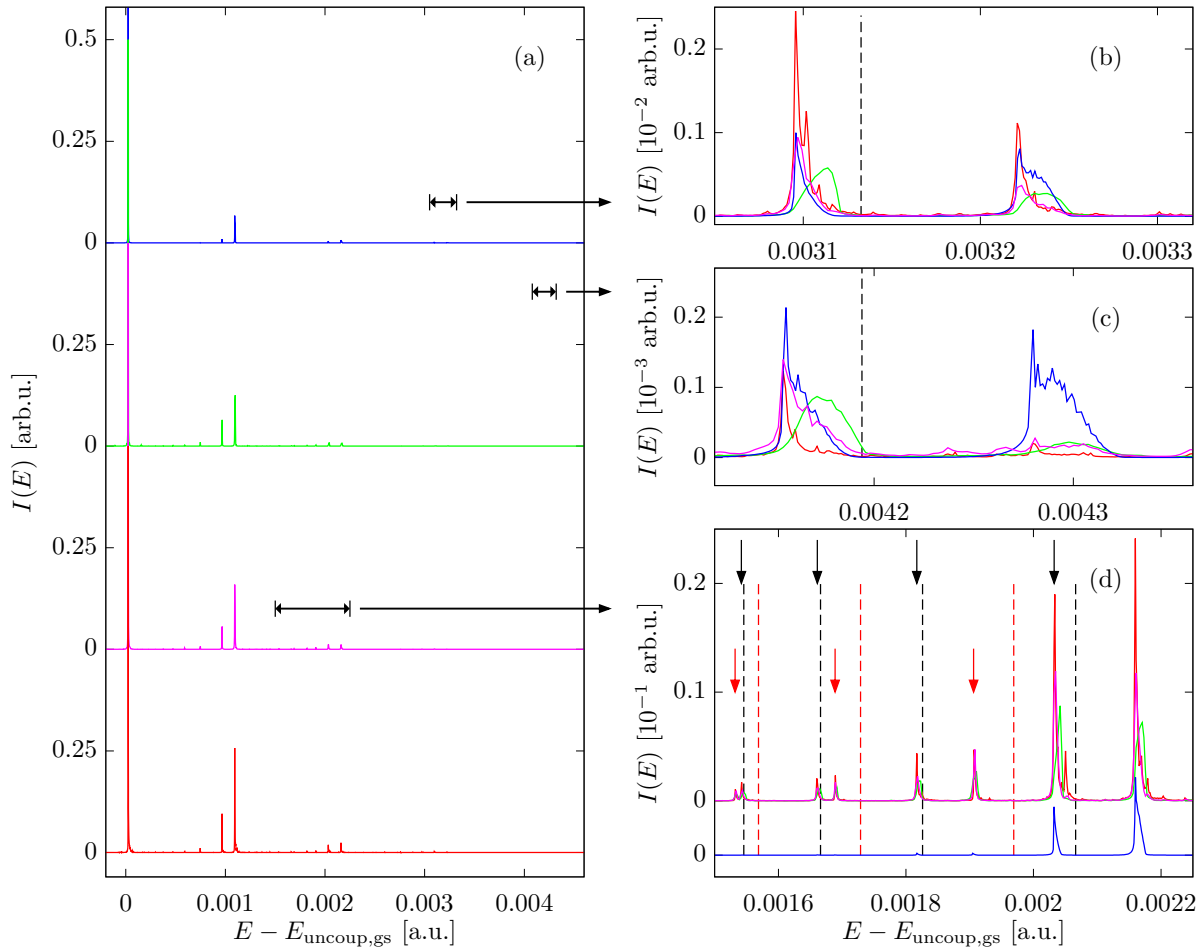

Figure 4.4.: Spectrum of an iodine-like Morse oscillator coupled to a CL bath comprising 10 DOFs with $\omega_{\mathrm{max}} = \omega_{\mathrm{s}}$, $\omega_{\mathrm{c}} = \omega_{\mathrm{s}}/2$ and coupling $\eta_{\mathrm{eff}} = 0.5$. All spectra are renormalized as in Fig. 4.2 and the color scheme is also identical, with one addition: separable TA hybrid with 1 HK DOF (blue), full TA hybrid with 1 HK DOF (green), full TA hybrid with 2 HK DOFs (magenta), separable TA HK (red). The arrows in panel (d) designate bath excitations of first (black) and higher order (red), dashed vertical lines show the respective uncoupled counterpart.

ond excited state of the system, all remaining peaks are bath excitations (orange and black arrows). The dashed black lines correspond to peak positions of the form $(1, 0, \ldots, 0, 1, 0, \ldots, 0)$, i.e., only the system and one selected bath oscillator are in the first excited state. These lines have been obtained by adding the bath frequencies ω_i to the first excited system peak and thus illustrate where these bath peaks would be situated if the bath frequencies remained unchanged by the dynamics. In the same way, the dashed orange lines show the unchanged position of higher order bath peaks. The rightmost orange line, for example, shows the uncoupled position of the second excited state of the HO with highest frequency. One sees immediately that each bath peak lies to the left of a dashed line, which means that all of these bath oscillators are redshifted, as in the very simple cases in the previous section. Higher order bath excitations are shifted further, as it is expected. In order to make the separable hybrid result a bit more visible, it has been moved downwards to illustrate that the system and the highest bath excitation show up very accurately. By comparison to the other methods, the separable hybrid result once

more exhibits advantageous convergence properties. Most bath excitations are suppressed by the separable hybrid method but they can still be identified reliably upon closer inspection and turn out to be reproduced quite faithfully. Due to its numerical advantages, we will perform exclusively separable hybrid calculations in the remainder of this chapter and investigate both system and bath behavior for different bath characteristics.

4.3.1. FREQUENCY SHIFTS FOR DIFFERENT BATH SIZES AND ROLE OF THE CALDEIRA-LEGGETT COUNTER TERM

Having established that the separable hybrid method offers the same accuracy with respect to peak positions as the full HK treatment for the CL system, we now increase the bath size up to 60 bath HOs. Again, we use a very off resonant bath on the one hand and one with bath frequencies up to the system frequency on the other. In addition, we will analyse the influence of the CL counter term on the outcome of the spectral calculations for our examples. Using a normal mode analysis, E. Pollak and coworkers have shown analytically for a harmonic system with and without an additional cubic term that the system frequency shift induced by the CL bath in the form of Eq. (4.1) with an Ohmic spectral density is always towards higher frequencies, i.e., a blueshift [92,93]. In the case of a purely harmonic system, the new frequency $\tilde{\omega}_\mathrm{s}$ has the implicit form

$$\tilde{\omega}_\mathrm{s}^2 = \frac{\omega_\mathrm{s}^2}{1 + \dfrac{2}{\pi m_\mathrm{s}} \int\limits_{-\infty}^{\infty} \mathrm{d}\omega \dfrac{J(\omega)}{\omega(\omega^2 - \tilde{\omega}_\mathrm{s}^2)}}. \tag{4.11}$$

Assuming an Ohmic spectral density, which is nonzero for positive frequencies only, and an abrupt cutoff $J(\omega) = \eta\omega\Theta(\omega - \omega_\mathrm{c})$ instead of the exponential form in Eq. (4.6), one finds nonlinear equations for $\tilde{\omega}_\mathrm{s}$ depending on the size of the cutoff frequency,

$$\tilde{\omega}_\mathrm{s}^2 - \frac{2\eta}{\pi m_\mathrm{s}} \tilde{\omega}_\mathrm{s} \mathrm{arcoth}\left(\frac{\omega_\mathrm{c}}{\tilde{\omega}_\mathrm{s}}\right) - \omega_\mathrm{s}^2 = 0 \qquad \tilde{\omega}_\mathrm{s} < \omega_\mathrm{c} \tag{4.12}$$

$$\tilde{\omega}_\mathrm{s}^2 - \frac{2\eta}{\pi m_\mathrm{s}} \tilde{\omega}_\mathrm{s} \mathrm{artanh}\left(\frac{\omega_\mathrm{c}}{\tilde{\omega}_\mathrm{s}}\right) - \omega_\mathrm{s}^2 = 0 \qquad \tilde{\omega}_\mathrm{s} > \omega_\mathrm{c}. \tag{4.13}$$

It has been demonstrated in [27,37] for different bath parameters that this indeed amounts to a blueshift. In the case of an additional cubic anharmonicity, one can find an explicit expression assuming $\omega_\mathrm{s} \gg \omega_\mathrm{c}$ and $\tilde{\omega}_\mathrm{s} \gg \omega_\mathrm{c}$ [92]

$$\tilde{\omega}_\mathrm{s} = \omega_\mathrm{s}\left(1 + \frac{2\eta}{\pi m_\mathrm{s}} \frac{\omega_\mathrm{c}}{\omega_\mathrm{s}^2}\right)^{1/2} \approx \omega_\mathrm{s}\left(1 + \frac{\eta}{\pi m_\mathrm{s}} \frac{\omega_\mathrm{c}}{\omega_\mathrm{s}^2}\right). \tag{4.14}$$

For the cubic system, another analytical study has also shown a blueshift tendency for different bath spectral densities [94]. The same result has been obtained for a Morse oscillator coupled to a CL bath [95]. On the other hand, arguing that experimental results often report a redshift of the system frequency (as we will also see in Chapter 5), Georgievskii and Stuchebrukhov [96] have investigated the influence of the CL counter term on a cubic system potential and found that by omitting the counter term, both blueshift and redshift are possible depending on bath parameters. We will undertake a similar investigation and therefore look at the CL model in the form of Eq. (4.1) as well as a Hamiltonian without the counter term,

$$H = \frac{p_\mathrm{s}^2}{2m_\mathrm{s}} + V_\mathrm{s}(s) + \sum_{i=1}^{N_\mathrm{b}} \left\{ \frac{p_i^2}{2} + \frac{1}{2}\omega_i^2 y_i^2 + c_i y_i (s - s_\mathrm{eq}) \right\}. \tag{4.15}$$

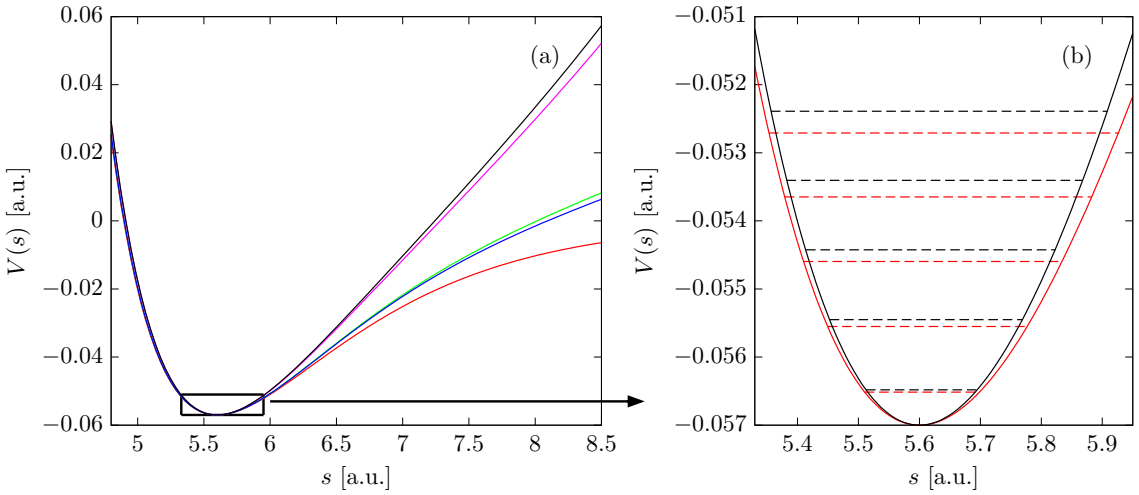

Figure 4.5.: (a) Pure Morse potential from Eq. (3.52) (red solid line) and Morse potential modified by the CL counter term as in Eq. (4.16) for different bath parameters: resonant bath with $\eta_{\text{eff}} = 0.1$ (blue) and $\eta_{\text{eff}} = 0.5$ (black), and low-frequency bath with $\eta_{\text{eff}} = 0.5$ (green) and $\eta_{\text{eff}} = 2.0$ (magenta). (b) Lowest eigenenergies for the unmodified Morse potential (red dashed lines) and the modified Morse potential for the strongly coupled resonant case (black dashed lines).

Since the counter term does not depend on the bath coordinates, it amounts effectively to a renormalization of the system potential, as pointed out before [97]. In Fig. 4.5(a), we have plotted the Morse potential from Eq. (3.52) as well as the Morse potential modified by the CL counter term, which becomes

$$V_{\text{s,mod}}(s) = D_{\text{e}}\left(1 - \mathrm{e}^{-\alpha(s-s_{\text{e}})}\right)^2 - D_{\text{e}} + \frac{\pi}{4}\frac{N_{\text{b}}}{a}\left(s - s_{\text{e}}\right)^2 \tag{4.16}$$

with the normalization parameter from Eq. (4.8), for the four different bath parameter combinations that we will look at. The prefactor of the counter term, $N_{\text{b}}/a = \eta\omega_{\text{c}}\left(1 - \mathrm{e}^{-\omega_{\max}/\omega_{\text{c}}}\right)$, does not depend on the number of bath DOFs, but grows with increasing effective coupling and cutoff frequency, thus making the effective system potential narrower. Using the analytic result for the pure Morse oscillator and numerical results for the modified potential, we see in Fig. 4.5(b) that this renormalization alone leads to a bigger distance of the eigenenergies $E_{\text{mod},n}$ (blueshift). To not compare apples and oranges, we will use these modified eigenenergies for the evaluation of the numerical results.

The following numerical investigations will comprise bath sizes of 10, 20, 40, and 60 DOFs, such that convergence with respect to the number of bath HOs can be established. Initial conditions and propagation times remain the same as before, but henceforth we will employ exclusively the separable hybrid scheme due to its favorable trade-off between computational effort and accuracy. As we are using a hybrid method, we can keep the number of trajectories constant at 10^4 for the differently sized baths. The number of HK DOFs has been either one or two. Especially for the low frequency bath it was sufficient to describe only the Morse oscillator with HK, while in the case of the high bath cutoff it was helpful to include the resonant bath oscillator into the HK part as well.

An exemplary overview of results for the different bath parameters is given in Fig. 4.6 for a bath with 20 DOFs, where again all spectra are normalized such that the respective

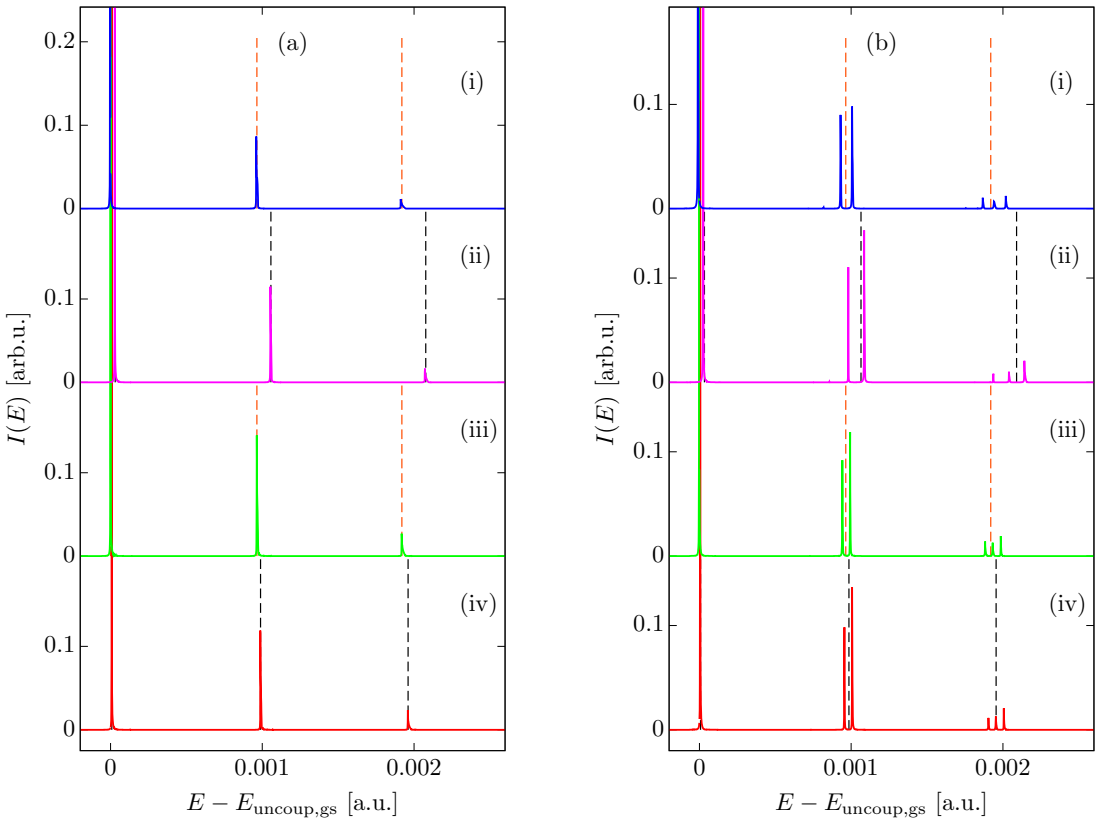

Figure 4.6.: Spectra for a Morse oscillator in a CL bath with 20 HOs for low and high cutoff frequency (left to right). In panel (a), bath parameters are $\omega_c = \omega_s/10$ and $\omega_{max} = \omega_s/2$, with effective couplings $\eta_{eff} = 0.5$ (solid red and green lines) and $\eta_{eff} = 2.0$ (magenta and blue). In panel (b), bath parameters are $\omega_c = \omega_s/2$ and $\omega_{max} = \omega_s$, with effective couplings $\eta_{eff} = 0.1$ (red and green lines) and $\eta_{eff} = 0.5$ (magenta and blue). Results (i) and (iii) are from calculations without the CL counter term, (ii) and (iv) from calculations including the CL counter term. The dashed lines represent eigenvalues of a regular 1D Morse potential (black) and of a 1D Morse potential modified by the CL counter term according to Eq. (4.16) (orange).

largest peak's size is one. We have also plotted eigenvalues of the 1D systems mentioned above, i.e., eigenvalues of the undisturbed Morse potential for calculations without CL counter term (orange dashed lines) and eigenvalues of the appropriately modified Morse potential for calculations including the counter term (black dashed lines). The spectra with low bath cutoff frequencies in panel 4.6(a) exhibit system peaks that are hardly different from the 1D result. If the CL counter term is included (spectra (ii) and (iv)), we see different blueshifts that can be attributed to the modification of the system potential by the counter term. For the cases without counter term (spectra (i) and (iii)), even the difference in effective coupling strength has little effect, at least on the scale of this figure. The higher cutoff frequency, on the other hand, has a much greater impact on the spectra, as depicted in subfigure 4.6(b). Instead of just the excited states of the system, there are groups of peaks now, corresponding to redshifted bath and blueshifted system excitations as discussed in the previous section. Again, the respective rightmost peak of each group belongs to the system while the others are first and second excited state of the resonant bath mode. The appearance of these bath peaks, or, more to the point,

the fact that they are no longer suppressed but show up so prominently here, is due to the fact that the resonant bath mode can be driven much more effectively by the system than the non-resonant one from the low-cutoff example. In addition, the resonant HO is now incorporated into the HK part of the calculation, which implies a sampling of initial conditions instead of just taking the central trajectory and thus means higher initial energy of this bath mode. The more interesting and more relevant feature for us, however, is that the stronger system-bath interaction results in a sizable blueshift of the system both for calculations with and without CL counter term and always relative to the respective modified or unmodified one-dimensional eigenvalues. For low effective system-bath coupling, the difference between the results with and without counter term is not very pronounced (lower graphs in Fig. 4.6(b)), which seems justified given that the effect of the potential renormalization is almost insignificant. The high coupling case, on the other hand, exhibits a greater blueshift of the system if the counter term is not included. Comparing high and low effective coupling, we see that an increase of η_{eff} leads to a bigger distance between system and bath peaks of the same group as a consequence of an enhancement of the respective trend towards blueshift or redshift.

For a more detailed quantitative discussion of the system's blueshift, we will now take a look at the first five system peaks for each of the different baths (Figs. 4.7 to 4.10). Peak positions have been determined as the value at the maximum amplitude rather than an average over the whole peak. We think this is justified because, as we have seen in Fig. 3.1 and discussed in App. D, the original separable approximation of the full HK approach introduces an asymmetry of the excited peaks that causes the averaged value to shift away from the analytic result. The maximum, however, remains at the correct position. The same trend can also be found upon close inspection of the semiclassical compared to the quantum results in Secs. 3.2.3 and 4.2. In Figs. 4.7 and 4.8, the shift of the peak energies is plotted. For a better comparison between different bath sizes and parameters, the energy of an appropriate uncoupled reference depending on the peak index is subtracted, which is the sum of the groundstate energies of the bath oscillators and the eigenenergy of the system,

$$E_{\text{uncoup},n} = E_{\text{s},n} + \sum_{i=1}^{N_\text{b}} \frac{\omega_i}{2}, \tag{4.17}$$

where the system eigenenergies $E_{\text{s},n}$ are now either the analytic eigenenergy E_n of the undisturbed Morse potential from Eq. (3.52) for the calculations without CL counter term, or the numerically calculated eigenenergy $E_{\text{mod},n}$ of the modified Morse potential from Eq. (4.16) for the calculations including the counter term. Thus, we visualize the net shift of the peaks, which includes the energy shifts of the system eigenstates and of the bath groundstate. A blueshift of the system is therefore characterized by a sequence of increasing values, whereas a redshift shows the opposite behavior. Figures 4.9 and 4.10 show the difference of consecutive excited Morse peaks. While the difference between peak positions in the coupled and uncoupled case, $E_{\text{coup},n} - E_{\text{uncoup},n}$, in Figs. 4.7 and 4.8 also contains a possible shift of the bath frequencies, this contribution drops out for the difference of consecutive MO eigenenergies, so the eigenenergies are denoted by $\tilde{E}_n$ in Figs. 4.9 and 4.10. This kind of representation is referred to as Birge-Sponer extrapolation and can be used experimentally to determine Morse potential parameters from spectroscopic data [98, 99]. Based on the analytic formula for the Morse eigenenergies (3.53), a linear fit of these points yields the harmonic approximation frequency ω_e as the intersection with the vertical axis and the anharmonicity $\omega_\text{e}x_\text{e}$, which is proportional to the slope of the line. An increase of the slope corresponds to a redshift whereas a decreasing slope means a bigger difference between eigenvalues and therefore a blueshift. We show a linear fit of the first

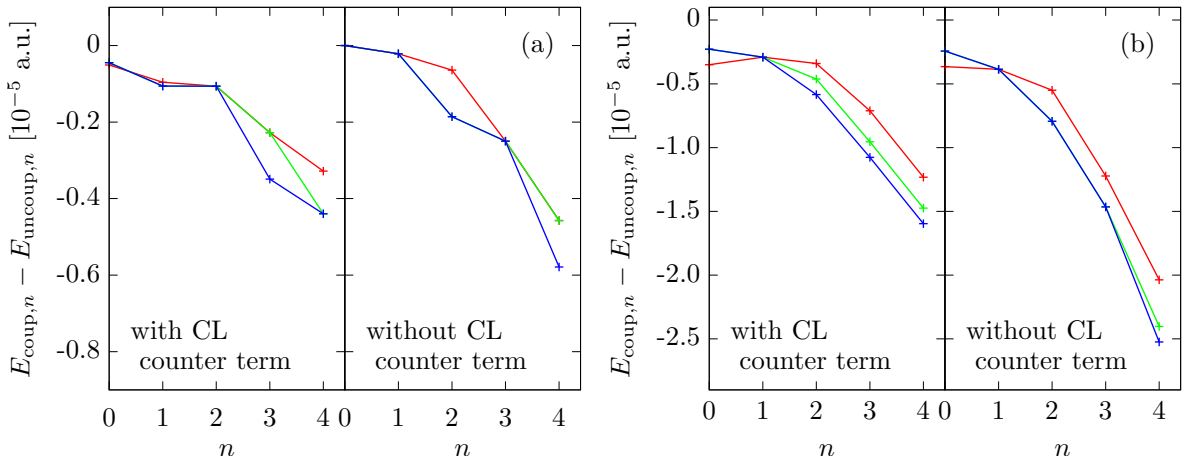

Figure 4.7.: Shift of the eigenenergies of a Morse oscillator coupled to a CL bath with parameters $\omega_{\mathrm{max}} = \omega_{\mathrm{s}}/2$, $\omega_{\mathrm{c}} = \omega_{\mathrm{s}}/10$, and different coupling strengths: $\eta_{\mathrm{eff}} = 0.5$ in panel (a) and $\eta_{\mathrm{eff}} = 2.0$ in panel (b). The bath comprises either 10 (red crosses), 20 (green), or 40 (blue) HOs, and the solid lines are just a guide to the eye. The CL counter term according to Eq. (4.1) is included in the calculations on the left side of each panel, and not included on the right side (Eq. (4.15)). As a consequence, the reference eigenenergies for the 1D MO are different depending on the presence of the counter term, according to Eq. (4.17).

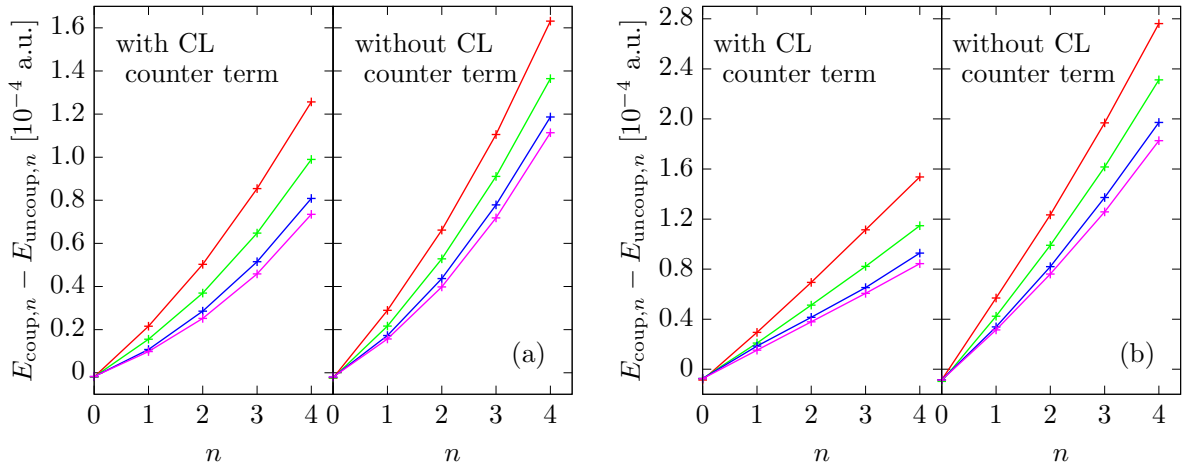

Figure 4.8.: Shift of the eigenenergies of a MO coupled to a CL bath with parameters $\omega_{\mathrm{max}} = \omega_{\mathrm{s}}$, $\omega_{\mathrm{c}} = \omega_{\mathrm{s}}/2$, and coupling strengths $\eta_{\mathrm{eff}} = 0.1$ in panel (a) and $\eta_{\mathrm{eff}} = 0.5$ in (b). All plot specifications as in Fig. 4.7, with the addition of results for 60 bath DOFs (magenta crosses).

four system energy differences and compare this result to the one-dimensional Morse oscillator or its modified version (black "×", dashed line), for which the intersection with the vertical axis has also been obtained by Birge-Sponer fit.

The analysis is interesting especially for the low-frequency bath, where we could not see much in the overview plot (Fig. 4.6). Results are presented in Figs. 4.7 and 4.9 for calculations with 10 (red crosses), 20 (green crosses), and 40 bath DOFs (blue crosses), and with two different system-bath couplings, $\eta_{\mathrm{eff}} = 0.5$ on the left (panel (a)), and for $\eta_{\mathrm{eff}} = 2.0$ on the right (panel (b)). Due to the fits in the Birge-Sponer plots in Fig. 4.9 being almost identical, we have plotted only one line in each case. For low coupling, we see an almost negligible redshift. The effect of

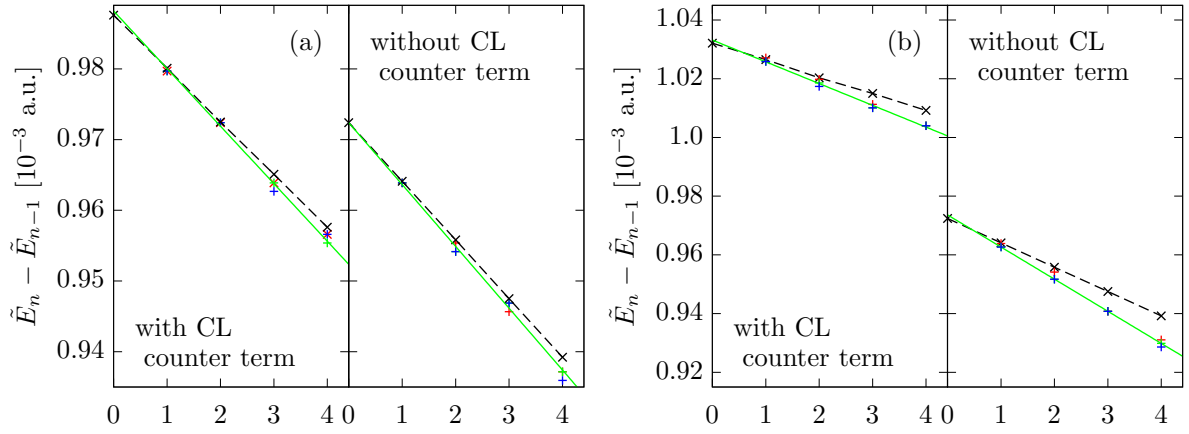

Figure 4.9.: Birge-Sponer fit to the difference of consecutive eigenenergies $\tilde{E}_n$ of the Morse oscillator coupled to a low-frequency CL bath from Fig. 4.7. Bath parameters are $\omega_{\max} = \omega_s/2$, $\omega_c = \omega_s/10$, and couplings are $\eta_{\text{eff}} = 0.5$ in panel (a) and $\eta_{\text{eff}} = 2.0$ in (b). The "+" crosses denote results with 10 (red), 20 (green), and 40 (blue) bath HOs. The solid green line is a linear fit to the 20 DOFs result, and the dashed black line with "×" crosses is the corresponding 1D MO reference, i.e., $E_n - E_{n-1}$ (Eq. (3.52)) or $E_{\text{mod},n} - E_{\text{mod},n-1}$ (Eq. (4.16)), respectively.

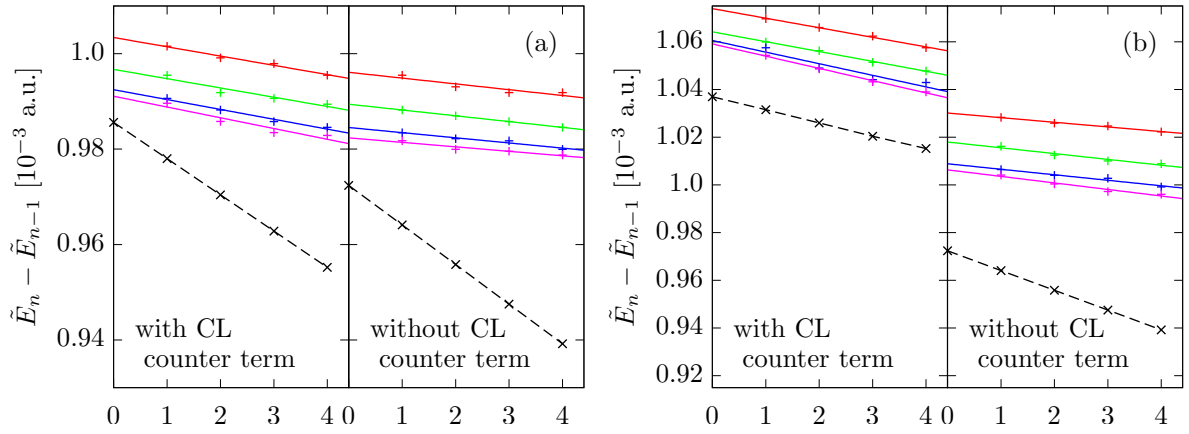

Figure 4.10.: Birge-Sponer fit to the difference of consecutive eigenenergies $\tilde{E}_n$ of the Morse oscillator coupled to a high-frequency CL bath from Fig. 4.8. Bath parameters are $\omega_{\max} = \omega_s$, $\omega_c = \omega_s/2$, and couplings are $\eta_{\text{eff}} = 0.1$ in panel (a) and $\eta_{\text{eff}} = 0.5$ in (b). All lines are fits to points of the same color as in Fig. 4.9, with the color code from Fig. 4.8.

the CL counter term is nicely illustrated by the Birge-Sponer plot: the result with counter term is clearly blueshifted with respect to the original Morse eigenvalues, but it is almost on top of the appropriately modified 1D energies. The influence of the system-bath dynamics is much smaller by comparison, especially given that our energy grid resolution is $\Delta E = 1.2 \times 10^{-6}$ a.u. These findings are corroborated by the calculations with higher system-bath coupling strength. Here, the redshift is much more pronounced, but again, for the original CL potential the main contribution to the energy shift is due to the counter term. For all calculations with low bath cutoff frequency, the number of bath oscillators does not have much impact on the system spectrum. In the low coupling case, the difference between all three bath sizes is one frequency grid point at most. For the higher coupling, 10 bath DOFs influence the system somewhat less than 20 and 40 bath HOs, which yield very similar results. This weak dependence on

bath size is of course a consequence of the low cutoff and maximum bath frequencies. While the bath mode with highest frequency is always the same, most additional bath oscillators are far off-resonant. As a conclusion, we can say that we find the same about 40 bath DOFs to be sufficient to describe a continuous bath in this low frequency case, as it has been reported in [59].

The case of baths with a high cutoff and resonant maximum frequency is investigated in detail in Figs. 4.8 and 4.10. We have used the same color scheme for bath size and reference states, but added calculations with 60 bath DOFs (magenta crosses). The overall behavior of the system is completely different compared to the low-frequency case, with strong blueshifts for each bath setup, as already seen in the overview figure 4.6. For $\eta_{\text{eff}} = 0.1$, the effect of the bath on the system is somewhat bigger without the CL counter term, as shown on the left side of Fig. 4.7(a). The counter term, which is harmonic in the system coordinate, restricts the system dynamics and thus also the system-bath interaction. Due to the offset of the 1D eigenenergies by the counter term, the total blueshifts in Fig. 4.10(a) are quite similar with and without counter term. Unlike before, the results change considerably with bath size, which is quite understandable given that each increase adds in particular some oscillators that are close to the system frequency and therefore strongly influence the system's dynamics. As the differences between results get smaller with each addition of bath HOs, we are approaching convergence with respect to a continuous bath description with 60 bath DOFs. The higher system-bath coupling amplifies these trends. Now, the difference of coupled and uncoupled peak energies (Fig. 4.8(b)) is almost twice as big for the calculation without CL counter term compared to the one that includes it. However, the modification of the 1D eigenenergies induced by the counter term is so big now that the total blueshift becomes clearly larger than without counter term. Again, we can see that the results converge with increasing bath size.

Finally, it is interesting to note that the difference between coupled and uncoupled result $E_{\text{coup},n} - E_{\text{uncoup},n}$ is smaller than or equal to zero at $n = 0$ in each panel in Figs. 4.7 and 4.8. The global groundstate energy is thus shifted to a lower value upon coupling of system and bath DOFs. In the cases with high bath cutoff frequency, we have seen from the Birge-Sponer plots (Fig. 4.10) that the harmonic approximation frequency and thus the system groundstate energy increases, making the system contribution to the aforementioned difference positive. The new global groundstate being at a lower energy can therefore only be due to a redshift of the bath frequencies. We will take a closer look at this effect in the concluding section of this chapter. Before that, we will pick up on an earlier comment and discuss the influence of bath modes with nonzero initial momentum on the above results.

4.3.2. INFLUENCE OF INITIAL BATH EXCITATION

As mentioned before, we have chosen to excite only the system mode at the beginning of the propagation because otherwise the number of contributions to the spectrum renders peak identification impossible as soon as the number of bath DOFs gets larger than about ten. On the other hand, these simple initial conditions might underestimate the bath influence on the system dynamics because all bath modes stay very close to their respective potential minima given that their only excitation comes from the system.

To shed a bit of light onto the dynamics with initially excited bath, we make use of the multiple coherent states (MC) version of HK TA SC-IVR that has been developed by M. Ceotto and coworkers [30, 31, 33, 72–74]. This formalism makes use of the fact that each single trajectory in the phase space integral (3.34) exactly reproduces those peaks that are closest to its own energy, as we have also seen in App. D. Consequently, we will use single trajectories

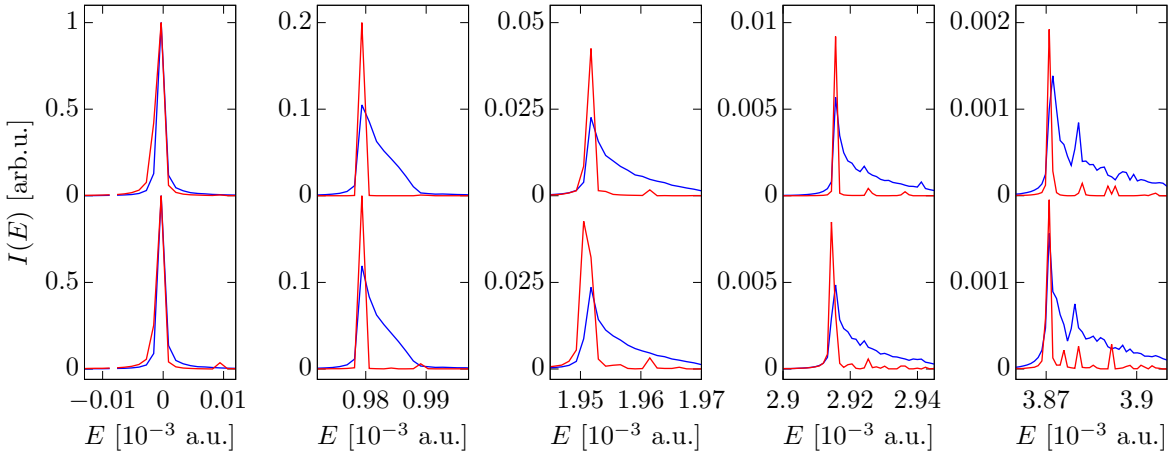

Figure 4.11.: Ground and first four excited state peaks (from left to right) of a Morse oscillator in a CL bath obtained with separable hybrid TA method (blue lines) and with single trajectory MC TA SC-IVR approach (red lines). Bath parameters are $\omega_{\max} = \omega_s/2$, $\omega_c = \omega_s/10$, and $\eta_{\text{eff}} = 0.5$. The upper part of each panel is the result with 10 bath HOs, the lower part is for 20 bath HOs. Hybrid calculations are performed without, single trajectory calculations with initial bath excitation. The energy has been shifted by the energy of the respective uncoupled ground state.

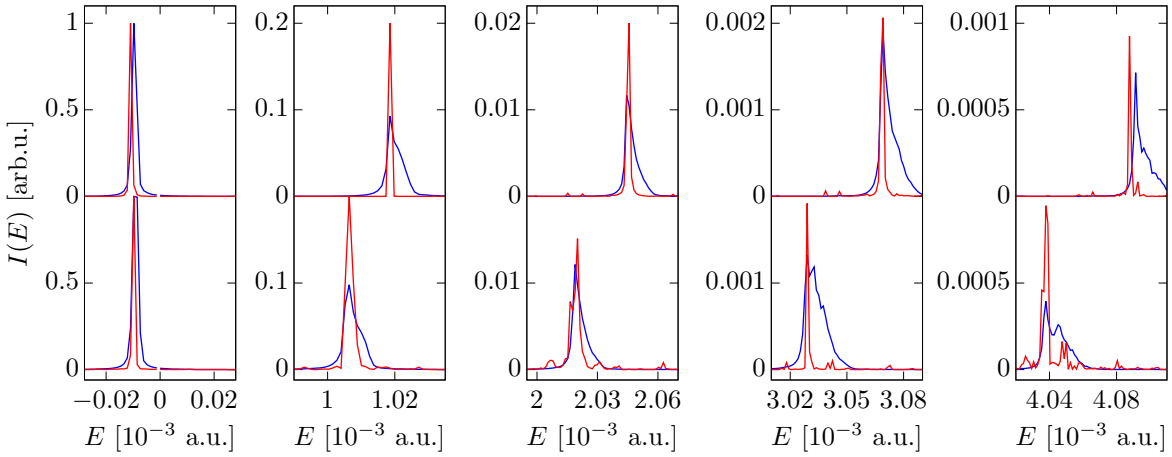

Figure 4.12.: Ground and first four excited state peaks (from left to right) of a Morse oscillator in a high-cutoff CL bath. Bath parameters are $\omega_{\max} = \omega_s$, $\omega_c = \omega_s/2$, and $\eta_{\text{eff}} = 0.5$. All plot specifications as in Fig. 4.11.

with initial system momenta corresponding to the peak energies found above. Each bath mode has initial momentum corresponding to its groundstate energy, i.e., $p_i(0) = \sqrt{\omega_i}$. For peak identification, we make use of a filter that originates also from the MC TA SC-IVR framework [74]. The single reference state $|\chi\rangle = \prod_{i=1}^{N} |g(p_i(0), 0)\rangle \equiv \prod_{i=1}^{N} |\chi_i\rangle$ in Eq. (3.34) is replaced by a superposition with two contributions per DOF, $|\chi_i\rangle = |g(p_i(0), 0)\rangle + |g(-p_i(0), 0)\rangle$. This choice of reference state filters out even contributions of each DOF; thus, in particular first bath excitations are strongly suppressed and only a few clearly defined peaks remain in the spectrum. In order to find the odd system peaks, we have to invert the relative sign in that coordinate, $|\chi_s\rangle = |g(p_s(0), 0)\rangle - |g(-p_s(0), 0)\rangle$. Since this approach requires a reference

state with 2^N contributions (and, consequently, the same number of FFTs in the numerical evaluation), these calculations are feasible only for a relatively low number of DOFs. We therefore restrict our considerations to 10 and 20 bath HOs.

The results in Figs. 4.11 and 4.12 demonstrate exemplarily that initial bath excitation is indeed not decisive for low-energy system peaks in the case of harmonic bath DOFs. For both small and high bath cutoff frequency, the previously obtained hybrid results without initial bath excitation agree perfectly with the single trajectory results where all bath modes carry initial momentum. The MC TA SC-IVR peaks are much sharper and symmetric, since they have been obtained as the result of a single trajectory calculation rather than a phase space integration. Peak positions, however, are at most one frequency grid point off the hybrid result (except for one peak in Fig. 4.12). The same behavior is found for all other cases discussed in the previous section, at least for 10 and 20 bath modes. Considering that the hybrid approximation might also account for some deviation, we conclude that our earlier choice of initial conditions is well justified.

Taking another look at Figs. 4.11 and 4.12, we can make an additional statement concerning the bath. Given that not only the differences between consecutive system peaks, but also the absolute peak positions remain unchanged by the initial bath excitation, it is clear that also the shift of the bath groundstate frequency by the coupling to the system is unaffected by the different initial conditions. Otherwise, the peak positions, which are the sum of all bath bath groundstate energies plus the respective system excitation, would be shifted. This finding is relevant for the following section, where we will discuss the impact of the system on bath modes that are not initially excited.

4.3.3. BATH FREQUENCY SHIFTS

Although the motivation for the development of the TA hybrid method was a more effective description of system-bath spectra where one is interested only in the system dynamics, it is worthwhile to take the reverse point of view for now and see if individual bath frequencies are still contained in the hybrid spectra. Figure 4.13 depicts part of the region between ground and first excited system state in a strongly enlarged fashion for two 40 DOFs baths with low and high cutoff frequency, respectively. The energy on the abscissa is shifted by the global ground state energy such that bath frequencies can be read off directly from this axis. While all peaks are orders of magnitude smaller than the groundstate peak, at least these highest about 10 (low cutoff) or 20 (high cutoff) bath frequencies can be attributed unambiguously.

In the upper panels of Figs. 4.14 and 4.15, bath frequencies $\tilde{\omega}_i$, that have been shifted by the interaction with the system, are plotted against their initial values ω_i that arise from the frequency sampling according to Eq. (4.9). We pick only frequencies $\tilde{\omega}_i$ that can be read off the spectrum easily, i.e., those ones that are closest to the system frequency, and we start our discussion with the high cutoff bath (Fig. 4.14). Having in mind that this evaluation is reliable only for the highest frequencies due to our limited resolution, we can still establish the general trend towards a redshift. This is most obvious for the resonant and near-resonant modes, as seen in the lower panels. From the upper part of Fig. 4.14, it appears that all frequencies are shifted evenly, yielding a linear relation between coupled and original frequencies with a slope slightly smaller than one, which makes sense given that the coupling of each mode to the system is proportional to its frequency (Eq. (4.8)). For the smaller baths, where the frequency distribution is less dense, the resonant bath mode stands out as being shifted more strongly. Also, especially for high coupling, one can see on the lower panels how individual bath modes are changed by a larger amount for small bath size due to the system energy being transfered

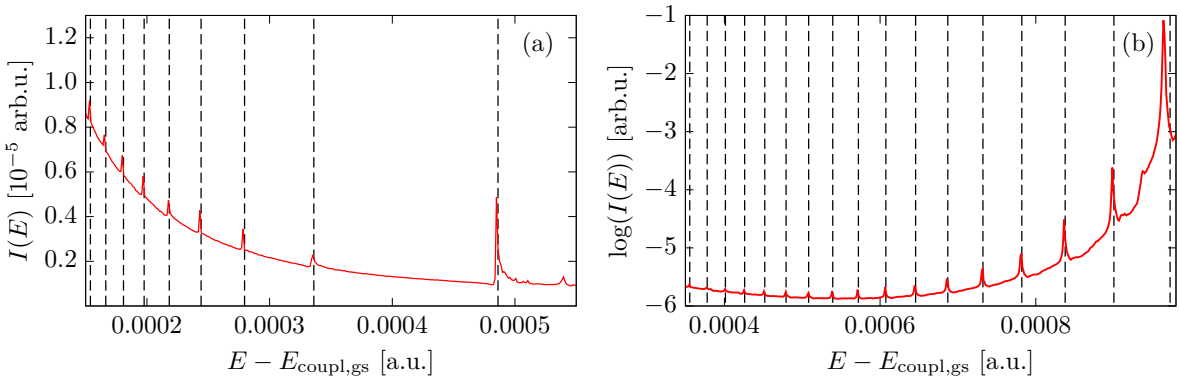

Figure 4.13.: Spectrum with first excited bath states relative to the groundstate peak (red line) for low-frequency bath with $\eta_{\mathrm{eff}} = 2.0$ (left) and bath with high cutoff and $\eta_{\mathrm{eff}} = 0.1$ (right). Both spectra from calculations with 40 bath DOFs; dashed vertical lines are corresponding uncoupled bath frequencies. In these units, the height of the ground state peak is one.

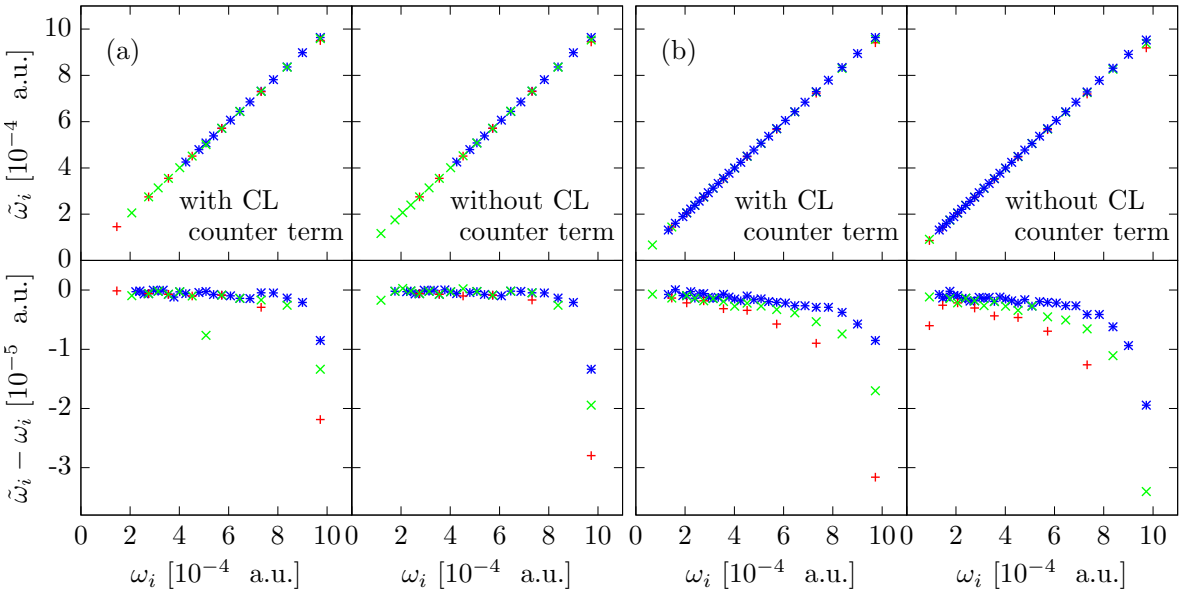

Figure 4.14.: Shift of individual bath frequencies for the high cutoff bath with coupling strengths (a) $\eta_{\mathrm{eff}} = 0.1$ and (b) $\eta_{\mathrm{eff}} = 0.5$. Sampled frequencies ω_i are on the horizontal axis, bath frequencies $\tilde{\omega}_i$ taken from the spectrum (upper) and their difference from the original value (lower panel) are on the vertical axis. Bath sizes are 10 (red), 20 (green), and 40 HOs (blue).

to fewer DOFs. Regarding calculations with and without counter term, we see that, just like the shift of the system frequencies before, the change of the bath frequencies is bigger if the counter term is not part of the Hamiltonian. This behavior can be explained by recalling that the counter term is quadratic in the system coordinate, making the system potential narrower and thereby restraining the system dynamics. The equivalent plot for smaller bath cutoff frequency is presented in Fig. 4.15. This is, however, not very meaningful because most deviations from the original values are inside or just above the frequency resolution. Only for large η_{eff}, the character of the shift of the highest frequency can be determined reliably and reveals the same trend as before.

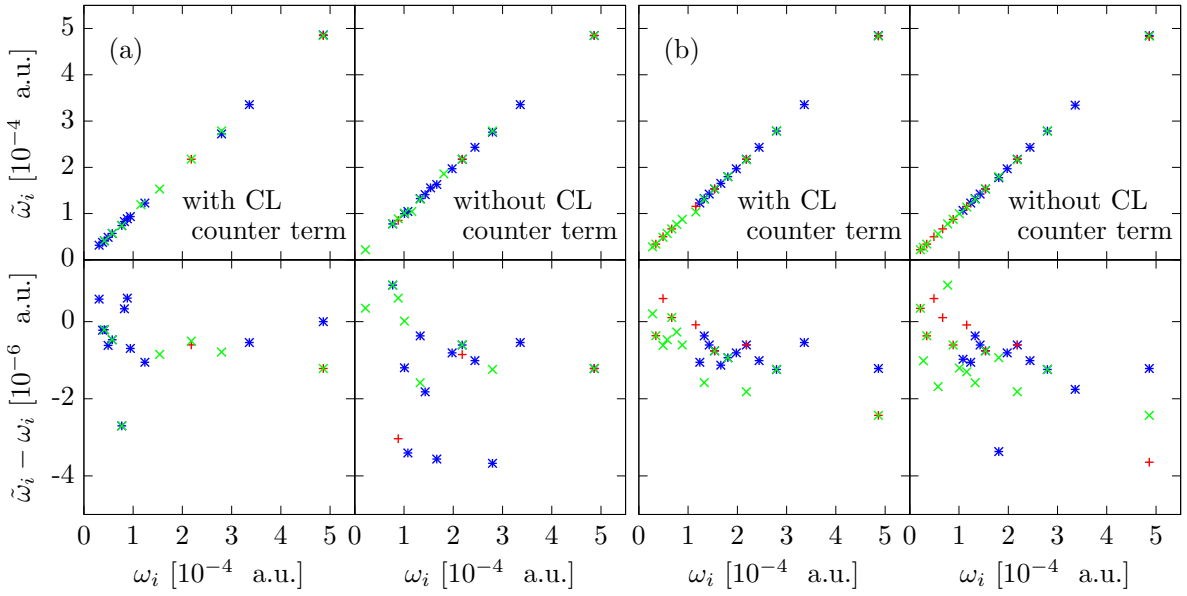

Figure 4.15.: Shift of individual bath frequencies for the low cutoff bath with coupling strengths (a) $\eta_{\text{eff}} = 0.5$ and (b) $\eta_{\text{eff}} = 2.0$. Specifications as in Fig. 4.14.

A summarizing quantification of the bath frequency shift is collected in Tabs. 4.2 and 4.3 for high and low frequency bath, respectively. The respective left columns show the bath frequency shift, which is the difference of the groundstate peak from the simulation and the uncoupled bath groundstate together with the shifted system energy,

$$\Delta E_{\text{b,c-uc}} = E_{\text{coup,gs}} - \sum_{i=1}^{N_{\text{b}}} \frac{\omega_i}{2} - E_{\text{s,coup,gs}}, \tag{4.18}$$

where $E_{\text{s,coup,gs}}$ is the new groundstate of the system calculated from the Birge-Sponer parameters. Negative values thus indicate a redshifted bath, and indeed all results are negative except one for the low-frequency bath with low coupling, where the frequency shift is much too small to be determined accurately. In all other cases, our earlier findings are corroborated. With increasing bath size, the effect of the system on the bath groundstate gets smaller. We also see that the shallower Morse potential without counter term has a stronger influence on the bath, as discussed before.

Looking at the upper panels of Figs. 4.14 and 4.15, one is inclined to wonder whether it is possible to determine the shifted bath groundstate energy directly by fitting the new frequencies as a linear function of the old, uncoupled ones. This can of course only be a crude estimate for two reasons: First, the distance of the frequency grid points is larger than the frequency shift for the off-resonant bath modes. Second, one has to be aware that bath peaks like those in Fig. 4.13, which have been used to create Figs. 4.14 and 4.15, belong to first excitations of the respective bath mode. Given that bath oscillators may become anharmonic due to the driving by the Morse system, the distance between eigenenergies of a given bath HO is no longer constant but decreasing. Thus, a fit to these first excited states overestimates the redshift.

With these precautions in mind, we first take a look at the high-cutoff bath. In the right hand columns of Tab. 4.2, we calculate the new bath groundstate from a first order fit but omit the resonant bath HO, which deviates visibly from such a line, and add it instead directly to the remaining, fitted bath modes. The assumption here is that all bath frequencies are shifted

	$\eta_{\text{eff}} = 0.1$		$\eta_{\text{eff}} = 0.5$	
	$\Delta E_{\text{b,c-uc}}$	$\Delta E_{\text{b,fit}}$	$\Delta E_{\text{b,c-uc}}$	$\Delta E_{\text{b,fit}}$
11D, w/ counter term	-1.1×10^{-5}	-1.2×10^{-5}	-2.7×10^{-5}	-3.3×10^{-5}
21D, w/ counter term	-0.8×10^{-5}	-1.7×10^{-5}	-2.1×10^{-5}	-6.5×10^{-5}
41D, w/ counter term	-0.6×10^{-5}	-1.6×10^{-5}	-1.9×10^{-5}	-7.3×10^{-5}
11D, w/o counter term	-1.5×10^{-5}	-1.7×10^{-5}	-4.0×10^{-5}	-4.4×10^{-5}
21D, w/o counter term	-1.2×10^{-5}	-1.4×10^{-5}	-3.3×10^{-5}	-4.8×10^{-5}
41D, w/o counter term	-0.9×10^{-5}	-1.6×10^{-5}	-2.8×10^{-5}	-5.3×10^{-5}

Table 4.2.: Difference of coupled and uncoupled bath groundstate energy (in a.u.) for the high cutoff bath. Values in the respective left columns calculated from the global groundstate peak, values in the right columns from a fit to individual bath frequencies in Fig. 4.14.

	$\eta_{\text{eff}} = 0.5$		$\eta_{\text{eff}} = 2.0$	
	$\Delta E_{\text{b,c-uc}}$	$\Delta E_{\text{b,fit}}$	$\Delta E_{\text{b,c-uc}}$	$\Delta E_{\text{b,fit}}$
11D, w/ counter term	-0.4×10^{-6}	$(-1.5 \pm 1.5) \times 10^{-6}$	-4.7×10^{-6}	-3.2×10^{-6}
21D, w/ counter term	-0.7×10^{-6}	$(-2.2 \pm 2.7) \times 10^{-6}$	-2.6×10^{-6}	-4.0×10^{-6}
41D, w/ counter term	-0.3×10^{-6}	$(-7.8 \pm 5.0) \times 10^{-6}$	-2.3×10^{-6}	-2.0×10^{-6}
11D, w/o counter term	-0.3×10^{-6}	-0.9×10^{-6}	-4.8×10^{-6}	-5.1×10^{-6}
21D, w/o counter term	$+0.1 \times 10^{-6}$	-0.2×10^{-6}	-2.7×10^{-6}	-4.8×10^{-6}
41D, w/o counter term	-0.2×10^{-6}	-3.0×10^{-6}	-3.0×10^{-6}	-2.8×10^{-6}

Table 4.3.: Difference of coupled and uncoupled bath ground state energy (in a.u.) for the low cutoff bath. Values in the respective left columns calculated from the global groundstate peak, values in the right columns as an extrapolation from the shift of the maximum bath frequency to all bath HOs.

evenly upon coupling to the system, except for the exceptionally strongly driven resonant one. The numbers show that this simplistic picture holds only for the smallest bath size, where the resonant bath HO really stands out. For the low-frequency bath in Tab. 4.3, a straightforward linear fit is again not advisable because, apart from the bath oscillator with highest frequency, the frequency shift of individual modes is smaller than the frequency resolution. Instead, we assume that all bath oscillators are shifted by the same percentage and simply multiply the uncoupled groundstate energy by the relative change of the highest frequency mode. The bath size dependent error estimate stated in the table is then the deviation caused by shifting this peak by one grid point. For small coupling, this overestimates the redshift; for large coupling, the highest frequency does not stand out as much any more and agreement is rather good, especially as the bath size approaches a continuum.

With these considerations on the bath redshift, we end the chapter on Morse oscillators embedded in CL baths. We have used this model system first to demonstrate the reliability of our method for small systems by comparison to full quantum results and second to shed some light onto the role of the counter term for the frequency shift of the system. The next chapter will see some applications of the semiclassical hybrid dynamics scheme to an iodine molecule embedded into an experimentally studied environment, namely, a matrix of krypton atoms.

5. MOLECULAR IODINE IN A KRYPTON ENVIRONMENT

The investigations in the last chapter have shown that the hybrid approach to semiclassical IVRs is a powerful tool for the description of system-bath problems with a large number of environmental DOFs. One might, however, argue that these results are not exactly surprising as the very nature of the CL model system mirrors the approximations made to derive the hybrid dynamics. Therefore, we will now proceed with a system with neither harmonic bath DOFs nor linear system-bath coupling by investigating again molecular iodine, but this time embedded in a krypton matrix. In general, experiments focusing on molecular dynamics in condensed phases are an important test for theoretical methods because they can be modeled efficiently in a system-bath description. The environment typically consists of rare gas clusters, solids or liquids [100–102]. More specifically, halogens in a rare gas environment have been the object of intense experimental study [80, 100, 101, 103–108]. For the vibrational dynamics of iodine in a krypton environment, dissipation and the loss of coherence have been investigated in detail by the group of Ara Apkarian [80, 101, 106, 108]. On the theoretical side, various quantum-classical and semiclassical approaches have been employed to model these systems and reproduce experimental results [66, 109–112].

Two questions will be addressed in this chapter. First, we will make use of the reduced density hybrid formalism introduced in Sec. 3.1 to describe the decay of vibrational coherence in a temperature dependent bath. In the second part, the focus will be on the influence of this non-harmonic bath on the iodine spectrum.

5.1. DECOHERENCE

The vibrational decoherence of an iodine molecule in its electronic ground state embedded in a krypton environment has been studied with time-resolved coherent anti-Stokes Raman spectroscopy (TRCARS) experiments in the group of Ara Apkarian [80, 106]. Temperature and initial state dependent rates for the loss of coherence have been determined. These rates could be reproduced theoretically with very good agreement using a mixed quantum-classical Liouville method [110, 111]. Given that analytical potentials are available for all interactions in this system, it is also suitable for an efficient semiclassical description. We will first set up a reduced model for iodine in its first solvation shell, then we will investigate vibrational decoherence using both semiclassical hybrid and full quantum calculations.

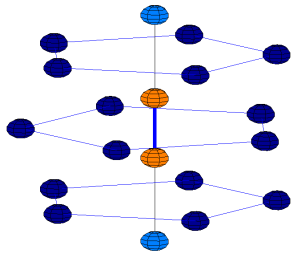

Figure 5.1.: Iodine molecule (orange) embedded in a D_{5h} symmetric cluster of krypton atoms (blue). Blue lines to help comprehension of spatial relations with two krypton atoms on the iodine molecular axis (light blue) and three five-rings centered at this axis.

interaction	D_e [a.u.]	s_e [a.u.]	α [a.u.]
I-I	0.057	5.0	0.99
I-Kr (Σ)	0.0013	7.1	0.79
I-Kr (Π)	0.00057	8.1	0.81

interaction	ϵ [a.u.]	σ [a.u.]
Kr-Kr	0.00063	6.8

Table 5.1.: Potential parameters taken from [109], with the value for ϵ of the Kr-Kr interaction corrected according to [103].

5.1.1. MODEL

The experimental results in [106] have been obtained for iodine in a cryogenic matrix environment with a ratio of one iodine molecule in several thousand krypton atoms, which is beyond the scope of an explicit semiclassical description. As shown in Fig. 5.1, our model will comprise only the first microsolvation shell which is a cluster of 17 krypton atoms surrounding the molecule in the form of a double-icosahedron. In terms of symmetry, this object belongs to the D_{5h} point group and thus differs from the matrix symmetry of the experimental system. We will address this difference in Sec. 5.2, where changes in the iodine spectrum are investigated. The reduced cluster model is obviously much easier to handle numerically, but there is another fundamental difference compared to a matrix environment: Since two of the krypton atoms are aligned with the iodine molecular axis, energy dissipation from the molecular vibration can cause the krypton atoms to dissociate from the cluster, thereby in principle giving rise to an observable that is directly related to the system-bath coupling. This is, however, more relevant for the vibrational dynamics of electronically excited iodine, which has also been studied in [37, 66].

In our explicit treatment of the model system, we have to account for all atom-atom interactions . For reasons of simplicity, the cluster potential is approximated as a sum over all pair potentials,

$$V = \sum_{J>K=1}^{N_{\text{atoms}}} V_{KJ}, \tag{5.1}$$

where capital letters are used to designate atom indices and $N_{\text{atoms}} = 19$ is the total number of atoms, and the iodine atoms will always be labeled as 1 and 2. As there are three different kinds of atomic interactions, we take three different pair potentials, with parameters given in Tab. 5.1. As an aside, we note that the iodine potential parameters are a little different from

the ones in Ch. 4, which were taken from a different reference. We also take a more accurate value for the iodine atomic mass, $m_\mathrm{I} = 231323$ a.u., and the krypton mass is $m_\mathrm{I} = 152757$ a.u.

The I-I interaction is a Morse potential according to Eq. (3.52) with parameters corresponding to iodine in its electronic ground state. For the I_2-Kr interaction, we are using a diatomics-in-molecules (DIM) approach [113, 114] that superimposes Σ and Π potentials

$$\begin{aligned} V_{\mathrm{I_2-Kr}} = \sum_{J=3}^{N_\mathrm{atoms}} & \cos^2(\theta_{1,J})\, V_\Sigma(R_{1,J}) + \sin^2(\theta_{1,J})\, V_\Pi(R_{1,J}) \\ & + \cos^2(\theta_{2,J})\, V_\Sigma(R_{2,J}) + \sin^2(\theta_{2,J})\, V_\Pi(R_{2,J}), \end{aligned} \tag{5.2}$$

where θ_{KJ} is the angle between the iodine molecular axis (depicted as a thick blue line in Fig. 5.1) and the vector connecting Kth iodine and Jth krypton atom, and V_Σ and V_Π are assumed to be of Morse form. Instead of this superposition, one might have taken a simple Lennard-Jones potential [110] here, but it has turned out that it is advantageous especially for spectral calculations to use this anisotropic form [69]. The Kr-Kr van der Waals interaction between atom K and atom J is modeled by a Lennard-Jones potential [115]

$$V_{\mathrm{Kr-Kr}}(R_{KJ}) = 4\epsilon\left(\frac{\sigma^{12}}{R_{KJ}^{12}} - \frac{\sigma^6}{R_{KJ}^6}\right), \tag{5.3}$$

where ϵ is the well depth and σ is the intersection of the potential with the horizontal axis.

The specific form of the iodine cluster in Fig. 5.1 arises from a geometry optimization. Using the above potentials, the minimum energy becomes -0.1034 a.u., which is slightly above the sum of I-I interaction and the 20 I-Kr as well as 45 Kr-Kr nearest-neighbor interactions at -0.0992 a.u. With 19 atoms, the I_2Kr_{17} has 51 internal DOFs; in order to make an informed selection especially for full quantum calculations, we perform a normal mode transformation [116]. The normal coordinates Q_i are related to mass-weighted Cartesian displacement coordinates

$$\tilde{q}_k = \sqrt{m_k}(x_k - x_{k,\mathrm{e}}) \tag{5.4}$$

by a linear transformation

$$Q_i = \sum_{k=1}^{3N_\mathrm{a}} l_{ik}\tilde{q}_k \tag{5.5}$$

where the lower-case characters in the indices of the two above equations now designate DOFs rather than atoms with m_k being the mass of the atom corresponding to the kth DOF. The matrix elements l_{ik} comprise the normalized eigenvectors of the Hessian of the potential from Eq. (5.2). The normal modes in this study are slightly modified with respect to the exact ones. All mixed second derivatives containing derivatives with respect to the position of either atom along the iodine molecular axis are set equal to zero in the Hessian matrix. Thus, we obtain symmetric stretching modes of iodine and of the two axial krypton atoms that have nonzero entries for the respective two atoms only. This allows for dissociation of the two outer krypton atoms from the cluster while the others remain attached, as discussed briefly above.

As an aside, we note that this normal coordinate description necessitates a transformation to Cartesian coordinates at every propagation step of the classical trajectories. This increases the numerical effort of semiclassical calculations especially due to the much more costly potential derivatives, as explained in App. E. The grid-based quantum calculation, on the other hand,

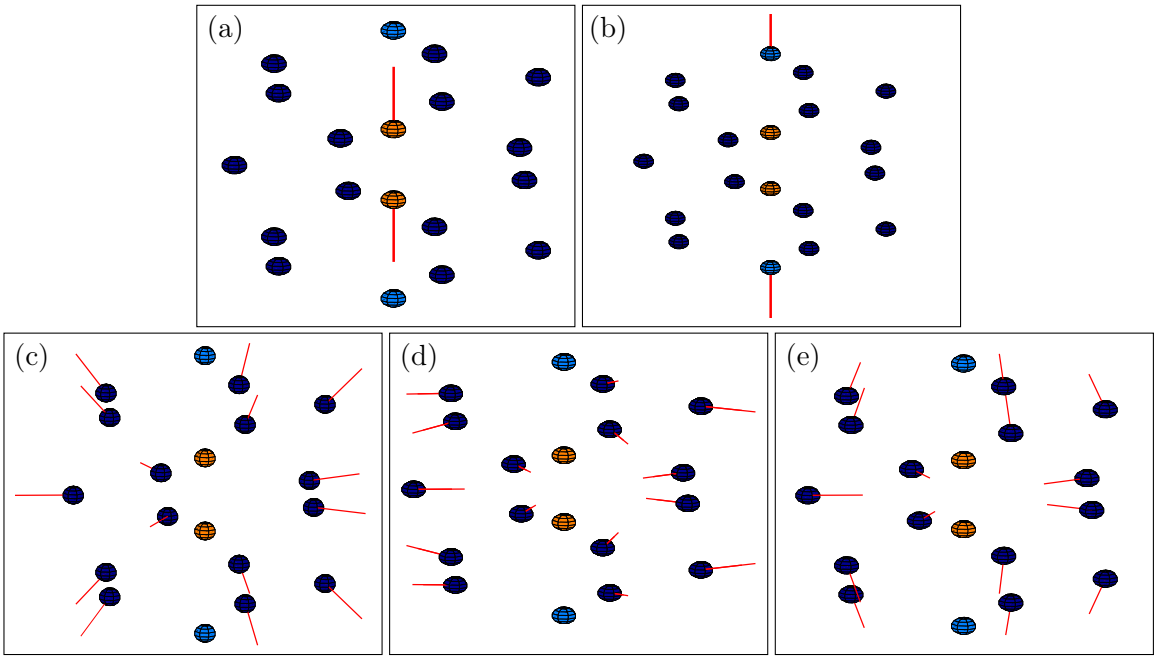

Figure 5.2.: The five totally symmetric normal modes that constitute the A_{1g} representation of the D_{5h} point group are (a) iodine vibration, (b) axial Kr vibration, (c) balloon mode, (d) hourglass mode, and (e) rugby ball mode.

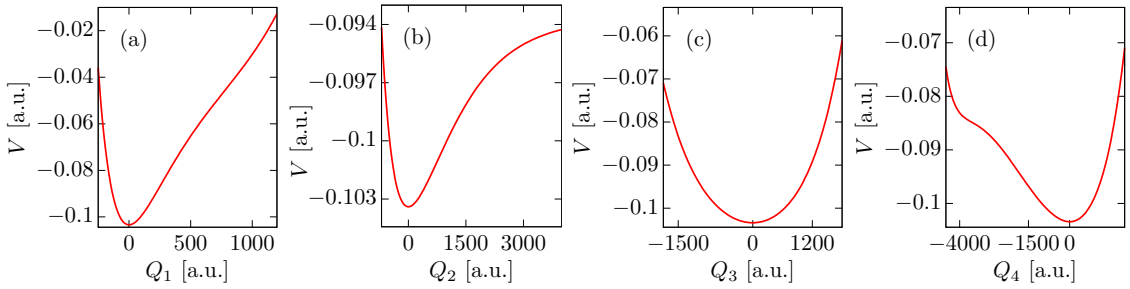

Figure 5.3.: 1D potential energy cuts of the four most strongly coupled, totally symmetric normal modes. From left to right, they are (a) iodine vibration, (b) axial Kr vibration, (c) hourglass mode, and (d) rugby ball mode.

does not suffer from this limitation because it requires the potential calculation only once at the very beginning of the propagation.

To perform full quantum calculations, we have to utilize a reduced model that contains just four DOFs at most. Therefore, we first take into account only totally symmetric bath normal coordinates because those modes are most strongly coupled to the system consisting of the totally symmetric iodine vibration. Apart from the two stretching modes of the axial iodine and krypton atoms, there are three more such modes which are referred to as “balloon”, “hour glass” and “rugby ball” mode; all five are depicted in Fig. 5.2. While the iodine frequency is separated from the highest bath frequencies by a factor of five, the totally symmetric bath modes are ranked between 16th and 35th highest frequency. In harmonic approximation, the oscillation periods of these bath modes are between 1100 and 1500 fs, or about seven to ten times as large as the approximately 150 fs period of the harmonic approximation to the system

potential. The bath mode with strongest coupling to the iodine system is the axial krypton stretch. The weakest of the three remaining totally symmetric ones is the balloon mode, which will therefore be omitted from the full quantum calculations.

Figure 5.3 shows 1D potential cuts for the system as well as the three bath modes. As requested, the axial krypton mode has a dissociative side. By contrast, the other two bath modes always have some krypton atoms approaching each other regardless of the sign of these modes and therefore always behave repulsively. The iodine dissociation is hindered due to the presence of the axial krypton atoms, which makes the potential take on a form that is reminiscent of modification caused by the CL counter term in Ch. 4. Indeed, the effect on the spectrum is similar, as will be discussed in the next section.

By identifying the four most important normal modes, we have reduced the complexity of the problem in a way that quantum dynamical calculations become feasible. We can now create a hierarchy of models by adding these bath modes one by one. As an aside, we note that some of these normal modes show a close resemblance to those obtained elsewhere for dihalogens in a rare gas matrix [114].

5.1.2. DECOHERENCE DEPENDENCE ON TEMPERATURE AND INITIAL STATE

We will now investigate the properties of the reduced description by calculating rates for the loss of coherence and compare them to experimental results [106]. This has been done before to good accuracy with mixed quantum-classical approaches [110, 111]. In this section, we will use only full quantum results, which have been obtained with the WavePacket software [90, 91] utilizing the split-operator method with Strang splitting [117, 118].

INITIAL STATES

The quantities of interest are the purity $P(t)$ and especially the vibrational coherence $\Pi_{ij}(t)$ as introduced in Ch. 3, because the latter is closely related to the experimentally measured quantity [110, 111]. Like in the section on open systems and the reduced density, system and bath are assumed to be initially in a product state

$$|\Phi(0)\rangle = |\Psi_\mathrm{s}(0)\rangle\,|\Psi_\mathrm{b}(0)\rangle\,, \tag{5.6}$$

where the bath part will comprise at most three modes in the full quantum calculations. The initial state of the iodine stretch system mode will be constructed as a superposition of either two Gaussians (a "Schrödinger Cat" state in the language of W. H. Zurek [119]) or two numerically calculated eigenstates of the iodine mode in the rigid Kr cage. Again, the latter setup allows for a comparison with experimental and earlier theoretical results, where rates for the loss of vibrational coherence $\Pi_{0n}(t)$ have been determined for system superpositions including the vibrational ground state $|0\rangle_\mathrm{s}$ as well as an excited eigenstate $|n\rangle_\mathrm{s}$ to eigenenergy $E_{\mathrm{s},n}$.

Although an arbitrary initial state such as $|n\rangle_\mathrm{s}$ can be decomposed in terms of Gaussians [120] to a given accuracy, thus allowing for a semiclassical treatment, this decomposition would strongly increase the numerical effort for such a calculation, especially in a reduced density formalism where the number of contributions grows with the square of terms in $|\Psi_\mathrm{s}\rangle$. Instead, we will be using the aforementioned cat state for the semiclassical calculations in the next subsection, which has just two contributions,

$$|\Psi_\mathrm{s}(0)\rangle = \frac{1}{\sqrt{2}}\left\{1+\mathrm{e}^{-\left(P_{\mathrm{s},\alpha}-P_{\mathrm{s},\alpha'}\right)^2/(4\gamma_\mathrm{s})}\cos\left[Q_\mathrm{s}\left(P_{\mathrm{s},\alpha}-P_{\mathrm{s},\alpha'}\right)\right]\right\}^{-1/2}\left(|\Psi_{\mathrm{s},\alpha}\rangle+\left|\Psi_{\mathrm{s},\alpha'}\right\rangle\right). \tag{5.7}$$

Both initial Gaussians are centered at the system potential minimum, $Q_\mathrm{s} = 0$. In the same manner as in the previous chapter, initial momenta are chosen as $P_{\mathrm{s},\alpha} = 0$ and $P_{\mathrm{s},\alpha'} = \sqrt{2E_{\mathrm{s},n}}$ such that one Gaussian corresponds to the vibrational ground state and the other one is centered at the energy of the nth eigenstate. As before, the width parameter of both Gaussians is $\gamma_\mathrm{s} = \omega_\mathrm{s}$ ($m_\mathrm{s} = 1$ in normal coordinates), with ω_s the eigenfrequency of the iodine stretching mode, making $\gamma_\mathrm{s} = 22.29$ a.u. We will couple this initial state to a thermal bath, propagate it with the semiclassical reduced density formalism and compare the resulting purity to full quantum results in the next subsection.

FULL QUANTUM CALCULATIONS

While we could describe the temperature dependent bath by the thermal density operator in the semiclassical calculations, we introduce finite bath temperature into the full quantum calculations by expressing the contributions to the density matrix as a thermal average over a number of independently propagated wave packets $|\Phi_n(t)\rangle$,

$$\hat{\rho}(t) = \frac{1}{Z_\mathrm{b}} \sum_n \mathrm{e}^{-\beta E_{\mathrm{b},n}} \, |\Phi_n(t)\rangle \, \langle\Phi_n(t)| \,, \tag{5.8}$$

where the initial states are $|\Phi_n(0)\rangle = |\Psi_\mathrm{s}(0)\rangle \, |n\rangle$, with $|n\rangle$ an (approximate) eigenstate of the bath with energy $E_{\mathrm{b},n}$. As explained in detail in App. B, we assume small system-bath coupling such that the bath modes are sufficiently weakly excited that they stay in the approximately harmonic region close to their respective potential minima. Then, we can choose the initial bath states as eigenstates of harmonic oscillators with frequencies corresponding to the eigenfrequencies found in the harmonic analysis. With an initial superposition of the vibrational ground state and one excited state in the iodine coordinate,

$$|\Psi_\mathrm{s}(0)\rangle = \frac{1}{\sqrt{2}} \left(|0\rangle_\mathrm{s} + |n\rangle_\mathrm{s} \right) , \tag{5.9}$$

the reduced density matrix at the beginning of the propagation becomes

$$\hat{\rho}_\mathrm{s}(0) = \frac{1}{2} \left(|0\rangle_\mathrm{s} \langle 0|_\mathrm{s} + |0\rangle_\mathrm{s} \langle n|_\mathrm{s} + |n\rangle_\mathrm{s} \langle 0|_\mathrm{s} + |n\rangle_\mathrm{s} \langle n|_\mathrm{s} \right) , \tag{5.10}$$

which makes the initial value of our quantity of interest $\Pi_{0n}(0) = |\, \langle 0|\hat{\rho}_\mathrm{s}(0)|n\rangle \,| = 0.5$.

For keeping computational times low, we first chose a setup with $T = 45$ K and $n = 20$ to get a strong decay of coherence already after a short propagation time. Capitalizing on the properties of the hierarchical model, we can now add one bath mode at a time to demonstrate that the growing number of channels indeed increases decoherence. The axial krypton stretch Q_2 is most strongly coupled to the iodine system in the sense that decoherence is faster than in any other calculation with a single bath DOF, so we add this one first. Figure 5.4 shows how $\Pi_{0n}(t)$ oscillates in time with a period of about 1170 fs, which corresponds to the harmonic approximation of the bath DOF (1102 fs). We also see that the maximum amplitudes decrease exponentially. This decay is accelerated if a second bath mode, Q_3, is added to the calculation. With yet another bath normal coordinate, the rugby ball mode Q_4, the decrease is further enhanced, with the coherence minima in between peaks coming close to zero, and the oscillation period doubles. This last change might be due to the fact the rugby ball mode has a larger harmonic period, namely, 1513 fs, than the other two bath modes which are pretty close in that respect. We can conclude that the number of bath modes in the simulation is crucial for

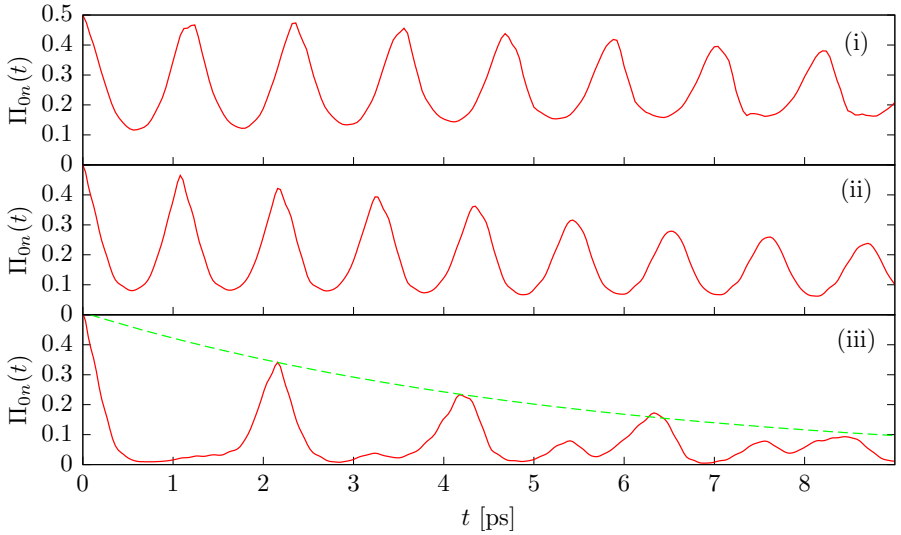

Figure 5.4.: Vibrational coherence of system mode Q_1 for iodine embedded in a krypton environment depending on bath size. Solid red lines: bath comprising one DOF in (i), two DOFs in (ii) and three DOFs in (iii) at $T = 45$ K and initial system excitation $n = 20$. Dashed green line: exponential decay fitted to local maxima of the coherence.

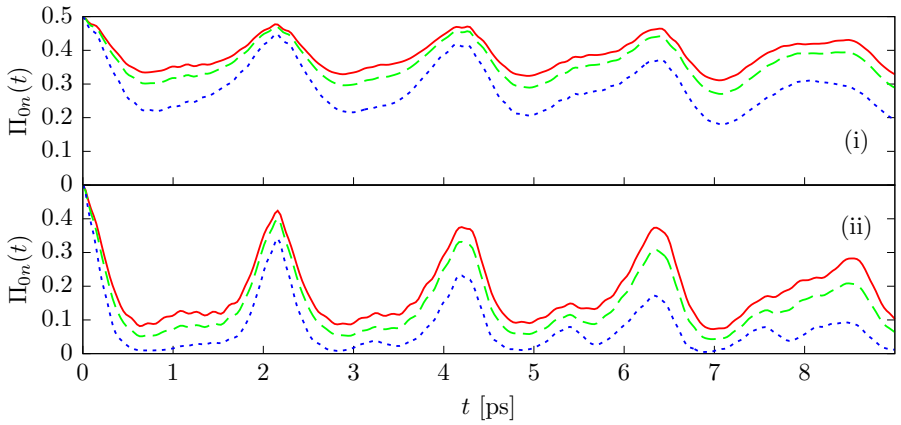

Figure 5.5.: Vibrational coherence of system mode Q_1 for iodine embedded in a krypton environment depending on initial system state. Four DOFs calculations with bath temperature $T = 10$ K (red solid line), $T = 20$ K (green dashed), and $T = 45$ K (blue dotted). The excited initial state is $n = 10$ in (i) and $n = 20$ in (ii).

the coherence decay. We will therefore use these 4 DOF calculations for the comparison to experimental results. With 128 grid points for the iodine vibration and either 16 or 32 grid points for each bath DOF, the memory requirement is such that computations can still be performed on a standard desktop computer. The time step for the split operator formalism is 1 fs.

The dependence of the coherence on initial states and bath temperatures is demonstrated by the results in Fig. 5.5. Initially, the system is in the same superposition of ground and excited vibrational eigenstate as before, with excited indices $n = 10$ and $n = 20$. The bath temperature varies between $T = 10$ K, $T = 20$ K and $T = 45$ K. Like in the experiment, both higher initial energy of the system and higher bath temperature result in a faster loss of coherence.

T [K]	45		20		10		
n	10	20	10	20	10	15	20
$\Gamma_{0n,\mathrm{exp}}$ [ps^{-1}]	0.100	0.34	0.040	0.10	0.029	0.044	0.060
$\Gamma_{0n,\mathrm{sim}}$ [ps^{-1}]	0.053	0.18	0.025	0.09	0.015	0.032	0.059

Table 5.2.: Dependence of vibrational coherence loss rates Γ_{0n} on initial excited system state and bath temperature. Experimental results from fits in [106], numerical results from 4D full quantum calculations.

In order to check if there is not only qualitative, but also quantitative agreement between experimental and numerical results, we have fitted the peaks in Fig. 5.5 with an exponential decay, $\Pi_{0n}(t) \sim \mathrm{e}^{-\Gamma_{0n}t}$ (see Fig. 5.4), which is the experimentally observed behavior. Results are collected in Tab. 5.2. Despite the simplicity of our model, which takes into account only the first solvation shell of krypton atoms, and despite the reduced description with a "bath" composed of three normal modes, we see that the decoherence rates extracted from our model are even quantitatively pretty close to the experimental ones. Two trends can be observed, namely, a systematic underestimation of these rates and an improvement towards high system initial energy and low bath temperature. Aside from the limited number of bath modes, the underestimation especially for high temperature can be assigned to our way of modeling the temperature dependence of the bath. At 45 K, the harmonicity assumption for the highest-lying bath eigenstates might be called into question, and, more importantly, the number of bath eigenstates with significant weight $\mathrm{e}^{-\beta E_{\mathrm{b},k}}$ gets so large that not all contributions can be taken into account. In addition, these neglected contributions are those with highest initial energy. For an initial state of the system with $n = 20$, one can clearly see the temperature influence on the accuracy of the result. At $T = 10$ K, the numerical result for the decoherence rate agrees almost exactly with the experimental one. In this case, we can consider a sufficient number m of bath initial states such that their summed-up weights come close to the exact bath partition function, $\sum_{k=1}^{m} \mathrm{e}^{-\beta E_{\mathrm{b},k}} / \sum_{k=1}^{\infty} \mathrm{e}^{-\beta E_{\mathrm{b},k}} \lesssim 1$. For $T = 45$ K, on the other hand, an initial bath comprising $m = 30$ eigenstates makes this fraction just 0.85 and consequently, the numerical rate is only half as big as the experimental one. From a numerical point of view, the necessity to cut short the initial bath arises not only from the sheer number of contributions, but also because higher bath excitations would require a larger grid for an appropriate representation of these states.

Having established the qualitative and surprisingly high quantitative agreement of our simple model with experimental and numerical results obtained with a larger number of bath atoms, we will now compare the coherence between selected elements of the reduced density matrix to the purity, which can be obtained more easily from the semiclassical reduced density formalism, as shown in Sec. 3.1.1. In Fig. 5.6, we have plotted the two quantities, multiplying the coherence by a factor of two to improve comparability. Not surprisingly, we find a close qualitative resemblance and, notably for weak decoherence, even quantitatively similar behavior. Decay rates are somewhat different, and the purity does not decay towards zero but towards a finite constant value, as discussed above. For this example, it can be concluded that the loss of vibrational coherence between the states forming the initial superposition corresponds to a more general loss of quantum character in general.

Finally, we investigate the influence of the shape of the initial superposition on the subsequent dynamics in Fig. 5.7. We compare the superimposed eigenstates from the previous calculations to the simpler "cat state" from Eq. (5.7), which is composed of two Gaussians. One Gaussian

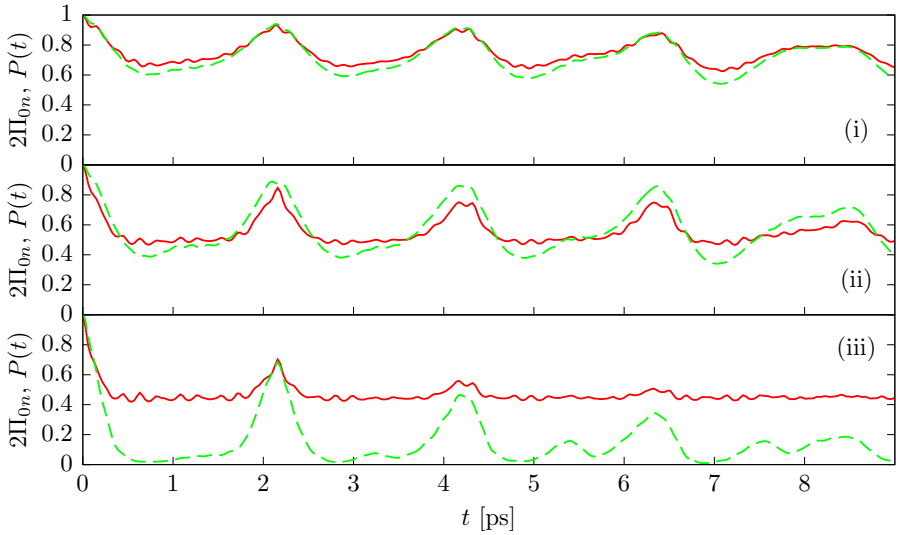

Figure 5.6.: Purity (solid red lines) vs. vibrational coherence (dashed green lines) of the iodine vibration in a krypton environment from 4 DOF quantum calculations with (i) $n = 10$, $T = 20$ K, (ii) $n = 15$, $T = 10$ K, and (iii) $n = 20$, $T = 45$ K.

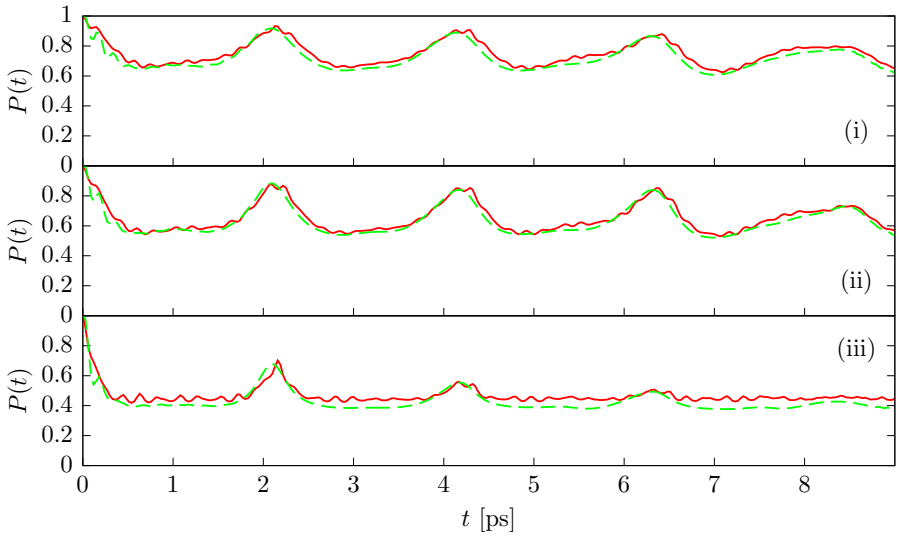

Figure 5.7.: The purity of the iodine vibration in a krypton environment for initial eigenstates (solid red lines) and initial Gaussians (dashed green lines) in the system coordinate. All temperatures and excited state indices as in Fig. 5.6.

is placed at the potential minimum with zero momentum initially, the other one has nonzero momentum such that its energy is identical to the ones of the respective excited eigenstates. Thus having changed only the form but not the energy of the initial states, we see almost identical results for the dynamics of the purity. The same period of the purity oscillations points at an overall identical bath dynamics, with some additional oscillations on top for the setup with initial eigenstates due to the higher complexity of this state. As the initial energy of the system is the obvious main factor contributing to the decoherence rate, we will now use the simpler initial Gaussians for semiclassical calculations. With these, we enable the incorporation

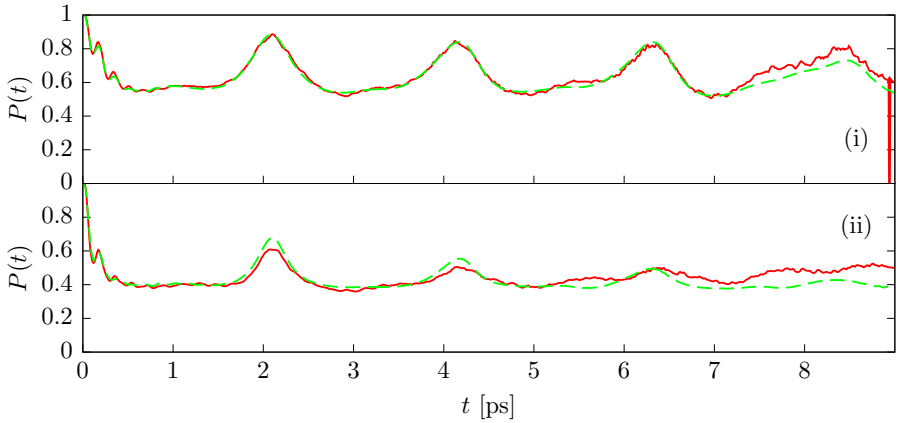

Figure 5.8.: Semiclassical (solid red lines) and full quantum (dashed green) results for the purity of the iodine vibration in a krypton bath for $T = 10$ K, $n = 15$ (top) and $T = 45$ K, $n = 20$ (bottom) from four DOF calculations (cf. Fig. 5.7).

of more bath DOFs, which will in particular show the effect of the non-symmetric bath DOFs that have been neglected so far.

SEMICLASSICAL CALCULATIONS

The first important question in any discussion of semiclassical results is of course their reliability with respect to full quantum results. Therefore, we take the initial cat like superposition of two Gaussians discussed in the previous section, and compare results obtained with the respective methods for different initial excited states and bath temperatures. This last parameter is quite interesting because of the two different approaches to the description of finite bath temperature. Figure 5.8 shows the outcome of calculations with initial conditions $T = 10$ K, $n = 15$ and $T = 45$ K, $n = 20$, respectively, where the same three bath DOFs are used as before. 10^5 classical trajectories have been run to converge the semiclassical hybrid expression for the reduced density from Eq. (3.18). Since SC-HD does not exactly conserve the norm of the reduced density, all semiclassical results have been renormalized.

For the case of low bath temperature and slow decoherence in subfigure (i), we see very good agreement until about seven picoseconds. For longer times, the result is not well converged yet and could be improved with more trajectories. For the high bath temperature case in subfigure (ii), the deviations with time become more apparent. While the higher initial energy of the overall system and the ensuing more complex dynamics, which necessitates a more meticulous phase space sampling, give rise to this long-times difference between semiclassical and quantum result, we also find that the well-converged first two semiclassical peaks are smaller than their quantum counterparts. This discrepancy shows the effect of the approximate temperature description in the quantum case. It can be understood if we recall the thermal average from Eq. (5.8) and the fact that we use only a limited number of contributions in the numerical quantum calculations. As discussed before, this means that bath eigenstates with the highest energies are neglected. The cumulated weight of these neglected states gets higher with temperature, leading to an underestimation of the effect of the bath on the decoherence dynamics, as seen by the comparison to experimental results in the previous section. The semiclassical result, which incorporates finite bath temperature more accurately via the thermal density operator, corroborates the validity of this explanation by displaying faster decoherence for the high

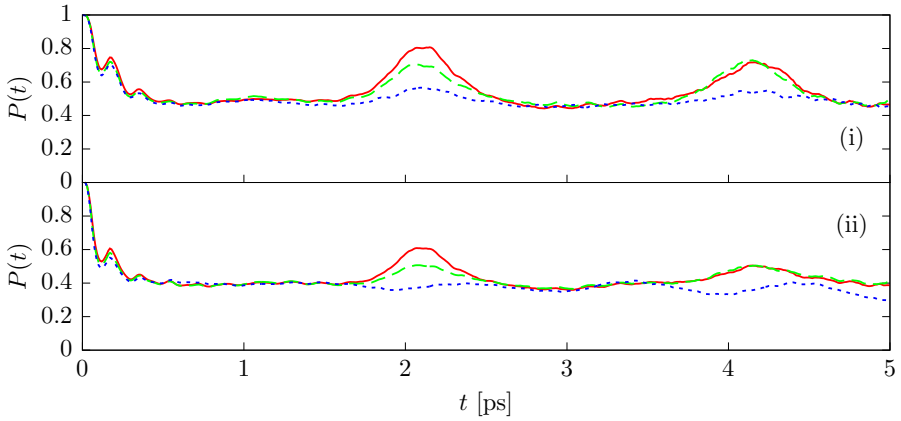

Figure 5.9.: Semiclassical results for the purity of the iodine vibration in a krypton bath with three (solid red line), four (dashed green) and 50 DOFs (dotted blue) for $n = 20$ and (i) $T = 10$ K and (ii) $T = 45$ K.

temperature case. For low temperature, where no significant percentage of bath eigenstates is neglected in the quantum calculations, the results are identical. We should emphasize once again the different setup in terms of quantity of interest and initial states compared to the calculations that lead to the decoherence rates. We can, however, infer from the comparisons in Figs. 5.6 and 5.7 that the findings from the cat state propagation are applicable also to the earlier situation.

The second factor that impacts the coherence loss rates from the quantum calculations is the limited number of bath DOFs. For the example with $T = 45$ K, $n = 20$, we have seen in Fig. 5.4 that decoherence gets much faster as the number of bath DOFs increases from one to three: fitting the result with one bath DOF exponentially, the resulting decay rate is 0.035 ps^{-1} and thus much lower than the 0.18 ps^{-1} from the case with three bath DOFs. We have therefore assumed in the previous section that the use of further bath DOFs might improve the agreement with experimental results. Since the semiclassical method allows for the use of more than four normal modes, we perform calculations with all five totally symmetric modes as well as with all 51 internal DOFs in order to find out how these incremental changes influence the purity. Choosing the initial system excitation as $n = 20$ and bath temperatures $T = 10$ K and $T = 45$ K, we look at one case with almost perfect agreement and one with a clear underestimation of the experimental result in order to get an idea if the solvation shell model converges towards the exact results or if especially the very good quantitative agreement of some quantum results is likely to be a coincidence due to the specific setup of these calculations.

Results obtained with 10^5 trajectories are presented in Fig. 5.9. The propagation time is now restricted to five picoseconds, which is approximately the point where the first sizable deviations from the quantum result appear, because the numerical effort becomes formidable especially if all vibrational modes are included[1]. For the low-temperature case in subfigure (i), we can see how the amplitudes of the purity oscillations are increasingly suppressed if first the fifth totally symmetric (green dashed line) and then the remaining vibrational bath modes (blue dotted line) are included. Considering that adding only one DOF to the original four DOFs calculation already has about half the effect on the first peak as the addition of

[1] A normal mode calculation with 51 DOFs takes about one hour of single core computational time per twenty trajectories, thus requiring a few thousand hours to achieve convergence.

the remaining 46 DOFs, the importance of the totally symmetric bath modes becomes very apparent. This is corroborated by the fact that the oscillation period of the purity remains the same regardless if only the three most strongly coupled normal modes or all 50 vibrational bath DOFs are included. By contrast, the second peak shows that the response of the bath modes, which are much slower than the system vibration, becomes important at later times, and that the remaining bath modes thus play a decisive role in the long-time dynamics.

The high-temperature case in subfigure (ii) displays a very similar behavior for the simulation with five DOFs. Again, the first peak is significantly reduced while the second one seems almost unaffected. Adding all internal DOFs, on the other hand, has very drastic consequences. Here, the dominating oscillations after about two and four picoseconds have disappeared completely and the purity stays close its minimum value around 0.4 throughout. We can thus conclude that with increasing temperature, which corresponds to higher initial excitation of all bath DOFs, the bath DOFs with a different symmetry become more relevant for the system dynamics. In that case, the reduced description comprising the totally symmetric bath DOFs only is no longer able to reproduce the details of the dynamics.

With these semiclassical considerations, we close the section on the purity and coherence calculations. We have seen that a simplified model consisting of iodine in its first solvation shell of 17 krypton atoms yields qualitative and sometimes even quantitative agreement with experimental results for coherence loss rates, even if only the most important bath vibrational coordinates are used in full quantum calculations. The semiclassical calculations, allowing for inclusion of all vibrational bath DOFs, have demonstrated the limitations of the temperature description in the quantum case as well as the importance of the non-symmetry preserving bath DOFs especially for high temperature.

5.2. IODINE SPECTRUM

Having discussed the dynamics of decoherence in the first part of this chapter, we now turn to a question that has already been asked in Ch. 4, namely, the shift of the iodine vibrational spectrum by the krypton environment. Unlike in the case of a CL bath, the bath modes are not harmonic and the system-bath coupling is no longer linear, giving rise to a dynamics that is potentially more challenging for a treatment with the semiclassical hybrid method.

We will first summarize arguments concerning the setup of an appropriate bath geometry from a vibrational self-consistent field study on iodine in an argon environment [69]. With the help of these considerations, we can then find an appropriate model for the krypton environment and perform numerical calculations again for a selection of bath modes only.

MODEL: IODINE IN A KRYPTON MATRIX

As shown in a closely related investigation of iodine in an argon matrix [69], there are two important caveats when it comes to spectral calculations of halogens in a rare gas matrix. First, it has been demonstrated that the halogen-rare gas interaction potential is essential in order to get the bond softening of the molecule that leads to the experimentally observed redshift. While an anisotropic interaction like in Eq. (5.2) yields an even quantitatively accurate frequency shift for iodine in argon [69], other (simpler) analytic interactions result in no shift at all or even a blueshift of the iodine frequencies. For this reason, we stick to the anisotropic interaction, whose sine and cosine terms make for a cumbersome calculation of first and in particular second potential derivatives. The krypton-krypton interaction is also the same as in Tab. 5.1, but we take a different set of Morse parameters for the iodine molecule due to a higher

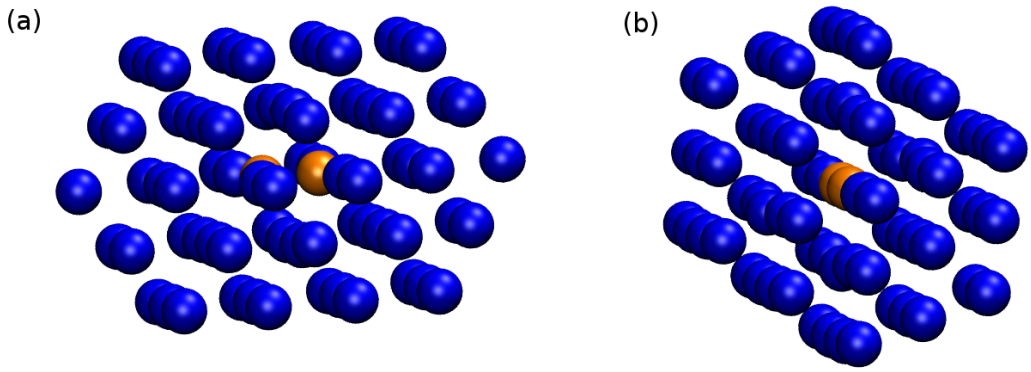

Figure 5.10.: Iodine molecule (orange) embedded in a D_{2h} symmetric matrix of 72 krypton atoms (blue). The outermost layer of fixed krypton atoms is not shown for reasons of visibility. The two pictures have been made with the Visual Molecular Dynamics (VMD) program package [121, 122].

accuracy close to the ground state energy, namely, $D_e = 0.083641$ a.u., $\alpha = 0.81282$ a.u., and $s_e = 5.038$ a.u. [69].

The second important point is the choice of a matrix rather than a cluster environment to reproduce the rare gas geometry faithfully, and in particular the use of a sufficient number of layers around the host molecule. For iodine in argon, four such layers were necessary for convergence with respect to the iodine frequency shift, corresponding to 448 argon atoms. Of these, however, only the two inner shells were taken to be mobile, while the two outer layers were fixed during the propagation; this choice of boundary conditions is called Dynamical Cell with Rigid Walls by the authors of [69]. We will use the same approach, but restrict the environment to just three layers with 218 atoms for the classical geometry optimization, where the outermost is fixed and the two inner ones, comprising 72 krypton atoms, are mobile. The iodine molecule is placed inside the face-centered cubic (fcc) krypton lattice by replacing two nearest-neighbor atoms. Then, we perform a geometry optimization for the iodine as well as the mobile krypton atoms, while the outer, fixed krypton atoms serve as containment. The minimum energy geometry is presented from two perspectives in Fig. 5.10, where iodine atoms are orange and the flexible krypton atoms are blue. As a result, only few atoms from the innermost shell are notably shifted, such that the D_{2h} symmetry of the original matrix is retained. For the semiclassical calculations, we use the two krypton layers shown in Fig. 5.10, and we now take only the 18 krypton atoms from the innermost layer to be mobile. Consequently, the normal mode analysis, which we perform with the MolDynSim code from the TrajLab software [123], includes a total of 20 mobile atoms and yields 8 totally symmetric normal modes. With the iodine vibration being one of these normal modes, we will once again put a special emphasis onto these most strongly coupled bath coordinates.

AN OVER-SIMPLIFIED APPROACH: IODINE IN A KRYPTON CLUSTER

Before we take on the krypton matrix environment calculations, we will show that the solvation shell approach from the first part of this chapter is not suitable to reproduce experimental results for the frequency shift correctly. To this end, we use the same geometry as in Fig. 5.1 as a basis for a geometry optimization with updated parameters for the iodine intramolecular interaction. This time, the normal mode analysis is performed without any modification and

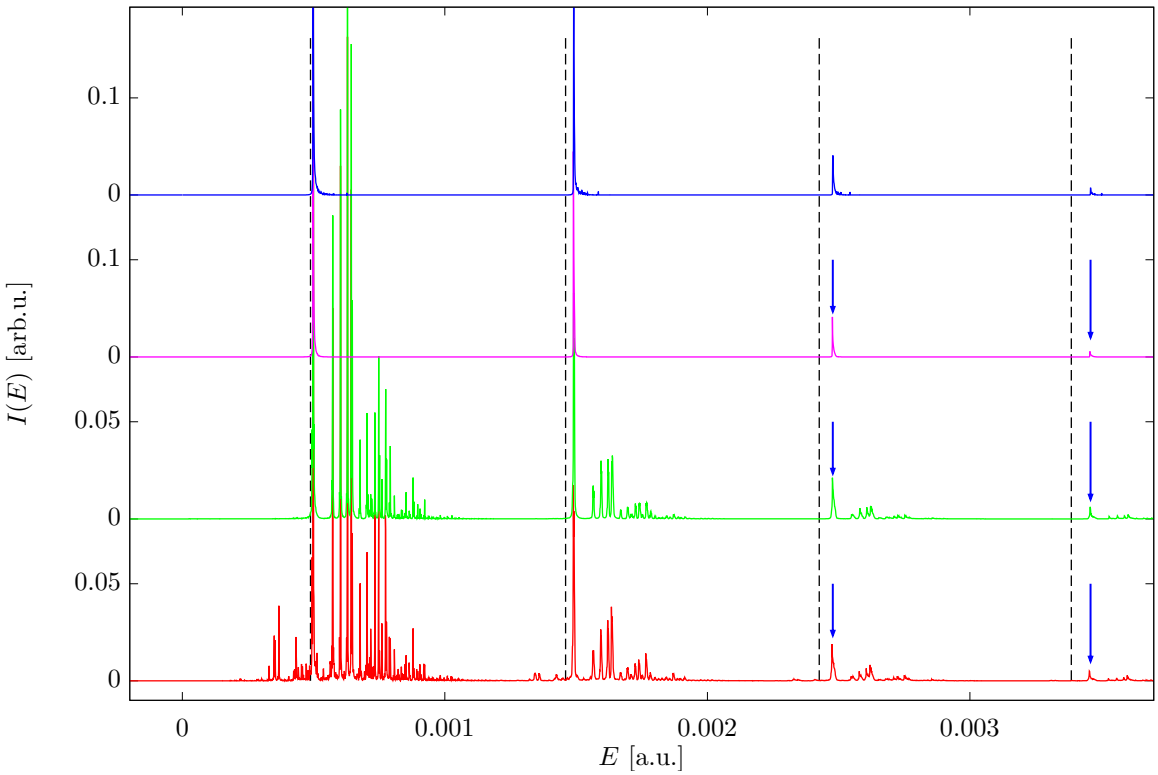

Figure 5.11.: Spectrum of the iodine vibration in the D_{5h} symmetric cluster comprising 17 krypton atoms from Fig. 5.1. From top to bottom: iodine vibration in the krypton cage without any bath DOFs (blue line), iodine vibration coupled to all four totally symmetric bath normal coordinates without (magenta line) and with initial bath excitation (green line), and iodine coupled to 24 bath DOFs, where only the totally symmetric ones have initial momentum (red line). All ground state peaks shifted to match the blue one. Blue arrows indicate the respective second and third excited peak of the blue line, and dashed lines for unrestricted iodine vibration. All spectra are normalized such that the biggest peak is unity.

yields again five totally symmetric normal modes, the iodine vibration and four bath modes now displaying collective motion of all krypton atoms.

Due to the anharmonic nature of the environment, not only the system but also bath normal coordinates should now carry an initial momentum in order to achieve a thorough dynamical phase space sampling that captures the influence of the bath DOFs on the system. For more than ten bath DOFs, however, the resulting spectra become virtually meaningless if no additional filtering as proposed by M. Ceotto and coworkers is employed [74]. We will therefore restrict initial bath excitation for now to the five totally symmetric normal modes, where each mode has initial momentum $P_i(0) = \sqrt{\omega_i}$, corresponding approximately to the ground state energy of the respective normal mode with harmonic frequency ω_i. For low bath dimension, we will discuss the influence of the bath excitations on the system by comparing calculations with and without initial bath momentum. The time step of the classical propagation is $\Delta t = T_s/60$ (T_s is the system vibrational period defined in Sec. 4.2), with a total of 2^{16} time steps to get an energy resolution of about 10^{-6} a.u. In order to reduce computational cost, we employ a Hessian update scheme [53] for the calculation of the second potential derivatives during three of the four substeps of the symplectic McLachlan algorithm [50,124]. Between 25000 and 50000

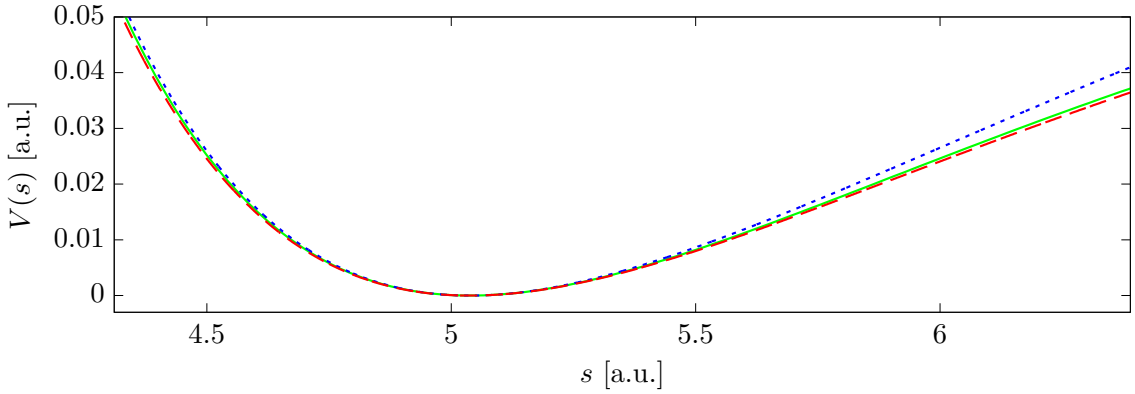

Figure 5.12.: Iodine potential without any environment (green solid line), iodine embedded in a solvation shell with 17 krypton atoms (blue dotted line), and iodine in an fcc krypton matrix with 218 atoms (red dashed line).

	exp. [69] (gas phase)	exp. [106] (in Kr)	1 DOF	5 DOFs ($\mathbf{p}_{\mathrm{b},t=0} = 0$)	5 DOFs ($\mathbf{p}_{\mathrm{b},t=0} \neq 0$)	25 DOFs
ω_e	214.6	211.6	218.9	218.9	218.9	218.7
$\omega_\mathrm{e}x_\mathrm{e}$	0.627	0.658	0.56	0.60	0.60	0.60

Table 5.3.: Spectroscopic parameters of the iodine Morse potential in a krypton environment from experimental data and different computations with a solvation shell environment comprising 17 krypton atoms (Fig. 5.11). All values in cm^{-1}.

trajectories suffice to get spectra that are converged with respect to the positions of the excited iodine peaks.

In Fig. 5.11, results from calculations with different numbers of bath DOFs are displayed. From top to bottom, the iodine molecule is confined by the rigid krypton cage (blue lines), coupled to the four totally symmetric bath DOFs without any initial bath excitation (magenta lines), coupled to the same four bath DOFs with initial bath momenta (green lines), and coupled to 24 bath DOFs (red lines), respectively. In that last case, only the totally symmetric bath DOFs are initially excited. For better comparison, all ground state peaks are shifted to the position of the one from the 1D calculation. The qualitative failure of this simple approach is obvious, given that all peaks are blueshifted instead of redshifted with respect to the gas phase result, indicated by the dashed lines. For this specific form of the krypton environment, the cage has the same influence on the system spectrum as the CL counter term discussed in the previous chapter, which always blueshifts the system potential. In Fig. 5.12, where s is the back-transformed iodine vibration coordinate Q_1, the effective iodine potential in the geometry optimized solvation shell environment (blue dotted line) is indeed narrower than the gas phase potential (green solid line) (cf. Fig. 4.5 from the CL chapter). Also, the iodine bond is tightened rather than loosened by this environment, with a smaller intramolecular distance of 5.029 a.u., compared to 5.038 a.u. in the gas phase.

Consequently, a Birge-Sponer fit of the first seven system peaks results in larger values of the harmonic approximation frequency ω_e for all calculations, as listed in Tab. 5.3. Upon coupling of the bath DOFs to the system, however, there is a second trend that is again reminiscent of the CL discussion. The anharmonicity $\omega_\mathrm{e}x_\mathrm{e}$ gets bigger compared to the result in the rigid krypton cage, thus indicating the experimentally observed redshift. This can also be found

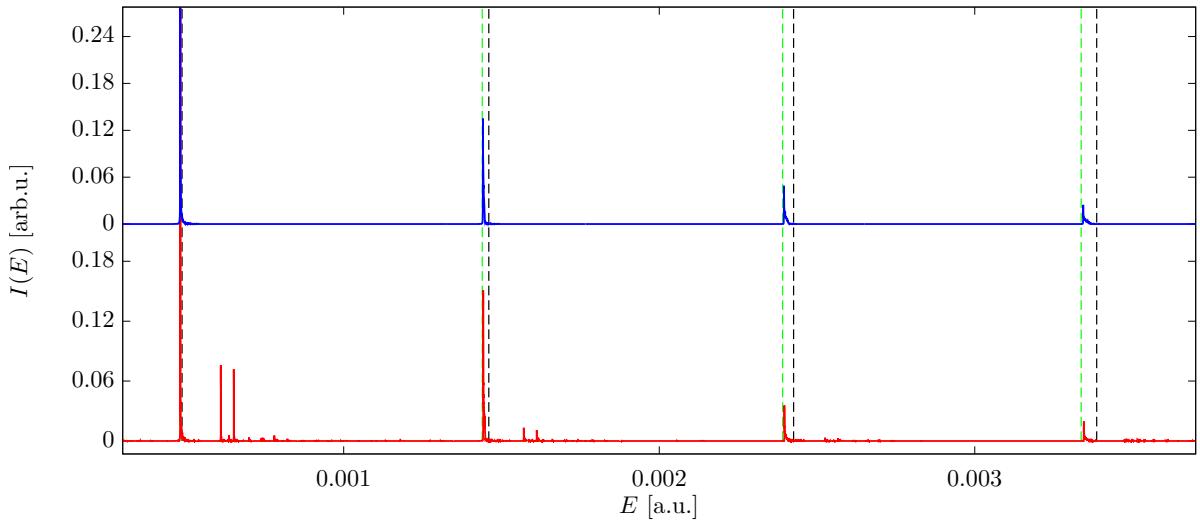

Figure 5.13.: Spectrum of the iodine vibration in the D_{2h} symmetric matrix comprising 72 krypton atoms from Fig. 5.10. Top: iodine vibration in the krypton cage without any bath DOFs (blue solid line), bottom: iodine vibration coupled to 7 totally symmetric bath normal coordinates without initial bath excitation (red solid line). The ground state peaks are plotted at the respective ground state energy of a Morse potential with parameters from the Birge-Sponer fit in Tab. 5.4. Vertical lines show the experimental iodine vibration in the gas phase (black dashed lines) and in a krypton matrix (green dashed lines).

upon close inspection of the excited peaks in Fig. 5.11, which are slightly to the left of the blue arrows representing the respective position in the rigid cage. With an addition of more bath DOFs, ω_e is finally getting slightly smaller, but not to the extend that it might counteract the original wrong tendency due to the overly simple krypton environment. For the different bath sizes employed here, there is not much of a difference in the spectroscopic parameters as long as there are any moving bath coordinates at all. This might, however, also be due to the fact that only four of the 24 bath DOFs are initially excited in the calculation with the largest bath.

REDSHIFT OF IODINE SPECTRUM IN A KRYPTON MATRIX

After the single solvation shell environment turned out to yield an overall blueshift, we now exchange this cluster geometry with a krypton matrix composed of three layers and 218 atoms, where only the 72 atoms of the two inner layers are moving, while the outermost layer is fixed, as described above. That this approach will be more successful can be deduced classically from Fig. 5.12, where the iodine potential in the krypton matrix (red dashed line) gets wider after geometry optimization. In addition, the softening of the iodine bond is reflected by a larger iodine-iodine distance of 5.051 a.u. This has been found to be an important precondition for a redshift of the system frequencies in the investigation of iodine in argon [69], where the difference in bond distance for caged and free iodine is smaller than in this study, corresponding to an overall smaller redshift.

For the semiclassical propagation, we take only the two inner krypton layers with 72 atoms from the optimized geometry. The normal mode analysis is restricted to the iodine molecule and the 18 krypton atoms of the inner layer, while the outer layer is fixed. We now use 2^{17} semiclassical time steps of length $\Delta t = T_s/15$ for an energy resolution of about 10^{-7} a.u. (0.02 cm^{-1}),

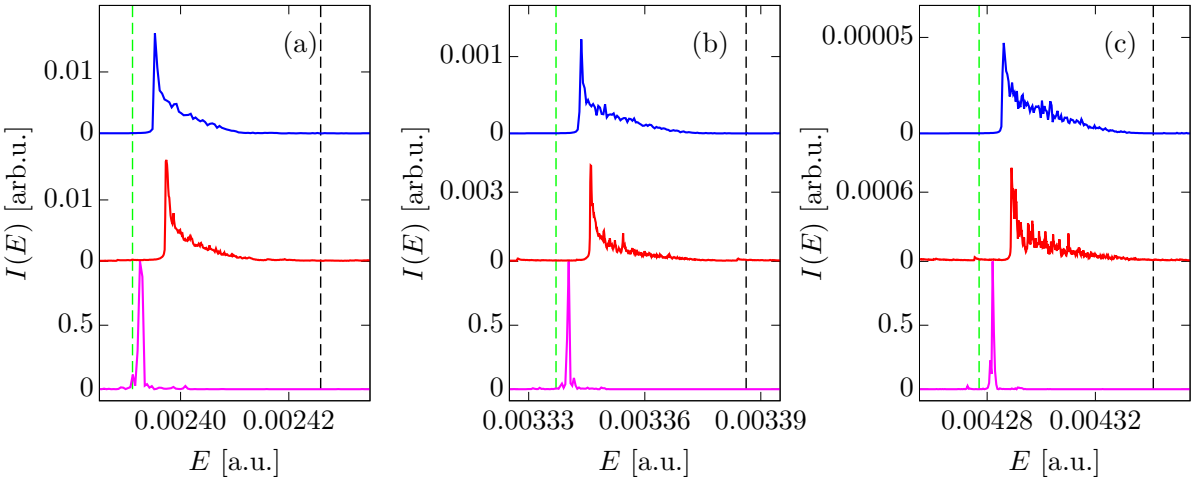

Figure 5.14.: Spectrum of the iodine vibration in krypton, from left to right: (a) second, (b) third and (c) forth excitation. Top: iodine vibration in the krypton cage without any bath DOFs (blue solid line), middle: iodine vibration coupled to 7 totally symmetric bath normal coordinates with initial bath excitation (red solid line), bottom: MC TA SC-IVR result for 20 DOFs with initial bath excitation (magenta solid line). Vertical lines show the experimental iodine vibration in the gas phase (black dashed lines) and in a krypton matrix (green dashed lines).

and each semiclassical time step is subdivided into 16 substeps to keep the classical calculation accurate. 5000 trajectories are sufficient for the TA SC-HD calculations to yield a result where the first six iodine excitations can be attributed unambiguously.

Results are presented in Figs. 5.13, 5.14, and Tab. 5.4. In Fig. 5.13, we compare the spectrum of the iodine vibration in the completely rigid krypton cage (solid blue line) to the result of a TA SC-HD calculation comprising the iodine vibration as well as the seven fully symmetric bath normal coordinates (solid red line), which do not carry initial excitation. The redshifted experimental peak positions are indicated by dashed green lines, the original gas phase peaks by dashed black lines. We see not only the qualitatively correct trend towards a redshift, but also good quantitative agreement of the numerical peaks with the experimental result, both for rigid and flexible cage. In addition, the spectrum with the flexible bath modes shows two of the bath normal coordinates being strongly excited by the system, while the others are barely visible. For a more quantitative analysis, we compare the results of Birge-Sponer fits including the first six peaks of the 1D calculation from Fig. 5.13 and a calculation with eight totally symmetric normal modes, where now all DOFs are initially excited with an energy corresponding to the respective ground state, as before. As can be seen from Tab. 5.4, taking only these seven bath DOFs is not sufficient to influence the iodine spectrum significantly. This is corroborated by the detailed views of three excited iodine peaks in Fig. 5.14, where the peaks from the 1D calculation are even a bit closer to the respective experimental peak positions.

For further improvement, we resort to the MC TA SC-IVR method [74] that we have described in Sec. 4.3.2, and include an additional 12 bath modes for a total of 20 DOFs. While the full spectrum provided by TA SC-HD becomes unreadable if all of these 20 DOFs carry initial excitation, the MC TA SC-IVR allows to filter out specific peaks by choosing an appropriate superposition as a reference state in Eq. (3.34). In order to find the six first iodine peaks, we have to propagate six trajectories with energies that are close to the peaks' positions, as we

	exp. [69] (gas phase)	exp. [106] (in Kr)	1 DOF	8 DOFs (TA SC-HD)	20 DOFs (MC TA SC-IVR)
ω_e	214.6	211.6	211.8	212.0	211.7
$\omega_e x_e$	0.627	0.658	0.62	0.63	0.61

Table 5.4.: Spectroscopic parameters of iodine Morse potential in krypton environment from experimental data and different computations with a matrix environment comprising 72 krypton atoms (Fig. 5.13). All values in cm^{-1}.

have also explained in App. D, and apply the filter for even or odd peaks. The results are shown by the solid magenta lines in Fig. 5.14, and we find that the peaks are clearly redshifted with respect to the two other spectra, so the additional bath DOFs have the desired effect on the iodine vibration. This is reflected by the Birge-Sponer fits in Tab. 5.4, where the harmonic approximation frequency is almost exactly identical with the experimental result. However, we do not see an improvement of the anharmonicity.

In this chapter, we have demonstrated the applicability of the semiclassical hybrid formalism beyond the CL model system from Ch. 4, using the example of an iodine molecule in a krypton environment which is experimentally relevant and at the same time appropriate for a semiclassical description because of the availability of analytic parameters for the interactions. The first part has revealed that a reduced description with iodine in its first solvation shell reproduces the temperature and initial system state dependence of the decoherence dynamics correctly, even if only a few important bath coordinates are used. The semiclassical results in that section agreed nicely with quantum calculations and showed that, at least for low temperature, the inclusion of more normal modes does not dramatically change the decoherence dynamics. In the second section, we have studied the effect of the krypton environment on the iodine spectrum. While the solvation shell model turned out to be incapable of capturing the bath influence correctly for this quantity, a more refined matrix description resulted in an accurate qualitative and, at least for the harmonic approximation frequency, quantitative reproduction of experimental findings.

6. SEMICLASSICAL DESCRIPTION OF TWO ELECTRON SCATTERING

The following chapter will be dedicated to a more fundamental question rather than, like the rest of this work, applications of hybrid semiclassical dynamics to larger molecular systems. We will investigate whether the effect of the Pauli principle which, as a consequence of indistinguishability, requires two fermions with parallel spin to be in orthogonal spatial states, is included in the semiclassical propagation schemes from Ch. 2. Several approaches to the dynamics of indistinguishable particles have been developed in the past, first in the context of nuclear physics [34, 35, 125–130] and later in molecular physics [36, 131, 132].

The first idea to include spin effects into classical dynamics was the introduction of an additional momentum-dependent potential to model an additional effective repulsion of fermions with the same spin. In order to account for identical spins of two fermions i and j, one can introduce the so-called Pauli potential as

$$V_{\mathrm{P}}(X_{ij}) = \frac{\zeta^2\hbar^2}{2m}\frac{X_{ij}}{\mathrm{e}^{X_{ij}}-1}, \tag{6.1}$$

where the variable X_{ij} is the phase space distance between the particles,

$$X_{ij} = \frac{1}{2}\left[\zeta^2\left(q_i-q_j\right)^2 + \frac{1}{\hbar^2\zeta^2}\left(p_i-p_j\right)^2\right], \tag{6.2}$$

and ζ is a fitting parameter. The choice of the Pauli potential is of course not unique, and we should also mention that a phase space distance based potential is not applicable to arbitrary multi fermion systems. This can be seen easily by considering electrons in different atomic orbitals which are not subject to Pauli exclusion independent of their phase space distance. Semiclassical GWP calculations in nuclear physics have also used this approach [35], or a Pauli blocking probability that forbids collisions depending on the final state [128, 129]. Since these artificially introduced potentials also bring about artifacts and thus wrong results for some quantities, another class of methods has been developed.

These semiclassical methods, known as antisymmetric molecular dynamics (AMD) or fermionic molecular dynamics (FMD) [130–132], are based on Hartree products of GWPs, which are symmetrized or antisymmetrized to yield determinants $|\Psi\rangle = |\phi\{q_i, p_i\}|$ comprising GWPs and spin. Using the Lagrangian of the TDSE, $L = \langle\Psi|\mathrm{i}\hbar(\mathrm{d}/\mathrm{d}t) - \hat{H}|\Psi\rangle$, a set of equations of motions can be derived with the variational principle that automatically obey both the Pauli

principle and the uncertainty relation. However, these new equations differ considerably from the classical ones and are much more complicated. On a more general level, a semiclassical approach to the dynamics of fermions has been developed recently by T. Engl and coworkers [133, 134], starting from an exact path integral representation of the fermionic propagator in terms of Grassmann variables.

Apart from Pauli potential and AMD/FMD approaches, there have been some successful semiclassical descriptions of two electron systems using simple Hartree products of GWPs. Different HK propagations have been used to reproduce the binding energy of one-dimensional "collinear" helium [135], the harmonium binding energy [136], and singlet states of helium [137]. Another trajectory guided method was shown to work for the electrons in a hydrogen molecule [138]. Also, the cross section for Mott scattering of not only electrons, but identical particles in general was shown to be semiclassically exact [139].

We will investigate the scattering of two electrons with the semiclassical methods introduced in Ch. 2, but using symmetrized and antisymmetrized initial states instead of simple Hartree products in order to find out if spin effects are contained in such a minimal approach [140].

6.1. TWO ELECTRON SCATTERING POTENTIAL AND INITIAL STATES

Our test system consists of two scattering electrons that are either in a singlet or a triplet state initially and should therefore approach each other to a different degree. As many-electron systems are governed by pairwise two-particle interactions, it is reasonable to assume that an accurate description for this reduced example implies good results also for larger systems. The two electrons interact with each other but are free otherwise; in particular, the Hamiltonian does not contain any spin component. We will study the scattering in one dimension with a soft-core interaction for which numerical quantum calculations are easier than for the bare Coulomb potential. In atomic units, the Hamiltonian then reads

$$\hat{H} = \frac{\hat{p}_1^2}{2} + \frac{\hat{p}_2^2}{2} + \frac{1}{\sqrt{(x_1 - x_2)^2 + c_0}}, \tag{6.3}$$

where the softening parameter is chosen as $c_0 = 0.55$ a.u. This value has been used, e.g., in a 1D helium model, where it yields a ground-state energy that is close to that of the real 3D helium atom [141].

Initially, we place the electrons far apart. One electron is situated at the origin with zero momentum, while the other one starts at $q_0 = 15$ a.u., moving towards the first one with initial momentum $p_0 = -2$ a.u., as described by spatial orbitals

$$\varphi_1(x) = \left(\frac{\gamma}{\pi}\right)^{1/4} \exp\left\{-\frac{\gamma}{2}x^2\right\} \tag{6.4}$$

$$\varphi_2(x) = \left(\frac{\gamma}{\pi}\right)^{1/4} \exp\left\{-\frac{\gamma}{2}(x - q_0)^2 + \mathrm{i}p_0 x\right\}, \tag{6.5}$$

with a width parameter $\gamma = 0.25$ a.u. The initial states are then acquired by combining these spatial orbitals with a spin component to obtain either a singlet

$$\Psi_{\mathrm{sing}}(x_1, x_2) = \frac{1}{2}\left(\begin{vmatrix}\varphi_{1\uparrow} & \varphi_{1\uparrow}\\ \varphi_{2\downarrow} & \varphi_{2\downarrow}\end{vmatrix} - \begin{vmatrix}\varphi_{1\downarrow} & \varphi_{1\downarrow}\\ \varphi_{2\uparrow} & \varphi_{2\uparrow}\end{vmatrix}\right) \tag{6.6}$$

$$= \frac{1}{2}\left[\varphi_1(x_1)\varphi_2(x_2) + \varphi_2(x_1)\varphi_1(x_2)\right]\left[|\uparrow\downarrow\rangle - |\downarrow\uparrow\rangle\right] \tag{6.7}$$

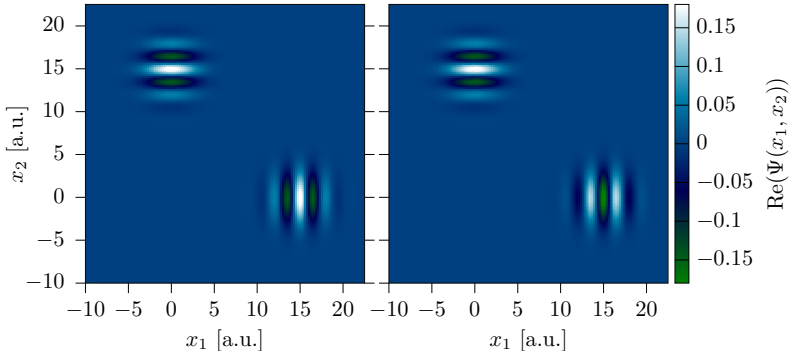

Figure 6.1.: Initial states for singlet (left) and triplet configuration (right).

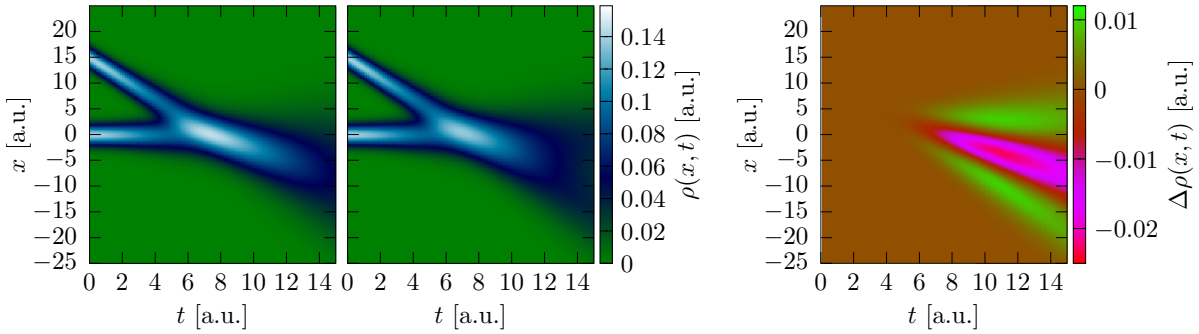

Figure 6.2.: Quantum results for two electron scattering: singlet initial state (left), triplet initial state (middle) and difference of the two (right).

or a triplet

$$\Psi_{\mathrm{trip}}(x_1, x_2) = \frac{1}{\sqrt{2}} \begin{vmatrix} \varphi_{1\uparrow} & \varphi_{1\uparrow} \\ \varphi_{2\uparrow} & \varphi_{2\uparrow} \end{vmatrix} \tag{6.8}$$

$$= \frac{1}{\sqrt{2}} \left[\varphi_1(x_1)\varphi_2(x_2) - \varphi_2(x_1)\varphi_1(x_2)\right] |\uparrow\uparrow\rangle \tag{6.9}$$

wave function, where we use the spin components only to find the appropriate spatial initial states for the propagation. The electrons are sufficiently far apart for the energy of the two states to be identical. We stress that the only difference in the spatial components is the sign connecting the two products, which corresponds to a phase difference (Fig. 6.1).

The results of an exact quantum propagation are depicted in Fig. 6.2. We plot the electron density $\rho(x,t) = \int \mathrm{d}x_2 \Psi^*(x, x_2, t)\Psi(x, x_2, t)$ and find that the results for singlet and triplet are very similar at the beginning, when the electrons are still far apart. After the scattering, one can see that the triplet density is significantly wider. This is further illustrated by the right panel in Fig. 6.2, where we plot the difference density $\Delta\rho(x,t) = \rho_{\mathrm{trip}}(x,t) - \rho_{\mathrm{sing}}(x,t)$. The inner strip is dominated by the singlet result (negative values), while the outer area has a higher contribution from the triplet calculation. This is a direct consequence of the Pauli principle: the electrons in the triplet carry parallel spins and will therefore not approach each other as closely as the singlet configuration. Quantitatively, one can see the difference in the time-dependent expectation value of the distance between the two electrons, expressed by the

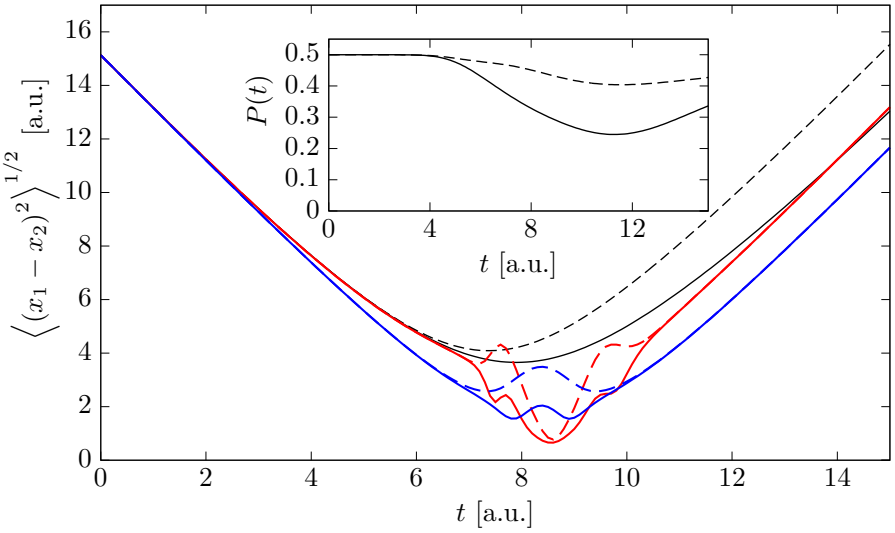

Figure 6.3.: Single trajectory results from TGWD (red line) and FG calculations (blue) for the distance of the two electrons for singlet (solid lines) and triplet initial state (dashed). For comparison, quantum results are depicted by black lines. Inset: quantum result for the purity.

observable $\langle(\hat{x}_1 - \hat{x}_2)^2\rangle^{1/2}$. Figure 6.3 demonstrates how the distance at the point of maximum approach is bigger for the triplet initial state (black dashed line) than for the singlet initial state (black solid line), and how the distance remains bigger after the scattering event.

6.2. SEMICLASSICAL RESULTS

With a quantum result for comparison in place, we will now use the initial states in Eq. (6.6) and (6.8) for semiclassical propagations in order to find out what ingredients are needed in order to describe the effect of the Pauli principle. Since HK accounts only approximately for normalization, the results need to be divided by $\sqrt{N(t)}$ at each time step, where $N(t) = \langle\Psi(t)|\Psi(t)\rangle$ is the norm of the HK propagated wavefunction.

Among the semiclassical methods described in Ch. 2, the computationally and conceptually simplest approaches are the single trajectory ones. The most basic mechanism is a frozen Gaussian (FG) approach where the wave function is calculated according to Eq. (2.6), but for the central trajectory only. A bit more sophisticated is the TGWD from Eq. (2.16), where the width of the wave packet is time dependent, thus rendering the method exact for at most harmonic potential. Results are reported in Fig. 6.3 and show that a single trajectory is not enough to reproduce the effect of the Pauli principle correctly. The distances of singlet and triplet states differ only in the region of closest approach, but are again identical for later times. The different behavior of singlet and triplet in the scattering region is not due to interference between trajectories, but because two different contributions to the wave function have to be propagated which are then either added or subtracted.

Taking a closer look at frozen and thawed results, we see that the initial agreement with the quantum results lasts significantly longer for the TG propagation. This is due to TGWD being exact especially for free particles, whereas FG dynamics is not. In the inset, we have plotted the purity of the reduced systems for both initial configurations to get an idea at which point in time the electrons are starting to interact strongly, thus rendering a free particle description useless. Indeed, the purity starts to deviate significantly from its original value after about four

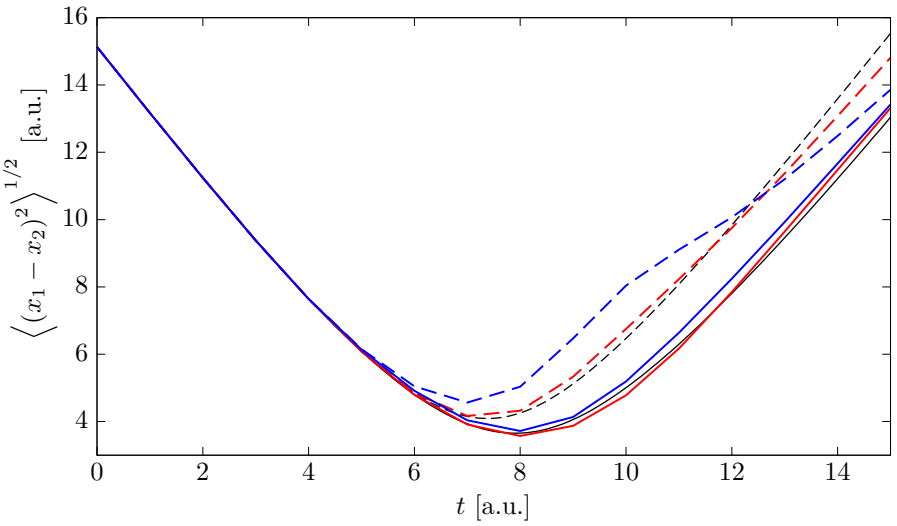

Figure 6.4.: Multiple trajectories results for the distance of the two electrons for singlet (solid lines) and triplet initial state (dashed) from regular HK (red line) and prefactor one calculations (blue). For comparison, quantum results are depicted by black lines.

or five time units, which is just the time when the TGWD distance starts to deviate from the full quantum result. We should also mention that for these single trajectory cases, the problem can be solved analytically and the result corroborates the findings of Fig. 6.3 [140]. One can show in particular that the triplet distance is always larger than the singlet distance, and that the difference between singlet and triplet disappears for longer times.

Going a step further in semiclassical complexity, we now treat the initial states with the HK propagator from Eq. (2.6). As shown by the results from propagations with 10^5 trajectories in Fig. 6.4, agreement with the exact result is excellent. The difference between singlet and triplet is reproduced not only qualitatively, but almost quantitatively. To support the notion that the phase space sampling is the decisive ingredient, we use a simpler version of the HK propagator where the prefactor C_t from Eq. (2.11) is set to one. As we have mentioned in Sec. 2.1, this approach has first been proposed by E. Heller under the name of Frozen Gaussian approximation [45]. Later, it was shown to be a simple special case of a prefactor free SC-IVR description [142]. As before, the wave function must be renormalized [142]. The result for the same number of trajectories as in the previous case is plotted in Fig. 6.4. While not very accurate on a quantitative level, there is still a clear and qualitatively correct distinction between singlet and triplet result. We can therefore conclude that interfering trajectories are the key factor for the semiclassically correct distinction of singlet and triplet state, creating "collective correlation" in the language of Heller [45]. The reason for the good performance of the HK method for this example is twofold. On the one hand, the exact time evolution operator does not contain a spin degree of freedom and acts only on the spatial part of the initial state, just like its semiclassical counterpart. On the other hand, all semiclassical methods in this sections are symmetric with respect to electron exchange, thus preserving the antisymmetry of the respective initial states.

Some interesting further calculations are summarized in the plots of Fig. 6.5. We obtain a classical comparison from the LSC-IVR formalism, which has been introduced in Sec. 2.3, by propagating a density matrix with the correct initial states. As there are no interfering trajectories due to a missing complex phase, it is not very surprising to learn that LSC-IVR

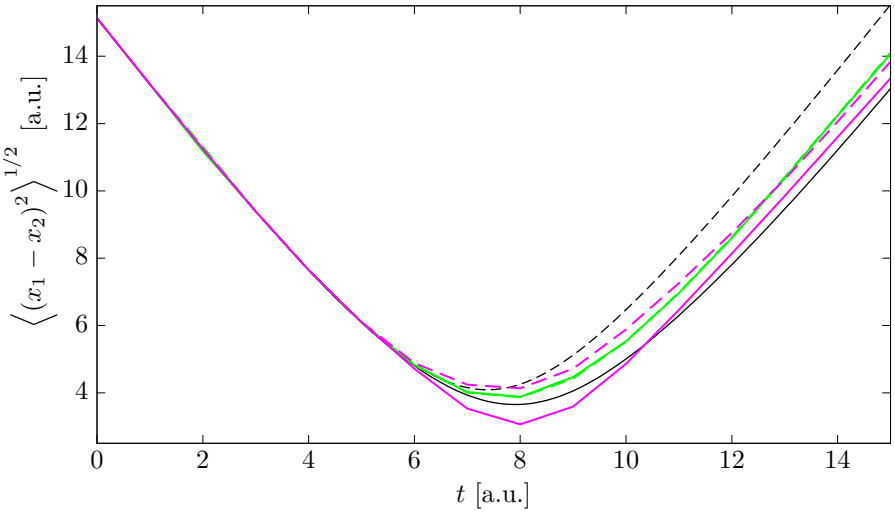

Figure 6.5.: The distance of two scattering electrons, calculated with LSC-IVR (green lines) and hybrid results (magenta lines). The solid lines are singlet, dashed lines denote triplet results; quantum results are indicated in black.

(green line in Fig. 6.5) does not differentiate between singlet and triplet. In fact, the two distances are exactly the same throughout the propagation time, and they coincide with the result that one gets quantum mechanically from an unsymmetrized initial state. The hybrid result (magenta lines in Fig. 6.5), where we have propagated electron 1 with HK and electron 2 with TG, is also quite instructive, because it is indeed a mixture of HK and TGWD result here. During the collision, the singlet-triplet difference is resolved correctly on a qualitative level, as it is with HK. By contrast, the triplet approaches the singlet result after the scattering, as it does in the TGWD case. We also note that the first deviations from the exact result occur at about the same time as in the TGWD calculations.

As a final remark, we review our model and realize that the Coulomb repulsion is not very strong here. In fact, due to our choice of initial conditions and soft Coulomb parameter, the initial kinetic energy is higher than the potential maximum. Taking the bare Coulomb potential instead would not be feasible for quantum calculations, but we can make c_0 very small in order to get a more repulsive potential. The result for $c_0 = 0.005$ a.u. is shown in Fig. 6.6. The difference between singlet and triplet is smaller now because the stronger electronic interaction keeps the electrons further apart, thus diminishing the effect of the spin states. However, we can still see that HK resolves the difference faithfully. In addition to the distance, we have also plotted the purity which is a more complicated quantity in the sense that off-diagonal elements of the reduced density matrix are required for its computation, making it more sensitive to deviations of the semiclassical results. These deviations from the quantum result set in right after the interaction of the electrons starts to affect the dynamics, i.e., at the moment when the purity deviates from its initial value of 0.5. Overall, the singlet-triplet difference is captured correctly by the HK calculation as well as the general shape of the quantum curves. On a side note, we point out that, while the distances for singlet and triplet are not as far apart as in the case of weaker Coulomb interaction in Fig. 6.3, there is about the same difference in decoherence. This seems very appropriate given that the purity is a non-classical quantity just as spin is a fundamentally quantum concept.

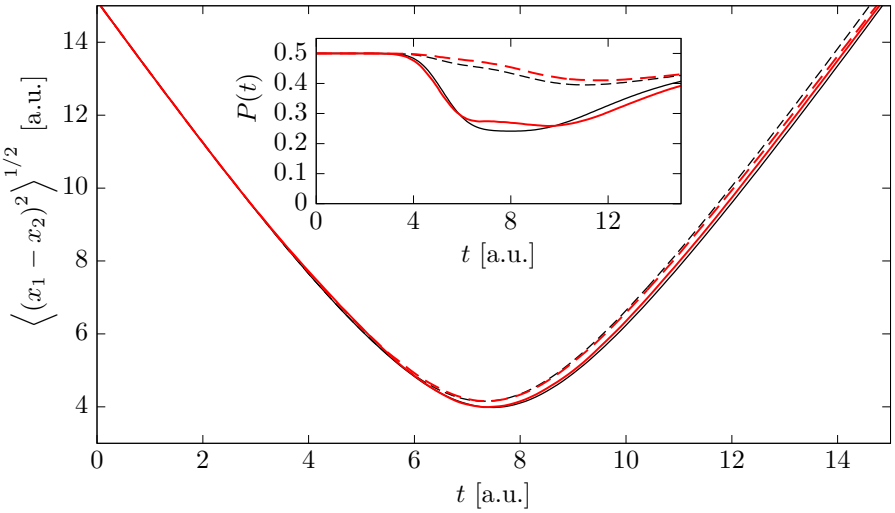

Figure 6.6.: HK (red lines) and quantum results (black) for electron scattering with soft Coulomb parameter $c_0 = 0.005$ a.u. Solid lines are singlet, dashed lines denote triplet results. The innset shows the purity with the same color scheme.

With that, we close the discussion on semiclassical IVR calculations of two-electron scattering. As a central result, we have seen that interfering trajectories are necessary in order to reproduce the effect of the Pauli principle on the distance of electrons in different spin states. Using a single trajectory approach as in TGWD is not sufficient to observe this difference. By contrast, the HK propagator with appropriate initial states captures the difference between singlet and triplet during the interaction almost exactly.

7. SUMMARY AND OUTLOOK

In this thesis, we have investigated applications of semiclassical IVRs to atomic and molecular systems, putting specific emphasis on the hybrid description of vibrational spectra of molecules.

To this end, we have first developed a mixed time-averaging SC-IVR approach that combines the existing TA SC-IVR with a hybrid description, thus allowing for a rigorous Herman-Kluk treatment of a limited number of system DOFs while using computationally cheap thawed Gaussian dynamics for the remaining, weakly coupled (bath) DOFs. The resulting twofold time integral could be simplified with a harmonic approximation that is similar in spirit to the original separable approximation of TA SC-IVR, yielding an expression with reduced peak weight, but still exact peak positions for harmonic bath DOFs. Overall, computational effort is much diminished by this simplification, because now the phase space integration includes only a few important DOFs, leading to a much more favorable scaling of the number of trajectories needed for convergence with respect to total system size. At the same time, results for the system DOF(s) are still very accurate, at least in terms of peak position if not in terms of peak weight.

As a first tentative application, we have studied the influence of an Ohmic Caldeira-Leggett bath on an iodine-like Morse oscillator. Taking into account just one or two bath oscillators in the beginning, we have shown that the hybrid TA SC-IVR approach does indeed reproduce quantum results faithfully over a wide range of bath parameters. Even in the case of one or two resonant bath oscillators and high coupling strength, peak positions for both system and bath closely agree with exact results. Going a step further towards an actual bath, we have compared TA Herman-Kluk and TA hybrid calculations for a Morse oscillator strongly coupled to ten bath DOFs. Again, agreement of system and bath peaks alike is excellent. After establishing the reliability of the hybrid approach for this problem, we have turned to bath sizes of up to 60 HOs in order to exploit the specific advantages of the hybrid approximation. In particular, we have shed some light on the role of the CL counter term. While it is obvious that this additional harmonic contribution induces a blueshift of the system frequencies, leaving it out has different consequences for resonant and non-resonant baths, respectively. If the bath contains some HOs with frequencies close to the system frequency, there is still a blueshift of the system by the bath oscillators. If, on the other hand, all bath oscillators have lower frequencies than the system, the calculation without the counter term shows a redshift of the system frequency with respect to the unperturbed result. This is qualitatively consistent with experimental findings, where a redshift of the iodine spectrum embedded in a rare gas matrix has been observed [80]. We have also seen that at least first excited bath peaks can be found

easily in the spectrum, and that every kind of bath shows an overall redshift.

Moving away from CL systems that are almost tailor-made for a hybrid description, we have then investigated iodine embedded in krypton as an example for an anharmonic bath with nonlinear system-bath coupling. Employing a reduced model with iodine in its first solvation shell and a limited number of flexible bath normal coordinates, we have performed full quantum calculations in order to reproduce the dependence of the decay of iodine vibrational coherence on temperature and initial excitation. Quantitatively, decoherence rates showed different degrees of agreement with experiments, from being almost identical for low bath temperature and high initial iodine excitation to underestimating exact results by a factor of two for high bath temperature. The latter discrepancy is likely due to the approximate description of bath temperature in the quantum calculations, as we have seen from comparison to semiclassical results for the purity. Adding the remaining bath coordinates into the hybrid calculations, we could see a further increase of decoherence rates, but the minimum values as well as the shape of the purity curves remained largely unchanged, underscoring the outstanding role of the totally symmetric bath coordinates in the dynamics.

In the second part of our investigations concerning iodine in krypton, we have made use of the hybrid TA SC-IVR to calculate the shift of the iodine vibrational spectrum by the krypton environment. The much simplified solvation shell model employed for the decoherence rates was not appropriate for the spectral calculations, yielding a qualitatively wrong blue instead of a redshift. With a larger krypton matrix environment comprising one flexible and one rigid layer of atoms in fcc geometry, a redshift of the iodine frequencies was observed. Quantitatively, the harmonic approximation frequency could be closely reproduced even with a completely rigid krypton cage. Adding only the totally symmetric bath modes and applying the TA hybrid method resulted in an accurate reproduction of the full spectrum of iodine as well as bath frequencies. For finding specifically the iodine peaks from a spectrum with additional non-totally symmetric bath DOFs, where each normal coordinate carries initial excitation, the multiple coherent state TA SC-IVR [74] was the better choice.

Finally, we have addressed a more fundamental question, namely, the minimum requirement for a correct semiclassical description of fermionic systems. More precisely, we have studied the effect of different initial spin configurations of two electrons on their mutual distance during a scattering event. Following full quantum calculations, we have used single and multiple trajectory SC-IVRs to propagate appropriately symmetrized or antisymmetrized initial states of electrons that interact only through a soft Coulomb interaction. Single trajectory methods turned out to be insufficient to capture the distance difference between singlet and triplet states during and after scattering. Multiple trajectory methods, on the other hand, show the correct behavior as long as they allow for interference between different trajectories, with the traditional Herman-Kluk propagator result almost exactly on top of the quantum one. This also holds if the soft Coulomb parameter is chosen much smaller such that the interaction comes closer to the bare Coulomb potential.

Overall, we have further established the hybrid approach as a valuable resource for the semiclassical description of complex molecular systems, both for the model CL Hamiltonian and a Hamiltonian comprising empirical parameters. The biggest asset is a much more favorable scaling of the number of trajectories that are needed for convergence, with a negligible loss of accuracy for the DOFs of interest provided the coupling to environmental modes is not too strong. On the downside, the stability matrix, which requires second derivatives, still has to be calculated for the total system, thus effectively limiting the number of DOFs for which a numerical treatment is feasible. As mentioned before, however, there are propositions of approximations to the stability matrix, which can be easily adopted and incorporated into the

hybrid formalism.

In particular, there are a few interesting future applications of the hybrid TA SC-IVR for the calculation of molecular spectra. In recent publications on the experimental relevance of the CL system, the question has come up whether it is possible to map realistic systems on a CL Hamiltonian [143]. While this seems not to be the case in general, it might be worthwhile to explore systems such as iodine in a rare gas environment where such an equivalence might exist for certain ambient parameters [144].

Furthermore, the hybrid approach can be even more favorable compared to a full Herman-Kluk description for systems where no analytic potentials are available. If the classical trajectories and stability matrix elements have to be calculated on-the-fly, they will likely take up a much larger share of total computational time. In that case, having a method at hand that allows for convergence with a relatively small number of trajectories will be advantageous. Being part of the European Research Council-funded SEMICOMPLEX project [145] that is dedicated (in a broader fashion than this thesis) to developing semiclassical methods for the description of complex systems, the basic idea for future applications of the hybrid SC-IVR is the study of the full spectra of molecules in clusters, liquids or attached to surfaces. In each of these cases, one can in principle identify a few interesting DOFs that are most relevant for the spectrum, and treat the remaining modes as the bath.

A possible starting point for such calculations would be the investigation of the full spectrum of water in water, i.e., of a water molecule surrounded by other water molecules. This system is more complex than iodine in krypton, but the approach for its description would be similar in spirit to what we have done in this thesis: take a single water molecule, add an increasing number of water molecules as the solvent, and find out the effect of the surrounding cluster on the original molecule's spectrum. As a next step, one might take glycine or a small peptide instead of a water molecule, again put it into a cluster of water molecules, and see the effect on the spectrum. Studying either of these systems requires numerically expensive classical calculations because one has to make use of ab-initio potentials [146–149], so it is to be expected that the hybrid SC-IVR will contribute to make the corresponding spectral calculations more accessible.

A. STABILITY MATRICES AND TGWD WAVEFUNCTIONS

In this appendix, we provide some additional details about two basic aspects of the semiclassical methods in Ch. 2. First, we will state the time evolution of the stability matrix $\mathbf{M}(t)$ that is an essential part of every SC-IVR discussed in this work. Then, we will comment on the relation of the two different versions of Heller's TGWD that have been laid out in Sec. 2.2.1. This has been done before for 1D as an exercise in [8], and, with different conventions for width and phase, for multiple dimensions in [55, 56], but we think it is worthwhile to summarize it all in one place for our choice of variables.

A.1. TIME EVOLUTION OF THE STABILITY MATRIX

The stability matrix $\mathbf{M}$(t), whose submatrices are contained in the HK prefactor from Eq. (2.9), is defined as [8]

$$\mathbf{M}(t) = \begin{pmatrix} \mathbf{m}_{11,t} & \mathbf{m}_{12,t} \\ \mathbf{m}_{21,t} & \mathbf{m}_{22,t} \end{pmatrix} \equiv \begin{pmatrix} \frac{\partial \mathbf{p}_t}{\partial \mathbf{p}} & \frac{\partial \mathbf{p}_t}{\partial \mathbf{q}} \\ \frac{\partial \mathbf{q}_t}{\partial \mathbf{p}} & \frac{\partial \mathbf{q}_t}{\partial \mathbf{q}} \end{pmatrix}. \tag{A.1}$$

It arises by considering a second trajectory $[\tilde{\mathbf{p}}_t(\tilde{\mathbf{p}}, \tilde{\mathbf{q}}), \tilde{\mathbf{q}}_t(\tilde{\mathbf{p}}, \tilde{\mathbf{q}})]$ that is close to the original trajectory $[\mathbf{p}_t(\mathbf{p}, \mathbf{q}), \mathbf{q}_t(\mathbf{p}, \mathbf{q})]$ and can thus be expanded to first order in the difference of the initial conditions $(\delta\mathbf{p}, \delta\mathbf{q})$. In the form of a matrix equation, the relation between initial and final deviation of the trajectories then reads

$$\begin{pmatrix} \delta\mathbf{p}_t \\ \delta\mathbf{q}_t \end{pmatrix} = \mathbf{M}(t) \begin{pmatrix} \delta\mathbf{p} \\ \delta\mathbf{q} \end{pmatrix}, \tag{A.2}$$

where $\delta\mathbf{p} = \tilde{\mathbf{p}} - \mathbf{p}$, $\delta\mathbf{p}_t = \tilde{\mathbf{p}}_t(\tilde{\mathbf{p}}, \tilde{\mathbf{q}}) - \mathbf{p}_t(\mathbf{p}, \mathbf{q})$, etc. The time evolution of the stability matrix follows from a first order expansion of Hamilton's equations of motion for $\delta\mathbf{p}_t$ and $\delta\mathbf{q}_t$, which yields

$$\frac{\mathrm{d}}{\mathrm{d}t}\mathbf{M}(t) = -\mathbf{J}\mathbf{H}\mathbf{M}(t), \tag{A.3}$$

where $\mathbf{J}$ is the skew symmetric matrix

$$\mathbf{J} = \begin{pmatrix} \mathbf{0}_N & \mathbf{1}_N \\ -\mathbf{1}_N & \mathbf{0}_N \end{pmatrix} \tag{A.4}$$

and $\mathbf{H}$ is the Hessian of the Hamiltonian, i.e., the matrix of second derivatives with respect to positions and momenta. From the definition of $\mathbf{M}$ in Eq. (A.1), one gets the simple initial condition

$$\mathbf{M}(0) = \mathbf{1}_{2N}. \tag{A.5}$$

The equations of motion (A.3) can be employed to prove the relation

$$\frac{\mathrm{d}}{\mathrm{d}t}\left[\mathbf{M}(t)\right]^{\mathrm{T}}\mathbf{J}\mathbf{M}(t) = 0, \tag{A.6}$$

which, using the initial conditions for $\mathbf{M}$, leads to

$$\left[\mathbf{M}(t)\right]^{\mathrm{T}}\mathbf{J}\mathbf{M}(t) = \left[\mathbf{M}(0)\right]^{\mathrm{T}}\mathbf{J}\mathbf{M}(0) = \mathbf{J} \tag{A.7}$$

Writing this out explicitly, one gets the helpful relations

$$\mathbf{m}_{22,t}^{\mathrm{T}}\mathbf{m}_{11,t} - \mathbf{m}_{12,t}^{\mathrm{T}}\mathbf{m}_{21,t} = \mathbf{1}_N \qquad \forall t \tag{A.8}$$

$$\mathbf{m}_{11,t}^{\mathrm{T}}\mathbf{m}_{21,t} - \mathbf{m}_{21,t}^{\mathrm{T}}\mathbf{m}_{11,t} = \mathbf{0}_N \qquad \forall t \tag{A.9}$$

$$\mathbf{m}_{22,t}^{\mathrm{T}}\mathbf{m}_{12,t} - \mathbf{m}_{12,t}^{\mathrm{T}}\mathbf{m}_{22,t} = \mathbf{0}_N \qquad \forall t. \tag{A.10}$$

The above equations also hold for the non-square submatrices $\tilde{\mathbf{m}}_{ij,t}$ defined in Eq. (2.22) and are used in the derivations of the hybrid expressions in Chs. 2 and 3. Furthermore, Eq. (A.7) has numerical implications, as it establishes that $\mathbf{M}$ is a symplectic matrix whose time evolution can be found with a robust symplectic integration scheme [50]. Additionally, Eqs. (A.8) to (A.10) can be used to show that the determinant of $\mathbf{M}$ is unity at all times, which is equivalent to the conservation of phase volume. Monitoring the determinant of $\mathbf{M}$ thus provides an effective tool for checking the stability of a numerical calculation.

A.2. EQUIVALENCE OF THE TGWD WAVEFUNCTIONS

To start this discussion of the two alternative formulations of the TGWD wavefunctions, we restate the original ansatz of Heller [25, 55] from Eq. (2.13)

$$\begin{aligned}\Psi_\alpha(\mathbf{x},t) = &\left(\frac{2^N \det\boldsymbol{\gamma}_0}{\pi^N}\right)^{1/4} \\ &\times \exp\left\{-\left(\mathbf{x}-\mathbf{q}_{\alpha,t}\right)^{\mathrm{T}}\boldsymbol{\gamma}_t\left(\mathbf{x}-\mathbf{q}_{\alpha,t}\right) + \frac{\mathrm{i}}{\hbar}\mathbf{p}_{\alpha,t}^{\mathrm{T}}\left(\mathbf{x}-\mathbf{q}_{\alpha,t}\right) + \frac{\mathrm{i}}{\hbar}\delta_t\right\},\end{aligned} \tag{A.11}$$

which is plugged into the TDSE with the potential expanded to second order around the central trajectory to yield equations of motion as in (2.14) and (2.15),

$$\dot{\mathbf{p}}_{\alpha,t} = -\frac{\partial V}{\partial \mathbf{q}}(\mathbf{q}_{\alpha,t},t) \tag{A.12}$$

$$\dot{\mathbf{q}}_{\alpha,t} = \mathbf{m}^{-1}\mathbf{p}_{\alpha,t} \tag{A.13}$$

$$\dot{\delta}_t = L - \hbar^2\,\mathrm{tr}(\mathbf{m}^{-1}\boldsymbol{\gamma}_t) \tag{A.14}$$

$$\dot{\boldsymbol{\gamma}}_t = -2\mathrm{i}\hbar\boldsymbol{\gamma}_t\mathbf{m}^{-1}\boldsymbol{\gamma}_t + \frac{\mathrm{i}}{2\hbar}\frac{\partial^2 V}{\partial\mathbf{q}\partial\mathbf{q}^{\mathrm{T}}}(\mathbf{q}_{\alpha,t},t). \tag{A.15}$$

We will show that this can indeed be written in the form of Eq. (2.16),

$$\begin{aligned}\Psi_\alpha(\mathbf{x},t) = &\left(\frac{\det\boldsymbol{\gamma}}{\pi^N}\right)^{1/4}\left[\det\left(\mathbf{m}_{22,t}+\mathrm{i}\hbar\mathbf{m}_{21,t}\boldsymbol{\gamma}\right)\right]^{-1/2} \\ &\times\exp\left\{-\frac{1}{2}\left(\mathbf{x}-\mathbf{q}_{\alpha,t}\right)^{\mathrm{T}}\left(\mathbf{m}_{11,t}\boldsymbol{\gamma}-\frac{\mathrm{i}}{\hbar}\mathbf{m}_{12,t}\right)\left(\mathbf{m}_{22,t}+\mathrm{i}\hbar\mathbf{m}_{21,t}\boldsymbol{\gamma}\right)^{-1}\left(\mathbf{x}-\mathbf{q}_{\alpha,t}\right)\right. \\ &\left.+\frac{\mathrm{i}}{\hbar}\mathbf{p}_{\alpha,t}^{\mathrm{T}}\left(\mathbf{x}-\mathbf{q}_{\alpha,t}\right)+\frac{\mathrm{i}}{\hbar}S_t(\mathbf{p}_\alpha,\mathbf{q}_\alpha)\right\}.\end{aligned} \tag{A.16}$$

This choice of variables differs from the one in Heller's works [25, 55, 56], where the width parameter is defined as $\mathbf{A}_t \equiv \mathrm{i}\hbar\boldsymbol{\gamma}_t$ and the normalizing prefactor in Eq. (A.11) is absorbed in the imaginary part of the initial phase factor, $\mathrm{Im}(\delta_{t=0})$. To avoid confusion, we also note that the phase, which is called δ_t here, is labeled γ_t in Heller's publications. In the same spirit, we want to emphasize that $\mathbf{m}$ without indices designates the diagonal matrix containing the masses, while the stability submatrices $\mathbf{m}_{ij}$ always have two lower indices.

In order to bring Eq. (A.11) into the form of Eq. (A.16), we recall Heller's observation [55] that, instead of solving the differential equations (A.14) and (A.15) for $\boldsymbol{\gamma}_t$ and δ_t, one can find an alternative representation for $\boldsymbol{\gamma}_t$,

$$\boldsymbol{\gamma}_t = \frac{1}{2}\mathbf{P}_t\mathbf{Z}_t^{-1}, \tag{A.17}$$

where $\mathbf{P}_t$ and $\mathbf{Z}_t$ are $N\times N$ matrices. One assumes

$$\dot{\mathbf{Z}}_t = \mathrm{i}\hbar\mathbf{m}^{-1}\mathbf{P}_t \tag{A.18}$$

and finds the equation of motion for $\mathbf{P}_t$ by inserting Eq. (A.17) into Eq. (A.15)

$$\dot{\mathbf{P}}_t = \frac{\mathrm{i}}{\hbar}\frac{\partial^2 V}{\partial\mathbf{q}\partial\mathbf{q}^{\mathrm{T}}}(\mathbf{q}_{\alpha,t},t)\mathbf{Z}_t. \tag{A.19}$$

The two above equations describe a system of harmonic oscillators with positions $\mathbf{Z}_t$ and momenta $\tilde{\mathbf{P}}_t \equiv \mathrm{i}\hbar\mathbf{P}_t$. The solution follows immediately with the stability matrix from Eq. (A.1)

$$\begin{pmatrix}\tilde{\mathbf{P}}_t\\ \mathbf{Z}_t\end{pmatrix} = \mathbf{M}\begin{pmatrix}\tilde{\mathbf{P}}_0\\ \mathbf{Z}_0\end{pmatrix}, \tag{A.20}$$

which can be found directly by symplectic integration or by running several trajectories with close-by initial conditions and taking finite differences. The initial conditions have to be chosen such that Eq. (A.17) is fulfilled; a simple choice is

$$\tilde{\mathbf{P}}_0 = \mathrm{i}\hbar\mathbf{P}_0 = 2\mathrm{i}\hbar\boldsymbol{\gamma}_0 \qquad \mathbf{Z}_0 = \mathbf{1}. \tag{A.21}$$

The phase δ_t follows by expressing $\boldsymbol{\gamma}_t$ in Eq. (A.14) in terms of $\mathbf{Z}_t$ and $\dot{\mathbf{Z}}_t$ with Eqs. (A.17) and (A.18)

$$\dot{\delta}_t = L + \frac{\mathrm{i}\hbar}{2}\mathrm{Tr}\left(\dot{\mathbf{Z}}_t\mathbf{Z}_t^{-1}\right), \tag{A.22}$$

which can be integrated over time to yield

$$\delta_t = S_t + \frac{\mathrm{i}\hbar}{2}\mathrm{Tr}\left(\ln\mathbf{Z}_t\right) + \delta_0, \tag{A.23}$$

where $\mathrm{Im}(\delta_0) = 0$ due to our choice of the prefactor of the wavefunction in Eq. (A.11). With Eqs. (A.17), (A.20) and (A.23), one finds $\boldsymbol{\gamma}_t$ and δ_t, and thus the time-evolved wavefunction (A.11), directly from classical trajectories of the system [55]. Now, δ_t can be inserted into Eq. (A.11) with the real part of δ_0 set to zero as well, and we replace $\boldsymbol{\gamma}_t$ with Eq. (A.17). Keeping in mind that

$$\det(\mathbf{A}) = \exp\left[\mathrm{Tr}(\ln \mathbf{A})\right], \tag{A.24}$$

for a matrix $\mathbf{A}$, the wavefunction takes the form

$$\begin{aligned}\Psi_\alpha(\mathbf{x}, t) = &\left[\frac{\det(2\boldsymbol{\gamma}_0)}{\pi^N}\right]^{1/4} (\det \mathbf{Z}_t)^{-1/2} \\ &\times \exp\left\{-\frac{1}{2}\left(\mathbf{x} - \mathbf{q}_{\alpha,t}\right)^{\mathrm{T}} \mathbf{P}_t \mathbf{Z}_t^{-1} \left(\mathbf{x} - \mathbf{q}_{\alpha,t}\right) + \frac{\mathrm{i}}{\hbar}\mathbf{p}_{\alpha,t}^{\mathrm{T}}\left(\mathbf{x} - \mathbf{q}_{\alpha,t}\right) + \frac{\mathrm{i}}{\hbar} S_t\right\}.\end{aligned} \tag{A.25}$$

The penultimate step is to write $\mathbf{P}_t$ and $\mathbf{Z}_t$ from Eq. (A.20) with initial conditions from (A.21) explicitly

$$\mathbf{P}_t = 2\mathbf{m}_{11,t}\boldsymbol{\gamma}_0 - \frac{\mathrm{i}}{\hbar}\mathbf{m}_{12,t} \tag{A.26}$$

$$\mathbf{Z}_t = \mathbf{m}_{22,t} + 2\mathrm{i}\hbar\mathbf{m}_{21,t}\boldsymbol{\gamma}_0. \tag{A.27}$$

Finally, we set the remaining free parameter by establishing the relation between the initial generalized width parameter $\boldsymbol{\gamma}_0$ and the real-valued, diagonal width parameter matrix $\boldsymbol{\gamma}$,

$$\boldsymbol{\gamma}_0 \equiv \boldsymbol{\gamma}/2. \tag{A.28}$$

Comparing the four last equations with Eq. (A.16), we see that we have indeed recovered the latter.

B. BATH TEMPERATURE IN QUANTUM CALCULATIONS

For a full quantum description of a system embedded in a finite temperature bath as in Ch. 5, one might choose the thermal bath density operator in coherent state representation from Ch. 3 as part of an initial product state and then solve the Liouville-von Neumann equation. Since we are using the WavePacket software [90,91] which provides a very efficient split operator fast Fourier transform based algorithm for the calculation of the dynamics of wave functions rather than densities, our approach is a bit different. We will present the underlying considerations in this appendix.

In order for a density matrix to describe the time evolution of a system, has to be a solution to the Liouville-von Neumann (LvN) equation

$$\mathrm{i}\hbar\frac{\partial}{\partial t}\hat{\rho}(t) = \left[\hat{H}, \hat{\rho}(t)\right], \tag{B.1}$$

with the open system Hamiltonian $\hat{H} = \hat{H}_\mathrm{s} + \hat{H}_\mathrm{b} + \hat{H}_\mathrm{sb}$. If the initial state is a pure state

$$|\Phi_n(0)\rangle = |\Psi_\mathrm{s}(0)\rangle\,|n\rangle\,, \tag{B.2}$$

where $|n\rangle$ denotes eigenstates of the bath, $\hat{H}_\mathrm{b}|n\rangle = E_{\mathrm{b},n}|n\rangle$, the corresponding initial density takes the form

$$\hat{\rho}_n(0) = |\Psi_\mathrm{s}(0)\rangle\,\langle\Psi_\mathrm{s}(0)|n\rangle\,\langle n| \tag{B.3}$$

The wave function evolving from initial condition (B.2) is described by the time-dependent Schrödinger Eq. (2.1) and denoted by $|\Phi_n(t)\rangle$. Multiplying Eq. (2.1) by $\langle\Phi_n(t)|$ and subtracting the complex conjugate of this expression, one finds the LvN Eq. (B.1) fulfilled by

$$\hat{\rho}_n(t) = |\Phi_n(t)\rangle\,\langle\Phi_n(t)|\,. \tag{B.4}$$

If we choose the initial bath density not as an individual pure state but instead as a thermal state weighted by Boltzmann factors,

$$\hat{\rho}(0) = \frac{1}{\mathrm{Tr}(\mathrm{e}^{-\beta\hat{H}_\mathrm{b}})}\sum_n |\Psi_\mathrm{s}(0)\rangle\,\langle\Psi_\mathrm{s}(0)|\,\mathrm{e}^{-\beta\hat{H}_\mathrm{b}}\,|n\rangle\,\langle n| \tag{B.5}$$

$$= \frac{1}{Z_\mathrm{b}}\sum_n \mathrm{e}^{-\beta E_{\mathrm{b},n}}\,|\Phi_n(0)\rangle\,\langle\Phi_n(0)|\,, \tag{B.6}$$

where $\beta = 1/k_\mathrm{B}T$ is the inverse temperature and Z_b is the bath partition sum, the time evolution after insertion of the individual contributions $|\Phi_n(t)\rangle$ according to Eq. (B.1) amounts to

$$\mathrm{i}\hbar\frac{\partial}{\partial t}\hat{\rho}(t) = \frac{1}{Z_\mathrm{b}}\sum_n \mathrm{e}^{-\beta E_{\mathrm{b},n}}\left[\hat{H},\hat{\rho}_n(t)\right] = \left[\hat{H},\hat{\rho}(t)\right]. \tag{B.7}$$

Thus, we can describe the time evolved reduced density matrix as

$$\hat{\rho}(t) = \frac{1}{Z_\mathrm{b}}\sum_n \mathrm{e}^{-\beta E_{\mathrm{b},n}}\left|\Phi_n(t)\right\rangle\left\langle\Phi_n(t)\right|, \tag{B.8}$$

where $E_{\mathrm{b},n}$ is the sum of the bath eigenenergies to a set of eigenstates denoted by $|n\rangle_\mathrm{b}$. For the practical implementation of the FFT algorithm, we use the third order Strang splitting propagation method [117, 118] as implemented in the WavePacket software [90, 91]. With this code, we can propagate individual wave functions $|\Phi_n(t)\rangle$ and afterwards sum up the different contributions according to Eq. (B.8). Since we assume the bath DOFs to be harmonic close to their respective potential minima, we use one-dimensional harmonic oscillator eigenstates $|n_j\rangle_\mathrm{b}$ to construct the initial bath states,

$$|n\rangle_\mathrm{b} = \prod_{j=0}^{N_\mathrm{b}}|n_j\rangle_\mathrm{b}. \tag{B.9}$$

The frequencies of these oscillators are the harmonic approximations obtained in the normal coordinate transformation. Consequently, the bath eigenenergy in the weight factor of Eq. (B.8) is the sum of the eigenenergies of the states pertaining to $|n\rangle$,

$$E_{\mathrm{b},n} = \sum_{j=0}^{N_\mathrm{b}} E_{\mathrm{b},n_j}, \tag{B.10}$$

where the n_jth excited state of bath oscillator j has energy $E_{\mathrm{b},n_j} = \hbar\omega_j(n_j + 0.5)$.

As can be seen in Eq. (B.8), the number of bath states that contribute significantly to the partition sum $Z_\mathrm{b} = \sum_{n=1}^{\infty}\mathrm{e}^{-\beta E_{\mathrm{b},n}}$ grows with temperature. With the numerical treatment requiring a cutoff at a finite number of bath states, we find another reason why this approach works best in a low-temperature regime, as discussed in Ch. 5.

C. CALCULATION OF THE HARMONIC OSCILLATOR SPECTRUM WITH THE TIME AVERAGED HYBRID METHODS

In this appendix, we will show that the hybrid results derived in Sec. 3.2.2 reproduce the analytic spectrum of a GWP in a harmonic potential with frequency ω accurately. We restrict the discussion to one HO in thawed Gaussian approximation, i.e., we take the limit $N = N_{\mathrm{tg}} = 1$ and $N_{\mathrm{hk}} = 0$ of Eqs. (3.46) and (3.51).

The analytic result for the spectrum is part of any introductory quantum mechanics course and can be found elegantly with creation and annihilation operators [150]. We state it here just for reference without derivation. A coherent state $|\alpha\rangle$ in position representation

$$\Psi_\alpha(x) = \left(\frac{m\omega}{\pi\hbar}\right)^{1/4} \exp\left\{-\frac{m\omega}{2\hbar}\left(x - q_\alpha\right)^2 + \frac{\mathrm{i}}{\hbar} p_\alpha \left(x - q_\alpha\right)\right\} \tag{C.1}$$

can be expanded in terms of HO eigenstates $\varphi_n(x)$

$$\Psi_\alpha(x) = \mathrm{e}^{-|\alpha|^2/2} \sum_{n=0}^{\infty} \frac{\alpha^n}{\sqrt{n!}} \varphi_n(x), \tag{C.2}$$

where α is the eigenvalue of the annihilation operator to eigenvector $|\alpha\rangle$,

$$\alpha = \sqrt{\frac{m\omega}{2\hbar}} q_\alpha + \mathrm{i}\sqrt{\frac{1}{2m\omega\hbar}} p_\alpha. \tag{C.3}$$

The spectrum of this state is a series of peaks, whose heights are Poisson distributed, at eigenenergies E_n

$$I(E) = \mathrm{e}^{-|\alpha|^2} \sum_{n=0}^{\infty} \frac{|\alpha|^{2n}}{n!} \delta\left(\hbar\omega\left[n + \frac{1}{2}\right]\right) \tag{C.4}$$

$$= \exp\left\{-\frac{m\omega}{2\hbar} q_\alpha^2 - \frac{1}{2m\omega\hbar} p_\alpha^2\right\} \sum_{n=0}^{\infty} \frac{1}{2^n n!} \left(\frac{m\omega}{\hbar} q_\alpha^2 + \frac{1}{m\omega\hbar} p_\alpha^2\right)^n \delta\left(\hbar\omega\left[n + \frac{1}{2}\right]\right). \tag{C.5}$$

In the following, we will use Eq. (C.1) as the initial state for dynamical calculations to show that the full hybrid expression yields the exact same result. After that, we demonstrate how the separation approximation that we proposed in Sec. 3.2.2 affects the outcome.

C.1. FULL HYBRID CALCULATION

In order to derive the analytic HO result (C.4) with the TG approximation, we use expression (3.46) for the case $N = N_{\mathrm{tg}} = 1$ and assume the initial GWP to be centered at phase space point (p_α, q_α) from the previous section and to have width $\gamma = m\omega/\hbar$

$$\begin{aligned} I(E) = \frac{1}{2\hbar}\frac{1}{\pi\hbar T}\,\mathrm{Re}\left(\int_0^T \mathrm{d}t_1 \int_{t_1}^{\infty} \mathrm{d}t_2 \exp\left\{\frac{\mathrm{i}}{\hbar}E(t_1-t_2) + \frac{\mathrm{i}}{\hbar}\left[\phi_{t_1}\left(p_\alpha,q_\alpha\right) - \phi_{t_2}\left(p_\alpha,q_\alpha\right)\right]\right\}\right. \\ \times \sqrt{\frac{1}{\det\left(\mathbf{A}^{\mathrm{sd}}_{t_1} + \left[\mathbf{A}^{\mathrm{sd}}_{t_2}\right]^*\right)}} \\ \left.\times \exp\left\{\frac{1}{4}\left(\mathbf{b}^{\mathrm{sd}}_{t_1} + \left[\mathbf{b}^{\mathrm{sd}}_{t_2}\right]^*\right)^{\mathrm{T}}\left(\mathbf{A}^{\mathrm{sd}}_{t_1} + \left[\mathbf{A}^{\mathrm{sd}}_{t_2}\right]^*\right)^{-1}\left(\mathbf{b}^{\mathrm{sd}}_{t_1} + \left[\mathbf{b}^{\mathrm{sd}}_{t_2}\right]^*\right) + c^{\mathrm{sd}}_{t_1} + \left(c^{\mathrm{sd}}_{t_2}\right)^*\right\}\right). \end{aligned} \tag{C.6}$$

We use the results for time evolved trajectory and classical action of the harmonic oscillator,

$$p_t = p_\alpha \cos\omega t - m\omega q_\alpha \sin\omega t \tag{C.7}$$

$$q_t = q_\alpha \cos\omega t + \frac{p_\alpha}{m\omega}\sin\omega t \tag{C.8}$$

$$S_t = \left(\frac{p_\alpha^2}{2m\omega} - \frac{m\omega q_\alpha^2}{2}\right)\cos\omega t \sin\omega t - p_\alpha q_\alpha \sin^2\omega t, \tag{C.9}$$

to calculate the different terms appearing in Eq. (C.6). Before we can do so, we need the stability matrix elements defined in Eqs. (2.22):

$$m_{11,t} = m_{22,t} = \cos\omega t \qquad m_{12,t} = -m\omega\sin\omega t \qquad m_{21,t} = \frac{\sin\omega t}{m\omega}. \tag{C.10}$$

For the phase of the HK prefactor, we get

$$\phi_t = \mathrm{phase}\left\{\left\{\det\left[\frac{1}{2}\left(m_{11,t} + m_{22,t} - \mathrm{i}\hbar\gamma m_{21,t} + \frac{\mathrm{i}}{\hbar\gamma}m_{12,t}\right)\right]\right\}^{1/2}\right\} \tag{C.11}$$

$$\phi_t = -\omega t/2. \tag{C.12}$$

The matrix $\mathbf{A}^{\mathrm{sd}}_{t_1} + \left(\mathbf{A}^{\mathrm{sd}}_{t_2}\right)^*$, that has been defined in Eqs. (3.41) through (3.44), becomes a constant in time, as do its inverse and determinant according to

$$\mathbf{A}^{\mathrm{sd}}_t = \frac{1}{4\hbar}\begin{pmatrix} 1/(m\omega) & \mathrm{i} \\ \mathrm{i} & m\omega \end{pmatrix} \tag{C.13}$$

$$\left(\mathbf{A}^{\mathrm{sd}}_{t_1} + \left[\mathbf{A}^{\mathrm{sd}}_{t_2}\right]^*\right)^{-1} = 2\hbar\begin{pmatrix} m\omega & 0 \\ 0 & 1/(m\omega) \end{pmatrix} \tag{C.14}$$

$$\det\left(\mathbf{A}^{\mathrm{sd}}_{t_1} + \left[\mathbf{A}^{\mathrm{sd}}_{t_2}\right]^*\right) = \frac{1}{4\hbar^2}. \tag{C.15}$$

The components of $\mathbf{b}^{\mathrm{sd}}_t$, as defined in Eqs. (3.39) and (3.40), take the form

$$b^{\mathrm{sd}}_{1,t} = \frac{1}{2\hbar}\left(\mathrm{e}^{-\mathrm{i}\omega t} - 1\right)\left(\frac{p_\alpha}{m\omega} + \mathrm{i}q_\alpha\right) \tag{C.16}$$

$$b^{\mathrm{sd}}_{2,t} = -\mathrm{i}\frac{m\omega}{2\hbar}\left(\mathrm{e}^{-\mathrm{i}\omega t} - 1\right)\left(\frac{p_\alpha}{m\omega} + \mathrm{i}q_\alpha\right) - \frac{\mathrm{i}}{\hbar}p_\alpha, \tag{C.17}$$

so the first part of the TG exponent in Eq. (C.6) becomes

$$\begin{aligned}\frac{1}{4}\left(\mathbf{b}_{t_1}^{\mathrm{sd}}+\left[\mathbf{b}_{t_2}^{\mathrm{sd}}\right]^*\right)^{\mathrm{T}}\left(\mathbf{A}_{t_1}^{\mathrm{sd}}+\left[\mathbf{A}_{t_2}^{\mathrm{sd}}\right]^*\right)^{-1}\left(\mathbf{b}_{t_1}^{\mathrm{sd}}+\left[\mathbf{b}_{t_2}^{\mathrm{sd}}\right]^*\right)\\ =\frac{m\omega}{2\hbar}\left(\frac{p_\alpha^2}{m^2\omega^2}+q_\alpha^2\right)\left(\mathrm{e}^{\mathrm{i}\omega(t_2-t_1)}-\mathrm{e}^{\mathrm{i}\omega t_1}-\mathrm{e}^{\mathrm{i}\omega t_2}+1\right).\end{aligned} \tag{C.18}$$

We calculate the scalar c_t^{sd} in the exponent using the definition from Eq. (3.37)

$$c_t^{\mathrm{sd}}=\frac{m\omega}{2\hbar}\left(\frac{p_\alpha^2}{m^2\omega^2}+q_\alpha^2\right)\left(\mathrm{e}^{-\mathrm{i}\omega t}-1\right), \tag{C.19}$$

insert all above results into Eq. (C.6) and finally arrive at an expression for the dynamically calculated spectrum that reads

$$\begin{aligned}I(E)=\frac{1}{\pi\hbar T}\,\mathrm{Re}\left(\int_0^T\mathrm{d}t_1\int_{t_1}^{\infty}\mathrm{d}t_2\;\exp\left\{\frac{\mathrm{i}}{\hbar}\left[E(t_1-t_2)-\frac{\hbar\omega}{2}(t_1-t_2)\right]\right\}\right.\\ \left.\times\exp\left\{\frac{m\omega}{2\hbar}\left(\frac{p_\alpha^2}{m^2\omega^2}+q_\alpha^2\right)\left(\mathrm{e}^{-\mathrm{i}\omega(t_1-t_2)}-1\right)\right\}\right).\end{aligned} \tag{C.20}$$

We can now change integration variables to $\tau_1=t_1$ and $\tau=t_2-t_1$ and carry out the integration over τ_1 to get

$$I(E)=\frac{1}{\pi\hbar}\,\mathrm{Re}\left(\int_0^{\infty}\mathrm{d}\tau\;\exp\left\{\frac{\mathrm{i}}{\hbar}\left(E-\frac{\hbar\omega}{2}\right)\tau+\frac{m\omega}{2\hbar}\left(\frac{p_\alpha^2}{m^2\omega^2}+q_\alpha^2\right)\left(\mathrm{e}^{\mathrm{i}\omega\tau}-1\right)\right\}\right). \tag{C.21}$$

The penultimate step is to take out the time independent term and do a power series expansion of the second part of the exponential

$$\begin{aligned}I(E)=\exp\left\{-\frac{p_\alpha^2}{2m\omega\hbar}-\frac{m\omega q_\alpha^2}{2\hbar}\right\}\\ \times\sum_{n=0}^{\infty}\frac{1}{2^n n!}\left(\frac{p_\alpha^2}{m\omega\hbar}+\frac{m\omega q_\alpha^2}{\hbar}\right)^n\frac{1}{\pi\hbar}\,\mathrm{Re}\left(\int_0^{\infty}\mathrm{d}\tau\;\exp\left\{-\frac{\mathrm{i}}{\hbar}\left[E-\hbar\omega\left(n+\frac{1}{2}\right)\right]\tau\right\}\right),\end{aligned} \tag{C.22}$$

which leaves an integration that results in the desired series of HO eigenfrequencies

$$I(E)=\exp\left\{-\frac{p_\alpha^2}{2m\omega\hbar}-\frac{m\omega q_\alpha^2}{2\hbar}\right\}\sum_{n=0}^{\infty}\frac{1}{2^n n!}\left(\frac{p_\alpha^2}{m\omega\hbar}+\frac{m\omega q_\alpha^2}{\hbar}\right)^n\delta\left[E-\hbar\omega\left(n+\frac{1}{2}\right)\right]. \tag{C.23}$$

This outcome is identical with the exact one in Eq. (C.4), which does not come as a surprise since the TG approximation is exact for harmonic potential. We will use the results from this section to motivate our suggestion for a separation into factors that depend on t_1 or t_2 only.

C.2. SEPARABLE HYBRID CALCULATION

In order to find out how the proposed separation approximation affects the hybrid result for the harmonic oscillator spectrum, we start at Eq. (3.51), again for $N = N_{\mathrm{tg}} = 1$

$$\begin{aligned} I(E) = \frac{1}{4\pi\hbar^2 T} \Bigg| \int_0^T \mathrm{d}t \, \mathrm{e}^{\mathrm{i}[Et+\phi_t(p_\alpha,q_\alpha)]/\hbar} \\ \times \left[\det\left(\mathbf{A}_t^{\mathrm{sd}} + \left[\mathbf{A}_t^{\mathrm{sd}}\right]^*\right)\right]^{-1/4} \exp\left\{\frac{1}{4}\left(\mathbf{b}_{\mathrm{m},t}^{\mathrm{sd}}\right)^{\mathrm{T}}\left(\mathbf{A}_t^{\mathrm{sd}} + \left[\mathbf{A}_t^{\mathrm{sd}}\right]^*\right)^{-1}\mathbf{b}_{\mathrm{m},t}^{\mathrm{sd}} + c_t^{\mathrm{sd}}\right\}\Bigg|^2 . \end{aligned} \tag{C.24}$$

We can first look at Eqs. (C.19) and (C.21) to note that, in the transformed variable τ, the part of the exponential that stems from the TG approximation is identical with c_t^{sd} (up to complex conjugation, which is irrelevant here since we are only interested in the real part of the integrand). Comparing Eq. (C.21) to Eq. (C.24), it is obvious that the c_t^{sd} term has to be the only contribution to the TG exponential after separation. If the separation is done as proposed in Eq. (3.47), $\mathbf{b}_{\mathrm{m},t}^{\mathrm{sd}}$ has to be chosen as

$$\mathbf{b}_{\mathrm{m},t}^{\mathrm{sd}} = \begin{pmatrix} b_{1,t}^{\mathrm{sd}} \\ b_{2,t}^{\mathrm{sd}} + \mathrm{i}p_{\alpha,\mathrm{tg}}/\hbar \end{pmatrix} \tag{C.25}$$

to make the first term in the exponential disappear. This modification is only natural since the constant imaginary part of the second component vanishes in the full expression on the LHS in (3.47), so there should be no contribution from it after the separation either. The prefactor $\left|\mathbf{A}_{t_1}^{\mathrm{sd}} + \left(\mathbf{A}_{t_2}^{\mathrm{sd}}\right)^*\right|^{-1/2}$ does not depend on time for the HO, so we simply use separation (3.50) to get the same overall prefactor as before.

Inserting results from the previous section into Eq. (C.24), we obtain

$$I(E) = \frac{1}{2\pi\hbar T}\left|\int_0^T \mathrm{d}t \;\exp\left\{\frac{\mathrm{i}}{\hbar}\left(Et - \frac{\hbar\omega}{2}t\right) + \frac{m\omega}{2\hbar}\left(\frac{p_\alpha^2}{m^2\omega^2} + q_\alpha^2\right)\left(\mathrm{e}^{-\mathrm{i}\omega t} - 1\right)\right\}\right|^2 . \tag{C.26}$$

We can do the same power series expansion as before and take out the constant part of the exponential, then unravel the modulus

$$\begin{aligned} I(E) = {} & \exp\left\{-\frac{p_\alpha^2}{m\omega\hbar} - \frac{m\omega q_\alpha^2}{\hbar}\right\}\frac{1}{2\pi\hbar T} \\ & \times \left|\sum_{n=0}^{\infty}\frac{1}{2^n n!}\left(\frac{p_\alpha^2}{m\omega\hbar} + \frac{m\omega q_\alpha^2}{\hbar}\right)^n \int_0^T \mathrm{d}t \;\exp\left\{\frac{\mathrm{i}}{\hbar}\left[E - \hbar\omega\left(n+\frac{1}{2}\right)\right]t\right\}\right|^2 \end{aligned} \tag{C.27}$$

$$\begin{aligned} = {} & \exp\left\{-\frac{p_\alpha^2}{m\omega\hbar} - \frac{m\omega q_\alpha^2}{\hbar}\right\}\frac{1}{2\pi\hbar T}\sum_{n,m}\frac{1}{2^{n+m}n!m!}\left(\frac{p_\alpha^2}{m\omega\hbar} + \frac{m\omega q_\alpha^2}{\hbar}\right)^{n+m} \\ & \times \int_0^T \mathrm{d}t_1 \int_0^T \mathrm{d}t_2 \;\exp\left\{\frac{\mathrm{i}}{\hbar}\left[\left(E - \hbar\omega\left(n+\frac{1}{2}\right)\right)t_1 - \left(E - \hbar\omega\left(m+\frac{1}{2}\right)\right)t_2\right]\right\}. \end{aligned} \tag{C.28}$$

The double time integration yields non-zero results only for $m \neq n$, so the double sum collapses into a single summation and the remaining time integration can be performed as in the previous

section to result in

$$I\left(E\right)=\exp\left\{-\frac{p_\alpha^2}{m\omega\hbar}-\frac{m\omega q_\alpha^2}{\hbar}\right\}\sum_{n=0}^{\infty}\frac{1}{(n!)^2}\left(\frac{p_\alpha^2}{2m\omega\hbar}+\frac{m\omega q_\alpha^2}{2\hbar}\right)^{2n}\delta\left[E-\hbar\omega\left(n+\frac{1}{2}\right)\right] \quad \text{(C.29)}$$

From Eq. (C.29), we see that the separable approximation reproduces the HO peak positions exactly, while peak weights are the exact ones (C.23) squared. Therefore, excited TG (bath) states will be suppressed in the total spectrum compared to exact, HK and full hybrid results, but no accuracy is lost compared to the full hybrid calculation.

Although this reasoning is exact only for the HO, it is still sufficient to motivate Eq. (3.51) as a fast but still accurate tool for the description of system-bath dynamics. First, bath states are expected to be close to equilibrium and with that, their evolution will take place in the almost harmonic region of the potential. Second, we remind the reader that this separation of time variables is carried out only for the "bath" subsystem which is described by the TG approximation, i.e., for those DOFs where we assume harmonic behavior anyway. Third, more highly excited bath states that are not reproduced exactly will be suppressed automatically in the final outcome.

Finally, it should be mentioned that due to the very simple form of the terms that enter into the hybrid expression for the HO case, the way to perform the separation is somewhat arbitrary. A minimalistic alternative would be to set the non-separable term in the exponential of Eq. (3.46) or Eq. (C.6) to zero and the determinantial prefactor to one. The spectrum then becomes

$$I(E)\sim\int \mathrm{d}^{N_\mathrm{hk}}p\;\mathrm{d}^{N_\mathrm{hk}}q\;\left|\int_0^T\mathrm{d}t\;\mathrm{e}^{\mathrm{i}Et/\hbar+\mathrm{i}\phi_t(\mathbf{p}_{\alpha,0},\mathbf{q}_{\alpha,0})/\hbar+c_t^\mathrm{sd}}\left\langle g_{\mathrm{hk},\alpha}|g_{\alpha,t,\mathrm{hk}}(\mathbf{p}_{\alpha,0},\mathbf{q}_{\alpha,0})\right\rangle\right|^2. \quad \text{(C.30)}$$

This approximation corresponds to a HK calculation where only some DOFs are sampled, while others are propagated with single frozen Gaussians. For the HO, it still recovers the exact peak positions, but it is below the level of the hybrid description.

D. NUMERICAL CONSIDERATIONS FOR EXCITED STATE CALCULATION

In Ch. 2, we have shown that the time averaged HK method in separable approximation is capable of reproducing both ground and first excited state energies of the 1D Morse oscillator with high accuracy. Given that the separable approximation is exact for the harmonic oscillator, one might argue that a much better test for the reliability of the method would be to look at higher excitations and thus at regions of the Morse potential that are far from harmonic. While it might not be very relevant for most applications of the method to realistic systems because one is mainly interested in the dynamics close to the ground state, there still is a numerical subtlety that calls for a short discussion.

For this, we take the same Morse potential as in Sec. 3.2.3, i.e., $D_\mathrm{e} = 0.057$ a.u., $R_\mathrm{e} = 5.038$ a.u., and $\alpha = 0.983$ a.u., with reduced mass $m_\mathrm{r} = 1.165 \times 10^5$ a.u. This time, the initial position is still at equilibrium, but the initial momentum is now higher, namely at $p_0 = \sqrt{2 m_\mathrm{r} E_n}$, with E_n the analytic value of the nth eigenvalue of the Morse potential from Eq. (3.53), and the width parameter is taken to be $\gamma = m_\mathrm{r}\omega_\mathrm{e}$. The time grid is chosen such that the frequency resolution is about 10^{-6} a.u. All spectra in this appendix are normalized such that the respective biggest peak has height one.

D.1. SINGLE TRAJECTORIES AND PEAK SHAPES

In order to discuss the numerical implications for the higher excitations, we first have to understand the contribution of a single trajectory, which is also related to the asymmetric peak shape of the separable approximation TA HK result. Therefore, we perform a calculation with a single Gaussian with initial energy E_{10} to get the spectrum shown in Fig. D.1. We see immediately that the peak closest to the initial energy is reproduced most faithfully. This is intuitively clear and also well-known from the literature [30, 31, 33, 72–74]. The whole multiple coherent state time averaging methodology (MC TA SC-IVR) is based on this finding and has proven a numerically cheap tool for the accurate determination of peak positions for realistic systems with anharmonic potentials that have to be calculated on-the-fly.

What is more interesting, however, is the position of the other numeric peaks with respect to the analytic ones. As can be seen in the figure and also from Tab. D.1, they are *always* shifted to the right of the exact result. The reason for this behavior can be found from the difference of neighboring energies in the table. While this value should decrease for a Morse

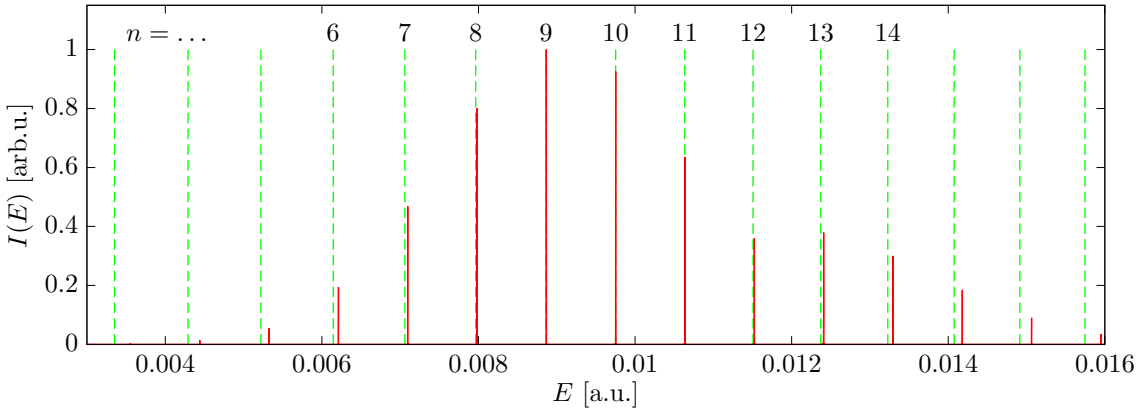

Figure D.1.: Single trajectory spectrum for initial energy E_{10} (red solid lines) and analytic result for the peak positions (vertical green dashed lines).

n	$E_{n,\text{exact}}$ [a.u.]	$E_{n,\text{numer}}$ [a.u.]	$\Delta E_{n,\text{exact}}$ [a.u.]	$\Delta E_{n,\text{numer}}$ [a.u.]
7	7.060×10^{-3}	7.097×10^{-3}	9.14×10^{-4}	8.85×10^{-4}
8	7.966×10^{-3}	7.982×10^{-3}	9.06×10^{-4}	8.85×10^{-4}
9	8.863×10^{-3}	8.868×10^{-3}	8.98×10^{-4}	8.85×10^{-4}
10	9.753×10^{-3}	9.753×10^{-3}	8.89×10^{-4}	8.85×10^{-4}
11	1.063×10^{-3}	1.064×10^{-2}	8.81×10^{-4}	8.85×10^{-4}
12	1.151×10^{-2}	1.152×10^{-2}	8.73×10^{-4}	8.86×10^{-4}
13	1.238×10^{-2}	1.241×10^{-2}	8.65×10^{-4}	8.85×10^{-4}

Table D.1.: Energies and energy differences $E_n - E_{n-1}$ for excited states of the Morse spectrum in Fig. D.1. The energy of the single trajectory is $E_{10} = 9.753 \times 10^{-3}$ a.u.

potential, the underlying assumption of harmonicity by the single trajectory calculation yields a constant energy difference $\Delta E_{n,\text{numer}}$, which is equal to the so-called local frequency $\omega_{\text{loc}}(E)$ of a classical Morse oscillator [27, 151] at energy E,

$$\omega_{\text{loc}}(E) = \omega_{\text{e}} \sqrt{1 - \frac{E}{D_{\text{e}}}}. \tag{D.1}$$

For trajectories with an eigenenergy E_n from Eq. (3.53) taken as the initial energy, ω_{loc} becomes the mean value of the two neighboring eigenenergies

$$\omega_{\text{loc}}(E_n) = \omega_{\text{e}} \left[1 - 2x_{\text{e}} \left(n + \frac{1}{2}\right)\right] = \frac{E_{n+1} + E_{n-1}}{2} \tag{D.2}$$

$$= \frac{E_{n+1} - E_n + (E_n - E_{n-1})}{2} \equiv \frac{\Delta E_{n+1,\text{exact}} - \Delta E_{n,\text{exact}}}{2}, \tag{D.3}$$

where we have included the last line to make it easier to see that this works out nicely in our example in Tab. D.1. Now taking the exactly reproduced peak at E_n as the reference, it is clear that subtracting multiples of ω_{loc}, which is smaller than $\Delta E_{k,\text{exact}}$ for $k < n$, yields energies E_k that are larger than the exact results. Conversely, $\omega_{\text{loc}}(E_n)$ is larger than $\Delta E_{k,\text{exact}}$ for $k > n$. Adding multiples to the reference peak results in peak positions that are also shifted to the right. Thus, the single trajectory result overestimates all peak positions except for the

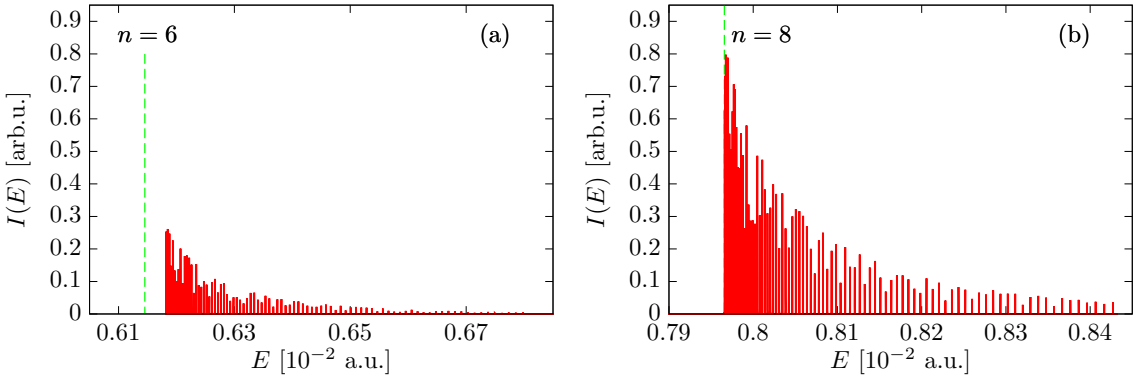

Figure D.2.: Individual spectral contributions of 90 trajectories with energies uniformly distributed between 0.827×10^{-2} a.u. and 1.702×10^{-2} a.u. Each trajectory contributes one red line to both the left and the right panel. The green dashed line indicates the exact, analytic peak position. The units for $I(E)$ are the same ones as in Fig. D.3.

ones closest to the trajectory's energy. As a consequence, we note that the single trajectory spectrum is not the spectrum of a harmonic oscillator with frequency $\omega_{\mathrm{loc}}(E_n)$ in the sense that in general there will be no ground state with energy $\omega_{\mathrm{loc}}/2$. Returning to the question of peaks shapes that stood at the beginning of this section, we once again take a look at the separable approximation TA HK expression from Eq. (3.34),

$$I(E) = \frac{1}{(2\pi\hbar)^N} \frac{1}{2\pi\hbar T} \int \mathrm{d}^N p \int \mathrm{d}^N q \left| \int_0^T \mathrm{d}t \, \langle \chi | g(\mathbf{p}_t, \mathbf{q}_t) \rangle \, \mathrm{e}^{\mathrm{i}[S_t(\mathbf{p},\mathbf{q}) + Et + \phi_t(\mathbf{p},\mathbf{q})]/\hbar} \right|^2 . \tag{D.4}$$

One of the reasons for its favorable numerical properties compared to the exact Eqs. (3.30) and (3.32) was that the phase space integrand is a positive definite quantity. However, this form also means that contributions from different trajectories no longer cancel each other. The exact peak positions emerge because each single trajectory spectrum has the highest amplitudes at the peaks that it reproduces accurately. Contributions to other peaks, which are always larger than the exact value, get damped out but do not vanish completely.

The buildup of an asymmetric peak shape as in Figs. 3.1 and D.3 is demonstrated by Fig. D.2. Here, we show the regions close to two different exact peak positions (dashed green lines), together with the respective two contributions from 90 different single trajectories (solid red lines) whose energies are no longer eigenenergies but distributed uniformly on an interval starting a bit above the 8th and ending a bit below the 19th excited state. Since the higher eigenenergy E_8 (Fig. D.2(b)) is almost contained in this interval, some trajectories are very close to it energetically and therefore we see peaks all the way to the exact position. By contrast, they end a bit short of the exact value for the lower eigenenergy (Fig. D.2(a)) because none of the trajectories is close enough to reproduce it exactly. Amplitudes increase as expected, though not monotonically due to the discreteness of the frequency grid. We also notice that distances between peaks increase with peak energy. This can be understood by remembering that the less accurate peaks are a multiple of some frequency ω_{loc} away from an accurately reproduced high energy peak; small differences in trajectory energy thus show up in an amplified fashion. The higher peak density close to the exact value also means that, for a sufficiently high number of trajectories, it is increasingly likely to find contributions from more than one trajectory at the

same energy grid point. Therefore, the peak in the final spectrum is narrower than suggested by Fig. D.2.

As a consequence of these peak shapes, the exact peak value to be read off these separable TA HK spectra is not a weighted average over the asymmetric peak, but the value at maximum amplitude.

D.2. GHOST PEAKS DUE TO PHASE SPACE SAMPLING

For the numerical evaluation of the phase space integral (D.4), a Monte Carlo integration is necessary in order to keep computational times low. The objective of this section is to show that the required phase space sampling is one possible source of unphysical "ghost peaks" for the example of the 1D Morse oscillator. Keeping in mind that there are of course other reasons for the appearance of unwanted features in the spectrum, especially for systems with many coupled degrees of freedom, we still think it is worthwhile to discuss this specific numerical peculiarity which can be nicely explained with the findings from the previous section.

Assuming an initial state $|\chi\rangle$ of Gaussian form centered at $(\mathbf{p}_\alpha, \mathbf{q}_\alpha)$, the initial phase space points are sampled with a weight that has the form of a Husimi distribution,

$$|\langle\chi|g(\mathbf{p},\mathbf{q})\rangle|^2 = \exp\left\{-\frac{1}{2}\left(\mathbf{q}-\mathbf{q}_\alpha\right)^{\mathrm{T}}\boldsymbol{\gamma}\left(\mathbf{q}-\mathbf{q}_\alpha\right) - \frac{1}{2\hbar^2}\left(\mathbf{p}-\mathbf{p}_\alpha\right)^{\mathrm{T}}\boldsymbol{\gamma}^{-1}\left(\mathbf{p}-\mathbf{p}_\alpha\right)\right\} \tag{D.5}$$

as proposed by Kaledin and Miller in the original paper on TA SC-IVR [29]. Through the sampling, the distribution function enters into the phase space integrand, which happens naturally for calculations where a function of this form is part of the semiclassical expression, as in the case of the semiclassical spectrum without time averaging in Eq. (3.30). In Eq. (D.4), we have to introduce it by multiplying the integrand by an appropriate unity,

$$\begin{aligned} I(E) = \frac{1}{(2\pi\hbar)^N}\frac{1}{2\pi\hbar T}\int \mathrm{d}^N p \int \mathrm{d}^N q \; |\langle\chi|g(\mathbf{p},\mathbf{q})\rangle|^2 \, |\langle\chi|g(\mathbf{p},\mathbf{q})\rangle|^{-2} \\ \times \left| \int_0^T \mathrm{d}t \, \langle\chi|g(\mathbf{p}_t,\mathbf{q}_t)\rangle \, \mathrm{e}^{\{\mathrm{i}[S_t(\mathbf{p},\mathbf{q})+Et+\phi_t(\mathbf{p},\mathbf{q})]/\hbar\}} \right|^2 . \end{aligned} \tag{D.6}$$

In the numerics, the first red term enters implicitly through the sampling, so the second one has to be an explicit part of the phase space integrand in order to get the correct relative weight of the peak amplitudes. While this works fine as long as the central trajectory is close to the vibrational ground state and the interest is solely in the first few excited states, the inverse of the sampling function might cause problems especially for highly excited reference states. If we pick a set of initial conditions that are very far away from the central trajectory, the correction weight of the corresponding trajectory becomes very large. Like every other one, this far off trajectory overestimates the positions of all peaks except for those close to its own energy. Due to its high weight, however, these values now show up prominently as artifacts or "ghost peaks" in the spectrum. An example is shown by the red lines in Fig. D.3. To show the general applicability of the considerations that follow, we no longer choose an exact eigenenergy of the Morse potential as the energy of the central trajectory. Instead, we use the simpler form $\tilde{E}_m = \omega_\mathrm{e}\,(m+0.5)$, and first discuss the case $m = 10$. Although 5×10^5 trajectories have been used in order to get Fig. D.3, the result looks horrifying, displaying a lot of ghost peaks that are in some cases bigger than the nearest exact value.

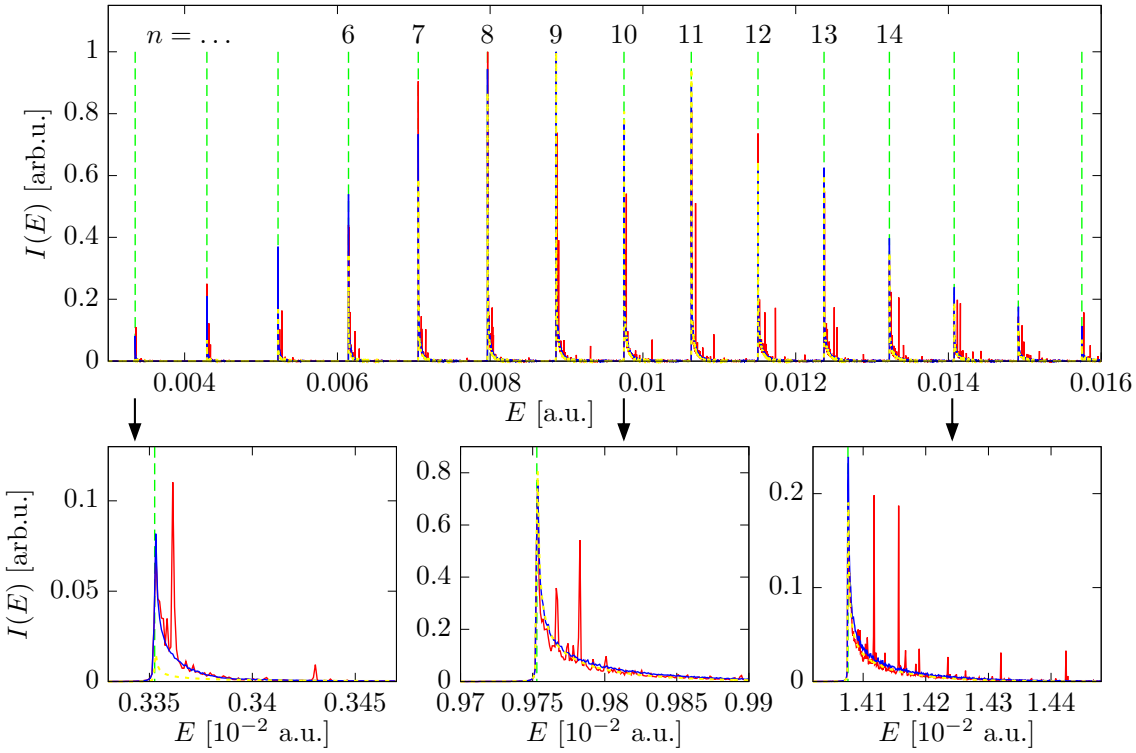

Figure D.3.: Spectrum for initial energy $\tilde{E}_{10} = 0.01021$ a.u. (red solid lines) and analytic result (green dashed lines). Trajectories with $D_{\mathrm{ps}} > 6$ have been discarded to get the blue line. No sampling correction has been made in calculations leading to the dotted yellow line. The black arrows indicate the peaks that are shown inflated in the lower panels.

The first idea how to get rid of these artifacts might be to just leave the correction factor out of the phase space integration. Since the factor is not time dependent, only the relative weight between trajectories is affected, leading to different peak amplitudes but still correct peak positions. This change does in fact remove the unphysical peaks, as shown by the dotted yellow curves in the lower panels of Fig. D.3. Neglecting the correction term causes a suppression of peaks far away from the one with maximum amplitude because it gets bigger with distance between trajectories in phase space, thus in particular for trajectories with much higher or lower energy than the central trajectory. The leftmost panel is a good example. While it is nice to solve the ghost peak problem in this easy manner, we would like to demonstrate that it is possible to keep the correction term and still get a sufficiently clear spectrum.

Having identified trajectories with a large initial phase space distance $D_{\mathrm{ps}} \equiv \gamma(q - q_\alpha)^2/2 + (p - p_\alpha)^2/(2\hbar^2\gamma)$ from the central trajectory as a possible source for the unwanted peaks, we can devise a mechanism where we discard trajectories above a certain value $D_{\mathrm{ps,max}}$. This is shown in a rough sketch in Fig. D.4, where the central energy trajectory is marked in blue, the region of allowed initial conditions is green and the minimum and maximum energy trajectories are marked as red ellipses. In the red shaded regions of phase space, no trajectories are propagated at all. Of course, the trajectories are not elliptic for an anharmonic potential, only the green area keeps this form. We perform calculations with a limiting value of $D_{\mathrm{ps,max}} = 6$, corresponding to a weight factor 400 compared to the central trajectory, resulting in about 0.25% of all trajectories being discarded. The consequence is again a complete and utter

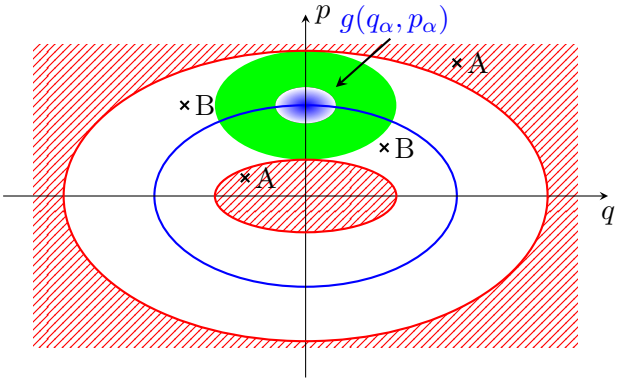

Figure D.4.: Cartoon picture of the discard mechanism.

disappearance of all ghost peaks from the spectrum, shown by the dark blue line in Fig. D.3.

Since there are different kinds of discarded trajectories, it would be interesting to know which ones cause the ghost peaks in the original expression: those that have either lower or higher energy than any of the accepted trajectories (red shaded regions in Fig. D.4, for example initial conditions at points with index A) or those that are in the same energy window as the accepted ones (points with index B).

We now look at a numerically cheaper example with 5000 trajectories and $D_{\mathrm{ps,max}} = 4$, but otherwise unchanged parameters of the propagation. In the upper part Fig. D.5, four results with different discarding criteria are compared. Discarding only the 53 trajectories with too high or too low energies (spectrum (iii)) is no different from discarding no trajectories at all (spectrum (iv)). An explanation for this can be found by looking again at Eq. (D.6). The overlap of the central Gaussian and the time-evolved trajectory, $\langle \chi | g(\mathbf{p}_t, \mathbf{q}_t) \rangle$, is very small for all times t if the energetic difference is large. Thus, these energetically very disparate trajectories do not contribute much to the phase space integrand. The trajectories with great phase space distance but small energetic difference from the central trajectory, on the other hand, do not have a particularly small time-dependent overlap. Consequently, neglecting only these 40 trajectories has the desired effect on the spectrum (spectrum (ii)), which is now pretty much identical with the one where all trajectories above $D_{\mathrm{ps,max}}$ are discarded.

In the lower part of Fig. D.5, we have plotted the results with and without discarding trajectories as before. In addition, we have plotted the results from four different single trajectory calculations (dotted green lines), where discarded initial conditions are chosen whose energies are distributed over the whole "green" energy range between 0.32 $\tilde{E}_{10}$ and 2.1 $\tilde{E}_{10}$, namely, at 0.35 $\tilde{E}_{10}$, 0.46 $\tilde{E}_{10}$, 1.1 $\tilde{E}_{10}$, and 2.0 $\tilde{E}_{10}$. One can see that the peak positions of the single trajectories are indeed reflected as artifacts in the regular spectrum, whereas these artifacts have disappeared from the spectrum where far off trajectories have been neglected. A closer look reveals that the two prominent peaks in the low energy region in the left panel originate from the two low energy trajectories, whereas the ghost peaks in the high energy panel are caused by the high energy trajectories, as expected.

Finally, we demonstrate the full glory of the separable TA SC-IVR by looking at a spectrum from a calculation with initial energy $\tilde{E}_{40}$. Again, we use 5×10^5 trajectories. Here, the aforementioned problem with disparate initial conditions renders the full spectrum useless (red line in Fig. D.6). Without knowledge of the exact spectrum, it becomes difficult to differentiate between real peaks and noisy contributions. With a phase space distance cutoff of $D_{\mathrm{ps,max}} = 6$, discarding the 0.25% of trajectories that are above this value produces the clean

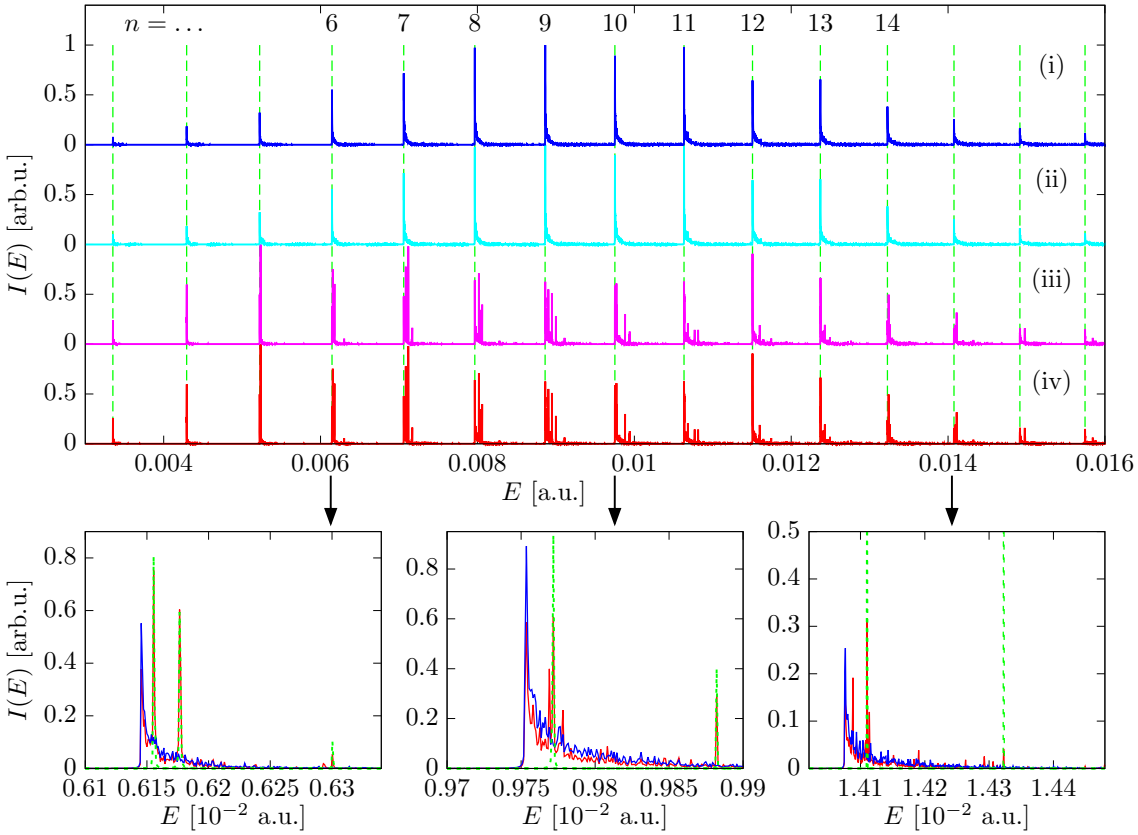

Figure D.5.: Spectra obtained from calculations with 5000 trajectories by discarding all trajectories above $D_{\mathrm{ps,max}}$ (solid blue lines), discarding only those from the white region in Fig. D.4 (light blue), discarding only those with highest and lowest energies (magenta) and by discarding no trajectories at all (red lines). Dashed green lines in the upper panel represent analytic peak positions, the dotted green lines in the lower panels are single trajectory calculations with initial conditions that have been discarded to obtain the blue curves. The black arrows indicate the peaks that are shown inflated in the lower panels.

and unambiguous upper graph in the picture (blue line). The missing weight of the neglected trajectories brings about a background close to the central energy, which does, however, not impeach the clarity of the spectrum. We append one last Tab. D.2 where we collect some of the 80 energy eigenvalues that can be identified clearly in the spectrum. It is impressive to see that even the peaks at the outer edges of the spectrum are reproduced exactly within the frequency resolution, especially high energies up to 0.0552 a.u., which is already close to the dissociation energy $D_{\mathrm{e}} = 0.057$ a.u. deep in the anharmonic region of the potential.

In summary, we have first demonstrated in this appendix how the positive definite phase space integrand of the separable approximation TA SC-IVR brings about asymmetric peak shapes. Second, ghost peaks in one-dimensional calculations with high initial energy have been explained as artifacts from the sampling correction. These artifacts can be removed by either discarding very few critical trajectories or neglecting the correction term, resulting in spectra with a huge number of peaks that can be identified, all of which are exactly at the analytic

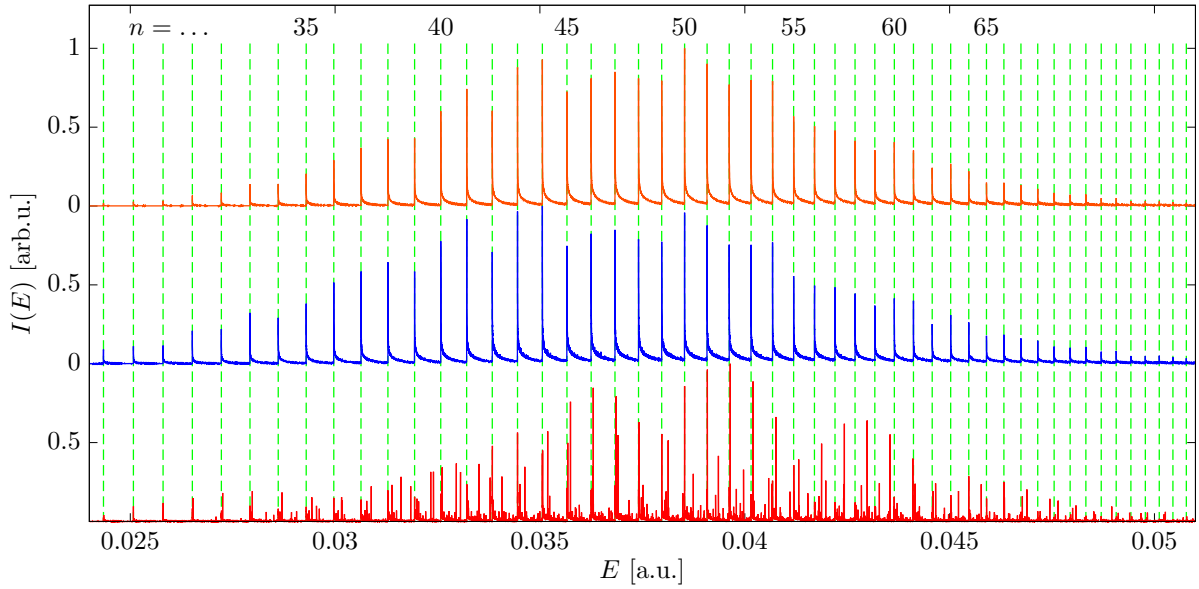

Figure D.6.: Spectrum for central trajectory with energy 0.0394 a.u.: standard phase space sampling (solid red lines), with discarding trajectories (blue) and without correction term (orange). Exact eigenenergies are indicated by dashed green lines.

n	$E_{n,\text{exact}}$	$E_{n,\text{numer}}$	n	$E_{n,\text{exact}}$	$E_{n,\text{numer}}$	n	$E_{n,\text{exact}}$	$E_{n,\text{numer}}$
17	1.5748	1.5747	42	3.3836	3.3836	80	5.1403	5.1404
18	1.6570	1.6570	43	3.4452	3.4452	81	5.1704	5.1704
19	1.7385	1.7386	44	3.5059	3.5059	82	5.1996	5.1996
20	1.8192	1.8191	45	3.5658	3.5658	83	5.2280	5.2281
21	1.8990	1.8989	46	3.6249	3.6250	84	5.2556	5.2556
22	1.9780	1.9779	47	3.6832	3.6832	85	5.2823	5.2823
23	2.0562	2.0561	48	3.7406	3.7407	86	5.3082	5.3082
24	2.1335	2.1334	49	3.7972	3.7972	87	5.3333	5.3334
25	2.2100	2.2099	50	3.8530	3.8530	88	5.3575	5.3576
26	2.2856	2.2856	51	3.9079	3.9080	89	5.3810	5.3810
27	2.3605	2.3605	52	3.9620	3.9620	90	5.4035	5.4036
28	2.4345	2.4345	53	4.0153	4.0153	91	5.4253	5.4253
29	2.5077	2.5077	54	4.0677	4.0678	92	5.4462	5.4463
30	2.5801	2.5800	55	4.1194	4.1194	93	5.4663	5.4664
31	2.6516	2.6515	56	4.1702	4.1702	94	5.4856	5.4857
32	2.7223	2.7222	57	4.2201	4.2202	95	5.5041	5.5041
33	2.7921	2.7921	58	4.2693	4.2693	96	5.5217	5.5217

Table D.2.: Energies extracted from the blue spectrum in Fig. D.6. The energy of the reference state is $\tilde{E}_{40} = 3.9382 \times 10^{-2}$ a.u. Resolution is 10^{-6} a.u., all values in the table are in 10^{-2} a.u.

energies. We stress once again that this is certainly not the only source of wrongly placed peaks, but that it might be a relevant contribution also for higher dimensional systems.

E. DERIVATIVES OF THE IODINE-KRYPTON POTENTIAL IN NORMAL COORDINATES

In this appendix, we will list the analytic expressions for the potential derivatives of the iodine in krypton problem discussed in Ch. 5. As mentioned in App. A and shown in more detail in App. B of [37], these derivatives are needed for the symplectic integration routine that is employed to find the time evolution of both the classical trajectories and their respective monodromy matrix elements. For the latter, the second derivatives of the Hamiltonian with respect to momentum and position are required. This does not introduce any fundamental algebraic difficulties, but the fact that we work in normal coordinates, while the pair potentials are given in Cartesian coordinates, makes the numerical evaluation of the position derivatives very cumbersome, as we will see below.

Recalling the normal coordinate transformation and its inverse from Eq. (5.5)

$$Q_i = \sum_{k=1}^{3N_\mathrm{a}} l_{ik}\tilde{q}_k \qquad \leftrightarrow \qquad \tilde{q}_k = \sum_{j=1}^{3N_\mathrm{a}} l_{kj}Q_j, \tag{E.1}$$

where Q_i are the normal coordinates, $\tilde{q}_k = \sqrt{m_k}(x_k - x_{k\mathrm{eq}})$ are mass-weighted displacement coordinates describing the deviation from equilibrium, l_{ik} are elements of the transformation matrix, and N_a is the number of atoms in the molecule. The momentum derivatives are simple because the kinetic energy has the same form as in Cartesian coordinates [116],

$$T = \frac{1}{2}\sum_{k=1}^{3N_\mathrm{a}} \dot{Q}_k. \tag{E.2}$$

With Eq. (E.1), the first and second derivatives of the potential with respect to the normal coordinates read

$$\frac{\partial V}{\partial Q_i} = \sum_{k=1}^{3N_\mathrm{a}} \frac{\partial \tilde{q}_k}{\partial Q_i}\frac{\partial V}{\partial \tilde{q}_k} = \sum_{k=1}^{3N_\mathrm{a}} l_{ki}\frac{\partial V}{\partial \tilde{q}_k} \tag{E.3}$$

$$\frac{\partial V}{\partial Q_i \partial Q_j} = \frac{\partial}{\partial Q_j}\sum_{k=1}^{3N_\mathrm{a}} l_{ki}\frac{\partial V}{\partial \tilde{q}_k} = \sum_{k=1}^{3N_\mathrm{a}}\sum_{l=1}^{3N_\mathrm{a}} l_{ki}l_{lj}\frac{\partial V}{\partial \tilde{q}_k \partial \tilde{q}_l}. \tag{E.4}$$

From a numerical perspective, it is important to note the double sum in the second line because each of these summations runs over all $N = 3N_\mathrm{a}$ Cartesian DOFs of the original problem. As a consequence, the calculation of the second derivatives takes up a big part of the total propagation time, mostly due to this transformation.

An example: the computational time for the most complicated phase space integrand, namely, the one for the reduced density contribution in Eq. (3.18), is about 16 seconds per trajectory with 500 semiclassical time steps and on a grid with 2^{14} grid points, if all 51 vibrational normal coordinates are used. Calculating the underlying two classical trajectories with 5000 time steps, on the other hand, takes about 96 seconds. Out of these 96 seconds, 87 seconds are required for the transformation from Eq. (E.4). For this reason, we use a Hessian update scheme as described by Zhuang et al [53] to facilitate the symplectic fourth-order, four-steps McLachlan integration [50, 124]. The exact second derivatives are calculated only once per two full classical steps, while we are making use of the gradients to calculate an approximate Hessian during the remaining seven sub-steps. This way, the 96 seconds for two classical trajectories are reduced to 27 seconds with still sufficient accuracy.

The expression for the derivatives with respect to the Cartesian displacement coordinates in Eqs. (E.4) and (E.4) would be very straightforward (see App. B of [37]) if it wasn't for the anisotropic I-Kr interaction from Eq. (5.2) that introduces a dependence not only on the modulus of the vector connecting the specific iodine and krypton atom, but also on the vector itself. However, as discussed for the iodine in argon problem in [69], using this form is imperative in order to recover the correct shift of the iodine spectrum.

After replacing the (normal) coordinate index k by an index consisting of atom number K and dimension ν, the first derivative becomes

$$\frac{\partial V}{\partial \tilde{q}_{K,\nu}} = \sum_{I\neq K}^{N_\mathrm{a}} \frac{\partial x_{K,\nu}}{\partial \tilde{q}_{K,\nu}} \frac{\partial V_{KI}}{\partial x_{K,\nu}} = \frac{1}{\sqrt{m_\mathrm{K}}} \sum_{I\neq K}^{N_\mathrm{a}} \frac{\partial V_{KI}}{\partial x_{K,\nu}}, \tag{E.5}$$

where $(x_{K,\nu} - x_{I,\nu})$ are the x, y and z components of the vector $\mathbf{R}_{KI,\nu}$ connecting atoms K and I, and V_{KI} is the respective pair potential. For the I-I and Kr-Kr interactions which depend only on the modulus R_{KI}, the coordinate derivative is simply

$$\frac{\partial V_{KI}\left(R_{KI}\right)}{\partial x_{K,\nu}} = \frac{\left(x_{K,\nu} - x_{I,\nu}\right)}{R_{KI}} \frac{\partial V_{KI}}{\partial R_{KI}}. \tag{E.6}$$

To calculate the derivatives of the I-Kr interaction from Eq. (5.2), we write the sine and cosine terms as

$$\cos^2(\theta_{KI}) \equiv \cos^2_{KI} = \left(\frac{\mathbf{R}_{12}^\mathrm{T}\mathbf{R}_{KI}}{R_{12}R_{KI}}\right)^2 \qquad \sin^2(\theta_{KI}) \equiv \sin^2_{KI} = 1 - \cos^2_{KI} \tag{E.7}$$

and arrive at a first derivative that depends on the derivative being with respect to an iodine

$$\begin{aligned} K = \begin{cases} 1 \\ 2 \end{cases},\ I \geq 3 : \frac{\partial V_{KI}}{\partial x_{K,\nu}} = \frac{\left(x_{K,\nu} - x_{I,\nu}\right)}{R_{KI}} \left[\cos^2_{KI} \frac{\partial V_\Sigma\left(R_{KI}\right)}{\partial R_{KI}} + \sin^2_{KI} \frac{\partial V_\Pi\left(R_{KI}\right)}{\partial R_{KI}}\right] \\ + 2\cos_{KI}\left[V_\Sigma(R_{KI}) - V_\Pi(R_{KI})\right] \left\{ \frac{\left(x_{1,\nu} - x_{2,\nu}\right) \pm \left(x_{K,\nu} - x_{I,\nu}\right)}{R_{12}R_{KI}} \right. \\ \left. - \left[\frac{\pm\left(x_{1,\nu} - x_{2,\nu}\right)}{R_{12}^2} + \frac{\left(x_{K,\nu} - x_{I,\nu}\right)}{R_{KI}^2}\right] \cos_{KI} \right\} \end{aligned} \tag{E.8}$$

or a krypton atom

$$K \leq 2,\ I \geq 3: \frac{\partial V_{KI}}{\partial x_{I,\nu}} = \frac{(x_{I,\nu} - x_{K,\nu})}{R_{KI}} \left[\cos^2_{KI} \frac{\partial V_\Sigma(R_{KI})}{\partial R_{KI}} + \sin^2_{KI} \frac{\partial V_\Pi(R_{KI})}{\partial R_{KI}}\right] + 2\cos_{KI}\left[V_\Sigma(R_{KI}) - V_\Pi(R_{KI})\right] \left\{\frac{(x_{2,\nu} - x_{1,\nu})}{R_{12}R_{KI}} - \frac{(x_{I,\nu} - x_{K,\nu})}{R^2_{KI}} \cos_{KI}\right\}. \tag{E.9}$$

In each case, the respective first line corresponds to Eq. (E.6), while the additional terms originate from the angle dependence and turn out to be a rather small correction to the first part, which is, however, important for the long-time dynamics.

For the second derivatives with respect to the displacements coordinates, we again have to differentiate,

$$K = J: \frac{\partial^2 V}{\partial \tilde{q}_{K,\nu} \tilde{q}_{K,\mu}} = \frac{1}{m_{\mathrm{K}}} \sum_{I \neq K}^{N_{\mathrm{a}}} \frac{\partial^2 V_{KI}}{\partial x_{K,\nu} \partial x_{K,\mu}} \tag{E.10}$$

$$K \neq J: \frac{\partial^2 V}{\partial \tilde{q}_{K,\nu} \tilde{q}_{K,\mu}} = \frac{1}{\sqrt{m_{\mathrm{K}}}\sqrt{m_{\mathrm{J}}}} \frac{\partial^2 V_{KJ}}{\partial x_{K,\nu} \partial x_{J,\mu}}. \tag{E.11}$$

For the solely R_{KI} dependent interactions, the derivatives with respect to Cartesian coordinates are then

$$K = J: \frac{\partial^2 V_{KI}}{\partial x_{K,\nu} \partial x_{K,\mu}} = \left[\frac{1}{R_{KI}}\delta_{\nu\mu} - \frac{(x_{K,\nu} - x_{I,\nu})(x_{K,\mu} - x_{I,\mu})}{R^3_{KI}}\right] \frac{\partial V_{KI}}{\partial R_{KI}} + \frac{(x_{K,\nu} - x_{I,\nu})(x_{K,\mu} - x_{I,\mu})}{R^2_{KI}} \frac{\partial^2 V_{KI}}{\partial R^2_{KI}} \tag{E.12}$$

$$K \neq J: \frac{\partial^2 V_{KJ}}{\partial x_{K,\nu} \partial x_{J,\mu}} = -\left[\frac{1}{R_{KJ}}\delta_{\nu\mu} - \frac{(x_{K,\nu} - x_{J,\nu})(x_{K,\mu} - x_{J,\mu})}{R^3_{KJ}}\right] \frac{\partial V_{KJ}}{\partial R_{KJ}} - \frac{(x_{K,\nu} - x_{J,\nu})(x_{K,\mu} - x_{J,\mu})}{R^2_{KJ}} \frac{\partial^2 V_{KJ}}{\partial R^2_{KJ}}. \tag{E.13}$$

Due to the angular dependence, the second derivatives of the I-Kr interaction become complicated to a point where algebra slips and mistakes in the numerical implementation are almost inevitable; therefore, we introduce a simplification by assuming that the iodine molecule moves along the z axis throughout the propagation, i.e., $x_{1,1} = x_{1,2} = x_{2,1} = x_{2,2} = 0$. This approximation is exact if symmetry preserving vibrational normal modes only are used in a propagation that starts from fully symmetric initial conditions. Adding non-symmetric normal modes violates the assumption, since a few of those modes comprise movement of the iodine atoms away from the z axis. However, the non-symmetric bath modes are coupled very weakly to the symmetric modes, especially to the system, so we get good results even for that case.

The cosine term is much simpler now,

$$\cos_{KI} = \mathrm{sgn}\left[(x_{1,3} - x_{2,3})\right] \frac{(x_{K,3} - x_{I,3})}{R_{KI}} = \frac{(x_{K,3} - x_{I,3})}{R_{KI}}, \tag{E.14}$$

where the second equality is ensured by choosing the initial positions of the iodine atoms accordingly. With this approximation, the first derivatives for $K \leq 2,\ I \geq 3$ from Eqs. (E.8)

and (E.9) become

$$\nu = 3: \quad \frac{\partial V_{KI}}{\partial x_{K,3}} = \frac{(x_{K,3} - x_{I,3})}{R_{KI}} \left[\cos^2_{KI} \frac{\partial V_\Sigma(R_{KI})}{\partial R_{KI}} + \sin^2_{KI} \frac{\partial V_\Pi(R_{KI})}{\partial R_{KI}}\right] + 2\cos_{KI}\left[V_\Sigma(R_{KI}) - V_\Pi(R_{KI})\right]\left\{\frac{1}{R_{KI}} - \frac{(x_{K,3} - x_{I,3})}{R^2_{KI}}\cos_{KI}\right\} \tag{E.15}$$

$$\frac{\partial V_{KI}}{\partial x_{I,3}} = \frac{(x_{I,3} - x_{K,\nu})}{R_{KI}} \left[\cos^2_{KI} \frac{\partial V_\Sigma(R_{KI})}{\partial R_{KI}} + \sin^2_{KI} \frac{\partial V_\Pi(R_{KI})}{\partial R_{KI}}\right] - 2\cos_{KI}\left[V_\Sigma(R_{KI}) - V_\Pi(R_{KI})\right]\left\{\frac{1}{R_{KI}} - \frac{(x_{K,3} - x_{I,3})}{R^2_{KI}}\cos_{KI}\right\}. \tag{E.16}$$

and

$$\nu \leq 2: \quad \frac{\partial V_{KI}}{\partial x_{I,\nu}} = \frac{(x_{I,\nu} - x_{K,\nu})}{R_{KI}} \left[\cos^2_{KI} \frac{\partial V_\Sigma(R_{KI})}{\partial R_{KI}} + \sin^2_{KI} \frac{\partial V_\Pi(R_{KI})}{\partial R_{KI}}\right] - 2\left[V_\Sigma(R_{KI}) - V_\Pi(R_{KI})\right]\frac{(x_{I,\nu} - x_{K,\nu})}{R^2_{KI}}\cos^2_{KI}. \tag{E.17}$$

Finally, the second derivatives with respect to Cartesian coordinates are split into a multitude of different cases, but each individual derivative is much simpler than it would be without the approximation. We differentiate between derivatives with respect to iodine coordinates only,

$$K = J \leq 2, I \geq 3, \ \nu = \mu = 3: \tag{E.18}$$

$$\begin{aligned}\frac{\partial^2 V_{KI}}{\partial x_{K,3}\partial x_{K,3}} = {} & \frac{1}{R_{KI}}\left[1 - \frac{(x_{K,3} - x_{I,3})^2}{R^2_{KI}}\right]\left[\cos^2_{KI}\frac{\partial V_\Sigma(R_{KI})}{\partial R_{KI}} + \sin^2_{KI}\frac{\partial V_\Pi(R_{KI})}{\partial R_{KI}}\right] \\ & + \frac{(x_{K,3} - x_{I,3})^2}{R^2_{KI}}\left[\cos^2_{KI}\frac{\partial^2 V_\Sigma(R_{KI})}{\partial R^2_{KI}} + \sin^2_{KI}\frac{\partial^2 V_\Pi(R_{KI})}{\partial R^2_{KI}}\right] \\ & + \frac{4\cos^2_{KI}\sin^2_{KI}}{R_{KI}}\left[\frac{\partial V_\Sigma(R_{KI})}{\partial R_{KI}} - \frac{\partial V_\Pi(R_{KI})}{\partial R_{KI}}\right] \\ & + \frac{2}{R^2_{KI}}\left(4\cos^4_{KI} - 5\cos^2_{KI} + 1\right)\left[V_\Sigma(R_{KI}) - V_\Pi(R_{KI})\right],\end{aligned}$$

mixed derivatives,

$$K \leq 2, \ J \geq 3, \ \nu = 3, \mu \leq 2: \tag{E.19}$$

$$\begin{aligned}\frac{\partial^2 V_{KJ}}{\partial x_{K,3}\partial x_{J,\mu}} = {} & \frac{(x_{K,3} - x_{J,3})(x_{K,\mu} - x_{J,\mu})}{R^3_{KJ}}\left[\cos^2_{KJ}\frac{\partial V_\Sigma(R_{KJ})}{\partial R_{KJ}} + \sin^2_{KJ}\frac{\partial V_\Pi(R_{KJ})}{\partial R_{KJ}}\right] \\ & - \frac{(x_{K,3} - x_{J,3})(x_{K,\mu} - x_{J,\mu})}{R^2_{KJ}}\left[\cos^2_{KJ}\frac{\partial^2 V_\Sigma(R_{KJ})}{\partial R^2_{KJ}} + \sin^2_{KJ}\frac{\partial^2 V_\Pi(R_{KJ})}{\partial R^2_{KJ}}\right] \\ & + 2\frac{(x_{K,\mu} - x_{J,\mu})}{R^2_{KJ}}\cos_{KJ}\left[\cos^2_{KJ} - \sin^2_{KJ}\right]\left[\frac{\partial V_\Sigma(R_{KJ})}{\partial R_{KJ}} - \frac{\partial V_\Pi(R_{KJ})}{\partial R_{KJ}}\right] \\ & + 4\frac{(x_{K,\mu} - x_{J,\mu})}{R^3_{KJ}}\cos_{KJ}\left[V_\Sigma(R_{KJ}) - V_\Pi(R_{KJ})\right]\left\{1 - 2\cos^2_{KJ}\right\}\end{aligned}$$

$$K \leq 2, \ J \geq 3, \ \nu = \mu = 3: \tag{E.20}$$

$$\frac{\partial^2 V_{KJ}}{\partial x_{K,3}\partial x_{J,3}} = -\frac{1}{R_{KJ}}\left(1 - \frac{(x_{K,3} - x_{J,3})^2}{R^2_{KJ}}\right)\left[\cos^2_{KJ}\frac{\partial V_\Sigma(R_{KJ})}{\partial R_{KJ}} + \sin^2_{KJ}\frac{\partial V_\Pi(R_{KJ})}{\partial R_{KJ}}\right]$$

$$
\begin{aligned}
&- \frac{\left(x_{K,3}-x_{J,3}\right)^2}{R_{KJ}^2}\left[\cos_{KJ}^2\frac{\partial^2 V_\Sigma\left(R_{KJ}\right)}{\partial R_{KJ}^2}+\sin_{KJ}^2\frac{\partial^2 V_\Pi\left(R_{KJ}\right)}{\partial R_{KJ}^2}\right]\\
&- \frac{4}{R_{KJ}}\cos_{KJ}^2\sin_{KJ}^2\left[\frac{\partial V_\Sigma\left(R_{KJ}\right)}{\partial R_{KJ}}-\frac{\partial V_\Pi\left(R_{KJ}\right)}{\partial R_{KJ}}\right]\\
&+ 2\frac{1}{R_{KJ}^2}\left[V_\Sigma\left(R_{KJ}\right)-V_\Pi\left(R_{KJ}\right)\right]\left\{5\cos_{KJ}^2-4\cos_{KJ}^4-1\right\},
\end{aligned}
$$

and derivatives with respect to krypton coordinates only,

$K\leq 2,\ J=I\geq 3,\ \nu\leq 2,\ \mu\leq 2:$ (E.21)

$$
\begin{aligned}
\frac{\partial^2 V_{KJ}}{\partial x_{J,\nu}\partial x_{J,\mu}} &= \frac{1}{R_{KJ}}\left[\delta_{\nu\mu}-\frac{\left(x_{K,\nu}-x_{J,\nu}\right)\left(x_{K,\mu}-x_{J,\mu}\right)}{R_{KJ}^2}\right]\left[\cos_{KJ}^2\frac{\partial V_\Sigma}{\partial R_{KJ}}+\sin_{KJ}^2\frac{\partial V_\Pi}{\partial R_{KJ}}\right]\\
&+ \frac{\left(x_{K,\nu}-x_{J,\nu}\right)\left(x_{K,\mu}-x_{J,\mu}\right)}{R_{KJ}^2}\left[\cos_{KJ}^2\frac{\partial^2 V_\Sigma\left(R_{KJ}\right)}{\partial R_{KJ}^2}+\sin_{KJ}^2\frac{\partial^2 V_\Pi\left(R_{KJ}\right)}{\partial R_{KJ}^2}\right]\\
&- 4\frac{\left(x_{K,\mu}-x_{J,\mu}\right)\left(x_{K,\nu}-x_{J,\nu}\right)}{R_{KJ}^3}\cos_{KJ}^2\left[\frac{\partial V_\Sigma\left(R_{KJ}\right)}{\partial R_{KJ}}-\frac{\partial V_\Pi\left(R_{KJ}\right)}{\partial R_{KJ}}\right]\\
&- 2\frac{\cos_{KJ}^2}{R_{KJ}^2}\left[\delta_{\nu\mu}-4\frac{\left(x_{K,\nu}-x_{J,\nu}\right)\left(x_{K,\mu}-x_{J,\mu}\right)}{R_{KJ}^2}\right]\left[V_\Sigma\left(R_{KJ}\right)-V_\Pi\left(R_{KJ}\right)\right]
\end{aligned}
$$

$K\leq 2,\ J=I\geq 3,\ \nu=3,\ \mu\leq 2:$ (E.22)

$$
\begin{aligned}
\frac{\partial^2 V_{KJ}}{\partial x_{J,3}\partial x_{J,\mu}} &= -\frac{\left(x_{K,3}-x_{J,3}\right)\left(x_{K,3}-x_{J,3}\right)}{R_{KJ}^3}\left[\cos_{KJ}^2\frac{\partial V_\Sigma\left(R_{KJ}\right)}{\partial R_{KJ}}+\sin_{KJ}^2\frac{\partial V_\Pi\left(R_{KJ}\right)}{\partial R_{KJ}}\right]\\
&- \frac{\left(x_{K,3}-x_{J,3}\right)}{R_{KJ}}\left[\cos_{KJ}^2\frac{\partial^2 V_\Sigma\left(R_{KJ}\right)}{\partial R_{KJ}^2}+\sin_{KJ}^2\frac{\partial^2 V_\Pi\left(R_{KJ}\right)}{\partial R_{KJ}^2}\right]\\
&+ 2\frac{\left(x_{K,\mu}-x_{J,\mu}\right)}{R_{KJ}^2}\cos_{KJ}\left(\sin_{KJ}^2-\cos_{KJ}^2\right)\left[\frac{\partial V_\Sigma\left(R_{KJ}\right)}{\partial R_{KJ}}+\frac{\partial V_\Pi\left(R_{KJ}\right)}{\partial R_{KJ}}\right]\\
&- 4\cos_{KJ}\frac{\left(x_{K,\mu}-x_{J,\mu}\right)}{R_{KJ}^3}\left(1-2\cos_{KJ}^2\right)\left[V_\Sigma\left(R_{KJ}\right)-V_\Pi\left(R_{KJ}\right)\right]
\end{aligned}
$$

$K\leq 2,\ J=I\geq 3,\ \nu=\mu=3:$ (E.23)

$$
\begin{aligned}
\frac{\partial^2 V_{KJ}}{\partial x_{J,3}\partial x_{J,\mu}} &= \frac{1}{R_{KJ}}\left[1-\frac{\left(x_{K,3}-x_{J,3}\right)^2}{R_{KJ}^2}\right]\left[\cos_{KJ}^2\frac{\partial V_\Sigma\left(R_{KJ}\right)}{\partial R_{KJ}}+\sin_{KJ}^2\frac{\partial V_\Pi\left(R_{KJ}\right)}{\partial R_{KJ}}\right]\\
&+ \frac{\left(x_{K,3}-x_{J,3}\right)^2}{R_{KJ}^2}\left[\cos_{KJ}^2\frac{\partial^2 V_\Sigma\left(R_{KJ}\right)}{\partial R_{KJ}^2}+\sin_{KJ}^2\frac{\partial^2 V_\Pi\left(R_{KJ}\right)}{\partial R_{KJ}^2}\right]\\
&+ \frac{\left(x_{K,3}-x_{J,3}\right)}{R_{KJ}}\frac{4}{R_{KJ}}\cos_{KJ}\sin_{KJ}^2\left[\frac{\partial V_\Sigma\left(R_{KJ}\right)}{\partial R_{KJ}}+\frac{\partial V_\Pi\left(R_{KJ}\right)}{\partial R_{KJ}}\right]\\
&- 2\frac{1}{R_{KJ}^2}\left\{5\cos_{KJ}^2-4\cos_{KJ}^4-1\right\}\left[V_\Sigma\left(R_{KJ}\right)-V_\Pi\left(R_{KJ}\right)\right],
\end{aligned}
$$

where the respective first two lines correspond to the purely distance depending cases in Eqs. (E.12) and (E.13).

BIBLIOGRAPHY

[1] E. Runge and E. K. U. Gross, "Density-Functional Theory for Time-Dependent Systems", Phys. Rev. Lett. **52**, 997 (1984).

[2] M. Fischer, J. Handt, and R. Schmidt, "Nonadiabatic quantum molecular dynamics with hopping. I. General formalism and case study", Phys. Rev. A **90**, 012525 (2014).

[3] N. T. Maitra, "Perspective: Fundamental aspects of time-dependent density functional theory", The Journal of Chemical Physics **144**, 220901 (2016).

[4] H.-D. Meyer, U. Manthe, and L. Cederbaum, "The multi-configurational time-dependent Hartree approach", Chemical Physics Letters **165**, 73 (1990).

[5] M. Beck, A. Jäckle, G. Worth, and H.-D. Meyer, "The multiconfiguration time-dependent Hartree (MCTDH) method: a highly efficient algorithm for propagating wavepackets", Physics Reports **324**, 1 (2000).

[6] O. Vendrell and H.-D. Meyer, "Multilayer multiconfiguration time-dependent Hartree method: Implementation and applications to a Henon–Heiles Hamiltonian and to pyrazine", The Journal of Chemical Physics **134**, 044135 (2011).

[7] R. P. Feynman, "Space-Time Approach to Non-Relativistic Quantum Mechanics", Rev. Mod. Phys. **20**, 367 (1948).

[8] F. Grossmann, Theoretical Femtosecond Physics, Springer (2008), 2nd. edition (2013).

[9] J. Vaníček, "Dephasing representation: Employing the shadowing theorem to calculate quantum correlation functions", Phys. Rev. E **70**, 055201 (2004).

[10] J. Vaníček, "Dephasing representation of quantum fidelity for general pure and mixed states", Phys. Rev. E **73**, 046204 (2006).

[11] F. Grossmann and A. L. Xavier Jr., "From the coherent state path integral to a semiclassical initial value representation of the quantum mechanical propagator", Physics Letters A **243**, 243 (1998).

[12] W. H. Miller, "The Semiclassical Initial Value Representation: A Potentially Practical Way for Adding Quantum Effects to Classical Molecular Dynamics Simulations", The Journal of Physical Chemistry A **105**, 2942 (2001).

[13] M. F. Herman and E. Kluk, "A semiclasical justification for the use of non-spreading wavepackets in dynamics calculations", Chemical Physics **91**, 27 (1984).

[14] K. G. Kay, "Integral expressions for the semiclassical time-dependent propagator", The Journal of Chemical Physics **100**, 4377 (1994).

[15] K. G. Kay, "Numerical study of semiclassical initial value methods for dynamics", The Journal of Chemical Physics **100**, 4432 (1994).

[16] S. Tomsovic and E. J. Heller, "Semiclassical dynamics of chaotic motion: Unexpected long-time accuracy", Phys. Rev. Lett. **67**, 664 (1991).

[17] X. Sun and W. H. Miller, "Semiclassical initial value representation for rotational degrees of freedom: The tunneling dynamics of HCl dimer", The Journal of Chemical Physics **108**, 8870 (1998).

[18] G. van de Sand and J. M. Rost, "Semiclassical time-dependent propagation in three dimensions for a Coulomb potential", Physical Review A **59**, R1723 (1999).

[19] X. Sun, H. Wang, and W. H. Miller, "Semiclassical theory of electronically nonadiabatic dynamics: Results of a linearized approximation to the initial value representation", The Journal of Chemical Physics **109**, 7064 (1998).

[20] X. Sun and W. H. Miller, "Forward–backward initial value representation for semiclassical time correlation functions", The Journal of Chemical Physics **110**, 6635 (1999).

[21] H. Wang, M. Thoss, and W. H. Miller, "Forward–backward initial value representation for the calculation of thermal rate constants for reactions in complex molecular systems", The Journal of Chemical Physics **112**, 47 (2000).

[22] M. Ovchinnikov, V. A. Apkarian, and G. A. Voth, "Semiclassical molecular dynamics computation of spontaneous light emission in the condensed phase: Resonance Raman spectra", The Journal of Chemical Physics **114**, 7130 (2001).

[23] A. O. Caldeira and A. J. Leggett, "Influence of Dissipation on Quantum Tunneling in Macroscopic Systems", Phys. Rev. Lett. **46**, 211 (1981).

[24] A. Caldeira and A. Leggett, "Path integral approach to quantum Brownian motion", Physica A: Statistical Mechanics and its Applications **121**, 587 (1983).

[25] E. J. Heller, "Time-dependent approach to semiclassical dynamics", The Journal of Chemical Physics **62**, 1544 (1975).

[26] F. Grossmann, "A semiclassical hybrid approach to many particle quantum dynamics", The Journal of Chemical Physics **125**, 014111 (2006).

[27] C.-M. Goletz and F. Grossmann, "Decoherence and dissipation in a molecular system coupled to an environment: an application of semiclassical hybrid dynamics", The Journal of Chemical Physics **130**, 244107 (2009).

[28] C.-M. Goletz, W. Koch, and F. Grossmann, "Semiclassical dynamics of open quantum systems: Comparing the finite with the infinite perspective", Chemical Physics **375**, 227 (2010).

[29] A. L. Kaledin and W. H. Miller, "Time averaging the semiclassical initial value representation for the calculation of vibrational energy levels", The Journal of Chemical Physics **118**, 7174 (2003).

[30] M. Ceotto, S. Atahan, G. F. Tantardini, and A. Aspuru-Guzik, "Multiple coherent states for first-principles semiclassical initial value representation molecular dynamics", The Journal of Chemical Physics **130**, 234113 (2009).

[31] M. Ceotto, D. dell'Angelo, and G. F. Tantardini, "Multiple coherent states semiclassical initial value representation spectra calculations of lateral interactions for CO on Cu(100)", The Journal of Chemical Physics **133**, 054701 (2010).

[32] A. L. Kaledin and W. H. Miller, "Time averaging the semiclassical initial value representation for the calculation of vibrational energy levels. II. Application to to H_2CO, NH_3, CH_4, CH_2D_2", The Journal of Chemical Physics **119**, 3078 (2003).

[33] R. Conte, A. Aspuru-Guzik, and M. Ceotto, "Reproducing Deep Tunneling Splittings, Resonances, and Quantum Frequencies in Vibrational Spectra From a Handful of Direct Ab Initio Semiclassical Trajectories", The Journal of Physical Chemistry Letters **4**, 3407 (2013).

[34] L. Wilets, E. Henley, M. Kraft, and A. Mackellar, "Classical many-body model for heavy-ion collisions incorporating the Pauli principle", Nuclear Physics A **282**, 341 (1977).

[35] G. Peilert, J. Randrup, H. Stöcker, and W. Greiner, "Clustering in nuclear matter at subsaturation densities", Physics Letters B **260**, 271 (1991).

[36] A. Kirrander and D. V. Shalashilin, "Quantum dynamics with fermion coupled coherent states: Theory and application to electron dynamics in laser fields", Phys. Rev. A **84**, 033406 (2011).

[37] C.-M. Goletz, "Semiclassical hybrid dynamics for open quantum systems", Ph.D. thesis, Technische Universität Dresden (2011).

[38] J. L. Sanz-Vicario, H. Bachau, and F. Martín, "Time-dependent theoretical description of molecular autoionization produced by femtosecond xuv laser pulses", Phys. Rev. A **73**, 033410 (2006).

[39] S. Römer and I. Burghardt, "Towards a variational formulation of mixed quantum-classical molecular dynamics", Molecular Physics **111**, 3618 (2013).

[40] J. H. van Vleck, "The Correspondence Principle in the Statistical Interpretation of Quantum Mechanics", PNAS **14**, 178 (1928).

[41] M. C. Gutzwiller, "Phase-Integral Approximation in Momentum Space and the Bound States of an Atom", Journal of Mathematical Physics **8**, 1979 (1967).

[42] R. Gelabert, X. Giménez, M. Thoss, H. Wang, and W. H. Miller, "Semiclassical description of diffraction and its quenching by the forward–backward version of the initial value representation", The Journal of Chemical Physics **114**, 2572 (2001).

[43] W. H. Press, Numerical Recipes 3rd Edition: The Art of Scientific Computing, Cambridge University Press (2007).

[44] M. F. Herman, "Time reversal and unitarity in the frozen Gaussian approximation for semiclassical scattering", The Journal of Chemical Physics **85**, 2069 (1986).

[45] E. J. Heller, "Frozen Gaussians: A very simple semiclassical approximation", The Journal of Chemical Physics **75**, 2923 (1981).

[46] K. G. Kay, "Semiclassical propagation for multidimensional systems by an initial value method", The Journal of Chemical Physics **101**, 2250 (1994).

[47] D. V. Shalashilin and M. S. Child, "The phase space CCS approach to quantum and semiclassical molecular dynamics for high-dimensional systems", Chemical Physics **304**, 103 (2004).

[48] W. H. Miller, "On the Relation between the Semiclassical Initial Value Representation and an Exact Quantum Expansion in Time-Dependent Coherent States", The Journal of Physical Chemistry B **106**, 8132 (2002).

[49] W. H. Miller, "An alternate derivation of the Herman-Kluk (coherent state) semiclassical initial value representation of the time evolution operator", Molecular Physics **100**, 397 (2002).

[50] S. K. Gray, D. W. Noid, and B. G. Sumpter, "Symplectic integrators for large scale molecular dynamics simulations: A comparison of several explicit methods", The Journal of Chemical Physics **101**, 4062 (1994).

[51] S. Garashchuk and J. C. Light, "Simplified calculation of the stability matrix for semiclassical propagation", The Journal of Chemical Physics **113**, 9390 (2000).

[52] H. Wu, M. Rahman, J. Wang, U. Louderaj, W. L. Hase, and Y. Zhuang, "Higher-accuracy schemes for approximating the Hessian from electronic structure calculations in chemical dynamics simulations", The Journal of Chemical Physics **133**, 074101 (2010).

[53] Y. Zhuang, M. R. Siebert, W. L. Hase, K. G. Kay, and M. Ceotto, "Evaluating the Accuracy of Hessian Approximations for Direct Dynamics Simulations", Journal of Chemical Theory and Computation **9**, 54 (2013).

[54] H. Wang, D. E. Manolopoulos, and W. H. Miller, "Generalized Filinov transformation of the semiclassical initial value representation", The Journal of Chemical Physics **115**, 6317 (2001).

[55] E. J. Heller, "Classical S-matrix limit of wave packet dynamics", The Journal of Chemical Physics **65**, 4979 (1976).

[56] E. J. Heller, "Wavepacket dynamics and quantum chaology", in M. J. Giannoni, A. Voros, and J. Zinn-Justin (editors), "Chaos et Physique Quantique/Chaos and Quantum Physics, Proc. Les Houches Summer School, Session LII 1989", North-Holland, Amsterdam (1991).

[57] X. Sun, H. Wang, and W. H. Miller, "On the semiclassical description of quantum coherence in thermal rate constants", The Journal of Chemical Physics **109**, 4190 (1998).

[58] H. Wang, X. Sun, and W. H. Miller, "Semiclassical approximations for the calculation of thermal rate constants for chemical reactions in complex molecular systems", The Journal of Chemical Physics **108**, 9726 (1998).

[59] H. Wang, M. Thoss, K. L. Sorge, R. Gelabert, X. Giménez, and W. H. Miller, "Semiclassical description of quantum coherence effects and their quenching: A forward–backward initial value representation study", The Journal of Chemical Physics **114**, 2562 (2001).

[60] E. J. Heller, "Quantum corrections to classical photodissociation models", The Journal of Chemical Physics **68**, 2066 (1978).

[61] J. Shao, J.-L. Liao, and E. Pollak, "Quantum transition state theory: Perturbation expansion", The Journal of Chemical Physics **108**, 9711 (1998).

[62] N. Makri and K. Thompson, "Semiclassical influence functionals for quantum systems in anharmonic environments", Chemical Physics Letters **291**, 101 (1998).

[63] J. Shao and N. Makri, "Forward-Backward Semiclassical Dynamics without Prefactors", The Journal of Physical Chemistry A **103**, 7753 (1999).

[64] E. Martin-Fierro and E. Pollak, "Forward-backward semiclassical initial value series representation of quantum correlation functions", The Journal of Chemical Physics **125**, 164104 (2006).

[65] E. Wigner, "On the Quantum Correction For Thermodynamic Equilibrium", Phys. Rev. **40**, 749 (1932).

[66] M. Buchholz, C.-M. Goletz, F. Grossmann, B. Schmidt, J. Heyda, and P. Jungwirth, "Semiclassical Hybrid Approach to Condensed Phase Molecular Dynamics: Application to the I_2Kr_{17} Cluster", The Journal of Physical Chemistry A **116**, 11199 (2012).

[67] M. Schlosshauer, Decoherence and the Quantum-To-Classical Transition, Springer (2008).

[68] K. M. Christoffel and J. M. Bowman, "Investigations of self-consistent field, scf ci and virtual stateconfiguration interaction vibrational energies for a model three-mode system", Chemical Physics Letters **85**, 220 (1982).

[69] Z. Bihary, R. B. Gerber, and V. A. Apkarian, "Vibrational self-consistent field approach to anharmonic spectroscopy of molecules in solids: Application to iodine in argon matrix", The Journal of Chemical Physics **115**, 2695 (2001).

[70] Y. Elran and K. G. Kay, "Improving the efficiency of the Herman-Kluk propagator by time integration", The Journal of Chemical Physics **110**, 3653 (1999).

[71] Y. Elran and K. G. Kay, "Time-integrated form of the semiclassical initial value method", The Journal of Chemical Physics **110**, 8912 (1999).

[72] M. Ceotto, S. Atahan, S. Shim, G. F. Tantardini, and A. Aspuru-Guzik, "First-principles semiclassical initial value representation molecular dynamics", Physical Chemistry Chemical Physics **11**, 3861 (2009).

[73] M. Ceotto, S. Valleau, G. F. Tantardini, and A. Aspuru-Guzik, "First principles semiclassical calculations of vibrational eigenfunctions ", The Journal of Chemical Physics **134**, 234103 (2011).

[74] M. Ceotto, G. F. Tantardini, and A. Aspuru-Guzik, "Fighting the curse of dimensionality in first-principles semiclassical calculations: Non-local reference states for large number of dimensions ", The Journal of Chemical Physics **135**, 214108 (2011).

[75] D. Tamascelli, F. S. Dambrosio, R. Conte, and M. Ceotto, "Graphics processing units accelerated semiclassical initial value representation molecular dynamics", The Journal of Chemical Physics **140**, 174109 (2014).

[76] M. Ceotto, Y. Zhuang, and W. L. Hase, "Accelerated direct semiclassical molecular dynamics using a compact finite difference Hessian scheme", The Journal of Chemical Physics **138**, 054116 (2013).

[77] P. M. Morse, "Diatomic molecules according to the wave mechanics. II. Vibrational levels", Phys. Rev. **34**, 57 (1929).

[78] D. Ter Haar, "The Vibrational Levels of an Anharmonic Oscillator", Physical Review **34**, 57 (1946).

[79] G. Herzberg and K.-P. Huber, Molecular Spectra and Molecular Structure: I. Spectra of Diatomic Molecules, Van Nostrand Reinhold Company Inc. (1950).

[80] M. Karavitis and V. A. Apkarian, "Vibrational coherence of I_2 in solid Kr", The Journal of Chemical Physics **120**, 292 (2004).

[81] H. Ahlborn, X. Ji, B. Space, and P. B. Moore, "A combined instantaneous normal mode and time correlation function description of the infrared vibrational spectrum of ambient water", The Journal of Chemical Physics **111**, 10622 (1999).

[82] J. Palmeri, M. Manghi, and N. Destainville, "Thermal Denaturation of Fluctuating DNA Driven by Bending Entropy", Phys. Rev. Lett. **99**, 088103 (2007).

[83] C. Harabati, J. M. Rost, and F. Grossmann, "Long-time and unitary properties of semiclassical initial value representations", The Journal of Chemical Physics **120**, 26 (2004).

[84] V. A. Mandelshtam and H. S. Taylor, "Harmonic inversion of time signals and its applications", The Journal of Chemical Physics **107**, 6756 (1997).

[85] V. A. Mandelshtam and H. S. Taylor, "Erratum: "Harmonic inversion of time signals and its applications" [J. Chem. Phys. 107, 6756 (1997)]", The Journal of Chemical Physics **109**, 4128 (1998).

[86] M. Buchholz, F. Grossmann, and M. Ceotto, "Mixed semiclassical initial value representation time-averaging propagator for spectroscopic calculations", The Journal of Chemical Physics **144**, 094102 (2016).

[87] A. J. Leggett, S. Chakravarty, A. T. Dorsey, M. P. A. Fisher, A. Garg, and W. Zwerger, "Dynamics of the dissipative two-state system", Rev. Mod. Phys. **59**, 1 (1987).

[88] P. Hänggi and G.-L. Ingold, "Fundamental aspects of quantum Brownian motion", Chaos **15**, 026105 (2005).

[89] G.-L. Ingold, "Path integrals and Their Application to Dissipative Quantum Systems", in A. Buchleitner and K. Hornberger (editors), "Coherent Evolution in Noisy Environments", Lecture Notes in Physics 611, 1–53, Springer-Verlag Berlin Heidelberg (2002).

[90] B. Schmidt and U. Lorenz, "WavePacket: A Matlab package for numerical quantum dynamics. I: Closed quantum systems and discrete variable representations", Computer Physics Communications **213**, 223 (2017).

[91] B. Schmidt and C. Hartmann, "WavePacket: A Matlab package for numerical quantum dynamics. II: Open quantum systems and optimal control", Manuscript in preparation (2017).

[92] A. M. Levine, M. Shapiro, and E. Pollak, "Hamiltonian theory for vibrational dephasing rates of small molecules in liquids", The Journal of Chemical Physics **88**, 1959 (1988).

[93] E. Pollak, "Transition-state theory for tunneling in dissipative media", Phys. Rev. A **33**, 4244 (1986).

[94] R. B. Williams and R. F. Loring, "Vibrational dephasing of an anharmonic solute strongly coupled to solvent", The Journal of Chemical Physics **110**, 10899 (1999).

[95] T. Joutsuka and K. Ando, "Vibrational spectroscopy and relaxation of an anharmonic oscillator coupled to harmonic bath", The Journal of Chemical Physics **134**, 204511 (2011).

[96] Y. I. Georgievskii and A. A. Stuchebrukhov, "Pure dephasing of a nonlinear vibrational mode. Non-Markovian line shape", The Journal of Chemical Physics **93**, 6699 (1990).

[97] M. Rosenau da Costa, A. O. Caldeira, S. M. Dutra, and H. Westfahl, "Exact diagonalization of two quantum models for the damped harmonic oscillator", Phys. Rev. A **61**, 022107 (2000).

[98] E. L. Lewis, C. W. P. Palmer, and J. L. Cruickshank, "Iodine molecular constants from absorption and laser fluorescence", American Journal of Physics **62**, 350 (1994).

[99] C. W. David, "The Birge Sponer Extrapolation", Chemistry Education Materials Paper 63 (2008).

[100] Z. Bihary, M. Karavitis, and V. A. Apkarian, "Onset of decoherence: Six-wave mixing measurements of vibrational decoherence on the excited electronic state of I_2 in solid argon", The Journal of Chemical Physics **120**, 8144 (2004).

[101] D. Segale, M. Karavitis, E. Fredj, and V. A. Apkarian, "Quantum coherent dissipation: A glimpse of the "cat"", The Journal of Chemical Physics **122**, 111104 (2005).

[102] F. Stienkemeier and K. K. Lehmann, "Spectroscopy and dynamics in helium nanodroplets", Journal of Physics B: Atomic, Molecular and Optical Physics **39**, R127 (2006).

[103] R. Zadoyan, Z. Li, C. C. Martens, and V. A. Apkarian, "The breaking and remaking of a bond: Caging of I2 in solid Kr", The Journal of Chemical Physics **101**, 6648 (1994).

[104] C. J. Bardeen, J. Che, K. R. Wilson, V. V. Yakovlev, V. A. Apkarian, C. C. Martens, R. Zadoyan, B. Kohler, and M. Messina, "Quantum control of I_2 in the gas phase and in condensed phase solid Kr matrix", The Journal of Chemical Physics **106**, 8486 (1997).

[105] M. Gühr, H. Ibrahim, and N. Schwentner, "Controlling vibrational wave packet revivals in condensed phase: Dispersion and coherence for Br_2 in solid Ar", Phys. Chem. Chem. Phys. **6**, 5353 (2004).

[106] M. Karavitis, T. Kumada, I. U. Goldschleger, and V. A. Apkarian, "Vibrational dissipation and dephasing of $I_2(\nu$=1-19) in solid Kr", Phys. Chem. Chem. Phys. **7**, 791 (2005).

[107] M. Gühr, M. Bargheer, M. Fushitani, T. Kiljunen, and N. Schwentner, "Ultrafast dynamics of halogens in rare gas solids", Phys. Chem. Chem. Phys. **9**, 779 (2007).

[108] D. Segale and V. A. Apkarian, "Dissipative quantum coherent dynamics probed in phase-space: Electronically resonant 5-color 4-wave mixing on I_2(B) in solid Kr", The Journal of Chemical Physics **135**, 024203 (2011).

[109] M. Ovchinnikov and V. A. Apkarian, "Condensed phase spectroscopy from mixed-order semiclassical molecular dynamics: Absorption, emission, and resonant Raman spectra of I_2 isolated in solid Kr", The Journal of Chemical Physics **105**, 10312 (1996).

[110] J. M. Riga, E. Fredj, and C. C. Martens, "Simulation of vibrational dephasing of I_2 in solid Kr using the semiclassical Liouville method", The Journal of Chemical Physics **124**, 064506 (2006).

[111] Z. Ma and D. F. Coker, "Quantum initial condition sampling for linearized density matrix dynamics: Vibrational pure dephasing of iodine in krypton matrices", The Journal of Chemical Physics **128**, 244108 (2008).

[112] X. Cheng and J. A. Cina, "Variational mixed quantum/semiclassical simulation of dihalogen guest and rare-gas solid host dynamics", The Journal of Chemical Physics **141**, 034113 (2014).

[113] F. O. Ellison, "A Method of Diatomics in Molecules. I. General Theory and Application to H_2O", Journal of the American Chemical Society **85**, 3540 (1963).

[114] A. Borowski and O. Kühn, "Towards a quantum mechanical description of the photochemistry of dihalogens in rare gas matrices", Journal of Photochemistry and Photobiology A: Chemistry **190**, 169 (2007), theoretical Aspects of Photoinduced Processes in Complex Systems.

[115] J. E. Lennard-Jones, "The electronic structure of some diatomic molecules", Transactions of the Faraday Society **25**, 668 (1929).

[116] E. B. Wilson, J. C. Decius, and P. C. Cross, Molecular Vibrations, McGraw-Hill, New York (1955).

[117] G. Strang, "On the Construction and Comparison of Difference Schemes", SIAM Journal on Numerical Analysis **5**, 506 (1968).

[118] J. A. Fleck, J. R. Morris, and M. D. Feit, "Time-dependent propagation of high energy laser beams through the atmosphere", Applied physics **10**, 129 (1976).

[119] W. H. Zurek, "Decoherence and the Transition from Quantum to Classical", Physics Today **44**, 36 (1991).

[120] I. Horenko, B. Schmidt, and C. Schütte, "Multidimensional classical Liouville dynamics with quantum initial conditions", The Journal of Chemical Physics **117**, 4643 (2002).

[121] W. Humphrey, A. Dalke, and K. Schulten, "VMD – Visual Molecular Dynamics", Journal of Molecular Graphics **14**, 33 (1996).

[122] J. Stone, "An Efficient Library for Parallel Ray Tracing and Animation", Master's thesis, Computer Science Department, University of Missouri-Rolla (1998).

[123] S. Röblitz, B. Schmidt, and M. Weber, "TrajLab: MATLAB based programs for trajectory simulations of molecules", (2014).

[124] R. I. McLachlan and P. Atela, "The accuracy of symplectic integrators", Nonlinearity **5**, 541 (1992).

[125] C. Dorso, S. Duarte, and J. Randrup, "Classical simulation of the Fermi gas", Physics Letters B **188**, 287 (1987).

[126] D. H. Boal and J. N. Glosli, "Quasiparticle model for nuclear dynamics studies: Ground-state properties", Phys. Rev. C **38**, 1870 (1988).

[127] V. Latora, M. Belkacem, and A. Bonasera, "Dynamics of Instabilities and Intermittency", Phys. Rev. Lett. **73**, 1765 (1994).

[128] T. Maruyama, A. Ohnishi, and H. Horiuchi, "Evolution of reaction mechanisms in the light heavy-ion system", Phys. Rev. C **45**, 2355 (1992).

[129] K. Niita, S. Chiba, T. Maruyama, T. Maruyama, H. Takada, T. Fukahori, Y. Nakahara, and A. Iwamoto, "Analysis of the (N, xN') reactions by quantum molecular dynamics plus statistical decay model", Phys. Rev. C **52**, 2620 (1995).

[130] A. Ono, H. Horiuchi, T. Maruyama, and A. Ohnishi, "Fragment formation studied with antisymmetrized version of molecular dynamics with two-nucleon collisions", Phys. Rev. Lett. **68**, 2898 (1992).

[131] L. Wilets and J. S. Cohen, "Fermion molecular dynamics in atomic, molecular, and optical physics", Contemporary Physics **39**, 163 (1998).

[132] H. Feldmeier and J. Schnack, "Molecular dynamics for fermions", Rev. Mod. Phys. **72**, 655 (2000).

[133] T. Engl, P. Plößl, J. D. Urbina, and K. Richter, "The semiclassical propagator in fermionic Fock space", Theoretical Chemistry Accounts **133**, 1 (2014).

[134] T. Engl, J. D. Urbina, and K. Richter, "The semiclassical propagator in Fock space: dynamical echo and many-body interference", Philosophical Transactions of the Royal Society of London A: Mathematical, Physical and Engineering Sciences **374** (2016).

[135] C. Harabati and K. G. Kay, "Semiclassical initial value calculations of the collinear helium atom", The Journal of Chemical Physics **127**, 084104 (2007).

[136] F. Grossmann and T. Kramer, "Spectra of harmonium in a magnetic field using an initial value representation of the semiclassical propagator", Journal of Physics A: Mathematical and Theoretical **44**, 445309 (2011).

[137] P. Elliott and N. T. Maitra, "Electron correlation via frozen Gaussian dynamics", The Journal of Chemical Physics **135**, 104110 (2011).

[138] D. V. Shalashilin and M. S. Child, "Electronic energy levels with the help of trajectory-guided random grid of coupled wave packets. I. Six-dimensional simulation of H_2", The Journal of Chemical Physics **122**, 224108 (2005).

[139] J. M. Rost and E. J. Heller, "Semiclassical scattering of charged particles", Journal of Physics B: Atomic, Molecular and Optical Physics **27**, 1387 (1994).

[140] F. Grossmann, M. Buchholz, E. Pollak, and M. Nest, "Spin effects and the Pauli principle in semiclassical electron dynamics", Phys. Rev. A **89**, 032104 (2014).

[141] D. Bauer, "Two-dimensional, two-electron model atom in a laser pulse: Exact treatment, single-active-electron analysis, time-dependent density-functional theory, classical calculations, and nonsequential ionization", Phys. Rev. A **56**, 3028 (1997).

[142] S. Zhang and E. Pollak, "A prefactor free semiclassical initial value series representation of the propagator", The Journal of Chemical Physics **121**, 3384 (2004).

[143] F. Gottwald, S. D. Ivanov, and O. Kühn, "Applicability of the Caldeira–Leggett Model to Vibrational Spectroscopy in Solution", The Journal of Physical Chemistry Letters **6**, 2722 (2015).

[144] F. Gottwald, S. D. Ivanov, and O. Kühn, "Vibrational spectroscopy via the Caldeira-Leggett model with anharmonic system potentials", The Journal of Chemical Physics **144**, 164102 (2016).

[145] "Divide and Conquer ab initio semiclassical molecular dynamics for spectroscopic calculations of complex systems", http://users.unimi.it/ceotto/erc.html, accessed: January 27th, 2017.

[146] Y. Wang and J. M. Bowman, "Towards an ab initio flexible potential for water, and post-harmonic quantum vibrational analysis of water clusters", Chemical Physics Letters **491**, 1 (2010).

[147] Y. Wang, X. Huang, B. C. Shepler, B. J. Braams, and J. M. Bowman, "Flexible, ab initio potential, and dipole moment surfaces for water. I. Tests and applications for clusters up to the 22-mer", The Journal of Chemical Physics **134**, 094509 (2011).

[148] Y. Wang and J. M. Bowman, "Ab initio potential and dipole moment surfaces for water. II. Local-monomer calculations of the infrared spectra of water clusters", The Journal of Chemical Physics **134**, 154510 (2011).

[149] Y. Wang and J. M. Bowman, "Calculations of the IR spectra of bend fundamentals of $(H_2O)_{n=3,4,5}$ using the WHBB_2 potential and dipole moment surfaces", Phys. Chem. Chem. Phys. **18**, 24057 (2016).

[150] C. Cohen-Tannoudji, B. Diu, and F. Laloe, Quantenmechanik, Walter de Gruyter, 2nd edition (1999).

[151] J. S. Bader, B. J. Berne, E. Pollak, and P. Hänggi, "The energy relaxation of a nonlinear oscillator coupled to a linear bath", The Journal of Chemical Physics **104**, 1111 (1996).

LIST OF PUBLICATIONS

- M. Buchholz, C.-M. Goletz, F. Grossmann, B. Schmidt, J. Heyda, and P. Jungwirth, "Semiclassical Hybrid Approach to Condensed Phase Molecular Dynamics: Application to the I_2Kr_{17} Cluster", The Journal of Physical Chemistry A, **116**, 11199 (2012)
- F. Grossmann, M. Buchholz, E. Pollak, and M. Nest, "Spin effects and the Pauli principle in semiclassical electron dynamics", Physical Review A, **89**, 032104 (2014)
- M. Buchholz, F. Grossmann, and M. Ceotto, "Mixed semiclassical initial value representation time-averaging propagator for spectroscopic calculations", The Journal of Chemical Physics, **144**, 094102 (2016)

ERKLÄRUNG

Hiermit versichere ich, dass ich die vorliegende Arbeit ohne unzulässige Hilfe Dritter und ohne Benutzung anderer als der angegebenen Hilfsmittel angefertigt habe; die aus fremden Quellen direkt oder indirekt übernommenen Gedanken sind als solche kenntlich gemacht. Die Arbeit wurde bisher weder im Inland noch im Ausland in gleicher oder ähnlicher Form einer anderen Prüfungsbehörde vorgelegt.

Die Arbeit wurde am Institut für Theoretische Physik der Technischen Universität Dresden unter Betreuung von Prof. Dr. Rüdiger Schmidt im Zeitraum vom 01.07.2011 bis 10.03.2017 angefertigt.

Ich erkenne die Promotionsordnung der Fakultät Mathematik und Naturwissenschaften der TU Dresden in der Fassung vom 23.02.2011 an.

Dresden, 10.03.2017

DANKSAGUNG

Zum Gelingen dieser Arbeit haben zahlreiche Menschen auf unterschiedliche Weise beigetragen. Ihnen allen möchte ich an dieser Stelle danken. Prof. Rüdiger Schmidt danke ich für die Aufnahme in die Arbeitsgruppe, in der stets ein freundschaftliches und kollegiales Klima herrschte, und für essentielle Unterstützung insbesondere bei der Finanzierung in der Endphase der Arbeit. Frank Großmann hatte immer ein offenes Ohr, hat das Thema gestellt und in vielen Diskussionen wichtige Anregungen geliefert und hat den Großteil der Finanzierung übernommen bzw. vermittelt. Darüber hinaus ist es ihm gelungen, mich immer wieder zu Besuchen bei und Gesprächen mit anderen Wissenschaftlern sowie zu Konferenzteilnahmen zu bewegen, was nicht unbedingt meinem Naturell entspricht und gerade deswegen sehr wertvoll war.

Allen anderen Doktoranden und sonstigen Mitgliedern der Arbeitsgruppe danke ich für viele interessante Gespräche mit und ohne Kaffee über Physik, Gott und die Welt, Autos, Häuser und Mensaessen. Bei gelegentlich auftretenden IT-Problemen war insbesondere Jan Handt eine weit über "Have you tried turning it off and on again?" hinaus gehende wertvolle Hilfe. Dank auch allen Korrekturlesern aus der Arbeitsgruppe.

Zwei Institutionen haben ebenfalls eine gewichtige Rolle gespielt. Die IMPRS "Dynamical Processes in Atoms, Molecules and Solids" des Max-Planck-Instituts für Physik komplexer Systeme Dresden hat mit ihren vielfältigen Angeboten an Seminaren, Retreats und Kursen wesentlich zur Weitung meines fachlichen Horizonts beigetragen. Bedanken möchte ich mich auch für 14 Monate Finanzierung. Zum Ende der Promotion hin war das Abschlussstipendium der Graduiertenakademie der TU Dresden ebenfalls eine große Hilfe.

It was my pleasure and privilege to meet many great scientists quite literally from all over the world. I would like to thank all collaborators for contributing to the enhancement of my understanding of physics. Visiting David Tannor at the Weizmann Institute was a great experience not only from a scientific perspective. Michele Ceotto deserves many thanks and much praise for his ongoing support and for proof-reading parts of this work. Burkhard Schmidt has provided valuable input at the beginning of my PhD studies.

Zuletzt danke ich natürlich auch meiner Familie. Insbesondere Sophie und Samuel hatten es nicht immer leicht mit mir in den letzten Jahren – vielen Dank für eure Unterstützung!